NONLINEAR ARRAY PROCESSING TECHNIQUES WITH APPLICATIONS TO CORRELATED MULTIPATH

by

© JAMES P. REILLY, B.A.Sc., M.Eng.

A Thesis
Submitted to the School of Graduate Studies
in Partial Fulfilment of the Requirements
for the Degree
Doctor of Philosophy

McMaster University

March, 1981

NONLINEAR ARRAY PROCESSING TECHNIQUES

TO MY WIFE, BETH

WHOSE LOVE AND SUPPORT DURING THIS WORK HAS

MADE THE WHOLE EFFORT A TRULY GREAT EXPERIENCE

and

TO MY DAUGHTER, SARAH

HOPING THAT SHE TOO WILL SOMEDAY

ASPIRE TO UNDERTAKE SOMETHING SUCH AS THIS

DOCTOR OF PHILOSOPHY (1981)
(Electrical Engineering)

McMaster University
Hamilton, Canada

TITLE: Nonlinear Array Processing Techniques with Applications to Correlated Multipath

AUTHOR: JAMES P. REILLY, B.A.Sc. (University of Waterloo), M.Eng. (McMaster University)

SUPERVISOR: Professor S. Haykin

NUMBER OF PAGES: xiv, 316

SCOPE AND CONTENTS: This thesis discusses new methods of estimating the angle of arrival of a plane wave incident upon an antenna array. Emphasis is placed on the situation where the original incident wave is corrupted by the effects of multipath propagation.

ABSTRACT

The estimation of the direction of a plane wave incident upon a linear receiving antenna array and field-mapping techniques are considered in this thesis. The emphasis of the presentation is directed towards radar, and specific attention is given to the situation where the incident plane wave is corrupted by the effects of multipath propagation.

First, the phenomenon of multipath and its experimental simulation are discussed. It is then pointed out how conventional linear array processing techniques fail in the presence of multipath propagation. These considerations lead us to consider other nonlinear array processing techniques.

There are two such approaches considered. The first is the modification of statistical time series analysis to suit the array processing application. The Burg method and the least-squares (LS) algorithm developed by Ulrych and Clayton are two time-series methods which are discussed in detail. Results show that the Burg method is not applicable in this application, whereas it is shown that the LS algorithm behaves well at high SNR.

The second appproach considered is the maximum likelihood (ML) formulation. There are also two realizations of this approach which are discussed in depth.

Both realizations are based on setting up the appropriate likelihood functions for the situation considered; then, the resulting structure is modified so that the required optimizations need only be performed in the specific parameter(s) of interest. This results in a more computationally efficient estimator.

The first ML formulation discussed is applicable only to the specular multipath environment. In this situation, the direct and reflected signal components are symmetrically positioned in elevation about the normal of the array. This configuration results in a particularly simple estimator structure. The second ML formulation considered is the case where the individual signal components may be incident from arbitrary directions. The results indicate that both these ML methods perform better than the time-series techniques.

The performance for each method is compared to the corresponding theoretical values. The results are checked by computer simulation and are validated by the use of an experimental multipath simulation system built during the course of this work.

TABLE OF CONTENTS

TABLE OF CONTENTS (cont'd)

LIST OF FIGURES

LIST OF FIGURES (cont'd)

LIST OF FIGURES (cont'd)

LIST OF FIGURES (cont'd)

ACKNOWLEDGEMENTS

I would like to acknowledge the considerable effort my supervisor, Dr. S. Haykin, has contributed to this work. He has given freely and patiently of his time, and has been a very favourable influence in my academic development.

Dr. R. de Buda has offered many helpful and constructive criticisms to this thesis. His comments have led to a more complete and improved effort. I also acknowledge the help of the two other members of my supervisory committee, namely, Dr. B. Garside and Dr. C. Carter. I am grateful for the helpful discussions with Dr. D. Taylor. His suggestions have helped conceive some of the important concepts central in this work.

I also thank my wife Beth, for contributing in so many ways to this thesis. She has made a great many sacrifices in my pursuit of these studies.

I also thank Ms. Nancy Sine and the others in the Word Processing Centre, for being so cooperative and helpful in the typing of this manuscript.

NOMENCLATURE

The following notational conventions are used throughout this thesis. In some cases, the same symbol will be used for more than one quantity, but the distinction will be obvious from the context of the discussion.

$\tilde{\cdot}$	tilde over the symbol indicates a complex quantity.
$\underline{\cdot}$	underbar with a small letter indicates a vector quantity, except for the symbols $\vec{k}$, $\vec{z}$.
$\underline{\underline{\cdot}}$	underbar with a capital letter indicates a matrix quantity.
$\{\cdot\}$	brace brackets indicate the set of all elements assumed by the symbol.
n	used as an index denotes variation in space.
i	used as an index denotes variation in time.
E[.]	denotes expectation of the quantity within the brackets.
T(H)	superscript indicates the (Hermitian) transpose of the corresponding matrix.
$\tilde{a}$	complex amplitude of incident plane wave.
$\underline{a}$	vector of autoregressive coefficients.
$\underline{c}$	vector of moving average coefficients.
d	distance between elements of array.
$e^{(M)}$	M'th order prediction error.
f_c	centre frequency of received signal.

$\vec{k}$ vector wavenumber of incident wave.

$x(n)$ excitation of the nth array element.

$w(n)$ Gaussian noise contribution at the nth element.

$\vec{z}$ unit vector pointing along the line of the array.

BW signal separation in standard beamwidths.

$L(\phi)$ quantity to be maximized in the symmetric ML structure. (Likelihood function.)

$L_A(\phi)$ quantity to be maximized in the asymmetric ML structure. (Likelihood function.)

K total number of time samples available.

M number of incident plane waves, or autoregressive filter order.

N number of elements of the array.

P_M M'th order prediction error power.

$\underline{R}$ autocorrelation matrix.

$RSS(\phi)$ approximation to the residual sum-of-squares of the noise components about the point ϕ.

$S_x(.)$ power spectral density of the process x.

$\underline{V}$ covariance matrix of observations.

α arbitrary phase shift quantity.

$\underline{\beta}$ vector of parameters.

λ wavelength of incident plane wave.

θ actual angle of incidence of plane wave measured from normal of the array.

ϕ electrical phase shift from element to element due to the plane wave incident from angle θ.

ρ reflection coefficient of reflecting surface.

ψ phase difference between direct and reflected plane waves at the centre of the array.

σ_w^2 variance of receiver front-end noise.

Furthermore, we define the following acronyms:

MEM maximum entropy method.

PEF prediction-error filter.

ML maximum likelihood.

LS least squares.

AR autoregressive.

MA moving average.

ARMA autoregressive-moving average.

rms root mean-square.

SNR signal-to-noise ratio.

CHAPTER 1

INTRODUCTION

1.1 General

Array processing in its most general sense is the name given to the estimation of the parameters describing a field into which a receiving array is immersed. The array in question is usually composed of a finite number of discrete sensors, arranged either in one dimension (linear) or in two dimensions (planar). It is possible to conceive of three-dimensional arrays; however, they are not given serious consideration in the literature and hence, will not be considered further here.

The fields into which the array is immersed will be of various types, depending on the specific application in which the array processing technique is used. For example, in a geophysical problem, the fields are caused by pressure waves propagating through the earth originated by some tremor. The velocity of propagation of the wave, its Fourier transform, and the direction of propagation are all parameters of interest which are to be estimated by the array processing algorithm.

Another area in which array processing is used extensively is sonar. In this instance, the fields are again caused by pressure waves, but in this case they are usually generated by an active source. These waves are then reflected from some solid mass in the water (e.g. the bottom, fish, submarine, etc.), back to the receiver array. The parameters of interest describing the field in this case would be the direction of propagation of the wave, and the delay time due to the wave propagation.

The emphasis of this thesis will be directed towards a third application area of array processing, namely, radar. In this case, the receiving array is used for estimation of target direction. Since it has been pointed out that array processing may be used in both geophysical and sonar areas, it is intended that the methods which will be discussed in this thesis are also applicable in these disciplines. However, the discussion from this point forward will be directed towards the application of array processing techniques in radar.

We shall now consider in more detail some aspects of array processing. Fig. 1-1 shows a uniformly spaced, linear array with N elements with a plane wave at angle θ incident upon it. We arbitrarily define a spatial origin at the centre of the array. Note that if the number of elements, N is odd, there will be an element at the origin. However, if

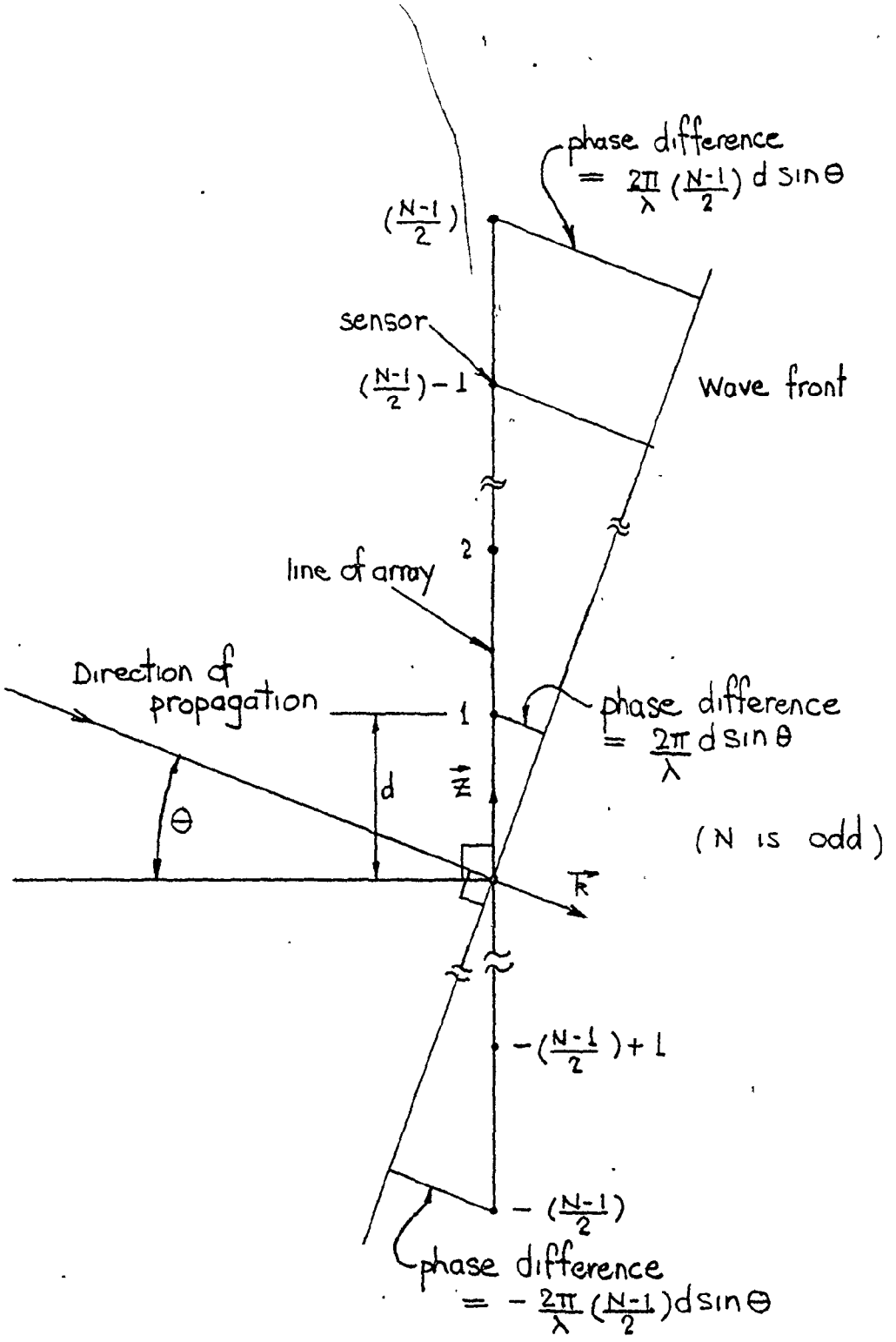

Fig 1-1 Geometrical configuration of a linear array with an incident plane wave

N is even, no element will be present at the origin, and the elements will be situated at normalized positions $\pm$ 1/2, $\pm$ 3/2, ..., $\pm$ (N-1)/2. It is implied throughout this thesis that the array is oriented in the vertical direction. The complex envelope of the excitation of the nth element $\tilde{x}(n)$ due to the incident plane wave, in the absence of noise, is given by

$$\tilde{x}(n) = \tilde{a}(t) \exp [j2\pi n \vec{k} \cdot \vec{z}] \qquad (1\text{-}1)$$

where $\tilde{a}(t)$ is the complex envelope of the received signal. This term describes the effect of any modulation the incident wave may have; e.g. a pulse or a chirp waveform in radar.

$\vec{k}$ is the vector wavenumber of the incident wave.

$\vec{z}$ is a unit vector pointing along the line of the array.

In the situation where a single plane wave with constant carrier frequency is incident upon a uniformly spaced linear array, (1-1) may be reduced to

$$\tilde{x}(n) = \tilde{a}(t) \exp \{j \frac{2\pi d}{\lambda} n \sin \theta\}$$

where d is the inter-element spacing

λ is the received radar wavelength.

The approximation in (1-1) is valid provided the inverse

bandwidth of $\tilde{a}(t)$ is small compared to the transit time of the signal across the array.

We now define the term ϕ as

$$\phi = \frac{2\pi d}{\lambda} \sin \theta \qquad (1-2)$$

which is the electrical phase-shift from element-to-element along the array. Substituting (1-2) into (1-1) we obtain

$$\tilde{x}(n) = \tilde{a}(t) \exp \{j\, n\, \phi\} \qquad (1-3)$$

$$-\frac{N-1}{2} \leq n \leq \frac{N-1}{2}$$

We therefore see that the response of the array to a single plane wave at a given instant of time is a rotating exponential. That is, the phase of the elemental excitations varies linearly with the spatial index n (or with the vertical position along the face of the array).

If, for example, M plane waves, originating from different direction angles θ_i, i=1, ..., M are incident upon the array, then the resultant spatial sequence will be a sum of rotating exponentials with different values for ϕ_i, i=1, ..., M. In the case when M=1, the phase angle of the excitation $\tilde{x}(n)$ is a simple linear function of n. However, for M>1, the phase of the quantity $\tilde{x}(n)$ takes the form

$$\text{ang}\{\tilde{x}(n)\} = \tan^{-1}\left[\frac{\text{Im}[\tilde{a}_1(t)\exp(n\phi_1)+\tilde{a}_2(t)\exp(n\phi_2)+\ldots+\tilde{a}_M(t)\exp(n\phi_M)]}{\text{Re}[\tilde{a}_1(t)\exp(n\phi_1)+\tilde{a}_2(t)\exp(n\phi_2)+\ldots+\tilde{a}_M(t)\exp(n\phi_M)]}\right] \quad (1\text{-}4)$$

This is a very cumbersome nonlinear expression, and it is this type of expression with which we must deal when handling general array processing problems.

Suppose now that we wish to estimate the parameter ϕ corresponding to a particular set of elemental excitations due to a single plane wave as defined by (1-3). One well known method is the approach where the excitation of the nth element is shifted by an amount $-n\alpha$, where $-180 < \alpha \leq 180$ degrees. The phase-shifted elemental contributions are then summed together. The output $S(\alpha,t)$ of this processor is obtained from (1-3) as

$$S(\alpha,t) = \tilde{a}(t) \sum_n \exp\{jn(\phi-\alpha)\}$$

$$= \tilde{a}(t)\cdot\frac{\sin N(\phi-\alpha)/2}{\sin(\phi-\alpha)/2} \quad (1\text{-}5)$$

This is a very familiar form and is shown plotted in Fig. 1-2 for $\alpha=0$, at a given time instant. Note that it has a maximum value of N at $\alpha = \phi$. Thus, in order to estimate ϕ we find the phase shift α which maximizes the sum of the phase-shifted elemental excitations. The true angle θ is

then obtained through (1-2). The quantity $S(\alpha,t)$ is a measure of the sensitivity of the array response to an incoming signal oriented at angle α, and it is referred to as the radiation pattern of the array. Because of the fact that the array is only finite in extent, the radiation pattern of Fig. 1-2 exhibits a main lobe or "beam" of finite width, and several side-lobes. These side-lobes will cause the array to respond to a wave incident in a direction other than that to which it is tuned. Also, because of the finite width of the main lobe, receiver noise will cause error in the estimate of the direction of incidence of the desired wave. We wish to accomplish the minimization of these two effects through the use of various array processing techniques, which will be described in more detail in the text of this thesis.

The angular separation from the peak of the main lobe to the first null of the response in Fig. 1-2 is referred to as a standard beamwidth of the array, equal to $2\pi/N$ radians. The symbol BW, which will be used extensively in this thesis, means angular separation in standard beamwidths.

In (1-5), each of the elemental signals are weighted uniformly. It is possible to change the shape of $S(\alpha,t)$ by applying a particular "weighting function" to the sensor outputs. The action of phase-shifting, weighting and summing the elemental outputs is referred to as beamforming.

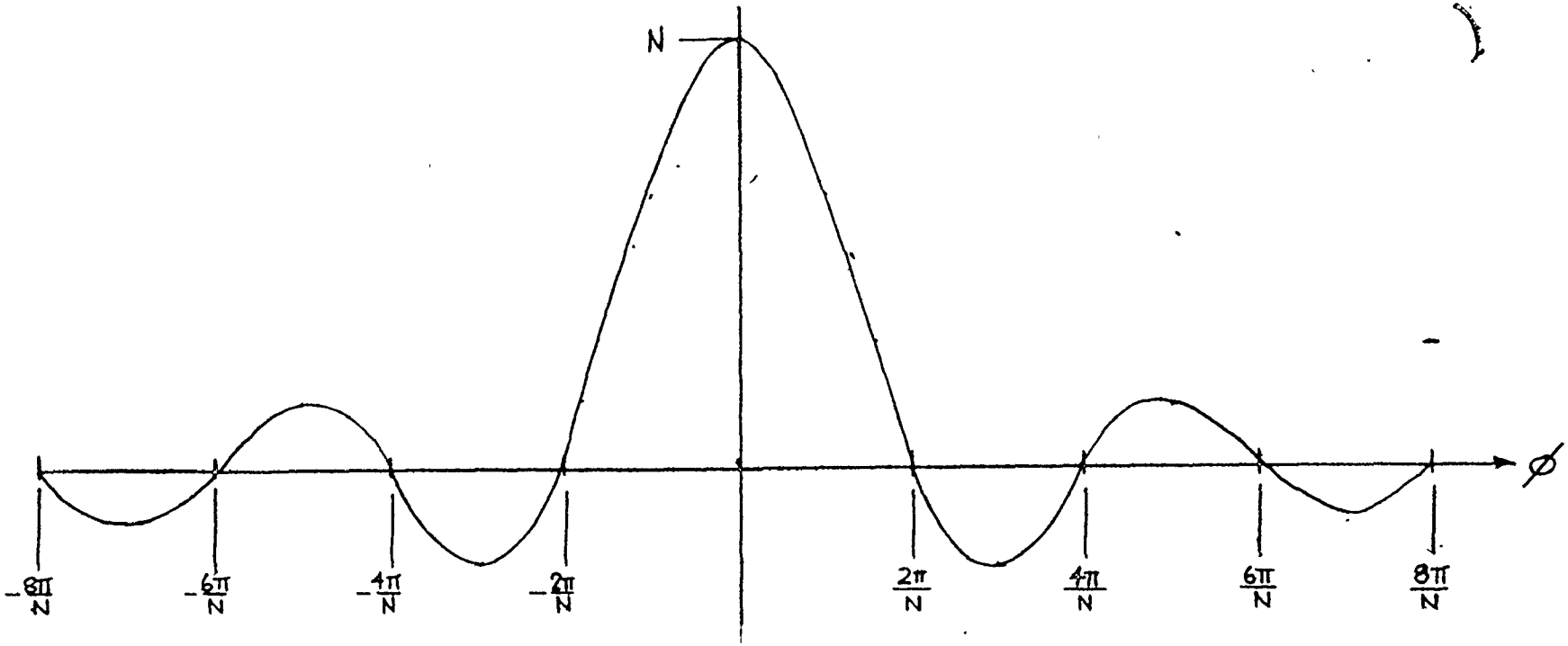

Fig. 1-2 Far-field radiation pattern of a uniformly weighted linear array, shown for N = 8.

Complete descriptions of conventional methods of beamforming, effects of weighting the elemental responses, and pattern synthesis are treated in [1-1] and [1-2].

It is important to realize that the far-field radiation pattern of the array as a function of angle, and the elemental excitation as a function of space are a Fourier transform pair. For example, the function $S(\alpha,t)$ shown in Fig. 1-2 is also very important and familiar from the analysis of time-sampled data systems, and is well-known to be one segment of the spectrum resulting from a uniform sequence of time samples. Also, the effects of applying window functions in discrete-time analysis [1-3] has exactly the same effect on the corresponding spectra that the application of weighting functions to the elements has on the far-field radiation pattern of an array.

This analogy between sampled time systems and arrays also extends to Nyquist restrictions on sampling rates. The spatial sampling rate along a particular dimension of an array must be sufficiently large so that the following inequality holds:

$$-\frac{1}{2} < \vec{k} \cdot \vec{z} \leq \frac{1}{2} \qquad (1\text{-}6)$$

This relation is exactly analogous to the usual definition of the Nyquist criterion;

$$-\frac{1}{2} \leq f_H \cdot T < \frac{1}{2}$$

where T is the temporal sampling period and f_H is the highest frequency component present in the signal to be sampled.

For a uniformly spaced linear array excited by a single plane wave, (1-6) takes the form

$$-\frac{1}{2} \leq \frac{d}{\lambda} \sin \theta \leq \frac{1}{2} \quad . \tag{1-7}$$

The range of values of θ which satisfy (1-7) for a given array geometry is called the "visible region" of the array. The region is symmetric about the normal of the array, and the limits, $\pm\theta_v$, are determined when the equality signs in (1-7) are satisfied. That is, when

$$\frac{d}{\lambda} \sin \theta_v = \pm \frac{1}{2}$$

or

$$\theta_v = \pm \sin^{-1} \frac{\lambda}{2d} \quad . \tag{1-8}$$

If, for a given value of d/λ, a value of θ exists which does not satisfy (1-7), then grating lobes will appear in the array response and the analog of spectral aliasing will occur. This, in effect, means that the incoming waves must be limited to the interval $-\theta_v \leq \theta < \theta_v$. A common value chosen for d/λ is 1/2, for which (1-7) is satisfied for all

θ, $|\theta| \leq \pi$. It is worthy of note that the quantity ϕ defined in (1-2) varies from $-\pi$ to π radians as θ goes from $-\theta_v$ to θ_v.

In view of the analogy that exists between sampled time sequences and array element excitations, estimation of direction angle in the array processing context may be considered to be equivalent to a spectral estimation problem. In the general case, there may be not just plane waves, but also diffuse waves spanning a finite angle that are incident on the receiver array. In this case, it is a complete spectrum, and not just the position of a single frequency that must be estimated. The one practical difference, however, which makes the array processing problem more difficult is that a spatial sample (i.e. an array element) is more difficult and expensive to obtain in most cases than a temporal sample in a discrete-time system. Thus, we find that the spectral analysis which must inherently be performed in the array processing problem must be accomplished with the absolute minimum number of spatial samples.

Attention has been given thus far only to linear (one-dimensional) arrays. A full discussion of the generalization of this theory to two- and three-dimensional array processing problems is given by McDonough in [1-4].

1.2 Scanning Techniques

In this section, we investigate scanning methods presently used in radar systems for estimating the elevation (or azimuth) angle of a target. In actual radar systems, angle estimation is not usually accomplished by determining what value of phase shift must be inserted into the receiver sections to produce a maximum in the summed output as was implied previously. Rather, in a well-known technique which is in common use, various devices are employed which cause the main lobe (or "beam") of the array radiation pattern to sweep or scan automatically at a continuous rate throughout the entire visible range of the array. The angle of interest is given by the position of the beam at the instant of detection. There have been many rather ingenious methods of creating this scanning effect, and some of these "scanning modulation techniques", as they are called, include:

(a) Frequency-modulation scanning techniques, originally developed by Cottony and Wilson [1-5].

(b) Time-modulation scanning techniques, originally developed by Shanks [1-6].

In both these array scanning techniques, the array sensor signals are multiplied by a signal set, the elements of which are mutually orthonormal. Haykin [1-7] has generalized this idea, and has discussed a unified treatment

of modulation scanning techniques using orthogonal functions. He also evaluates the performance of the system for estimating the angle of arrival of the received signal, and shows that the performance exhibits a threshold dependent on the signal-to-noise ratio, the number of array sensors, and the number of radar pulses integrated.

Another idea used to generate a scanned beam with an array is discussed by Davies [1-8]. The sensor outputs are mixed down to an I.F. frequency by means of a common sweeping local oscillator which sweeps at a rate f_s; the mixer outputs are then fed through delay lines of length nt_2, where n is the array sensor index and t_2 is a constant. The summed output again has the form of Fig. 1-2, and the target direction is given by the position of the peak of the summed output signal. Davies also discusses various types of distortion created by this scanning technique, and limitations which exist on the allowable scanning rate f_s usable with this system.

The techniques discussed so far have all embraced the concept of a scanned beam. That is, in order for the array to process information from all targets present within its visible range, the beam sweeps repetitively across the region of interest and thus exposes all targets within this region. However, techniques have been developed whereby the array "listens" for received radar pulses emanating from all

directions within its visible range simultaneously. An example of such a system is the Butler Matrix, which is discussed in [1-9]. The essence of this method is to evaluate a fast Fourier transform (FFT) using the sensor excitations $\{\bar{x}(n)\}$ as the input sequence. The transformed output corresponds to the distribution of fields incident upon the array from all directions within its visible region. The Butler matrix approach may be considered to consist of the superposition of a set of uncorrelated stationary beams pointing in equi-spaced directions throughout the visible range, in the manner shown in Fig. 1-3. It is of interest to note that the Butler matrix, which is in effect, an FFT, was discovered as an array processing technique long before it was realized that the same algorithm could be used to advantage in conventional Fourier analysis.

1.3 Tracking Techniques

One purpose to which an array processing system may be employed is in the tracking of airborne moving targets, such as satellites, aircraft or missiles. An important type of system which is in common use, and is intended specifically for this application is the monopulse radar. It's characteristics and features are discussed briefly in Skolnick [1-10], [1-11] and at length in Volume 1 of the

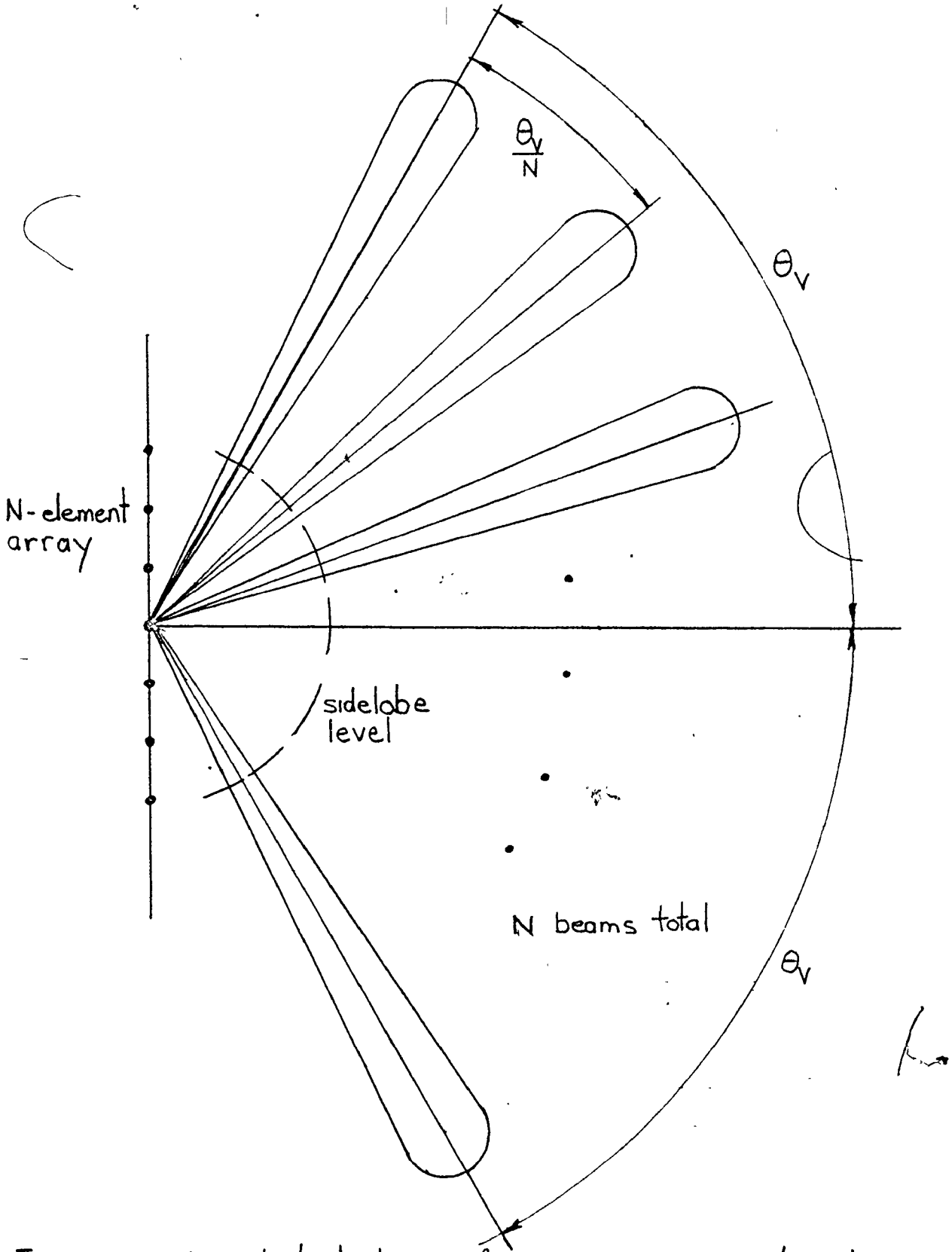

Fig. 1-3 The distribution of beams corresponding to a Butler matrix processor.

series "Radars", edited by Barton [1-12]. The name stems from the fact that only one received radar pulse is required to determine both elevation and azimuth information, as compared to the earlier type of tracking system known as the conical scan radar, which requires at least three returned pulses, and usually many more, to obtain direction information. This latter system is also described by Barton in [1-13].

In the low-angle (elevation) tracking of radar targets in a multipath environment, two signal components are incident on the array. The first is the direct component which propagates directly from the target to the array. The second is a "specular component", which bounces off the ground or the sea-surface before striking the array. This phenomenon will be discussed in more detail in Chapter 2. It usually happens in low-angle tracking applications that the angle between these two components at the array is less than a standard beamwidth. Since linear direction-estimation techniques cannot resolve between two incident components separated by less than a standard beamwidth, tracking systems built on linear methods often break down in low-angle tracking applications.

Nonlinear estimators as we shall see later, generally exhibit the quality of higher resolution than their linear counterparts. This higher resolution is usually obtained at

the expense of greater receiver complexity. Despite this drawback, they show a great potential in applications where elevation-estimation must be accomplished in a multipath environment. One such nonlinear technique is due to Capon [1-14], [1-15] and was devised for the purpose of frequency-wavenumber analysis with arrays in seismology. The method has been shown by other researchers, namely Gabriel [1-16] and Evans [1-17], to have poorer performance than other forms of nonlinear processors. Because of this, Capon's method will not be given further consideration in this thesis. However, other types of nonlinear estimators will be discussed and evaluated in some detail.

1.4 Scope and Outline of the Thesis

This thesis discusses nonlinear angle estimation methods in array processing. Particular emphasis is given to resolving the effects of multipath propagation as encountered in the estimation of elevation in low-angle tracking applications. The conditions assumed are that the multipath incident component, which bounces off a smooth sea-surface or terrain, arrives at the array and interferes with the direct incident component, thus severely degrading the performance of conventional elevation-angle estimators. Therefore, the techniques discussed are intended primarily to apply to the estimation of elevation angles, where the

array in question is oriented in the vertical direction. However, some of the methods discussed (particularly in Chapter 5) are not limited only to this situation.

There are three basic approaches considered. The first is a modification of statistical time series methods made to suit this array processing application. The second is an algorithm, based on maximum-likelihood principles, which takes advantage of the special symmetric geometric configuration of the specular multipath environment. The third is another algorithm, again based on maximum-likelihood methods, that is more general in application than the second approach.

A very important aspect of this study has been the implementation of an experimental system which has been designed and built to test and compare the various algorithms which have been developed. The details of this system are discussed in Appendix A.

Chapter 2 of this thesis will be devoted to a description of multipath phenomena. In Chapters 3-5, the maximum-entropy method (MEM) and two forms of the maximum-likelihood method will be discussed in some detail. The methods will be developed theoretically, and results based on theory, simulation and experiment will be presented and compared. Chapter 6 will make suggestions for further research and present the conclusions and final discussion.

CHAPTER 2

DISCUSSION OF THE PHENOMENON OF MULTIPATH

The last chapter briefly reviewed some of the more commonly known techniques for automatic scanning and tracking using arrays. The attention in this chapter will be directed towards the phenomenon of multipath and its effect on array processing systems, particularly with respect to tracking radars. We shall see that the presence of multipath severely alters the performance of such radars, and in some cases, causes the tracking algorithms to fail completely.

In Section 1, multipath and its modelling will be addressed, emphasizing the nature of diffuse and specular reflections. Section 2 will be directed to a discussion of the degradation of performance due to multipath on various tracking systems. Section 3 will discuss the effects of multipath on the spatial autocorrelation matrix derived from the array elements.

2.1 Multipath Phenomena

The generally accepted view of the phenomenon of multipath is that the spurious reflections consist of two components. The first is a specular component, which has a

definite geometrical configuration and leads nicely to tractable theoretical analysis. The other is a diffuse component which originates over a large physical area, and is very difficult to handle theoretically. However, Barton has developed some useful techniques in the analysis of both specular and diffuse reflections in [2-1], [2-2] and some of his results will be reviewed here.

Specular reflection problems may be approached by first considering the relationships for a flat reflecting plane as depicted in Fig. 2-1, for the case when the target range is much greater than the target height. The target radiates or reflects signals in all directions, and the radar receives a direct signal from an elevation angle θ_t plus a reflected signal from angle $\theta_r = -\theta_t$. The received baseband signal $\tilde{x}(n)$ at the nth element of the array due to these two components is given (in the absence of noise) by

$$\tilde{x}(n) = \tilde{a}_t \exp[jn\phi_t] + \rho_o \tilde{a}_r \exp[j(n\phi_r + \Psi)] \qquad (2\text{-}1)$$

$$0 \leq n \leq N-1$$

where: $\tilde{a}_t$, $\tilde{a}_r$ are the complex free-space field amplitudes of the target signal at the radar antenna and the image antenna (Fig. 2-1). It will be assumed that $\tilde{a}_t = \tilde{a}_r = \tilde{a}$, for the specular case only.

ρ_o is the reflection coefficient of the flat reflecting plane at grazing angle $\theta = \theta_t$.

$\phi_t = -\phi_r$ is given by (see (1-2))

$$\phi_t = \frac{2\pi d}{\lambda} \sin \theta_t \ .$$

ψ is the total phase shift between the direct and reflected signal components measured at the centre of the array.

N is the number of array elements.

It may be seen through Fig. 2-1 that ψ is given by

$$\psi = \frac{2\pi}{\lambda} \Delta R + \alpha \qquad (2\text{-}2)$$

where $\Delta R = R_1 + R_2 - R$

$$\simeq 2h_r \sin \theta_t .$$

$$\therefore \quad \psi \simeq \frac{4\pi}{\lambda} h_r \sin \theta_t + \alpha$$

where h_t and h_r are the heights of the target and the centre of the receiver array, respectively. The symbols R_1, R_2, R, and G are as defined in Fig. 2-1, and α is the phase shift induced on the wave by the reflecting surface.

Procedures and curves for evaluating ρ_o, ΔR, θ, and α are given in [2-3] and [2-4] for both flat and curved earth surfaces.

Note that as the target range increases enough so that the earth can no longer be considered flat, the reflecting surface in Fig. 2-1 will curve downwards, and the

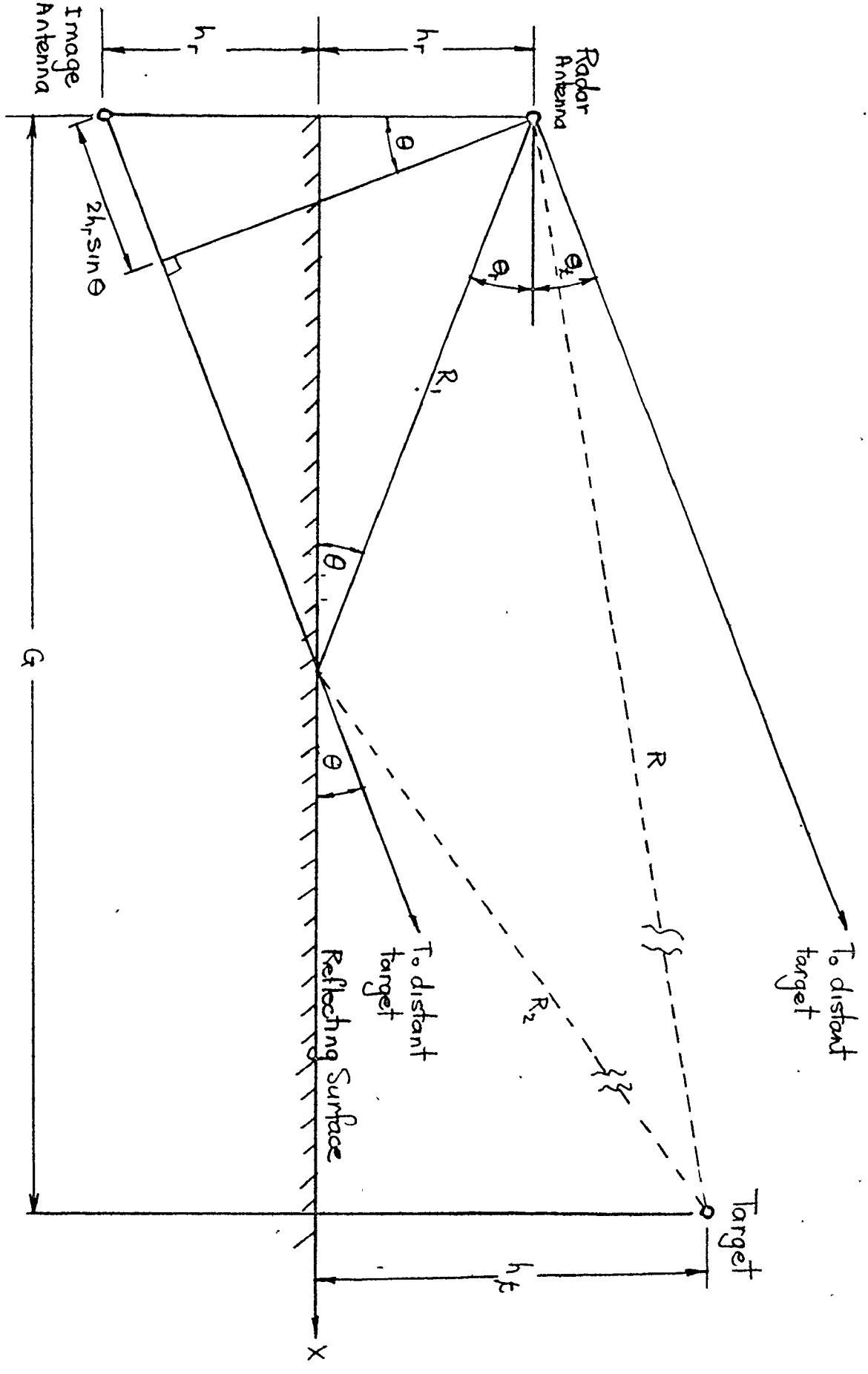

Fig 2-1 Geometry of specular multipath reflections

geometrical configuration shown will no longer be valid.

Barton [2-1] has pointed out that specular reflection applies when the difference in surface heights Δh within the first Fresnel zone (as shown in Fig. 2-2) meets the Rayleigh criterion

$$\Delta h < \frac{1}{8} \frac{\lambda}{\sin \theta} \tag{2-4}$$

A specular reflection of an EM wave off a smooth surface does not occur at just a single point in space, but rather within the area of the first Fresnel zone. Inequality (2-4) imposes the condition that all points of the reflected wavefront at the receiver array deviate by no more than an eighth of a wavelength from the corresponding ideal planar wavefront reflected from a perfectly smooth surface.

Because of the fact that the first Fresnel zone may be extensive in low-sited radar, the grazing angle θ, (and hence the allowable Δh) may vary significantly, as shown in Fig. 2-2. Because of the large extent of the reflecting surface in this case in real-world situations, random variations of the specular component about its root mean-square (rms) value are encountered as a function of target angles and local conditions. A more precise evaluation of the amplitude of the specular component is then obtained by

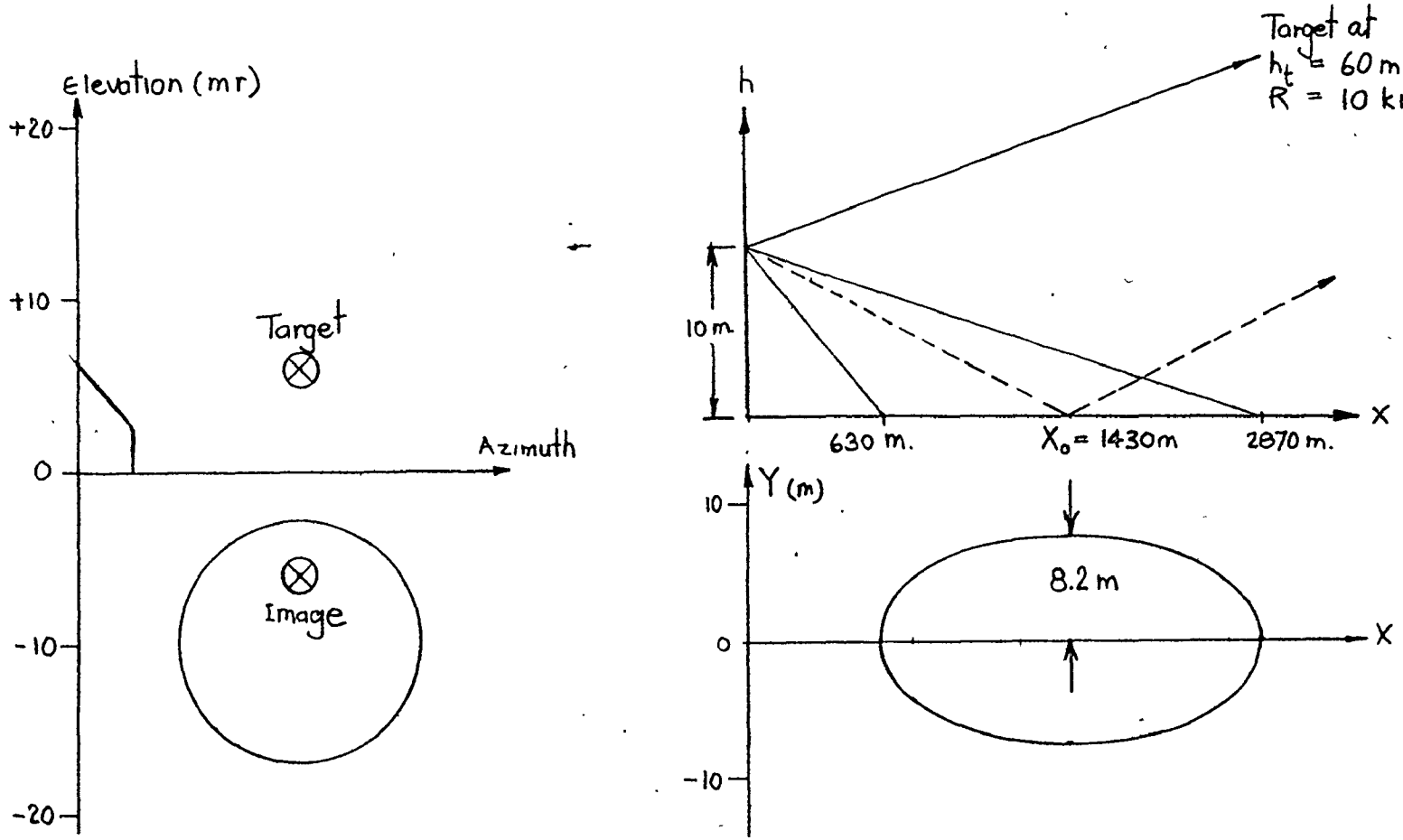

Fig. 2-2 First Fresnel zone for typical radar track:
λ = 0.005 m, hr = 10 m. [2-1]

including in (2-1) the product $\rho = \rho_o \rho_s$, where ρ_s is the rms specular scattering coefficient, given by [2-1]

$$\rho_s = \exp \left[- 2 \frac{(2\pi \sigma_h \sin \theta)^2}{\lambda} \right] \qquad (2\text{-}5)$$

where σ_h is the rms surface height variation (the surface height variation is assumed normally distributed). Most surfaces will contain both large-scale and small scale variations, requiring care in evaluating σ_h, θ, ρ_o and ρ_s for different areas of interest.

It is interesting to observe the variation of the elemental excitation $\tilde{x}(n)$ given by (2-1) across the face of the array for different parameter values. This is shown in Fig. 2-3 (a)-(c), for BW (which is the total signal separation between the two incident signal components, in standard beamwidths) equal to 1.0, 0.5 and 0.25. The figures show the spatial excitation patterns when both signal components are of the same strength (i.e., ρ=1) and both are symmetrically spaced about the normal of the array, as in Fig. 2-1. As a result of this particular choice of parameter values, the imaginary part of the contributions from the two incident signal components cancel out if the phase of the local oscillator is adjusted to $-\psi/2$ radians. This results in the purely real excitation function shown in Fig. 2-3. It is seen that the excitation patterns in

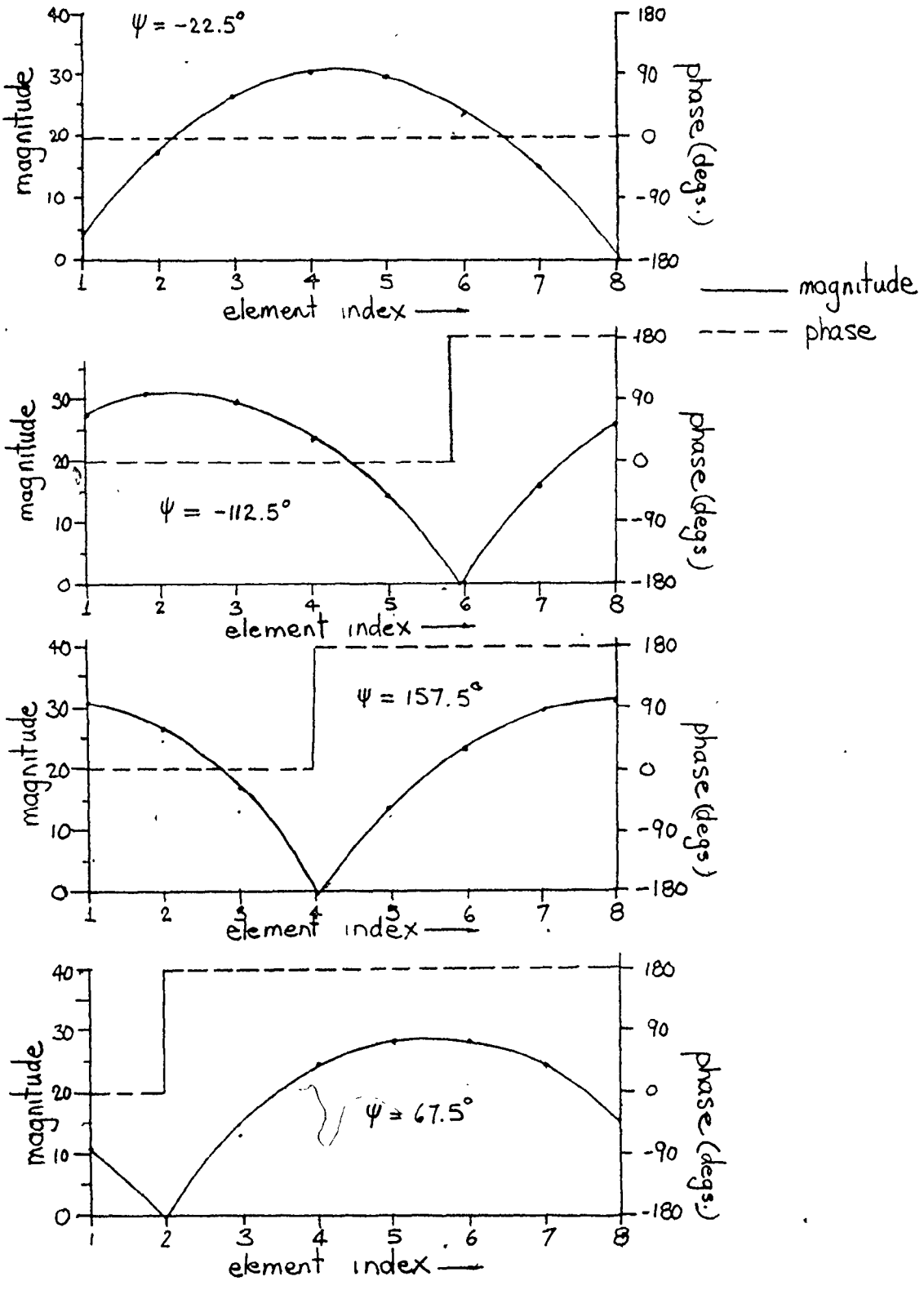

Fig. 2-3 (a) Elemental excitations in the presence of multipath. BW = 1.0

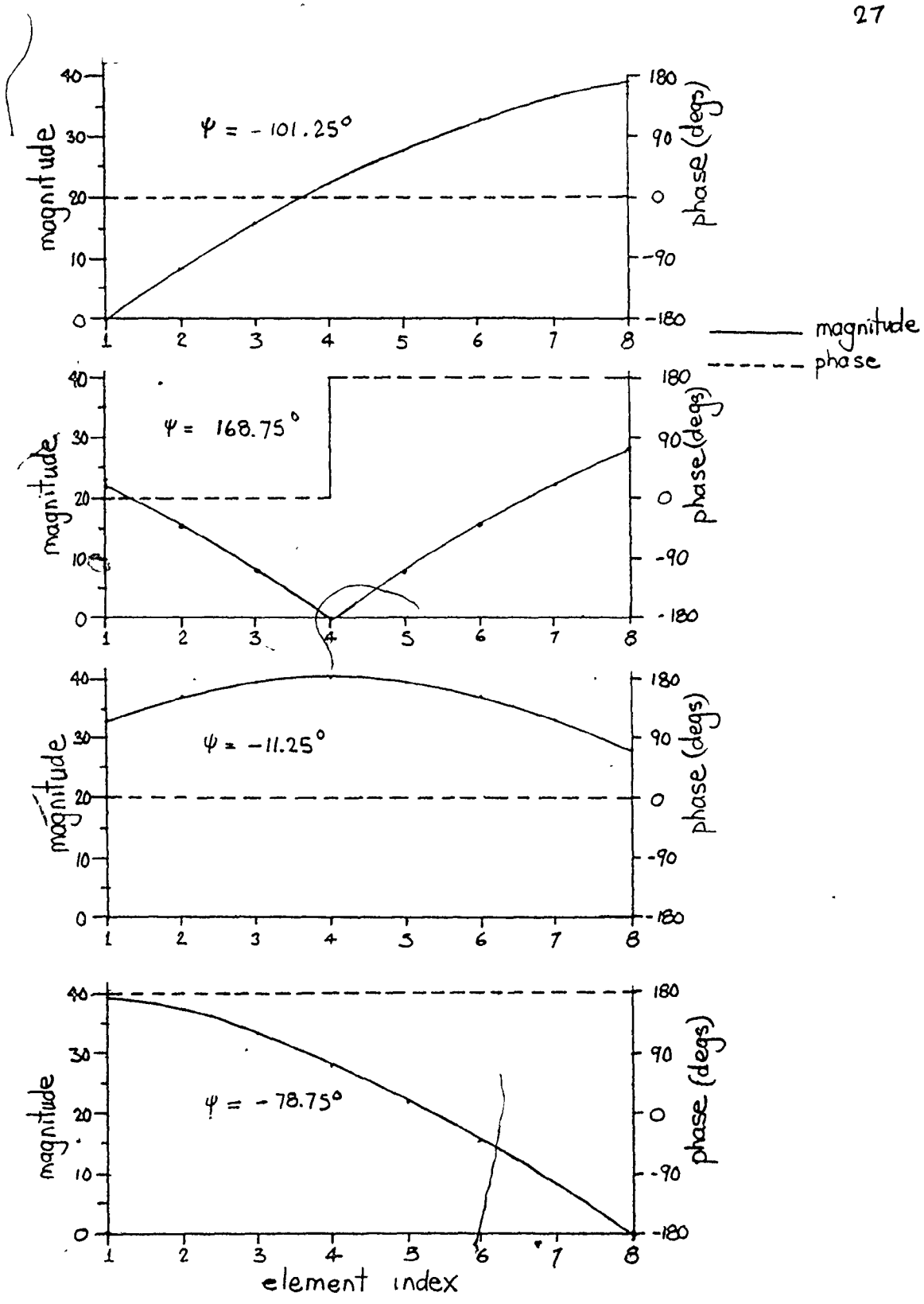

Fig. 2-3(b) Elemental excitations in the presence of multipath. BW = 0.5

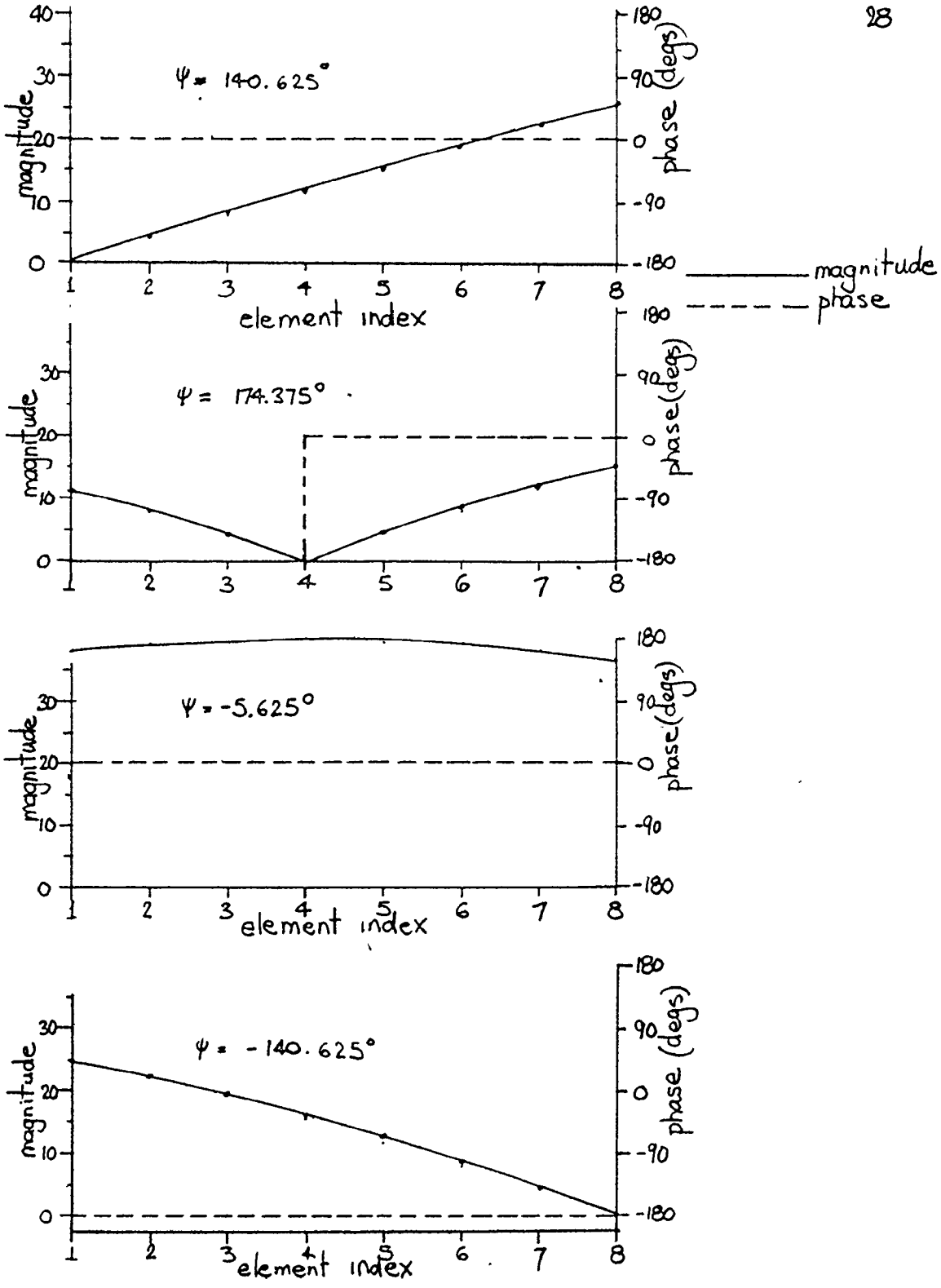

Fig 2-3(c) Elemental excitations in the presence of multipath. BW = 0.25

multipath environments are severely altered from the corresponding situations in which no specular multipath reflections exist. Note that the elemental excitations vary considerably with respect to ψ. In the absence of multipath, only the direct signal component is present (i.e. $\rho = 0$ in (2-1)) and the resulting excitation pattern is simply a rotating exponential with uniform magnitude across the face of the array.

Diffuse reflections are caused by power from the target which reaches the rough surface and is not absorbed or reflected specularly. The diffuse power reflection coefficient may be given by $\rho_o\rho_d$, where ρ_d is the diffuse scattering coefficient. Most of this diffuse power, from the homogeneous, assumed normally distributed surface, will reach the radar from the region within the "glistening" surface, shown in Fig. 2-4. The glistening surface represents an area over which the variation in surface height does not meet the Rayleigh criterion (2-4), and corresponds to the region from which power can be reflected to the radar by facets having slopes $\leq \sigma_\alpha$. Facets are small flat plates used to approximate the reflecting surface, often used in the modelling of radar scatter from sea-surfaces [2-5]. The quantity σ_α is the rms slope of the small surface facets.

Barton [2-1] has developed an expression for the

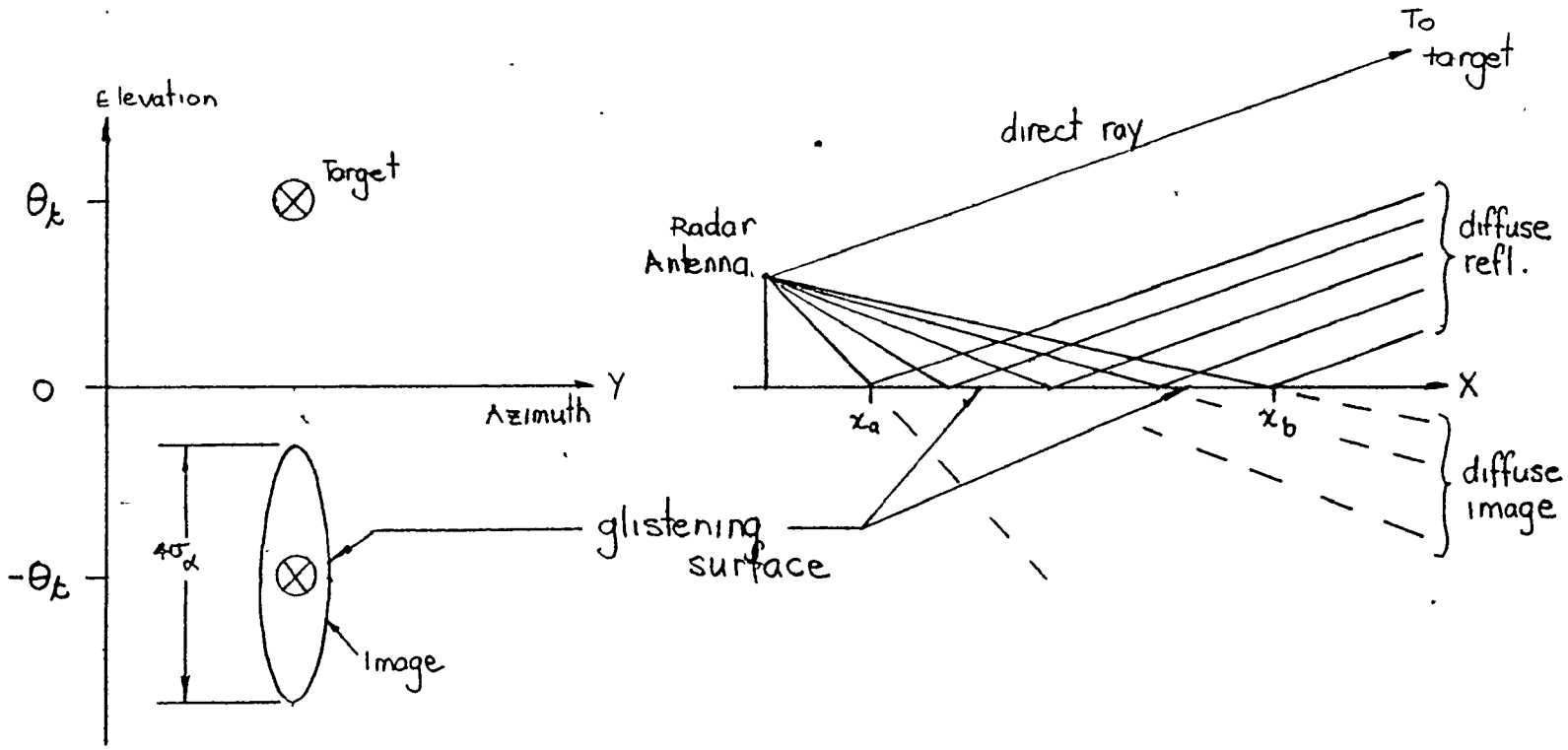

Fig. 2-4 Diffuse reflection from glistening surface [2-1]

diffuse scattering coefficient ρ_d, which has been evaluated for a variety of different situations.

An important aspect of specular multipath propagation which must be considered is the temporal cross-correlation $R_{DR}(n)$ which exists between the direct and reflected signals at the nth element. Equation 2-1 may be written as

$$\tilde{x}(n) = \tilde{x}_D(n) + \tilde{x}_R(n) \tag{2-6}$$

where $x_D(n)$ and $x_R(n)$ correspond to the first and second terms respectively of the RHS of (2-1). In the purely specular case, the quantities A_t, A_r, ϕ_t, ϕ_r, Ψ and ρ are virtually constant from pulse-to-pulse provided the target elevation has not changed considerably over the time interval considered. We may thus write

$$\begin{aligned} |R_{DR}(n)| &= | E [\tilde{x}_D(n) \cdot \tilde{x}^*_R(n)] | \\ &\approx \rho | \tilde{A}_t \cdot \tilde{A}_r^* | \end{aligned} \tag{2-7}$$

where $E[\cdot]$ is the expectation operator. Therefore, in the specular case, the direct and reflected signals are very highly correlated. However, in a purely diffuse reflection case, the quantity $\rho = \rho_o \rho_d$ varies considerably with time, and the phase difference between the two signal components at the nth element is uniformly distributed over the interval $0-2\pi$ radians at any given time instant. Therefore, for purely diffuse reflections, the two signal components are uncorrelated.

In this section we have presented a brief characterization of the nature of multipath propagation within the framework of radar. The next section shall be devoted to a discussion on the mechanism by which these multipath reflections degrade the performance of conventional tracking systems.

2.2 Performance Degradation due to Multipath Reflections

As may be observed from (2-1), the array excitation function in the presence of specular multipath is the sum of two exponentials. These two signal components will interfere with each other in a constructive or destructive manner as depicted in Fig. 2-3. For convenience, let ϕ_b be given by

$$\phi_b = \phi_t - \phi_r \,. \tag{2-8}$$

In order for the elemental excitations to properly represent the complete spatial behaviour corresponding to the given situation, the linear processors as discussed in Chapter 1 require that the physical extent of the array be such that

$$N\phi_b \geq 2\pi$$

or

$$\phi_b \geq \frac{2\pi}{N} \tag{2-9}$$

Therefore, the two incident signal components must be separated by at least one standard beamwidth of the array if the element spatial samples are to represent the underlaying

spatial process.

In low-angle tracking systems, the target elevation sometimes extends down to angles as low as 1 or 2 degrees. The total angle between the two incident signal components is then about 2-4 degrees, which is less than one standard beamwidth in many array systems. An obvious solution to this resulting resolution problem is to increase the number of array elements, thus producing a narrower beam. However, this is not always feasible due to both physical size and cost constraints. We notice therefore, that linear array processing systems can produce erroneous results when used in conventional low-angle elevation tracking situations, because the direct signal component and the predominant specular multipath component will lie within the same beam of the array.

The mechanism of failure of a monopulse radar in specular multipath environments is somewhat different than that of the linear array processor, and its causes and various solutions are discussed in [2-6].

Diffuse reflections also have degrading effects on the linear scanning systems. These diffuse signals cause distortion and dispersion in the processor output waveform (i.e. Fig. 1-2), effects which would then lead to the degradation of the performance of the target elevation-angle estimator.

It is to be noted that the effects of specular multipath are more difficult to correct, and result in more error in conventional elevation-angle estimators, than do the effects of diffuse multipath. It is for this reason that this thesis emphasizes the specular (correlated) multipath situation.

2.3 Effect of Multipath on the Correlation Matrix

In this section, we consider the effect of multipath on the spatially-varying autocorrelation function of the element excitations. The results of this discussion will be of importance in later chapters.

Consider the complex baseband signal $\tilde{x}(n)$ received by the nth element of the array in the specular multipath environment as depicted in Fig. 2-1. The signal may be denoted by

$$\tilde{x}(n) = A \exp[jn\phi_1] + \rho A \exp[jn\phi_2 + \psi] + w(n) \quad (2\text{-}10)$$

The symbols ϕ_1 and ϕ_2 are the electrical shifts due to the direct and reflected signal components respectively. In this analysis, we assume that the data record consists of only one snapshot.

The NxN cross-correlation matrix $\underline{R}$ is the matrix of correlations of $\tilde{x}(n)$ and $\tilde{x}(m)$ over the range of n,m. The n,mth element R(n,m) of $\underline{R}$ is determined by

$$R(n,m) = E[\tilde{x}(n)\ \tilde{x}(m)^*] \qquad (2\text{-}11)$$

Substituting (2-10) into (2-11), and performing some algebraic manipulation, we obtain

$$\begin{aligned} R(n,m) &= E[A^2]\exp[j(n-m)\phi_1] + E[\rho A]^2 \exp[j(n-m)\phi_2] \\ &+ 2E[\rho A^2]\exp[\tfrac{j}{2}(n-m)(\phi_1+\phi_2)]\cos[\tfrac{1}{2}(n+m)(\phi_1-\phi_2)-\psi] \\ &+ \sigma_w^2\,\delta_{n,m} \qquad (2\text{-}12) \\ n,m &= -(N-1)/2,\ \ldots,\ (N-1)/2 \end{aligned}$$

where $\delta_{n,m}$ is the Kronecker delta. For convenience, we have changed the range of n and m in (2-12) so that they vary over the indicated range instead of over 0, ..., N-1 as before. This is done so that the zeroth element is now at the centre of the array, and therefore the relative phase between the two signal components at the zeroth element is now ψ.

For the sequence described by x(n), n = -(N-1)/2, ..., (N-1)/2 to be wide-sense stationary in the dimension of space, the autocorrelation function R(n,m) must be a function of only the difference (n-m). For this to occur, the dependence on (n+m) contained in the third term of (2-12) must be removed.

This requirement may be satisfied if the direct and reflected signal components are temporally uncorrelated, as may be the case when the reflecting surface is rough, i.e., when diffuse multipath dominates. If this is the case, we find that

$$E\,[\rho e^{j\psi_A}] = 0\ . \qquad (2\text{-}13)$$

Otherwise, the process is, in general, nonstationary in the dimension of space, and the resulting wavenumber spectral estimate will not be defined in the strict sense.

The focus of attention in this thesis is the case when the specular multipath is dominant and (2-13) does not hold. In this instance, the requirement of wide-sense stationarity may still be satisfied if ψ is an odd multiple of 90^{o}. If we put $\psi = (2k-1)\ 90^{o}$, k integer, in (2-12), we find that the cos(·) term averages to zero over all the values of (n+m) that are possible when (n-m) is held constant.

It is of interest to note that if $(\phi_1-\phi_2)$ is fixed at $2\pi k/N$ radians, k integer, (i.e. the two signal components are separated by an integer number of standard beamwidths), the cos(·) term in (2-12) will also average to zero (for arbitrary ψ) over all values of (n+m), but only for the case when n-m=0. For any other value of spatial lag, the third term will not be eliminated and hence, the process is nonstationary in this case also.

We therefore note that the spatial behaviour of the process $\tilde{X}(n)$, as generated by the specular multipath environment, is generally nonstationary.

If the process $\tilde{X}(n)$ is nonstationary, then $R(\ell,k) \neq R(n,m)$ in general, for $(\ell-k) = (n-m)$, where $\ell \neq n$ and $k \neq m$.

That is, different elements on the same diagonal of the R-matrix are not equal. Therefore, we see that if a process is not wide-sense stationary, the corresponding autocorrelation matrix is not Toeplitz. This fact will be of concern later in Chapter 3.

An experimental system designed to model the specular multipath environment inside an anechoic chamber was constructed during the course of this work. The details of this system are given in Appendix A. This experimental system uses a novel I-Q sampling technique [2-8], on which a patent is pending. The algorithms which are discussed in Chapters 3-5 were tested using experimental data obtained through this system.

2.4 Summary

In this chapter we have examined various multipath phenomena and have determined that multipath reflections are composed of the specular and diffuse types. At low tracking angles or smooth surface conditions, the specular component dominates. The performances of a linear scanning processor and monopulse radar are seriously degraded, particularly in the presence of specular multipath. This degradation in the performance of conventional radar systems is the motivation that has lead us to investigate other nonlinear processing techniques.

CHAPTER 3

RATIONAL SPECTRAL ESTIMATION METHODS

The analysis of time series representing stochastic processes has progressed rapidly from the year 1958, when Blackman and Tukey published their work on the estimation of power spectra [3-1]. Methods have now been developed which lead not only to spectral estimates of the underlying time process, but also to mathematical modelling of the system producing the observed time series. These techniques may be exploited in array processing problems, since as we have already noticed, the spectral estimate produced from the array elemental excitations corresponds to the wavenumber response, or the field configuration incident on the array from the far-field. In the analysis that follows, the sequences involved will be assumed to be spatial, not temporal in nature, unless otherwise stated.

Modern time series techniques as documented by Childers [3-2], have recently received wide attention in the literature because of their ability to resolve closely-spaced spectral components better than the Blackman-Tukey, Welch [3-3] or periodogram methods. The high resolution capacity of these newer techniques does not come without its price, however, as shall be made more clear later in this

chapter.

In this chapter, we shall first discuss three widely accepted time-series modelling techniques. Then, we shall discuss and evaluate three specific algorithms (the Burg algorithm, the Pisarenko method, and the LS algorithm), all of which are linked closely to the time series modelling concepts. Results obtained by experiment and by simulation using these methods will then be given.

3.1 Review of Time-series Techniques

There exist three basic types of stationary space (time) series. These are the autoregressive (AR), moving average (MA) and mixed autoregressive-moving average (ARMA) processes. The AR process corresponds to the output of an all-pole filter, the MA process to the output of an all-zero filter, and the ARMA process corresponds to the output of a filter which has both poles and zeros. The filter input in each case is a pure white noise sequence. The techniques in this section are originated from an idea by Yule [3-4], that a space or time series in which successive values are highly dependent can be usefully regarded as generated from a series of independent "shocks" w(n). These shocks correspond to the samples drawn from the white noise input, which is usually assumed Gaussian. We shall now discuss briefly some of the salient features of the three classes of space

series.

(i) AR Processes [3-5]

A discrete AR process x(n) of order M is defined by the following difference equation:

$$x(n) = \sum_{k=1}^{M} h_k \, x(n-k) + w(n) \tag{3-1}$$

That is, the present value of the sequence is composed of a linear combination of M past values of the sequence plus a white noise term. The h_k are the weights of the process. We can rewrite (3-1) as

$$\sum_{k=0}^{M} a_k \, x(n-k) = w(n) \tag{3-2}$$

where

$$a_k = \begin{cases} 1 & , \; k=0 \\ -h_k & , \; k=1, \ldots, M \end{cases} \tag{3-3}$$

Since (3-2) is a convolution sum, we may take z-transforms of each side of (3-2):

$$A(z^{-1}) \, X(z^{-1}) = W(z^{-1}) \tag{3-4}$$

or

$$X(z^{-1}) = \frac{W(z^{-1})}{A(z^{-1})}$$

$$= F(z^{-1}) \, W(z^{-1}) \tag{3-5}$$

where the upper case quantities are transformed versions of the corresponding lower case quantities, and z^{-1} is the unit-delay operator. We therefore see that the AR process x(n) is obtained by passing a white noise sequence w(n) through an all-pole filter with transfer function $F(z^{-1})$. For wavenumber spectral analysis, we put $z^{-1} = \exp[-j2\pi\vec{k}\cdot\vec{z}]$, where the wavenumber vector $\vec{k}$ and the distance vector $\vec{z}$ are defined in (1-1). We may thus write

$$F(e^{-j2\pi\vec{k}\cdot\vec{z}}) = \frac{1}{1 + \sum_{m=1}^{M} a_m \exp[-j2\pi m\vec{k}\cdot\vec{z}]} \tag{3-6}$$

The wavenumber power spectrum $S_X(\vec{k})$ corresponding to the spatial sequence x(n) is therefore obtained through the relation [2-7]

$$S_X(\vec{k}) = \left| F(e^{-j2\pi\vec{k}\cdot\vec{z}}) \right|^2 S_w(\vec{k})$$

$$= \frac{\sigma_w^2}{\left| 1 + \sum_{m=1}^{M} a_m e^{-j2\pi m\vec{k}\cdot\vec{z}} \right|^2} \tag{3-7}$$

where σ_w^2 is the variance of the white noise input.

Let us now investigate some further properties relating to the AR difference equation (3-1). This relation may be interpreted as a filter $\{h_k\}$, k=1, ..., M operating on past values of the process x(n) to predict the value one

step forward. In a corresponding way, the filter defined by $\{a_m\}$, m = 0, 1, ..., M is known as a prediction-error filter (PEF). It's wavenumber response $G(z^{-1})$ for z^{-1} on the unit circle is given by

$$G(e^{-j2\pi \vec{k}\cdot\vec{z}}) = 1 + \sum_{m=1}^{M} a_m \exp\,[-j2\pi m\vec{k}\cdot\vec{z}] \qquad (3\text{-}8)$$

That is, its frequency response is the inverse to that of (3-6).

Prediction-error filtering is an important concept in speech processing, geophysical exploration etc. It is important to note that the prediction error filtering and autoregressive viewpoints of the analysis of stochastic processes are very closely interrelated.

(ii) MA processes

An MA stochastic process x(n) of order Q is defined by the difference equation

$$x(n) = w(n) - \sum_{k=1}^{Q} b_k\, w(n-k) \qquad (3\text{-}9)$$

where the set $\{b_k\}$ k=1, ..., Q contains the coefficients of the MA process. We note that x(n) is composed of weighted values of past input noise samples, plus the present sample value. By rewritting (3-9) as

$$x(n) = \sum_{k=0}^{Q} c_k \, w(n-k) \tag{3-10}$$

where

$$c_k = \begin{cases} 1 & k=0 \\ -b_k & k=1, \ldots, Q. \end{cases} \tag{3-11}$$

and taking z-transforms, we get

$$X(z^{-1}) = C(z^{-1}) \, W(z^{-1}) \tag{3-12}$$

where $C(z^{-1})$ is the z-transform of the sequence $\{c_k\}$. The MA process may then be generated by passing white noise through an all-zero filter, with wavenumber response

$$C(e^{-j2\pi \vec{k}\cdot\vec{z}}) = [1 + \sum_{m=1}^{Q} c_m \, e^{-j2\pi m \vec{k}\cdot\vec{z}}] \tag{3-13}$$

where (3-12) has been evaluated for z^{-1} on the unit circle.

A linear array consisting of Q+1 equally spaced uniformly weighted point-source radiators may be represented as a spatial filter described by (3-10) and (3-12). The magnitude of the far-field radiation pattern (or actually the wavenumber spectrum) $|X(\vec{k})|$, produced by the conventional linear processors, corresponding to this array can easily be verified to be [in the absence of noise]

$$|X(\vec{k})| = \frac{\sin\left[(Q+1)\pi\vec{k}\cdot\vec{z}\right]}{\sin(\pi\vec{k}\cdot\vec{z})} \qquad (3\text{-}14)$$

However, $X(z^{-1})$ for $z^{-1} = e^{-j2\pi k\cdot z}$ in (3-12), evaluated for the case $c_k=1$, $k=0, \ldots, Q$, and $W(z) = \sigma_w$ for all points z^{-1} on the unit circle, becomes

$$X(e^{-j2\pi\vec{k}\cdot\vec{z}}) = e^{-Q\pi\vec{k}\cdot\vec{z}} \frac{\sin\left[(Q+1)\pi\vec{k}\cdot\vec{z}\right]}{\sin\left[\pi\vec{k}\cdot\vec{z}\right]} \sigma_w. \qquad (3\text{-}15)$$

This relationship is formed by evaluating the sum in (3-13), and substituting the result into (3-12). We see that the magnitude of the response (3-15) is proportional to that given by (3-14).

A point-source radiator may be considered a spatial impulse function at position zero, and may be considered the input sequence w(n) in the filter structure of (3-10). The array element weights correspond to the sequence $\{c_k\}$, $k=0, \ldots, Q$ in (3-10), which for this example, are all equal to unity. The elemental excitation pattern of the array is the filter output sequence x(n).

The wavenumber domain representations of the input and weighting sequences of the array are then multiplied according to (3-12) to give the output wavenumber response of the array (i.e., the far-field radiation pattern), as given by (3-15). We have used a point source radiator as the elemental radiation pattern, and a uniformly weighted array in this example. However, the results may be

generalized to cover arbitrary element patterns and weightings [1-2].

We have used an impulse function for the input sequence w(n) instead of a white noise process as is required for the generation of a stochastic MA process. However, both the impulse and white noise sequences have the same wavenumber power spectrum; therefore, the wavenumber domain representations will be the same in both cases. The only difference is that the impulse input produces a deterministic process, whereas the white noise input produces a stochastic process.

We therefore see that an array is a spatial filtering system, and may be modelled by a deterministic version of an MA spatial process.

(iii) ARMA processes

The ARMA representation is the most general form of a stochastic process. A discrete ARMA process x(n) of order (M,Q) is defined by the difference equation

$$x(n) = \sum_{i=1}^{M} h_i \, x(n-i) + w(n) - \sum_{i=1}^{Q} b_i \, w(n-i) \qquad (3\text{-}16)$$

where all symbols are as defined previously. Rearranging and substituting (3-3) and (3-11) into (3-16), and taking z-transforms, the above becomes

$$\frac{X(z^{-1})}{W(z^{-1})} = \frac{C(z^{-1})}{A(z^{-1})} \tag{3-17}$$

and we see that the transfer function of the filter resulting from the difference equation (3-16) has both poles and zeros. The wavenumber response $H(z^{-1})$ of the filter defined by (3-17) is

$$H(e^{-j2\pi\vec{k}\cdot\vec{z}}) = \frac{\left[1 + \sum_{m=1}^{Q} c_m e^{-j2\pi m\vec{k}\cdot\vec{z}}\right]}{1 + \sum_{m=1}^{M} a_m e^{-j2\pi m\vec{k}\cdot\vec{z}}} \tag{3-18}$$

Therefore, the resulting wavenumber power spectral density $S_X(\vec{k})$, corresponding to x(n), an ARMA process, is

$$S_X(\vec{k}) = \sigma_w^2 \left| \frac{1 + \sum_{m=1}^{Q} c_m e^{-j2\pi m\vec{k}\cdot\vec{z}}}{1 + \sum_{m=1}^{M} a_m e^{-j2\pi m\vec{k}\cdot\vec{z}}} \right|^2 \tag{3-19}$$

Generally speaking, a finite order MA process may be expressed as an infinite order AR process, and vice-versa. This may be accomplished by evaluating the reciprocal of either $C(z^{-1})$ or $A(z^{-1})$ as the case dictates. However, according to the principle of parsimony [3-5], it is desirable to express the process with as few parameters as possible. This implies it is generally best to leave the process representations in their original forms.

3.2 Mixed ARMA Modelling of the Response of a Linear Array to Incident Plane Waves [3-11]

Suppose that an array is excited by a multitude of plane waves impinging on the array at angles $\theta_1, \theta_2, \ldots, \theta_L$ measured with respect to the normal of the array. This is illustrated in Fig. 1-1 for the case of a single incident wave. Assuming that the reciprocal of the received signal bandwidth is small compared to the transit time of the signal across the array, we may express the elemental signals of the array as follows:

$$x_n(t) = \sum_{\ell=1}^{L} A_\ell \cos(2\pi f_c t + n\phi_\ell + \psi_\ell) + w_n(t), \quad (3\text{-}20)$$

$$n = 0, 1, \ldots, N-1$$

where ϕ, ψ have been defined by (2-1), and the amplitude A_ℓ and phase angle ψ_ℓ in (3-20) are random variables representing fluctuations in the wave reflected from the pertinent targets. The $w_n(t)$ represents the contribution of receiver noise, which is assumed to be white, Gaussian, and with zero mean and variance σ_w^2. It is also assumed that the individual noise components of the array are uncorrelated. The f_c is the carrier frequency of received incident wave. Translating the signal $x_n(t)$ to its baseband from, we may write

$$\tilde{x}_n = \sum_{\ell=1}^{L} A_\ell \exp [jn\phi_\ell + j\psi_\ell] + \tilde{w}_n, \tag{3-21}$$

where $\tilde{x}_n$ and $\tilde{w}_n$ are complex amplitudes defined by

$$x_n(t) = \text{Re} \{\tilde{x}_n \exp [j2\pi f_c t]\} \tag{3-22}$$

and

$$w_n(t) = \text{Re} \{\tilde{w}_n \exp [j2\pi f_c t]\} \tag{3-23}$$

It is well-known that the sum of L phasors, namely,

$$\tilde{y}_n = \sum_{\ell=1}^{L} A_\ell \exp [jn\phi_\ell + \psi_\ell], \tag{3-24}$$

may be represented by a linear difference equation of order L, as shown by:

$$\tilde{y}_n = \sum_{k=1}^{L} \alpha_\ell \tilde{y}_{n-k}, \quad n=L, L+1, \ldots, N-1 \tag{3-25}$$

The roots of the characteristic equation

$$1 - \sum_{\ell=1}^{L} \alpha_\ell z^{-\ell} = 0 \tag{3-26}$$

lie on the unit circle in the complex z-plane, where z^{-1} is the unit-delay operator. Furthermore, the angles which these roots subtend with the real axis of the z-plane are equal to $\phi_1, \phi_2, \ldots, \phi_L$, so that we may write

$$1 - \sum_{\ell=1}^{L} \alpha_\ell z^{-\ell} = \prod_{\ell=1}^{L} [1 - \exp(j\phi_\ell) z^{-1}] \qquad (3\text{-}27)$$

Therefore, knowing the angles ϕ_ℓ, we may determine the coefficients α_ℓ, $\ell=1, 2, \ldots, L$ which define the characteristic equation. Note that these coefficients are independent of the random amplitudes A_ℓ and phase angles of the received wave.

At this point, it may appear that the effect of the additive noise w(n) is to make (3-25) into an AR process of order P, but it must be realized that, for an AR process given by (3-1), with y_n substituted for x(n), $E[y_n w_n] = \sigma_w^2$. However, for this case, $E[y_n w_n] = 0$.

Next, recognizing that

$$\tilde{y}_n = \tilde{x}_n - \tilde{w}_n \qquad (3\text{-}28)$$

and substituting this relation into (3-25), we obtain the desired result

$$\tilde{x}_n = \sum_{\ell=1}^{L} \alpha_\ell \tilde{x}_{n-k} + \tilde{w}_n - \sum_{\ell=1}^{L} \alpha_\ell \tilde{w}_{n-\ell}, \qquad (3\text{-}29)$$

$n = L, L+1, \ldots, N-1.$

which represents a special form of ARMA process of order (L,L), with the autoregressive and moving average components having the same coefficients. In order to use this recursive relation, however, there is need to know the initial L-1 values of w_n.

Expressing (3-29) in matrix form, we have

$$\underline{x}_n^T \underline{g} = \underline{w}_n^T \underline{g} \tag{3-30}$$

where

$$\underline{x}_n^T = (x_n, x_{n-1}, \ldots, x_{n-L}) \tag{3-31}$$

$$\underline{w}_n^T = (w_n, w_{n-1}, \ldots, x_{n-L}) \tag{3-32}$$

and

$$\underline{g}^T = (1, -\alpha_1, \ldots, -\alpha_L) \tag{3-33}$$

We now premultiply (3-30) by $\underline{x}_n$ and take expectations:

$$E[\underline{x}_n \underline{x}_n^T]\underline{g} = E[\underline{y}_n \underline{w}_n^T]\underline{g} + E[\underline{w}_n \underline{w}_n^T]\underline{g} \tag{3-34}$$

Therefore,

$$\underline{R}\, \underline{g} = \sigma_w^2 \underline{g} \tag{3-35}$$

where $\underline{R}$ is the Toeplitz autocorrelation matrix of the process.

The solution of (3-35) is an eigenproblem in which

the desired coefficient vector is the normalized eigenvector corresponding to the minimum eigenvalue. This fact is enunciated by Ulrych and Ooe [3-6], and developed originally by Marple [3-12], [3-13]. The solution of (3-35) corresponds to a method of spectral analysis suggested by Pisarenko [3-14]. Accordingly, the spectral estimate obtained using $\underline{g}$ from (3-35) will be the Pisarenko spectral estimate. Since this particular estimator has its poles directly on the unit circle, it has at least in principle, unlimited resolution capabilities. However, as demonstrated by Ulrych and Clayton [3-15], the Pisarenko method is very sensitive to the estimates $R(\ell)$, $\ell=1, \ldots, L$ and as such, in all but the long data record/high SNR case, leads to very imprecise estimates of the true pole locations. More will be said concerning the Pisarenko technique later in this chapter. Frost [3-16] has developed an iterative noise cancellation scheme, which is a modification of the Pisarenko method, that has been reported to yield higher resolution spectral estimates than the conventional AR techniques [3-5]. However, Frost's technique depends on perfect knowledge of the autocorrelation estimates $R(\ell)$ which, of course, are never available in practice.

The filter corresponding to the difference equation (3-29) is unusual in that its transfer function $H(z)$ has L poles at $z = \exp(j\phi_\ell)$, $\ell=1, \ldots, L$ on the unit circle in the

z-plane, and L zeros at the same locations as the poles. That is, the transfer function H(z) is the product of a stable (all-zero) filter and an unstable (all-pole) filter. For all frequencies corresponding to z on the unit circle, we find that $H(z) = 1$, except for the singularities at $z = \exp(j\phi_\ell)$. At these points, the transfer function H(z) is indeterminate. Accordingly, the spectral density of the filter output is the same as the spectral density of the filter input, except for the locations of the singularities on the unit circle at which points, as expected, there will be delta functions in the spectrum of the filter output.

It should be pointed out at this point that there is no contradiction in the MA model of an array as discussed in the last section, and the ARMA representation of the elemental excitations due to incident plane waves as discussed here. The latter assumes that the excitations are a finite-length sample of the complete spatial configuration resulting from a series of incident plane waves. The former gives the exact representation of the far-field pattern due to the finite length array. In the limit, as the spatial extent of the array becomes infinite, the two representations will coincide.

3.3 The Burg Algorithm

In this section, an algorithm for spectral analysis developed originally by Burg [3-17], [3-18] will be discussed. The algorithm was originally conceived as a high-resolution spectral estimator using entropy concepts. It bears a close relationship to the AR spectral estimates as previously discussed.

The Burg algorithm has been considered as a means of array processing by several authors. Gabriel [1-16] has given some results for array antennas based on computer simulation. Evans [1-17], [3-19], gives some field test results where the Burg method was used for an antenna operating in a diffuse multipath environment over a golf-course. Reilly and Haykin [3-20] discuss the use of the Burg algorithm in the presence of specular multipath. A significant work on this subject is given by McDonough [3-22], and Skinner et al [3-23] have also made contributions in this area of research. Finally, McDonough [1-4] gives a thorough theoretical treatment of linear array processing, including maximum-entropy array processing.

The true wavenumber spectrum of a random spatial process is, in principle, computable from an infinite span of values of the autocorrelation function $R(\ell)$, where $-\infty < \ell < \infty$, corresponding to an infinite sequence of elemental excitations. With a finite data span, $x(n)$, $n=0, 1, \ldots$

N-1, however, only estimates of $R(\ell)$ for $-(N-1) \leq \ell \leq N-1$ are available, where N is the number of spatial samples (array elements). The conventional linear wavenumber spectral estimators (involving delay-sum operations, or the equivalent) implicitly assume that $x(n) = 0$ for $n \geq N$, and hence $R(\ell) = 0$ for $|\ell| \geq N$, thereby introducing spectral sidelobes in the wavenumber spectrum. Burg proposed to use the available nonzero estimates $\hat{R}(\ell)$ for $|\ell| \leq N-1$ to construct a better, nonzero estimate of $R(\ell)$, $|\ell| \geq N$. These extrapolated values may then be used to extend the available correlation span used in the spectrum estimator, thereby improving its resolution properties. Burg computed the extrapolated correlation values such that the resulting sequence would have maximum entropy in the information theoretic sense.

A very informative reference on the philosophy of maximum-entropy spectral analysis is given by Ables [3-24].

Consider that: (a) the complex-valued space series $x(n)$, $n=0, 1, \ldots, N-1$ is Gaussian-distributed with zero mean, and (b) its wavenumber spectrum $S_x(\vec{k})$ is limited to the interval $\{-B,B\}$. The entropy rate of this series is proportional to

$$h = \int_{-B}^{B} \ell n \, [S_x(\vec{k})] \, d\vec{k} \qquad (3\text{-}36)$$

Maximization of h, subject to the constraints imposed by the measured values of the autocorrelation function of x(n), yields the desired estimate of the wavenumber spectrum, [3-9]

$$\hat{S}_X(\vec{k}) = \frac{P_M}{2B\left|1 + \sum_{m=1}^{M} a_m^{(M)} \exp\ (-j2\pi m\vec{k}\cdot\vec{z})\right|^2} \qquad (3\text{-}37)$$

where P_M is output power of an Mth order prediction-error filter ($\equiv \sigma_w^2$ of an M^{th} order AR process), and the $\{a_m^{(M)}\}$, m=1, ..., M are the M^{th} order PEF coefficients.

It is an amazing result that the spectral estimator in (3-37), derived on the basis of maximum entropy, is identical to that corresponding to the AR spectral estimator (3-7), for the case where B is normalized to 1/2. In fact, the equivalence of these two methods has been rigorously proven by van den Bos [3-25], and later generalized for the complex data case by McDonough [3-22].

Hence, the term maximum entropy spectral analysis (MESA) which is used in the literature is identical to autoregressive spectral analysis as discussed in this chapter. Historically, Yule [3-4] in 1927 was the first to develop the AR estimator, and then Burg [3-17] in 1967 introduced the method of maximum entropy. Later, in 1971, van den Bos [3-25] realized the equivalence of the two

methods.

It may be pointed out here that maximum entropy spectral estimation is not always appropriate. For example, spectral analysis of an MA process by ME methods will lead to poor results, since the wrong model form is assumed. Therefore, care must be exercised in the application of any spectral estimation method.

Use of the maximum-entropy spectral estimate defined by (3-37) requires knowledge of the PEF coefficients. Burg [3-18] has developed a recursive procedure, based on Levinson's recursion [3-7], [3-8], to carry out this computation. The details of this algorithm, which is called the Burg algorithm, will now be presented. The original form of the development was done for real-valued data; however, Haykin and Kesler [3-26] have extended the algorithm to include the complex-valued data case, and this is the version which will be presented here.

We may compute the PEF coefficients directly from the space series $\hat{x}(n)$, n-0, 1, ..., N-1, as follows:

(1) By minimizing the arithmetic mean of the forward prediction-error power (which results from operating the filter in the forward direction), and the backward prediction-error power (which results from operating the filter in the backward direction), we obtain the Burg formula for the reflection

coefficient $\rho_M = a_M^{(M)}$ namely,

$$\rho_M = -\frac{2\sum_{n=M}^{N-1} e_{f,n}^{(M-1)}\, e_{b,n-1}^{(M-1)*}}{\sum_{n=M}^{N-1} [|e_{f,n}^{(M-1)}|^2 + |e_{b,n-1}^{(M-1)}|^2]}, \quad M = 1,2,\ldots \tag{3-38}$$

where $e_{f,n}^{(M-1)}$ is the forward prediction error and $e_{b,n-1}^{(M-1)}$ is the delayed backward prediction-error, both for a filter of order M-1. The asterisk denotes complex conjugation. Both the forward and backward prediction errors may be generated according to the lattice structures shown in Fig. 3-1. A complete derivation of this realization is presented in [3-9]. According to this figure, we have

$$e_{f,n}^{(M)} = e_{f,n}^{(M-1)} + \rho_M\, e_{b,n-1}^{(M-1)}$$

and (3-39)

$$e_{b,n}^{(M)} = e_{b,n-1}^{(M-1)} + \rho_M^*\, e_{f,n}^{(M-1)} \quad , n-1, \ldots, N-M-1$$

Note that for M = 0,

$$e_{f,n}^{(0)} = e_{b,n-1}^{(0)} = \tilde{x}(n) \tag{3-40}$$

The difference between forward and backward operations of the PEF is illustrated in Fig. 3-2. We see that when the filter is operated in the backward direction, its coefficients are reversed in order and the complex-conjugated.

(2) Knowing the coefficients of a PEF of order M-1, we

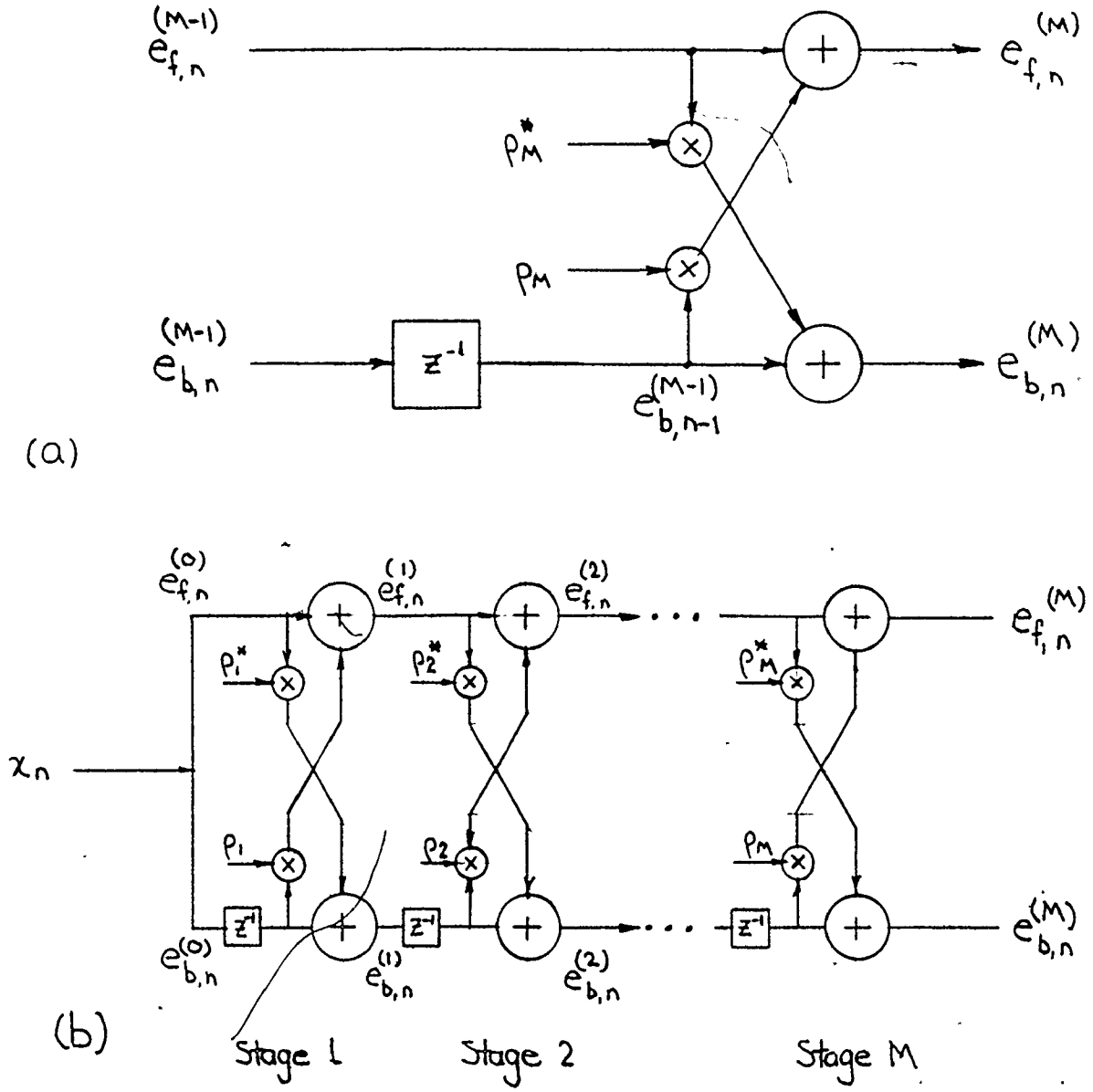

Fig. 3-1. (a) Signal-flow graph representation of the prediction errors, and (b) Lattice equivalent model of a prediction-error filter of order M.

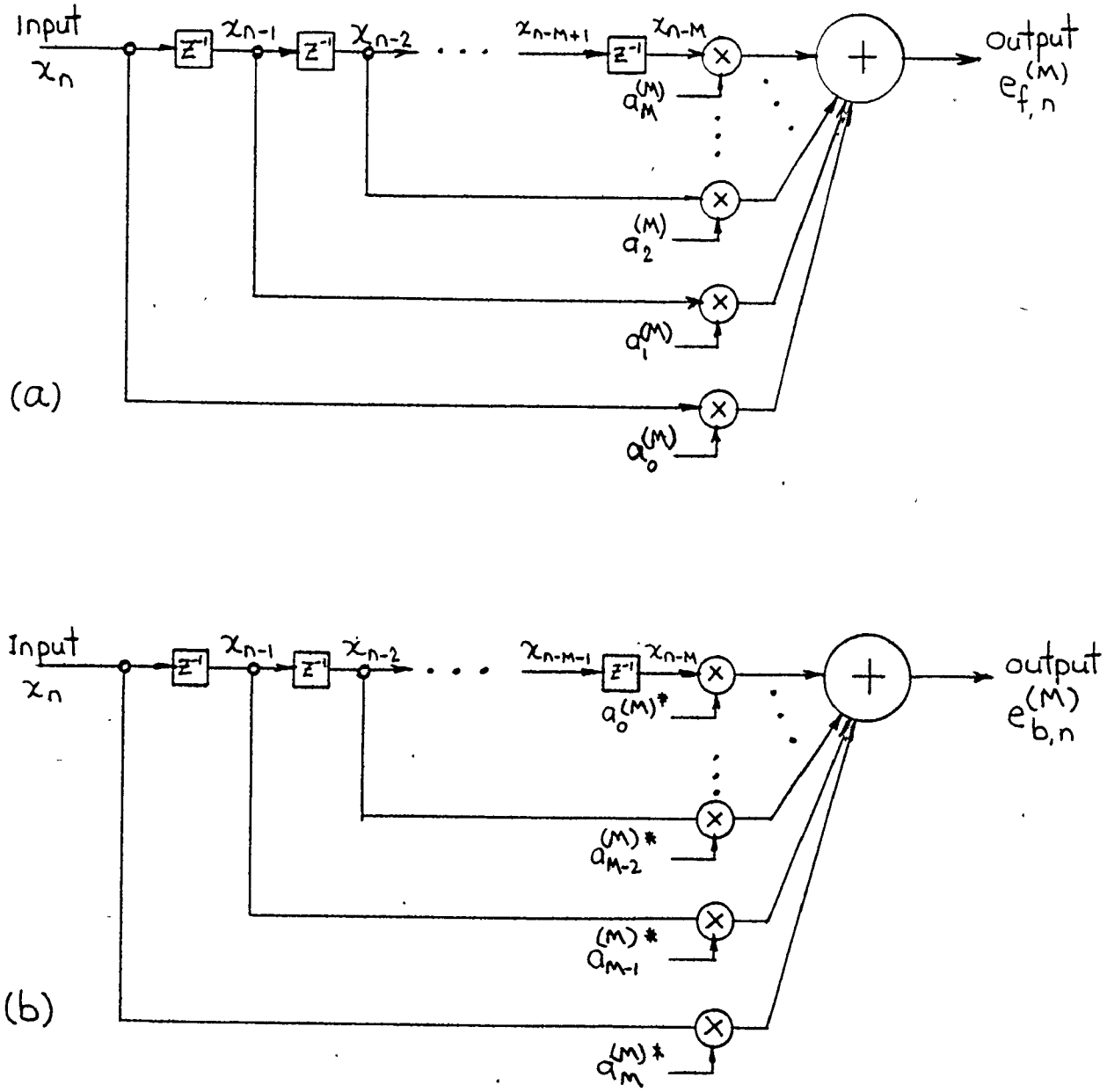

Fig. 3-2 (a) A prediction-error filter operating in the forward direction, and (b) the reverse direction.

may determine the coefficients of the corresponding PEF of order M by using the Levinson recursion, which is explained in detail in [3-9]. These coefficients of order M are given by

$$a_m^{(M)} = a_m^{(M-1)} + \rho_M \, a_{M-m}^{(M-1)*}, \quad m = 0,1,\ldots,M \qquad (3\text{-}41)$$

(3) The prediction-error power of a filter of order M, P_M, is related to that of a filter of order M-1 by the formula [3-9]

$$P_{M-1}(1 - |\rho_M|^2) \qquad (3\text{-}42)$$

We refer to ρ_M as a reflection coefficient by analogy of (3-42) with the behaviour of a transmission line. The computation procedure begins with M = 0, for which we note that

$$P_0 = \frac{1}{N} \sum_{n=0}^{N-1} |x(n)|^2 \qquad (3\text{-}43)$$

Next, for M = 1, we compute $\rho_1 = a_1^{(1)}$ using (3-38). Then, we increment the filter order by 1, that is, put M = 2, and repeat this procedure, which is continued until we reach an optimum value for the filter order.

A useful rule that may be used to determine the optimum filter order is the so-called final prediction-error (FPE) criterion developed by Akaike [3-27], [3-28]. According to this criterion, the optimum value of filter order, M_{opt}, is that value of M which minimizes the FPE given by

$$FPE(M) = \frac{N + M+1}{N - M-1} P_M \qquad (3-44)$$

The relation assumes that the space series $\hat{x}(n)$, n=0,1,...,N-1, has zero mean. Since the prediction-error power P_M decreases with M, while the factor (N + M + 1)/(N - M - 1) increases with M, we find that FPE(M) will have a minimum value, which defines M_{opt}.

Equation (3-38) is pivotal in the Burg algorithm. This equation, called the Burg formula, gives the value of ρ_M (i.e., $a_M^{(M)}$) which minimizes the average of the forward and backward prediction error powers at order M. The other coefficients, $\{a_m\}$ m=1, ..., M-1 follow iteratively from (3-41). We note therefore, that in the case of the Burg algorithm, the PEF power minimization at filter order M is accomplished with respect to the one parameter $a_M^{(M)}$ only. It is worthy of note that use of (3-38) ensures that $|\rho_M| \leq 1$ for any integer M, and hence, through (3-42), always ensures a positive semi-definite spectral estimate.

Both Nuttal [3-29] and Morf et al. [3-30] have developed multidimensional MEM analysis methods. The latter

method is based on a procedure where the (matrix) partial correlation coefficient (i.e., the reflection coefficient) is properly normalized. This technique, as opposed to the former (Nuttal), always guarantees a positive semi-definite spectral estimate, as does Burg's single dimensional algorithm. Further considerations of these methods, along with computer simulation examples, are given by Strand [3-31], and Jones [3-32]. A comprehensive review of the multidimensional MEM algorithm is presented in [3-9].

3.4 The Least-Squares Method

The previous two techniques (i.e. the Burg method and the Pisarenko) are both, at least implicitly, based on the Toeplitz matrix configuration of the autocorrelation matrix $\underline{R}$. It has been shown in Section 2.3 that $\underline{R}$ is not Toeplitz in general, unless the underlying process is spatially wide-sense stationary. In the least-squares (LS) approach, Ulrych and Clayton [3-15] have developed a method which does not depend on a Toeplitz autocorrelation matrix structure, and hence, is more amenable to spectral analysis when only short data records are available. The LS solution is obtained by minimizing the PEF output power with respect to all the AR coefficients for a particular AR order. The PEF output power is taken as the sum of the variances of the prediction errors obtained by operating in both the forward

and backward directions. The development which follows is presented in its form suitable for use with complex-valued data.

The nth complex-valued forward and backward errors of an Mth order PEF are defined as [3-6]

$$e_{f,n}^{(M)} = \tilde{x}(n) - \sum_{j=1}^{M} a_j^{(M)} \tilde{x}(n-j) \ ,$$

$$n = M, M+1, \ldots, N-1 \qquad (3\text{-}45)$$

and

$$e_{b,n}^{(M)} = \tilde{x}(n-M) - \sum_{j=1}^{M} a_j^{*(M)} \tilde{x}(n-M+j) \ ,$$

$$n = M, M+1, \ldots, N-1 \qquad (3\text{-}46)$$

The total Mth order PEF output power P_M^t is

$$P_M^t = \sum_{k=M}^{N-1} (|e_{f,k}|^2 + |e_{b,k}^*|^2) \qquad (3\text{-}47)$$

where in (3-47) it is necessary to consider $e_{b,k}^*$ instead of $e_{b,k}$, for reasons which will become evident later. In convenient matrix form, (3-47) may be written as

$$P_M^t = \underline{e}_f^H \underline{e}_f + (e_b^*)^H (\underline{e}_b^*)$$

$$= \underline{e}_f^H \underline{e}_f + (\underline{e}_b)^T (e_b^*)$$

$$= (\underline{\tilde{x}}_M - \underline{X}_f\,\underline{a})^H(\underline{\tilde{x}}_M - \underline{X}_f\,\underline{a})$$

$$+ (\underline{\tilde{x}}_o - \underline{X}_b\,\underline{a}^*)^T(\underline{\tilde{x}}_o^* - \underline{X}_b^*\,\underline{a}) \qquad (3\text{-}48)$$

where the superscript H denotes Hermitian transpose, and

$$\underline{\tilde{x}}_M^T = (\tilde{x}(M),\ \tilde{x}(M+1),\ \ldots,\ \tilde{x}(N-1)) \qquad (3\text{-}49)$$

$$\underline{\tilde{x}}_o^T = (\tilde{x}(0),\ \tilde{x}(1),\ \ldots,\ \tilde{x}(N-M-1) \qquad (3\text{-}50)$$

$$\underline{e}_f = \underline{\tilde{x}}(M) - \underline{X}_f\,\underline{a} \qquad (3\text{-}51)$$

$$\underline{e}_b = \underline{\tilde{x}}(o) - \underline{X}_b\,\underline{a} \qquad (3\text{-}52)$$

and $\underline{X}_f$ and $\underline{X}_b$ are the forward and backward propagating matrices for the problem

$$\underline{X}_f = \begin{bmatrix} \tilde{x}(M-1) & \tilde{x}(M-2) & \ldots. & \tilde{x}(o) \\ \vdots & & & \vdots \\ \tilde{x}(N-2) & \ldots. & & \tilde{x}(N-M-1) \end{bmatrix} \qquad (3\text{-}53)$$

and

$$\underline{X}_b = \begin{bmatrix} \tilde{x}(1) & \ldots. & & \tilde{x}(M) \\ \vdots & & & \vdots \\ \tilde{x}(N-M) & \ldots. & & \tilde{x}(N-1) \end{bmatrix} \qquad (3\text{-}54)$$

The vector $\underline{a}$ has elements which are the AR coefficients (as in (3-3)).

Minimizing (3-48) with respect to $\underline{a}$, and performing some algebraic manipulation, we obtain the normal equations

$$(\underline{X}_f^H \underline{X}_f + \underline{X}_b^T \underline{X}_b^*)\underline{a} = \underline{X}_f^H \underline{x}_M + \underline{X}_b^T \underline{x}_o^* \tag{3-55}$$

which can be written as

$$\underline{C}\ \underline{a} = \underline{s} \tag{3-56}$$

The elements of the MXM matrix $\underline{C}$ are given by

$$c_{ij} = \sum_{k=M}^{N-1} x^*(k-i)\ x(k-j) + \sum_{k=M}^{N-1} x(k-M+i)\ x(k-M+j)^* \tag{3-57}$$

$$i,j=1,2,\ldots M$$

and $\underline{s}$ is an M-length column vector with elements

$$s_j = \sum_{k=M}^{N-1} x^*(k-j)\ x(k) + \sum_{k=M}^{N-1} x(k-M+j)\ x^*(k-M) \tag{3-58}$$

$$j=1,2,\ldots,M.$$

The LS solution of the vector $\underline{a}$ is thus obtained by solving (3-56). The corresponding spectral estimate is then determined by the substitution of $\underline{a}$ from (3-56) into (3-7). It is worthy of note that the matrix $\underline{C}$ in (3-56) is symmetric but not in general Toeplitz; therefore the Levinson recursion may not be used by the LS algorithm in solving for $\underline{a}$. Extension of the LS method to deal with complex-valued data has also been given by Marple [3-33].

3.5 Time-dependence Considerations

The algorithms in Sections 3.2, 3.3, and 3.4 were all presented with the idea that the inputs in each case were series which varied only in space. In general, however, the data available to us varies both in space and in time. For example, in a radar situation in which the environment changes slowly compared to the radar pulse rate, many "snapshots" of data are available at each sensor, with each snapshot describing essentially the same radar environment. Therefore, assuming that we sample the received signal at each element in time, the complex-valued baseband form of the data which is available to the processor may be written $x(n,i)$, $n=0, \ldots, N-1$ and $i=0, \ldots, K-1$, where K is the total number of time samples received at each element. It is now apparent that the time-dependence of the data must be suppressed in some fashion in order to yield a series which

is indicative solely of the spatial behaviour of the process.

McDonough in [1-4] has rigorously developed the form of the spatial maximum entropy spectral estimator corresponding to the time-dependent set of received data $\{\mathfrak{X}(n,i)\}$. He uses the spatial cross-correlation matrix, introduced originally by Capon [1-14], as a means to effect the time-dependence removal of the data. Although McDonough's method was originally developed for 3-D space, the method will now be discussed briefly in the context of the linear (one dimensional) situation.

In this method, we generalize the form of expressing the desired power spectrum due to the space-time series $\{\mathfrak{X}(n,i)\}$ as received by the array. The generalized spectrum, $S_x(\vec{k},f)$ is given by

$$S_x(\vec{k},f) = \sum_{r=-\infty}^{\infty} P_x(r,f) \exp(-2\pi j r \vec{k}\cdot\vec{z}) \qquad (3\text{-}59)$$

where $S_x(\vec{k},f)$ is the frequency-wavenumber spectrum corresponding to the particular environment. The data is assumed stationary in both time and space. The quantity $P_x(r,f)$ in (3-59) is defined by

$$P_x(r,f) = \sum_{\ell=-\infty}^{\infty} R(r,\ell) \exp(-j2\pi f \ell) \qquad (3\text{-}60)$$

where

$$R(r,\ell) = E\{[\tilde{x}(n+r,\ i+\ell)][\tilde{x}^*(n,i)]\} \qquad (3\text{-}61)$$

The process $\tilde{x}(n,i)$ is assumed to have zero mean. The quantity $R(r,\ell)$ is the space-time autocorrelation function and may be regarded as the temporal autocorrelation function of the data for a given spatial lag r (i.e., between two elements spaced a distance r apart). The spatial frequency power spectrum $P_x(r,f)$ is obtained by evaluating the Fourier transform of $R(r,\ell)$ along the time axis for a fixed value of r. Thus we see that $P_x(r,f)$ is the frequency power spectrum of the process $\{\tilde{x}(n,i)\}$ corresponding to a particular spatial lag r. The sequence $P_x(r,f_c)$ for $r=-(N-1),\ldots,(N-1)$ and f_c constant is time-independent and characterizes the spatial behaviour of the process. Finally, the desired frequency-wavenumber spectrum is obtained by taking the Fourier transform of $P_x(r,f)$ along the spatial axis. In the case where a multitude of waves, all with a variety of frequency components and wavenumbers, is incident upon the array, the $S_x(\vec{k},f)$ describes the ambiguity profile of the bearing-frequency estimate corresponding to $\{\tilde{x}(n,i)\}$. This particular interpretation of $S_x(\vec{k},f)$ is valuable in geophysical applications, where this situation actually does occur in practice. However, in the radar case, where the frequency of the received signal is generally known to within a very small percentage of the transmitted frequency f_c, the $S_x(\vec{k},f_c)$ describes the distribution of wavenumbers

of all the waves incident upon the array.

In the actual implementation of this method, we realize that only finite-length data records are available in both the time and space dimensions. Therefore, only estimates of the Fourier transforms indicated in (3-59) and (3-60) are available. However, it is assumed that sufficiently long time-records are available to form an accurate estimate of the cross-spectrum between any two sensors. In the temporally and spatially stationary case, $R(r,\ell)$ may be estimated, as suggested in [1-4] by forming $\hat{R}(r,\ell)$:

$$\hat{R}(r,\ell) = \text{ave}\left\{ \frac{1}{K-\ell} \sum_{i=0}^{K-\ell-1} x(n,i+\ell)\, x^{*}(m,i) \right\}, \qquad (3\text{-}62)$$

$$\ell = 0,1,\ldots,K-1$$
$$n,m = 0,1,\ldots,N-1$$
$$r = n - m$$

where the averaging is done over all possible n,m such that $n-m = r =$ constant. Estimates $\hat{P}_x(r,f)$ of $P_x(r,f)$ are then formed by substituting the $\hat{R}(r,\ell)$ from (3-62) into (3-60), and by changing the limits $\pm\infty$ in the summation to $\pm(K-1)$. A weighting function may be incorporated into the sum in (3-60) if desired, and the combination may then be conveniently evaluated using an FFT algorithm.

A particular frequency of interest is then selected, (e.g. f_c) and the resulting time-independent spatial series

$\{\hat{P}_x(r,f_c)\}$, $r = 0,\ldots,N-1$ is used as the input sequence to any of the spectral analysis techniques discussed in previous sections. The spectral density given by one of these methods is the desired result; namely, the frequency-wavenumber spectrum corresponding to the space-time series $\{\tilde{x}(n,i)\}$.

The use of this time-dependence removal procedure, coupled with the spectral analysis techniques, is limited strictly to the processing of stationary processes. However, certain interesting situations in array processing lead to nonstationary spatial behaviour as we have seen from Section 2.3. Accordingly, considerations involved in removing the time-dependence of nonstationary processes will now be given attention.

A general form of the space-time autocorrelation matrix, $\underline{R}$, which may be applied to spatially nonstationary process, may be written

$$\underline{R} = \begin{bmatrix} R_{0,0}(\ell) & R_{0,1}(\ell) & \cdots & R_{0,N-1}(\ell) \\ R_{1,0}(\ell) & R_{1,1}(\ell) & \cdots & \cdot \\ \cdot & \cdot & & \cdot \\ \cdot & \cdot & & \cdot \\ R_{N-1,0}(\ell) & \cdot & \cdots & R_{N-1,N-1}(\ell) \end{bmatrix} \qquad (3\text{-}63)$$

where the n, mth element $R_{n,m}(\ell)$ is

$$R_{n,m}(\ell) = E\{\tilde{x}(n,i+\ell)\,\tilde{x}^{*}(m,i)\}, \qquad (3\text{-}64)$$

$$n,m = 0,\ldots,N-1$$
$$\ell = 0,\ldots,K-1.$$

Note that in the wide-sense, spatially stationary case, all elements along any diagonal of (3-63) will be equal (by definition) and hence, $\underline{R}$ will be Toeplitz. Then, the elements of $\underline{R}$ depend only on the difference $r = n-m$, and the space-time autocorrelation function becomes a single dimensioned sequence in space, as is evident from (3-61). However, in the nonstationary situation the individual terms in (3-62) in general will all be different; thus the space-time autocorrelation function must be expressed in the matrix form of (3-63), which in this case, is non-Toeplitz.

The form of (3-63) is not amenable to the application of the time-dependence removal procedure discussed here. However, one method of dealing with a spatially nonstationary process is to apply a suitable time-independent sequence derived from the $\{\tilde{x}(n,i)\}$ to the LS algorithm. This algorithm, as pointed out previously, is capable of handling the analysis of processes whose autocorrelation matrices are non-Toeplitz.

The method may be implemented in the following way.

1. Form the space-time cross-correlation matrix $\hat{R}(n,\ell)$ from the data record $\tilde{x}(n,i)$ by evaluating

$$\hat{R}(n,\ell) = \frac{1}{K-\ell} \sum_{i=0}^{K-\ell-1} [x(0,i+\ell)\ x^{*}(n,i)], \qquad (3\text{-}65)$$

for $\ell=0, \ldots, K-1$ for every sensor $n=0, \ldots, N-1$.

2. From the $\hat{R}(n,\ell)$ in (3-65), form the matrix $\hat{P}_x(n,f)$. Choose a frequency of interest, (e.g. f_c Hz), to generate a sequence $\{\hat{P}_x(n,f_c)\}$, $n=0, \ldots, N-1$.

3. The complex form of the LS algorithm may then be executed, using the sequence $\{\hat{P}_x(n,f_c)\}$ as the input. The desired wavenumber spectral estimate, at frequency f_c, is then determined by substituting the solution vector $\{a\}$ obtained from the LS algorithm into (3-7).

The LS algorithm is suggested for use in the nonstationary case because results, reported in [3-6], [3-15] indicate that the method works very well for the determination of the frequencies of sinusoids in white noise. In the array processing sense, this situation corresponds to incident plane waves, where the resulting space-time process is generally nonstationary in space.

An efficient time-dependence removal procedure has been developed by Reilly and Haykin [3-21], for application to the situation where it is known that only one plane wave is incident on the array, (e.g. as in direction-finding

applications).

3.6 Comments on the Applicability of Time-series Methods to Array Processing Problems

Generally, the spectral estimation techniques using time series are only applicable when the underlying process is stationary. The application of array processing of most concern in this thesis is that of a low-angle tracking radar operating in a multipath environment. The incident field configuration in this system leads to a spatially nonstationary process (see Section 2.3). Hence, the resulting wavenumber spectral estimate will not be a meaningful representation of the underlying spatial process unless the method is designed to deal with nonstationary processes.

We note however, that in the development of both the Burg and Pisarenko methods, a spatially stationary process and a Toeplitz R-matrix structure have been assumed. Since, in the practical implementation of the array processor, we cannot always be in phase quadrature, we may conclude that the use of the time-series techniques as applied in the specular-multipath radar environment is inappropriate. This conclusion is in agreement with results reported later in this chapter, and by White [3-34]. However, as White points out, these techniques may be well suited for certain

applications in geophysics and radio astronomy, where it may be assumed that the various signal components incident on the array are temporally uncorrelated. These methods might also be applicable in diffuse multipath radar environments, since in that case, (2-13) holds.

There has been a controversy in the literature between White [3-34] and Evans [3-19] with regard to the utility of the Burg algorithm in a radar multipath environment. Evans shows results from field tests which demonstrate that the method performs well in diffuse multipath. However White condemns the use of the algorithm in radar applications, particularly when applied to specular multipath environments.

There are two other works which are relevant to this discussion. A recent paper by Gabriel [3-35] discusses various nonlinear array processing techniques based on time-series methods. He discusses methods by which the processors may be made adaptive, but basically limits his discussion to the case where the individual incident signals are all uncorrelated. However, he does discuss a means whereby data from coherent spatial sources may be reduced to a Toeplitz form.

Griffiths, [3-35] discusses a method of making the AR spectral estimator adaptive, by suitably modifying the Widrow-Hoff LMS algorithm. His presentation is in

connection with the measurement of digital instantaneous frequency.

In the next section, results comparing performances of these three main estimation techniques will be given.

3.7 Results

3.7.1 Burg's Algorithm

Shown in Figs. 3-3 and 3-4 are experimental frequency-wavenumber spectra obtained by the Burg algorithm. Since in this case, the received signal frequency is known and fixed, the spectra referred to are simply wavenumber spectra. The curves in Fig. 3-3 pertain to 0.5 beamwidth total angular separation between the incident components, whereas those in Fig. 3-4 correspond to 1.1 beamwidths separation. In a low-angle tracking radar the angular separation between the two incident waves may be less than one standard beamwidth. It is for this situation that the array processing algorithms have the most difficulty in resolving the two incident signal components. Therefore, the results presented in this section will stress the sub-beamwidth separation case.

In Section 2.3 it was shown that the process is spatially nonstationary unless the phase shift ψ is an odd multiple of 90°. We therefore expect that the corresponding spectral estimates would, in general, be misleading. This assertion is firmly validated by the curves shown in Fig.

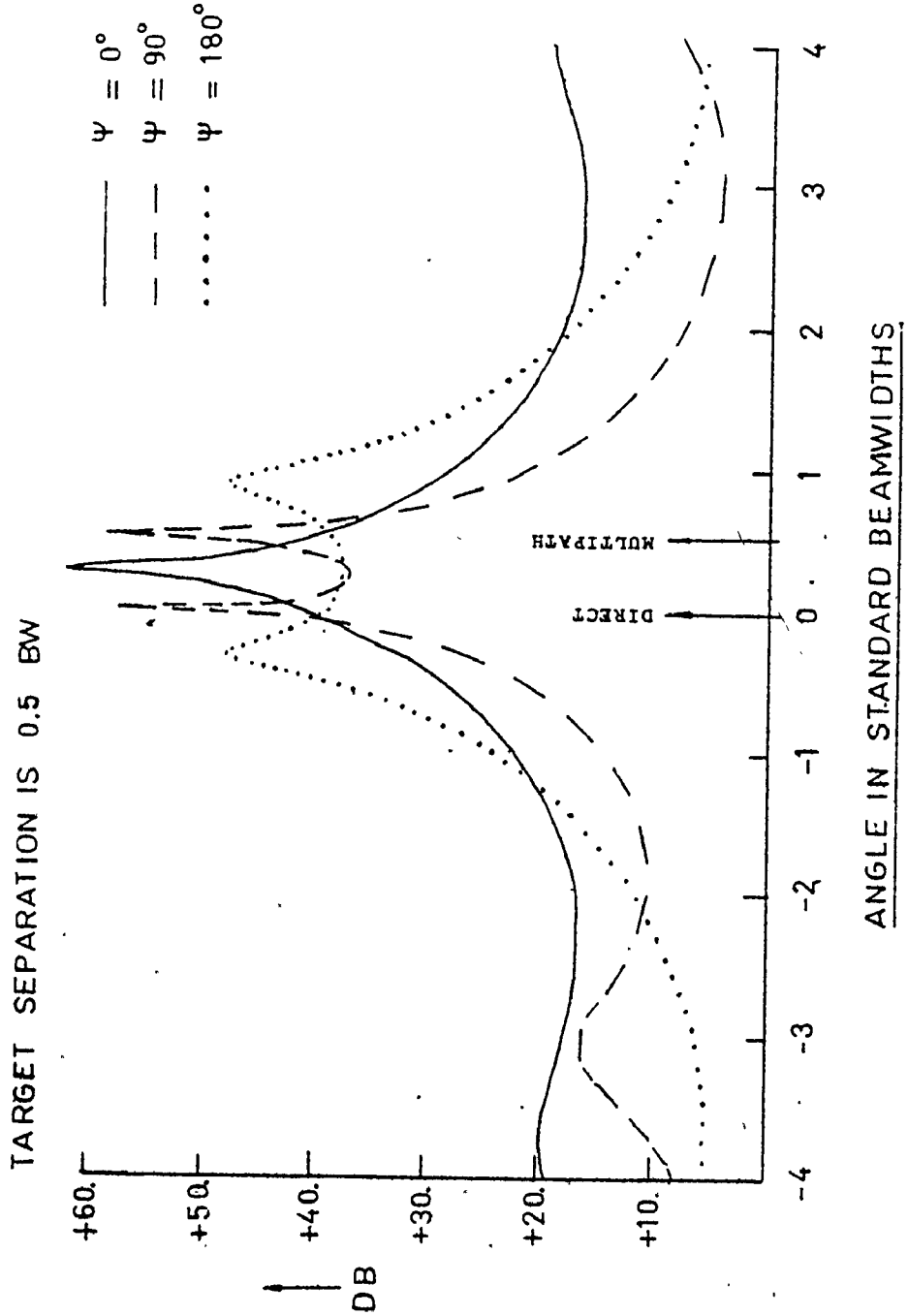

Fig. 3 - 3 Experimental Burg wavenumber spectra for BW = 0.5, and varying ψ

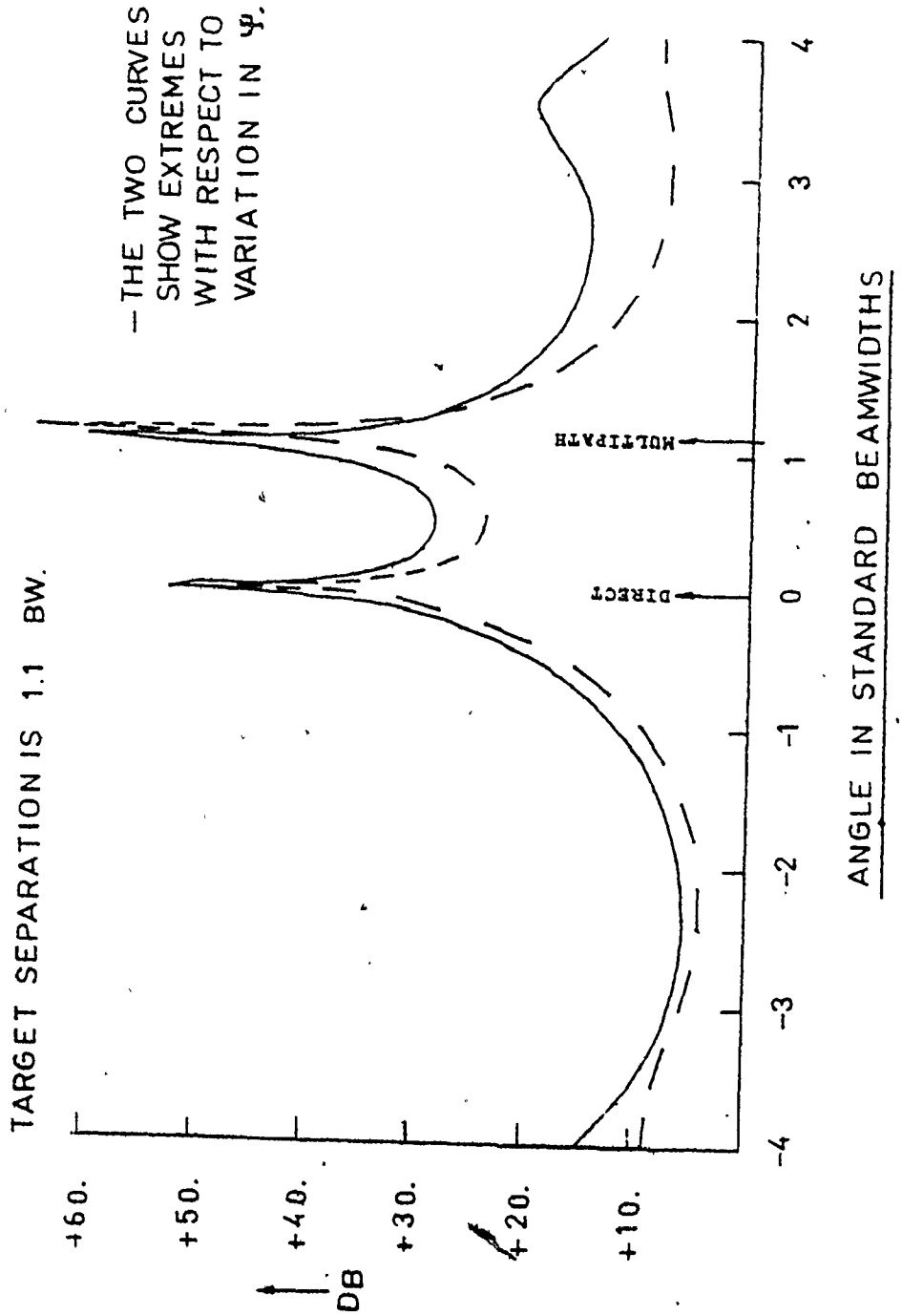

Fig. 3 - 4 Experimental Burg wavenumber spectra for BW = 1.1 and varying ψ

3-3. We see that in the case when $\psi = 0^{o}$, the two signal components coalesce into a single peak. When $\psi = 180^{o}$, the two spectral peaks are well-resolved; however, their positions bear no resemblance to the true angular positions of the incident signal components. It is only when $\psi = 90^{o}$ that the Burg algorithm yields useful results, as anticipated previously. The SNR corresponding to the curve for $\psi = 90^{o}$ is about 28 dB.

Fougere [3-37] has developed a technique which apparently gives good results for any value of ψ. His method is based on the idea that the mth order forward and backward PEF output power is minimized by jointly solving for the set of PEF coefficients $\{a_k\}$, k=1, ..., M. His method is thus similar to the LS algorithm, but Fougere's technique leads to the solution of a nonlinear system of equations; however, his solution unlike the LS algorithm, always guarantees a stable PEF filter.

Herring [3-38] has shown theoretically that the Burg algorithm will yield accurate unbiased spectral estimates for the case when the two incident signal components are separated by N/(N-1) standard beamwidths, for arbitrary ψ. This is true despite the fact that the process is non-stationary for $\psi \neq 90^{o}$. The experimental curves shown in Fig. 3-4 support this finding, where the signal separation corresponds to 8/7 = 1.14 standard beamwidths. The curves

indicate that the peaks of the Burg spectra accurately display the true elevations of the incident signals for any value of ψ.

Computer simulations, which were supported by experimental results, were run to determine the extent of the problems encountered with the Burg algorithm. In these simulations, artificial data corresponding to the elemental excitations were generated for selected values of ϕ_1, ϕ_2, ρ and ψ according to (3-21), which models the situations when two plane waves are incident on the array. Then, independent, zero-mean Gaussian noise samples of the proper variance were added to the data to generate a sequence having the desired SNR. The Burg spectral estimate corresponding to this sequence was then determined, and the positions of the spectral peaks were recorded. In order to obtain an idea of the statistical behaviour of the Burg estimator, different noise records were again added to the original data sequence, and the estimation process was repeated many times.

The results given by the Burg algorithm (or any other algorithm discussed in this thesis) are estimates only of the quantity ϕ (the electrical phase-shift from element-to-element). The corresponding true bearing angle θ must then be obtained through (1-2). The quantity ϕ will henceforth be referred to as the "electrical angle".

The SNR figures which will be quoted need interpretation. The actual SNR of the received signal set depends on the angle ψ. To establish a measure which is independent of ψ, the SNR figure quoted will always mean the SNR figure that would occur in a free-space environment (i.e. one incident plane wave only, when $\rho = 0$).

There are two practical methods of determining the spectral peak positions (which correspond to estimates of the angles ϕ_1, ϕ_2). One is to solve for the roots of the characteristic equation of the PEF coefficients. The angle of the roots then gives the values of the ϕ's corresponding to the various incident plane waves. The other method is to actually evaluate the wavenumber spectrum corresponding to the PEF coefficients, and then search for the spectral peaks. The peak positions are then recorded. In the simulations performed for this study, the latter method was chosen, since it is the fastest computationally. In view of this fact, this latter method is the one most likely to be implemented in a practical situation.

The maximum-entropy spectra display at most M peaks for a corresponding PEF filter of order M. Since it is known in these simulations that there are two incident signals, the value of M yielded by the FPE criterion should always be greater than or equal to 2. Sometimes, however, in the execution of the algorithm, the optimum FPE value

turned out to be 1. If this happened the value of M was then forced to 2.

These simulations were originally implemented with the idea in mind that the mean and variance of the Burg estimator be determined. These efforts, however, turned out to be meaningless. This is because in a large proportion of the trials, only one spectral peak was indicated (as in Fig. 3-3 for $\psi = 0^{\circ}$), even though the original data consisted of two distinct signal components. Therefore, it is not possible in this case to form meaningful statistics of the estimate corresponding to the position of <u>two</u> spectral peaks. Also, in other situations, the estimated peak positions were so far removed from their true positions that the variance due to the bias completely dominated the variance due to dispersion around the estimated mean.

Tables 3-1 and 3-2 show the results of the computer simulations. In Table 3-1, the values of ϕ_1 and ϕ_2 are chosen so that $(\phi_1-\phi_2)$ is equivalent to 0.5 standard beamwidth. In all the simulations, $\phi_1=-\phi_2$ in order to model the specular multipath environment in a symmetric manner. The number of elements N was fixed at eight for both these tables.

N = 8, BW = 0.5, $\phi_1 = 11.25^\circ$ (0.25), $\phi_2 = -11.25^\circ$ (-0.25), $\rho = .9$

SNR \ ψ	0°	90°	180°
10 dB	48/48	38/48 8.875° (.197) -41.18° (-.9148)	11/48 27.59° (.6133) -48.91° (-1.087)
20 dB	48/48	5/48 11.80° (.262) -11.20° (-.249) 3.08×10^{-1} 6.07×10^{-3}	0/48 26.76° (.595) -27.85° (-.619)
30 dB	47/48	0/48 11.46° (.255) -11.37° (-.253) 4.44×10^{-2} (1.50×10^{-2})	0/48 27.85° (.619) -26.58° (-.591)

LEGEND

A/48	
B (B')	C (C')
D (D')	E (E')

A: number of single-peak results out of 48 trials
B: mean of estimate corresponding to ϕ_1 excluding single-peak results
C: same as B except for ϕ_2
D,E: Variances of estimates, about true parameter values, excluding single-peak results. Only shown if results are meaningful.

Note: Quantities in brackets indicate equivalent of above quantity in standard beamwidths.

Table 3-1

Computer simulation results for the Burg algorithm, for 0.5 BW signal separation

Some interesting observations may be made from the results shown in Table 3-1. First, note that for $\psi = 0^{\circ}$ (i.e. the two incident signal components are in-phase at the centre of the array), the Burg algorithm almost always gives a single-peak result. That is, the Burg algorithm fails to resolve the two incident signal components for $\psi = 0$. Secondly, in the case when $\psi = 90^{\circ}$, excellent results are obtained, but only at high SNR (30 dB). However for even moderate SNR's (10 dB), the presence of the noise contributes to the lack of resolution of the two signal components, and consequently, the number of single-peak results increases sharply. Note also that in the 10 dB case, the mean value of the estimates are severely shifted from the corresponding true values. Thirdly, we note that for the $\psi = 180^{\circ}$ case, the number of single-peak results tends to be lower than for the previous two situations, but the means of the estimates are biased to positions way outside their true values. The magnitude of this shift is about 1/3 of a standard beamwidth. We also note that this bias exists even for high SNR. Finally, we note that the number of single-peak results decreases as ψ goes from 0° to 180°, independent of the SNR.

Table 3-2 shows results which were computed for the case $\phi_1 - \phi_2 = 1.14$ standard beamwidths. Note that this corresponds to the situation for which Herring [3-38] has shown

that the Burg algorithm will yield unbiased results (for N=8). We note that the figures indicate far better performance in this situation than in the previous; the number of single-peak results has dropped substantially, and the bias of the estimate is almost negligible for all values of ψ and even for moderate SNR. Note, however, that these results apply to a very specialized case, and may not be generalized to apply to separations not equal to an integer multiple of N/(N-1) standard beamwidths.

Simulations were also conducted for the case N=21 elements instead of N=8, in order to determine if the single-peak/bias effects are peculiar only to a low sampling density (i.e., low N). These simulation results have indicated that both these effects are just as severe for the 21-element case as for the 8-element case, when the signal separations are the same, measured in standard beamwidths. If the inter-element spacing is kept constant for the two cases, then the actual elevation angle bias error will be smaller in the 21-element case, but only because the corresponding beamwidth is smaller. The bias errors, measured in standard beamwidths, are almost the same. Also, the severity of the single-peaking problem is just as pronounced in the 21-element situation as for N=8.

The measure of angle in standard beamwidths corresponds to the number of spatial periods of the incident

N = 8, BW = 1.143, $\phi_1 = 25.7^\circ$ (.571), $\phi_2 = -25.7^\circ$ (-.571), $\rho = .9$

SNR \ ψ	0°	90°	180°
10 dB	6/48 27.6° (.614) -25.3° (-.562) 3.64 (1.79x10^{-3}) .203 (1.00x10^{-4})	1/48 28.3° (.628) -25.4° (-.566) 6.47 (3.197x10^{-3}) 7.74x10^{-2} (3.82x10^{-5})	0/48 27.7° (.616) -27.9° (-.619) 4.04 (1.996x10^{-3}) 4.7 (2.32x10^{-3})
20 dB	2/48 26.3° (.584) -25.4° (-.564) 5.38x10^{-1} (2.65x10^{-4}) 1.08x10^{-1} (5.333x10^{-5})	0/48 26.1° (.580) -25.9° (.576) 8.13x10^{-1} (4.02x10^{-4}) 3.48x10^{-2} (1.72x10^{-5})	0/48 26.7° (.593) -25.9° (.575) 8.37x10^{-2} (4.13x10^{-5}) 3.06x10^{-3} (1.51x10^{-6})
30 dB	0/48 25.9° (.576) -25.7° (-.571) 4.43x10^{-2} (2.19x10^{-5}) 1.94x10^{-3} (9.59x10^{-7})	0/48 25.9° (.577) -25.5° (-.568) 8.47x10^{-2} (4.182x10^{-5}) 2.93x10^{-2} (3.44x10^{-7})	0/48 25.7° (.571) -25.7° (-.571) 8.87x10^{-4} (3.44x10^{-7}) 2.92x10^{-3} 1.44x10^{-6}

LEGEND: see Table 3-1.

Table 3-2

Computer simulation results for Burg algorithm processor, for 1.143 BW signal separation.

field configuration "seen" by the array. Therefore, keeping the signal separation constant but increasing the number of elements has the effect of increasing the sampling density, but not of increasing the length of the data window. From the comparison of the 21- and 8-element results, we see that increased sampling density does not alleviate the bias and single peaking problems inherent in the Burg algorithm.

The results so far have applied only to moderately high values of SNR. It is therefore possible to argue that the single-peak/bias problems occur because of insufficiently high SNR. To show that this argument is not valid, simulations were run for SNR equal to 50 dB, with N = 21 elements, BW = 0.5 and ρ = 0.9. The results are shown in Table 3-3.

When ψ = 0 degrees, we see from the table that in every case (24 out of a total of 24 trials) the resulting spectrum has only a single peak at ϕ = +0.0735 standard beamwidths, or 0.63 degrees. (The true values are $\phi = \pm$ 0.25 beamwidths, or 4.29 degrees). Also, when ψ = 180 degrees the means of the estimates are, as in the lower SNR case, way outside their true values as shown in the table. Only when ψ = 90 degrees do the results behave well, displaying a low bias and low variance. The results shown in the table therefore demonstrate that the single peak/bias problems are inherent in the Burg algorithm itself, and are

not the direct result of low signal-to-noise ratios.

The reason for this single peak/bias problem may be understood by reference to Fig. 2-3. At sub-beamwidth signal separations, the spatial excitation pattern for $\psi=0^{\circ}$ is seen to appear very much like a single spatial sinusoid at the average of the two incident frequencies. This is why single peak spectra occur. Also, when $\psi = 180^{\circ}$, the spatial excitation function is the beat pattern between two sinusoids, except that the beat frequency appears larger than the true value. This is why bias problems exist when $\psi = 180^{\circ}$.

Experimental data were also analyzed by the Burg algorithm in order to compare these results to those obtained by computer simulation. The experimental data were generated with the sytem as described in Appendix A, and results will be shown for signal separations of 0.25, 0.5 and 1.1 beamwidths. The results are given for the case when the two targets were symmetrically spaced about boresight of the array. The direct and reflected transmitters were adjusted for equal power in each; this corresponds to a value of ρ approximately equal to 1.0. Although the simulation results were performed for $\rho = 0.9$, the two values should be close enough to make meaningful comparisons. The computer simulations were run for $\rho = 0.9$ because this is the maximum actual value of ρ in real-world situations.

N=21, BW=0.5, ϕ_1=4.29, ϕ_2=-4.29, ρ=0.9
(0.25) (-0.25)

ψ	means, variances for ϕ_1	means, variances for ϕ_2
0°	24/24 0.630° (0.0367)	N/A
90°	0/24 4.32° (0.252) $<.0108\,(\text{degrees})^2$	-4.32° (-0.252) $<.0108\,(\text{degrees})^2$
180°	0/24 9.3° (0.5425) $0.536\ (\text{degrees})^2$	-9.88 (-0.5766) $0.8205\ (\text{degrees})^2$

LEGEND: see Table 3.1

Table 3.3

Computer simulation results for the Burg algorithm for high SNR. (Elemental SNR = 50 dB).

Table 3-4 shows experimental results corresponding to signal separations of 1.1 standard beamwidths. The table shows entries for two different SNR values. The 28-dB row corresponds to the best SNR attainable with the system; the 10-dB results were obtained by adding artificial noise of the appropriate variance to the experimental data in order to decrease the SNR to the desired value. The determination of the actual value of the SNR is difficult to assess since the amount of error induced by the 60 Hz hum and the effect of elemental misalignment is not known and cannot be measured directly. However, the SNR of the data used in Table 3-4 was estimated by a method to be discussed in Chapter 4.

We note the true values for these estimates are $\phi = \pm 24.17^{o}$ ($\pm .537$), which are slightly different from the values used in the simulations. The experiment was actually set up for 1.0 beamwidth total separation, but because of measurement error etc., the actual signal separation turned out to be $\phi = \pm 24.17^{o}$. This value may be considered accurate and was determined by the use of the maximum likelihood method as will be discussed in Chapter 4, using the following technique. In the initialization of the recording of the data, one of the transmitters was turned off, after both had been adjusted to their respective positions. Data was then recorded when only one transmitter

N=8, BW=1.1, ϕ_1=24.17° (.537), ϕ_2=-24.17° (-.537)

ψ \ SNR	10 dB	28 dB
20.7°	3/24 26.8° (.595) -22.8° (-.506)	0/24 24.1° (.535) -22.2° (-.493)
112°	3/24 23.2° (.515) -27.1° (-.602)	0/24 24.7° (.548) -24.4° (-.543)
-157°	4/24 25.8° (.573) -21.8° (-.484)	0/24 26.5° (.589) -25.2° (-.560)
-66.22	2/24 22.0° (.488) -26.3° (-.584)	0/24 22.3° (.496) -25.2° (-.561)

LEGEND

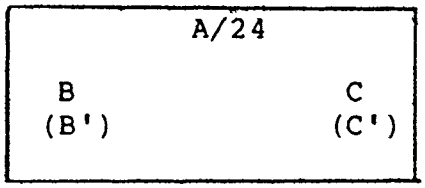

A: number of single peak results out of 24 different data sets
B: mean of estimate corresponding to ϕ_1 excluding single peak results
C: same as B except for ϕ_2.

Note: (1) quantities in brackets indicate equivalent of above quantity in standard beamwidth.
(2) only sufficient data were gathered to perform 24 trials.

Table 3-4

Experimental results using the Burg algorithm, for 1.1 BW signal separation.

antenna was active. Because of the fact that the simulated multipath interference had thus been eliminated, the maximum likelihood method was then able to make an accurate angle estimate based on this initial recorded data.

We see that the results based on experimental data, as shown in Table 3-4, show similar trends to those obtained by computer simulation (for the same separation), as shown in Table 3-2. In each case the number of single-peak results are low, and no significant biases exist for any value of ψ. The errors in the experimental estimates are greater than those corresponding to the simulation results, particularly in the 10-dB case. This is not a surprising result, and is due to factors which degrade system performance that are present in the experimental system, but which are not accounted for in the simulations.

Table 3-5 shows experimental Burg results obtained when the signal separation is 0.5 standard beamwidth. Again, the trends exhibited in the experimental case are similar to those shown by the corresponding simulation results; the number of single-peak occurences has risen substantially, and significant biases are exhibited when ψ approaches 180°. The errors in the estimates corresponding to the experimental data are generally higher than those for the simulation data, for the same reasons as discussed previously. The actual true parameter values in this case

N=8, BW=0.5, ϕ_1=11.8° (.264), ϕ_2=-11.8° (-.264)

SNR / ψ	10 dB	28 dB
-79.7°	8/24 13.9°(.309) -9.2°(-.204)	3/24 11.7°(.259) -11.6°(-.258)
-56.9°	9/24 3.6°(.08) -14.4°(-.320)	7/24 6.57°(.146) -11.5°(-.256)
-11.4°	24/24	24/24
34.15°	24/24	24/24
79.7°	19/24	13/24 3.8°(.084) -12.96°(-.288)
100°	6/24 13.3°(.295) -35.6°(-.7911)	0/24 12.0°(.267) -12.2°(-.271)
123°	3/24 17.8°(.395) -19.3°(-.429)	0/24 18.5°(.411) -17.5°(-.390)
168°	3/24 41.8°(.929) -29.3°(-.651)	0/24 28.3°(.629) -25.26°(-.561)
-146°	4/24 19.0°(.422) -44.7°(.993)	0/24 23.8°(.528) -21.4°(-.475)
-100°	7/24 9.8°(.218) -14.7°(.327)	0/24 13.11(.291) -13.11(.291)

LEGEND: see Table 3-4.

Table 3-5

Experimental results using the Burg algorithm, for 0.5BW signal separation.

were $\phi = \pm 11.8^{\circ}$ (.264 BW). We note for both the simulation and experimental results, severe shifts occur in the spectral peak positions for SNR = 10 dB. This is due to the rise of spurious peaks in the Burg spectral estimates due to the presence of noise.

In Table 3-6 results are presented corresponding to the situation where BW = 0.25, and it may be observed that the effects are even more severe in this case.

Experimental results were also obtained when the signal separation is 0.25 BW, and $\rho = 0.3$. In this case, at least 23/24 single-peak results occured, for every value of ψ considered (which were the same as shown in Table 3-6). Therefore, when ρ decreases to 0.3, the resolution capabilities of the Burg algorithm also appear to diminish.

We see that the results shown in both Tables 3-5 and 3-6 bear no real resemblance to the true angular positions indicated. It has therefore been demonstrated, both experimentally and by simulation, that the Burg algorithm when applied to direction estimation problems where two incident signal components are correlated (temporally and spatially), does not yield useful results.

3.7.2 Least-Squares Algorithm

We shall now discuss results obtained using the least-squares (LS) algorithm. In the previous case, we have

N=8, BW=0.25, ϕ_1=6.13° (.136), ϕ_2=-6.13° (-.136)

SNR / ψ	10 dB	28 dB
-38.7°	20/24	15/24 2.8° -2.32°
-27.6°	24/24	24/24
-5.52°	24/24	24/24
16.5°	24/24	24/24
38.7°	24/24	24/24
141.3°	6/24 17.38°(.386) -11.26°(-.250)	0/24 14.24°(.16) -12.24°(-.272)
152.4°	3/24 33.1°(.735) -16.87°(-.375)	0/24 16.89°(.375) -17.37°(-.386)
174.5°	0/24 27.1°(.602) -22.3°(-.495)	0/24 25.4°(.565) -29.6°(-.657)
-163°	1/24 20.7°(.460) -42.7°(.949)	0/24 18.7°(.417) -24.36(-.541)
-141.3°	7/24 12.8° -23.4°	0/24 10.4° -14.85

LEGEND: see Table 3-4.

Table 3-6

Experimental results using the Burg algorithm for 0.25 BW signal separation.

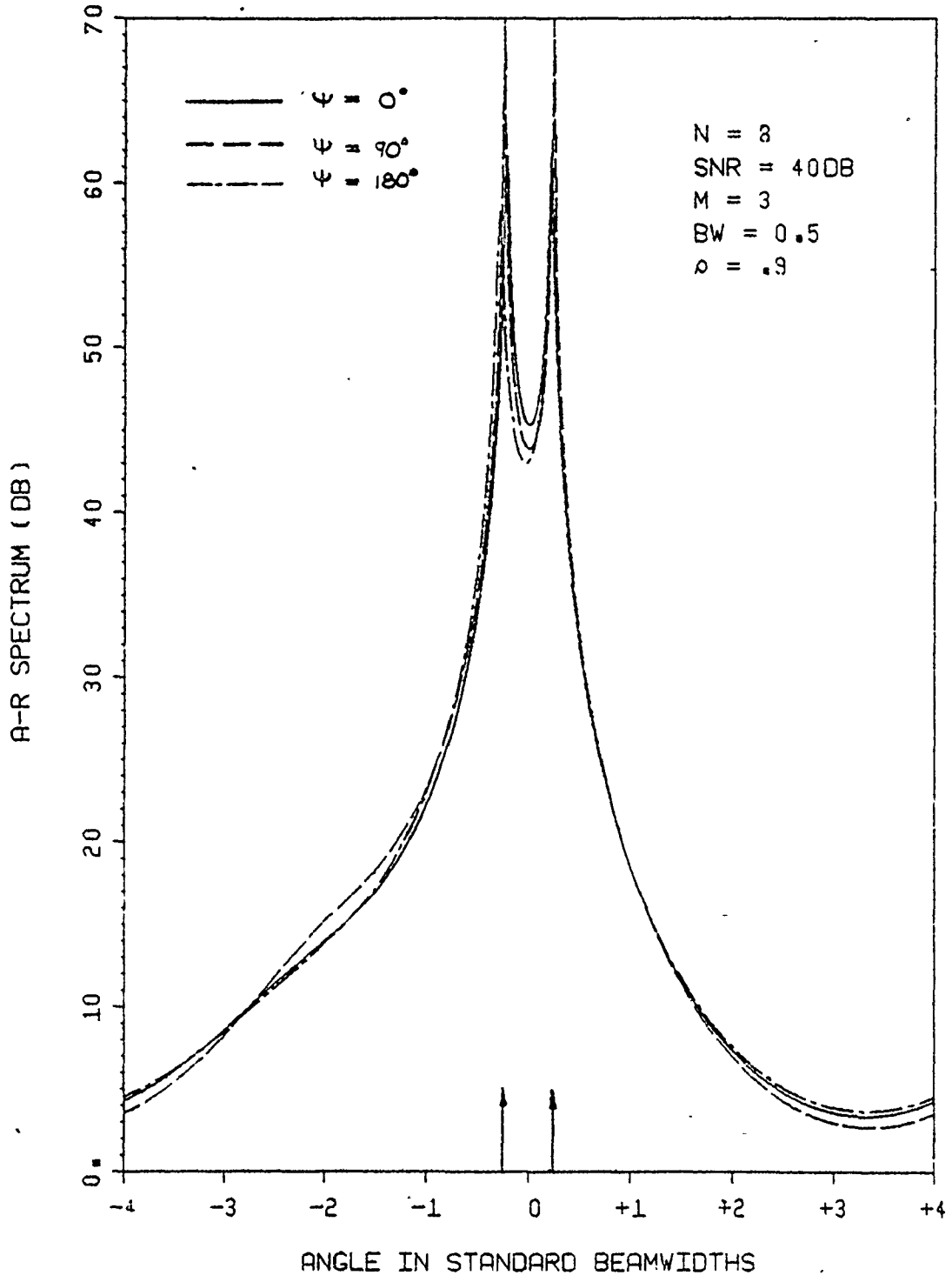

Fig. 3 - 5 Wavenumber spectra obtained from the LS algorithm by computer simulation, for BW = 0.5, N= 8, and varying ψ

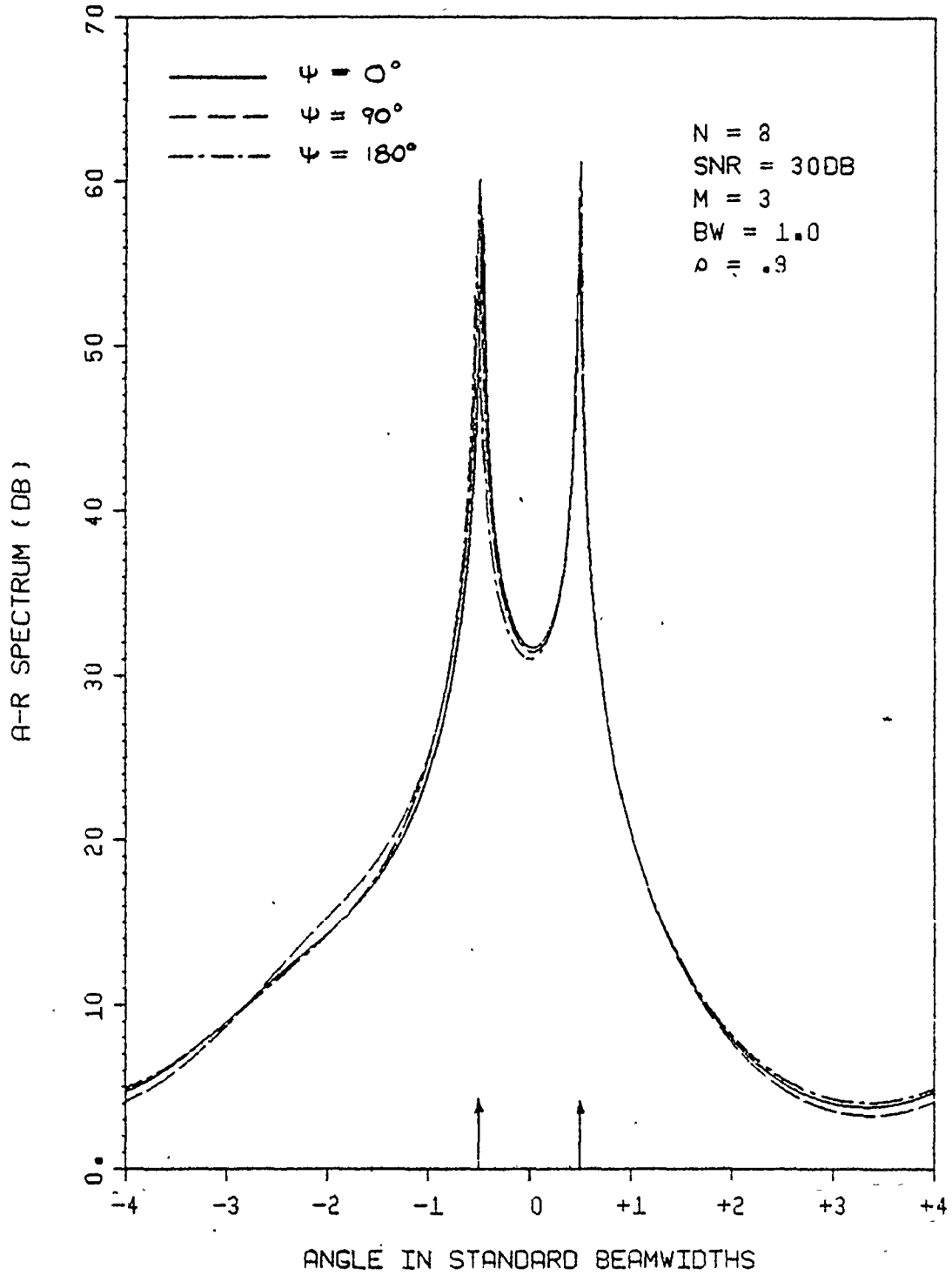

Fig. 3 - 6 Wavenumber spectra obtained from the LS algorithm by computer simulation, for BW = 1.0, N = 8, and varying ψ

seen poor performance demonstrated by the Burg method. However, we will now observe that the LS algorithm does not share many of the shortcomings inherent in the Burg results.

Shown in Fig. 3-5 and Fig. 3-6 are wavenumber spectra corresponding to BW = 0.5 and 1.0 respectively, for N = 8 elements, and ϕ = 0, 90 and 180 degrees in each case. The spectra display results from the LS algorithm, as obtained by computer simulation. These curves have virtually the same parameter values as those in Fig. 3-3, which correspond to the Burg results for BW = 0.5. We note in this case, however, that the spectra do not vary significantly with ψ, and hence yield more meaningful results. Therefore, useful results may still be obtained through the LS algorithm even though the input sequence is nonstationary. In Figs. 3-7 and 3-8 are also shown similar curves, except for the case N=21 elements. The individual curves for each value of ψ are almost indistinguishable in this latter set of figures.

As a matter of interest, the variation of the LS spectra with the filter order M is shown in Fig. 3-9. In each case we see that the spectral-peak positions, (corresponding to the same input data) are insensitive to the value of M, and that only the background noise spectrum changes significantly with filter order. The Akaike FPE criterion yielded a value M_{opt} = 7 for these particular

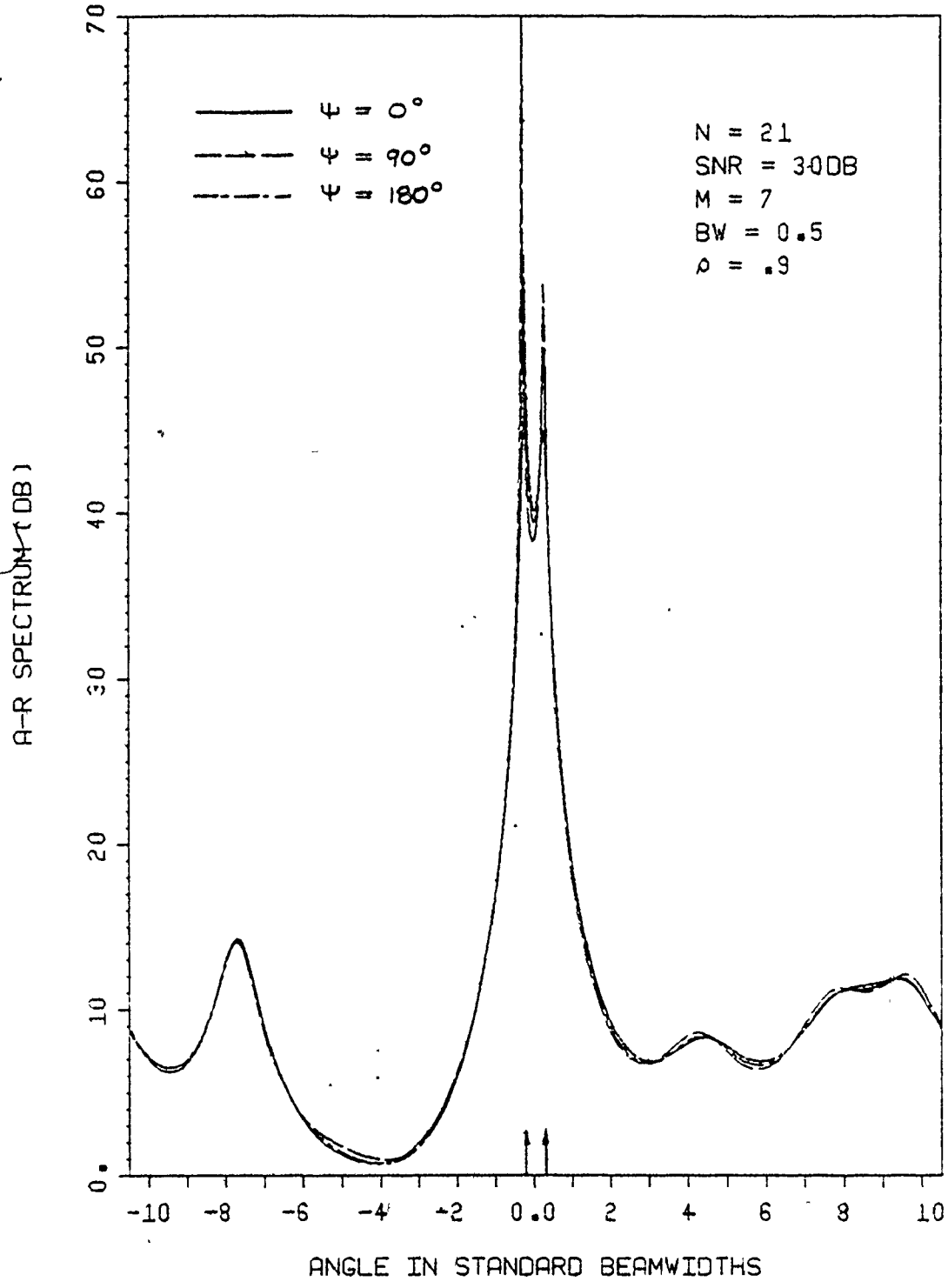

Fig. 3 - 7 Wavenumber spectra obtained from the LS algorithm by computer simulation, for BW = 0.5, N = 21, and varying ψ

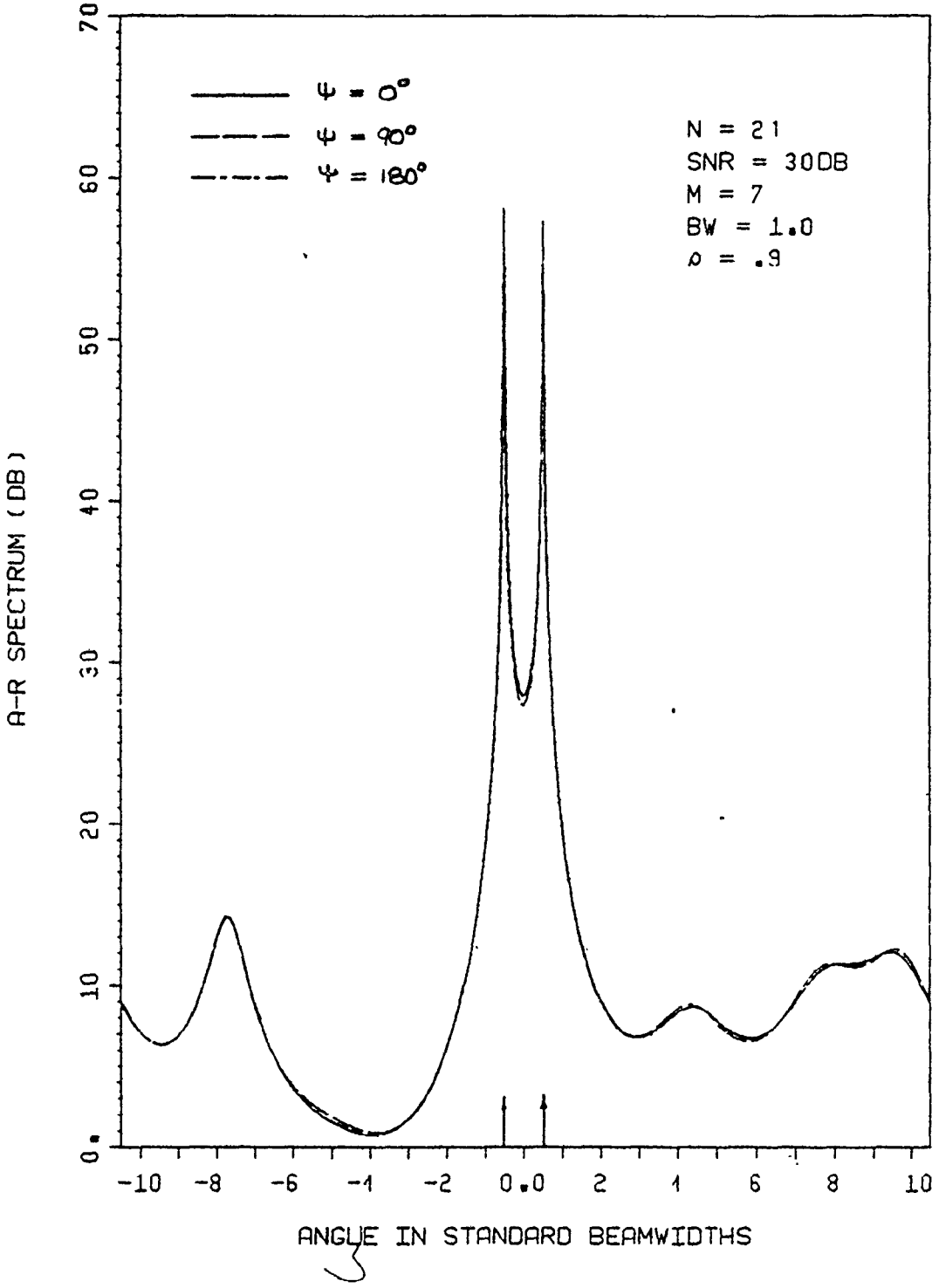

Fig. 3 - 8 Wavenumber spectra obtained from the LS algorithm by computer simulation, for BW = 1.0, N = 21, and varying ψ

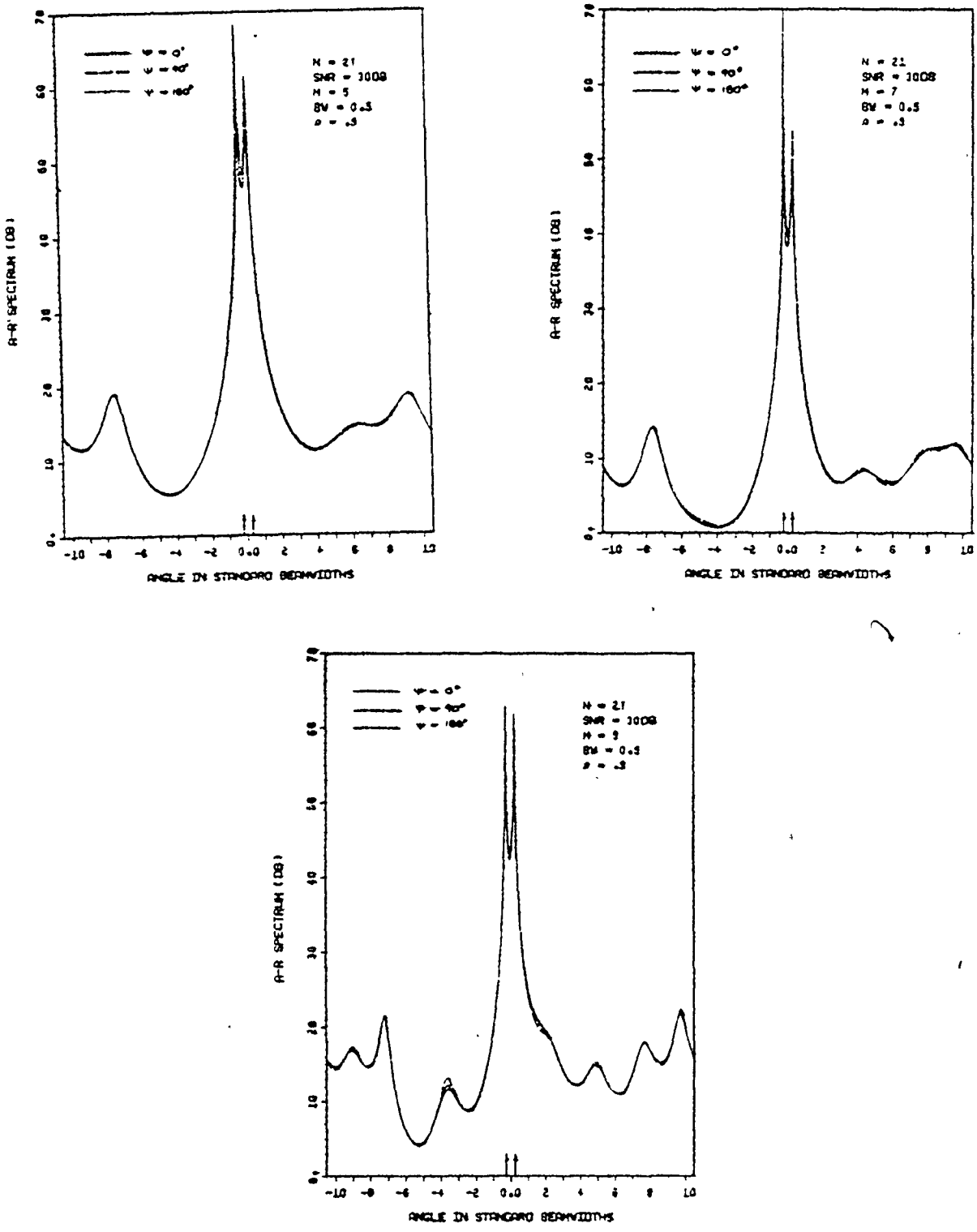

Fig. 3 - 9 Variation in wavenumber spectra, as obtained by the LS algorithm, with filter order M.

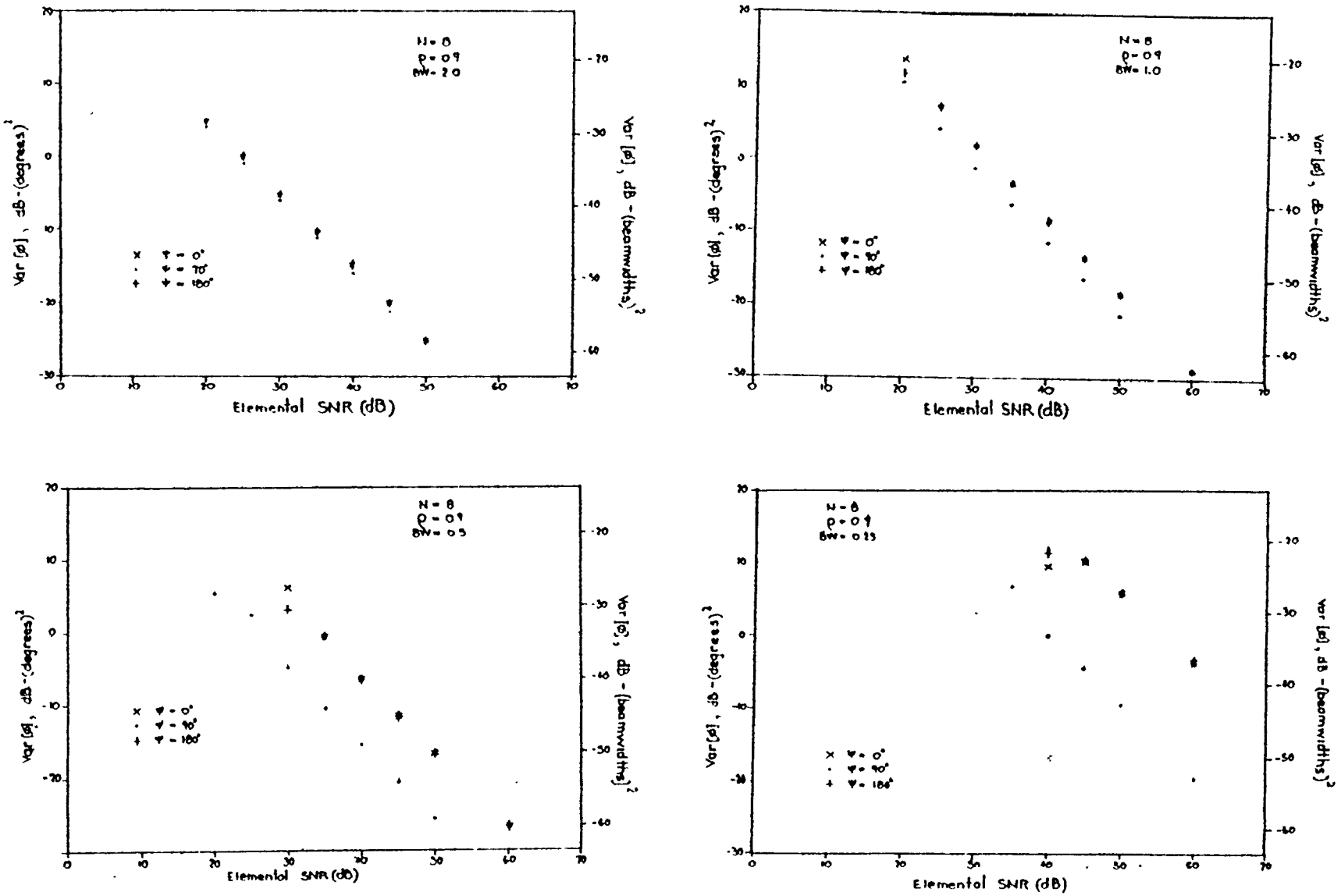

Fig. 3 - 10 Variances of ϕ_1 (stronger signal) as obtained by computer simulation, for the LS algorithm.

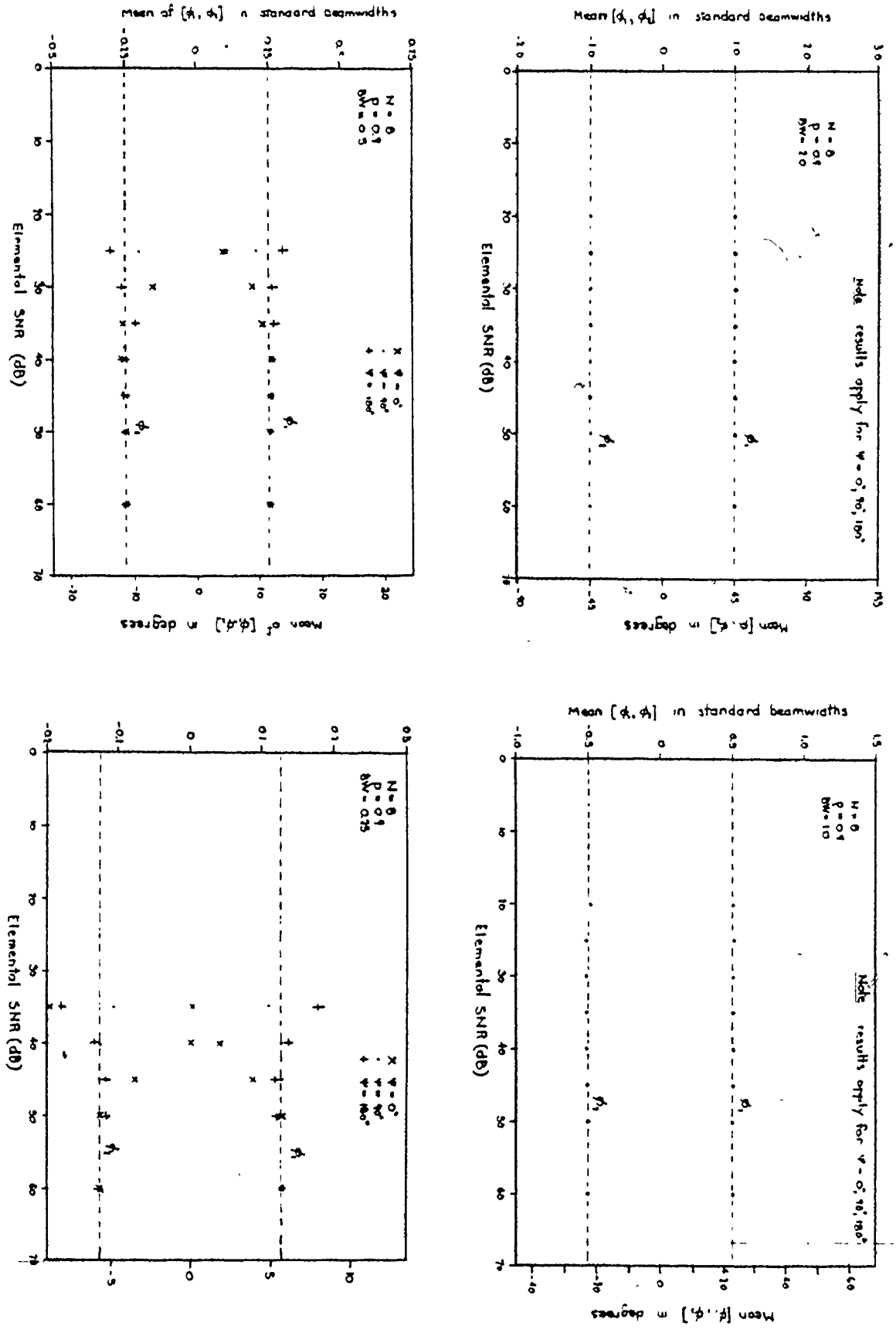

Fig. 3 - 11 Means of $\hat{\phi}_1, \hat{\phi}_2$ vs. SNR as obtained by computer simulation, for LS algorithm.

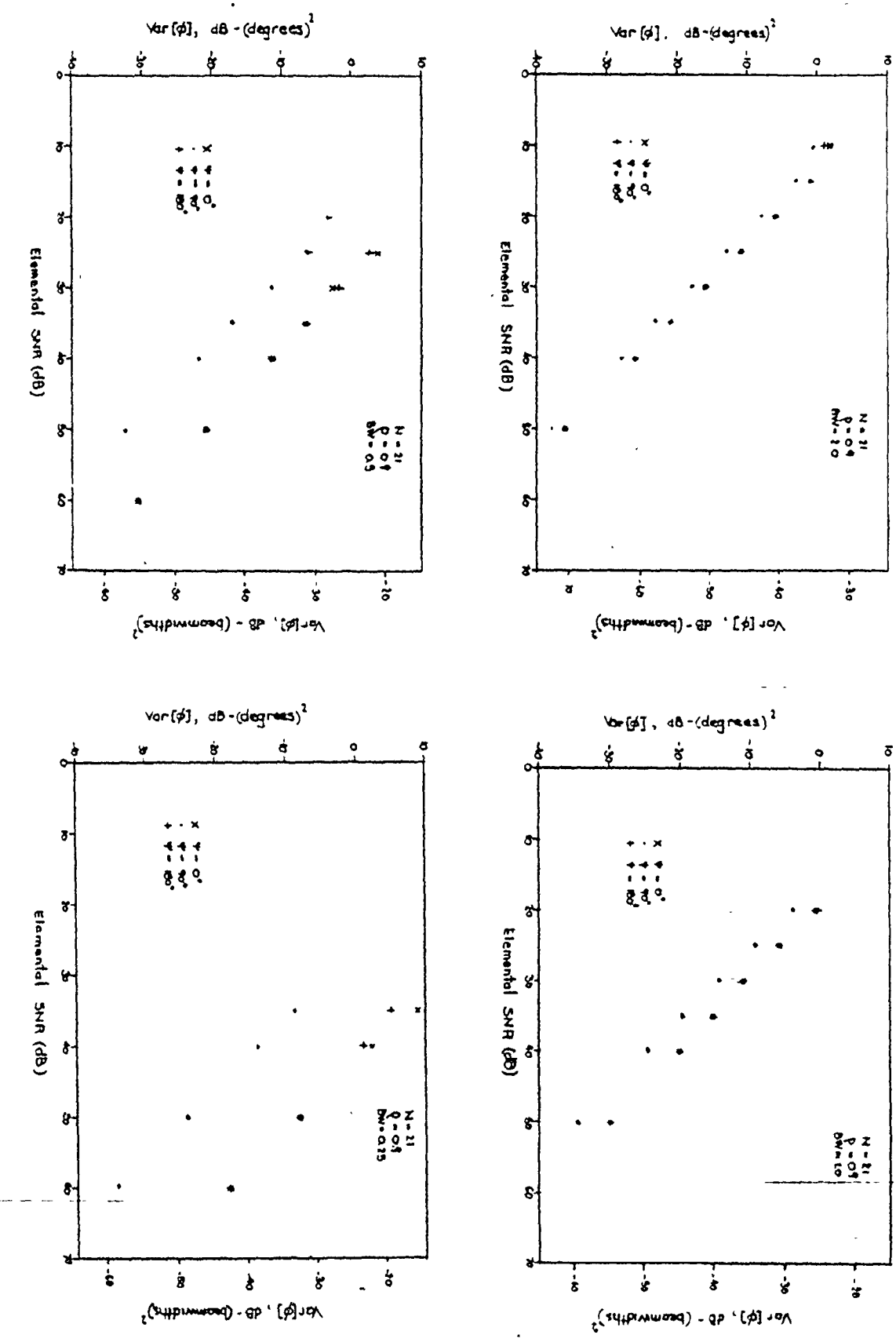

Fig. 3 - 12 Variances of $\hat{\phi}_1$ (stronger signal) vs. SNR as obtained by computer simulation, for the LS algorithm.

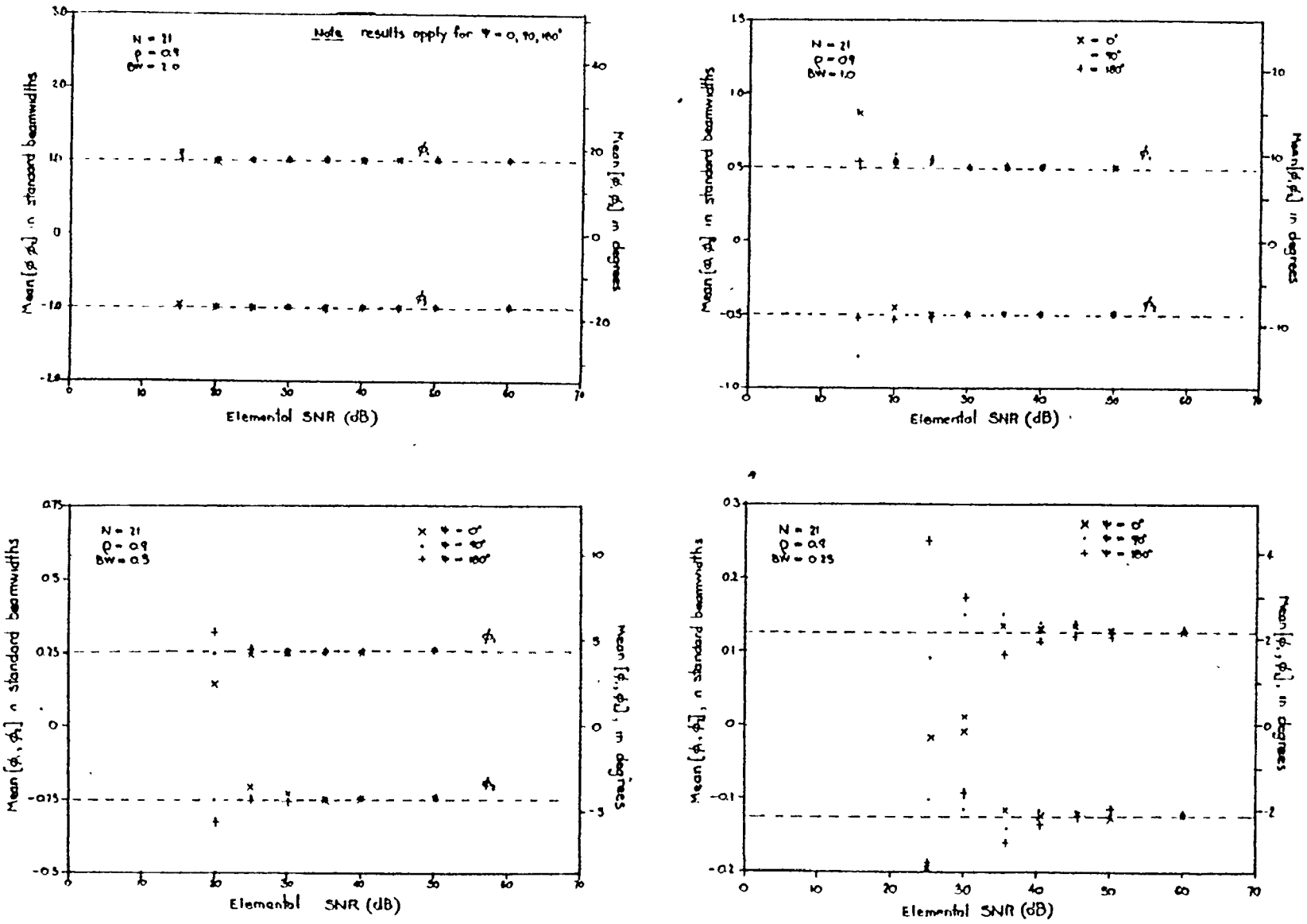

Fig. 3 - 13 Means of $\hat{\phi}_1, \hat{\phi}_2$ vs. SNR as obtained by computer simulation, for the LS algorithm

spectra. Therefore, the curves of Fig. 3-9 support the assertion that the exact choice of M is not a critical issue involved with the implementation of the LS algorithm.

Shown in Figs. 3-10 to 3-13 are the results of computer simulations evaluating the performance of the LS algorithm. Figures 3-10 and 3-11 show the mean and variance of the estimates obtained for N = 8 elements, whereas Figs. 3-12 and 3-13 show the same for N = 21 elements.

We note from these figures that the variances are uniformly better when $\psi = 90^{\circ}$ (spatially stationary sequence) than for $\psi = 0^{\circ}$ or 180°. However, the means of the estimates are independent of ψ at high SNR, a fact which makes the algorithm much more useful than the Burg algorithm in array processing problems.

We note from these results the presence of a threshold, which is dependent on the signal separation. For a given value of BW, the values of the angle estimates behave well until the SNR drops below the threshold value. After this point, the estimates bear no resemblance to the true incident angle values. This threshold effect is caused by the presence of spectral peaks induced by the noise in the wavenumber spectrum. These peaks overpower the effect of the signal as the SNR drops below threshold levels.

It is interesting to note that the LS algorithm also shows single-peak behaviour, but only below threshold. For

example, when N=21, and the signal separation is 0.5 standard beamwidths, there are 40 (out of a total of 45) single-peak results tallied by the computer simulation at SNR equal to 15 dB. This is in contrast, however, to the Burg results which show single-peak results at any value of SNR.

By way of example, the threshold for N=8 elements with a signal separation of 0.5 standard beamwidth occurs at about 30 dB SNR, and for N=21 elements the threshold is evident at 25 dB. These values may be too high to allow the LS algorithm to be of much use in practice. In fact, the experimental system as described in Appendix A could not produce a sufficiently high SNR to overcome the threshold.

Lang [3-40] has done work on the performance of maximum-entropy spectral estimators using the LS algorithm. His work includes a theoretical study evaluating the variance of the peaks of the spectrum obtained by the LS algorithm, when the input data is a short record composed of two closely spaced sinusoids. He finds that at high SNR's, the performance of the spectral estimator approaches the performance of the Cramer-Rao bound. This fact is supported by Tufts and Kumaresan [3-41], and also by results shown in Chapter 6 of this thesis. However, Lang fails to mention that the LS algorithm has a poorer performance at low SNR compared to maximum likelihood methods.

3.7.3 Pisarenko Method [3-11]

We shall now briefly discuss results from the Pisarenko method. Work by Ulrych and Clayton [3-15] has indicated that, although the Pisarenko method has excellent resolution capabilities, the spectral estimates are extremely sensitive to ψ. Figure 3-14 shows results reproduced from [3-15] showing variations in spectra as a function of ψ for both the Pisarenko and the LS algorithms. The extreme variation of the Pisarenko results with initial phase is evident from the figure.

Ulrych and Ooe [3-6] have shown that the poles of the Pisarenko spectral estimate are situated at the same angles as those of the Burg spectral estimate, but positioned more closely to the unit circle. This fact accounts for the high resolution of the Pisarenko estimate, but also indicates that this method would be equally sensitive to changes in ψ as is the Burg technique. Therefore, we see that the Pisarenko method is not a useful technique in the analysis of array data where the individual signal components are either temporally or spatially correlated. However, it is possible in situations where the autocorrelation matrix of data is Toeplitz, that both the Burg and the Pisarenko methods could perform acceptably well.

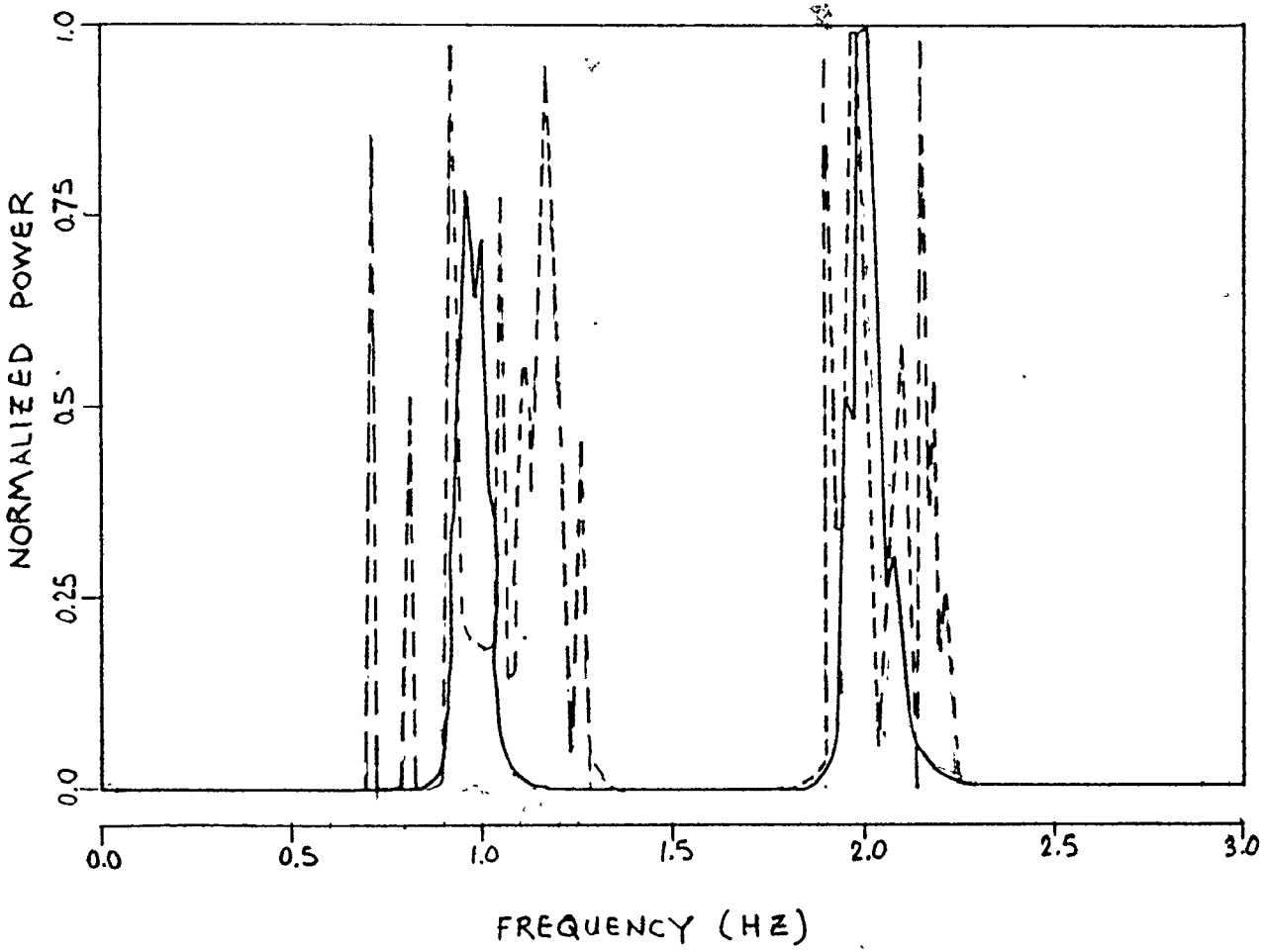

Fig 3-14 Variation of the spectrum of two sinusoids as a function of ψ computed using the LS estimate (full curve) and the Pisarenko estimate (dashed curve) [3-6]

3.8 Summary

In this chapter we have discussed various well-known time-series modelling techniques as they apply to array processing problems in a multipath environment with a highly correlated specular component. We have observed that the spectral analysis techniques (with the exception of the LS algorithm) are not applicable to the analysis of the resulting nonstationary data. Also, we have noted that when two or more plane waves are incident on an array a non-stationary data sequence results. Therefore, we find the Burg and the Pisarenko estimates are inappropriate in this application, and the results presented have certainly supported this assertion. The results have shown, however, that the LS algorithm behaves well in the analysis of incident plane waves, but suffers from a threshold effect which occurs at a relatively high SNR.

In the next two chapters we will discuss different maximum-likelihood methods applied to the array processing problem. We shall see that the results attainable with this method are superior to those given by the LS algorithm.

CHAPTER 4

MAXIMUM-LIKELIHOOD ESTIMATION TECHNIQUES (I)

In this chapter and the next we shall be discussing various maximum-likelihood (ML) estimation techniques as they apply in the array processing context. There are two separate techniques which will be considered. The first is a method to be presented in this chapter that was developed specifically to apply to the specular multipath environment as depicted in Fig. 2-1, and depends on the fact that the two incident signal components are symmetrically spaced in elevation about the normal of the array. The second method, to be presented in Chapter 5, is more general and is applicable to the situation where the signal components are incident from any direction. This chapter will begin with a general discussion of the philosophy of maximum likelihood estimation, and then proceed with a detailed description of the symmetric ML estimation technique.

4.1 Basic Concepts

Suppose that a particular variable $y(n)$, $n=0, \ldots, N-1$ is described by the following model:

$$y(n) = f(n, \beta) \tag{4-1}$$

where $f(\ )$ is some function which may be nonlinear in n and/or β, and β is a vector of parameters describing the

model. It is the value of this parameter vector which we wish to estimate. We then have available a set $\{x(n)\}$ of observations of $y(n)$ given by

$$x(n) = f(n, \underline{\beta}) + w(n) \qquad (4-2)$$
$$n = 0, \ldots, N-1$$

where the observation is corrupted by the addition of the noise term $w(n)$, which for this discussion, will be assumed Gaussian-distributed, but not necessarily independent. Since for a given set of observations $\{x(n)\}$, the parameters $\underline{\beta}$ may be considered constant, we may express the probability of a particular observation $\underline{x}$ (where $\underline{x}$ is a vector composed of $x(0), \ldots, x(N-1)$) given the parameter vector $\underline{\beta}$ as

$$p(\underline{x}|\underline{\beta}) = (2\pi^N|\underline{V}|)^{-1/2} \exp\left[-\frac{1}{2} (\underline{x}-f(\underline{\beta}))^T \underline{V}^{-1} (\underline{x}-f(\underline{\beta}))\right] \qquad (4-3)$$

where $\underline{V}$ is the NXN covariance matrix of the $w(n)$ and $\underline{f}(\beta)$ is the vector giving the true values of the observations $\underline{x}$. The superscript T denotes transpose. The right-hand side of (4-3) is the standard multi-variate Gaussian probability density function (pdf). Equation (4-3) may be written

$$L(\underline{\beta}) = (2\pi^N|\underline{V}|)^{-1/2} \exp\left[-\frac{1}{2} (\underline{x}-f(\underline{\beta}))^T \underline{V}^{-1} (\underline{x}-f(\underline{\beta}))\right] \qquad (4-4)$$

where $L(\underline{\beta})$ is called the likelihood function.

The maximum-likelihood estimate of the parameter vector $\underline{\beta}$ is that value of $\underline{\beta}$ which maximizes the likelihood

function $L(\beta)$ in (4-4).

The following heuristic argument may make the ML method seem plausible: the probability of observing a sample lying in a region $\delta\underline{x}$ around the actually observed sample $\underline{x}$ is given by $p(\underline{x}|\underline{\beta})\,\delta\underline{x} = L(\underline{\beta})\,\delta\underline{x}$. The value $\underline{\beta} = \hat{\underline{\beta}}$ for which this probability is greatest is the ML estimate. We say that $\hat{\underline{\beta}}$ is the most likely value of $\underline{\beta}$. Of all possible values of the parameters, $\hat{\underline{\beta}}$ is the one having the largest probability of giving rise to a sample within $\delta\underline{x}$ of the actually observed one.

Under relatively mild conditions on the form of the likelihood function, the ML estimate is consistent and asymptotically efficient. This is a strong argument for using the ML estimate when the sample size is large. The ML estimate does not usually possess any optimal properties for small sample sizes and is generally neither unbiased nor efficient (in a statistical sense) in this case. As Bard [4-1] states, sampling experiments have shown that the ML method produces acceptable estimates in many situations. Whereas better methods may be available in specific cases, a powerful argument for the use of the ML method is the generality and relative ease of application.

Since the logarithm is a monotonic increasing function of its argument, the value of $\underline{\beta}$ that maximizes $L(\underline{\beta})$ also maximizes $\log L(\underline{\beta})$. Since $\log L$ is frequently a

simpler function than L, it is in terms of maximizing log L that the problem is often formulated.

4.2 Development of the Symmetric ML Processor

White [4-2] has used the maximum-likelihood procedure to derive a structure for a receiver intended for application to the same problem we are considering. That is, the low-angle tracking radar (operating with a linear phased-array antenna) for the purpose of resolving the effect of multipath when the direct-path and specular multipath components of the received signal lie inside a beamwidth of the receiving array. In this chapter, we will present the derivation of a new structure for the receiver which is simpler to implement than White's processor. The derivation is obtained by recognizing that maximization of the likelihood function is equivalent to the maximization of the corresponding a posteriori probability function evaluated for the case of a uniform prior pdf [4-3]. This derivation is also presented by Haykin, Reilly and Taylor [4-4], and is novel compared to other forms of ML array-processing estimators in that all parameter values which are of no interest are integrated out. The resulting form is a function only of the one desired parameter ϕ.

Pollon and Lank [4-5] and Peebles [4-6] have also used maximum likelihood estimation methods for resolving the

effects of multipath; however, the former group applied the method to the processing of ring arrays, and neither paper takes advantage of the special symmetric signal configuration that may arise in a specular multipath environment.

Consider a linear array that consists of N identical antenna elements with no mutual coupling between them. The array is illuminated by the signal configuration as depicted in Fig. 2-1 (i.e. the specular multipath environment). The figure is reproduced on the next page for convenience. We may thus express the total received signal x(n,t) at the nth element of the array as follows:

$$x(n,t) = a_1 \cos(2\pi f_c t + n\phi + \Psi_1) + a_2 \cos(2\pi f_c t - n\phi + \Psi_2) + b(n) \cos[2\pi f_c t + \theta(n)] \qquad (4\text{-}5)$$

$$n = -\left(\frac{N-1}{2}\right), \ldots, \left(\frac{N-1}{2}\right)$$

$$-\pi \leq \phi \leq \pi$$

where: Ψ_1, Ψ_2 are the initial phase angles of the direct and multipath components

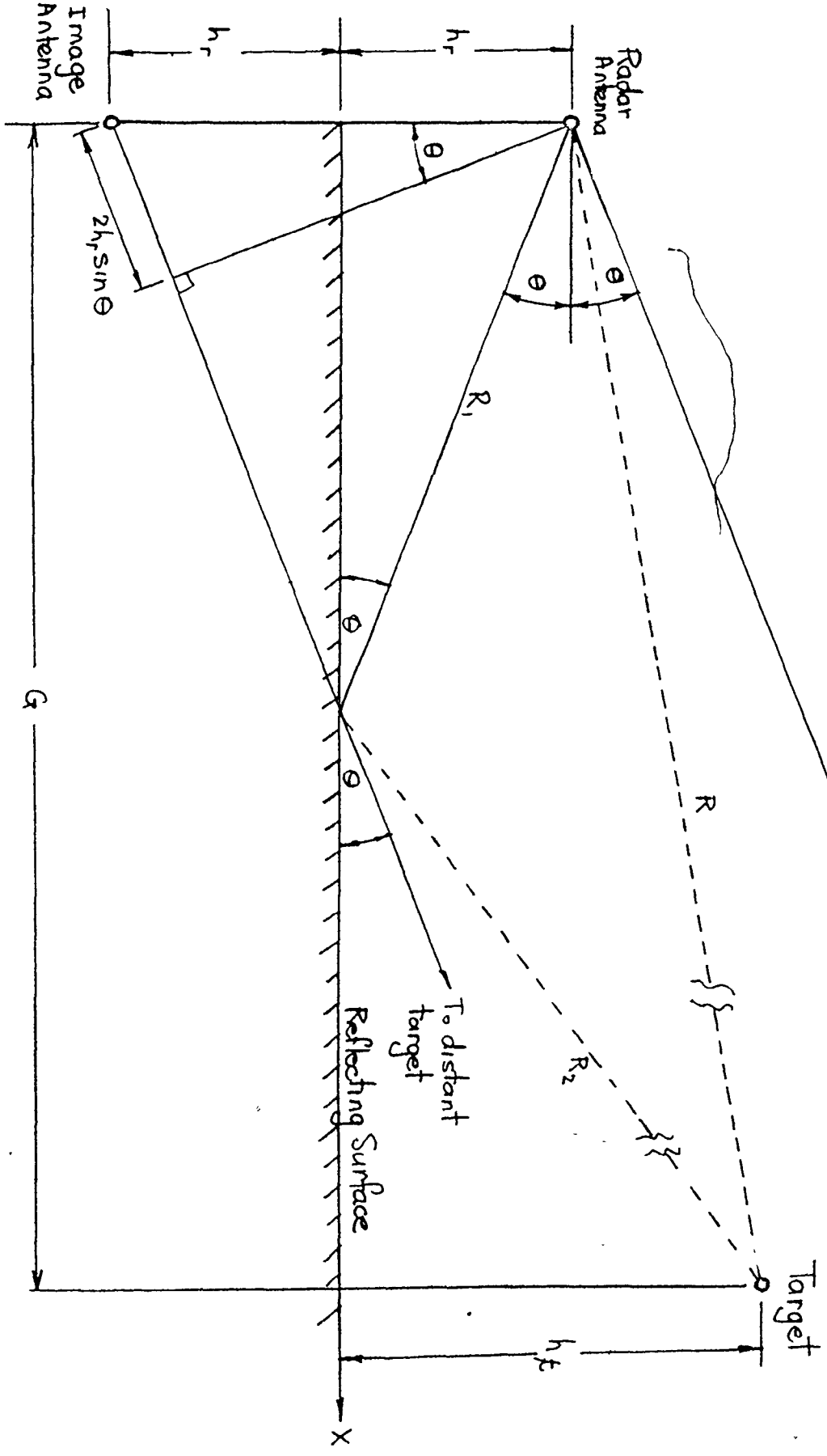

Fig 2-1 Geometry of specular multipath reflections

a_1, a_2 are the amplitudes of the direct and multipath components

$b(n)$, $\theta(n)$ are the envelope and phase angle of an additive narrowband Gaussian noise of zero mean and variance σ_w^2 at the nth element

and the other symbols are as defined previously. With no mutual coupling present between adjacent elements of the array, we find that the noise components at the various elements of the array are uncorrelated, i.e., the corresponding covariance matrix has only non-zero elements on the main diagonal.

The amplitude a_2 of the multipath component is related to the amplitude a_1 of the direct component by

$$a_2 = \rho\, a_1 \tag{4-6}$$

where ρ is the reflection coefficient of the reflecting surface, as discussed in Chapter 2. We note also that the phase angles ψ_1 and ψ_2 differ by an amount ψ as defined by (2-2). Variations in ψ may occur in practice due to inhomogeneities in the reflecting surface; however, these variations are typically small if the arrival angle of the

multipath does not vary significantly. In accordance then with (2-2) and (4-6), we find that the two components of the wave impinging on the array are usually highly correlated. This correlation causes the resulting spatial sequence as produced by the array to exhibit spatial nonstationarity, a fact which, as we have seen from Chapter 3, causes a severe deterioriation in the performance of most of the time-series techniques.

Expressing the received signal $x(n,t)$ in terms of its in-phase and quadrature components, we may write

$$x(n,t) = x_c(n) \cos(2\pi f_c t) - x_s(n) \sin(2\pi f_c t) \qquad (4-7)$$

The in-phase component $x_c(n)$ is defined by

$$x_c(n) = u_1 \cos n\phi + u_2 \sin n\phi + w_c(n) \qquad (4-8)$$

where

$$u_1 = a_1 \cos \Psi_1 + a_2 \cos \Psi_2 \qquad (4-9)$$

$$u_2 = -a_1 \sin \Psi_1 + a_2 \sin \Psi_2 \qquad (4-10)$$

$$w_c(n) = b(n) \cos[\theta(n)] \qquad (4-11)$$

The quadrature component $x_s(n)$ is defined by

$$x_s(n) = v_1 \cos n\phi + v_2 \sin n\phi + w_s(n) \qquad (4-12)$$

where

$$v_1 = a_1 \sin \Psi_1 + a_2 \sin \Psi_2 \qquad (4-13)$$

$$v_2 = a_1 \cos \Psi_1 - a_2 \cos \Psi_2 \qquad (4-14)$$

$$w_s(n) = b(n) \sin [\theta(n)] \tag{4-15}$$

Consider first the processing which must be done on the in-phase component $x_c(n)$ in (4-8). With the element index $n = -(\frac{N-1}{2}), \ldots, (\frac{N-1}{2})$ for N odd, we find that $\cos n\phi$ and $\sin n\phi$ are orthogonal over the interval considered for all values of ϕ and N, that is,

$$\sum_n \cos n\phi \sin n\phi = 0 \tag{4-16}$$

However, in general, the $\{\cos n\phi\}$ and $\{\sin n\phi\}$ sequences do not have equal energy. The in-phase noise component $w_c(n)$ is a Gaussian random variable of zero mean and variance σ_w^2 for each n. Also, $w_c(n)$ and $w_c(m)$ are uncorrelated for $n \neq m$. We now define the column vector $\underline{w}_c$ whose elements are

$$w_c(n) = x_c(n) - u_1 \cos n\phi - u_2 \sin n\phi \tag{4-17}$$
$$n = -(N-1)/2, \ldots, (N-1)/2$$

The conditional probability density function of $x_c(n)$ over the complete range of n, given u_1, u_2, ϕ is then

$$p(\underline{x}_c | u_1, u_2, \phi) = (2\pi\sigma_w^2)^{-N/2} \exp[-\frac{1}{2\sigma_w^2} \underline{w}_c^T \underline{w}_c]$$

The above has the same form as (4-3), and hence is the likelihood function for this particular estimation problem. By substituting (4-17) into the above, we obtain

$$p(\underline{x}_c | u_1, u_2, \phi) = (2\pi\sigma_w^2)^{-N/2} \cdot$$

$$\exp\left[-\frac{1}{2\sigma_w^2} \sum_n (x_c(n) - u_1 \cos n\phi - u_2 \sin n\phi)^2\right] \quad (4\text{-}18)$$

We now consider writing the above in terms of unit-energy basis signals, instead of the respective sin(·) and cos(·) functions. By setting $(2\pi\sigma_w^2)^{-N/2} = K$, we now write

$$p(\underline{x}_c | q_1, q_2, \phi) = K \exp\left\{-\frac{1}{2\sigma_w^2} \sum_n [x_c(n) - q_1 s_1(n,\phi) - q_2 s_2(n,\phi)]^2\right\} \quad (4\text{-}19)$$

where

$$s_1(n,\phi) = \frac{\cos n\phi}{(\sum_n \cos^2 n\phi)^{1/2}} \quad (4\text{-}20)$$

$$s_2(n,\phi) = \frac{\sin n\phi}{(\sum_n \sin^2 n\phi)^{1/2}}$$

$$q_1 = u_1 (\sum_n \cos^2 n\phi)^{1/2}$$

$$q_2 = u_2 (\sum_n \sin^2 n\phi)^{1/2} \quad (4\text{-}21)$$

By expanding (4-19) we obtain

$$p(\underline{x}_c | q_1, q_2, \phi) = K \exp\left[-\frac{1}{2\sigma_w^2} \sum_n x_c^2(n)\right]$$

$$\cdot \exp\left[-\frac{1}{2\sigma_w^2} [q_1^2 - 2q_1 \sum_n x_c(n)\, s_1(n,\phi)]\right]$$

$$\cdot \exp\left[-\frac{1}{2\sigma_w^2} [q_2^2 - 2q_2 \sum_n x_c(n)\, s_2(n,\phi)]\right] \quad (4\text{-}22)$$

where we have made use of the orthonormality of $s_1(\cdot)$ and $s_2(\cdot)$.

We next define the new quantities $L_1(\phi)$ and $L_2(\phi)$ respectively as

$$L_1(\phi) = \sum_n x_c(n)\ s_1(n\phi)$$

and

$$L_2(\phi) = \sum_n x_c(n)\ s_2(n,\phi) \qquad (4\text{-}23)$$

By substituting the two above equations into (4-22), we now obtain

$$p(\underline{x}_c|q_1,q_2,\phi) = K \exp\left[-\frac{1}{2\sigma_w^2}\sum_n x_c^2(n)\right] \cdot \exp\left[-\frac{1}{2\sigma_w^2}(q_1^2 - 2q_1\ L_1(\phi))\right] \cdot \exp\left[-\frac{1}{2\sigma_w^2}(q_2^2 - 2q_2\ L_2(\phi))\right] \qquad (4\text{-}24)$$

The three-dimensional maximization of (4-24) with respect to q_1, q_2 and ϕ would lead to ML estimates of these parameters. We note however that the only parameter of interest to us in (4-24) is ϕ; the q_1 and q_2 are undesired parameters. Therefore, it is our intent to form an estimator which is independent of q_1 and q_2. This may accomplished by forming the marginal pdf of the distribution (4-24) with respect to ϕ only, with the aid of Bayes' rule. The general definition of the marginal distribution of $p(\underline{x}_c, \phi)$ is

$$p(\underline{x}_c, \phi) = \int_{q_1} \int_{q_2} p(\underline{x}_c, \phi, q_1, q_2)\, dq_1\, dq_2 \qquad (4\text{-}25)$$

but

$$p(\underline{x}_c, \phi) = p(\phi|\underline{x}_c)\, p(\underline{x}_c)$$

and

$$p(\underline{x}_c, \phi, q_1, q_2) = p(\underline{x}_c|\phi, q_1, q_2) \cdot p(\phi, q_1, q_2)$$

Substituting the above two equations into (4-25), we obtain

$$p(\phi|\underline{x}_c) = \frac{1}{p(\underline{x}_c)} \int_{q_1} \int_{q_2} p(\underline{x}_c|q_1, q_2, \phi)\, p(\phi, q_1, q_2)\, dq_1\, dq_2 \qquad (4\text{-}26)$$

The expression on the left-hand side of (4-26) is called the a posteriori pdf; we wish to find the value of ϕ for which this distribution is a maximum. The distribution $p(\phi, q_1, q_2)$ is called the prior distribution; it describes the joint probability of the parameter values before the data to be analyzed is gathered. The $p(\underline{x}_c)$ is independent of any of the parameters of interest; hence, it plays the role of a normalizing constant such that the left-hand side of (4-26) integrates to unity over the entire range of ϕ.

The integration in (4-26) may be performed by first setting the prior pdf $p(\phi, q_1, q_2)$ equal to a constant over the range of all the parameters, and then completing the square in (4-24) and substituting the result into (4-26). After lumping the constants K, $1/p(x_c)$, and the prior pdf into a single constant K_1, we obtain

$$p(\phi|\underline{x}_c) = K_1 \int_{q_1}\int_{q_2} \exp[-\frac{1}{2\sigma_w^2}\sum_n x_c^2(n)]$$

$$\cdot \exp[-\frac{1}{2\sigma_w^2}(q_1 - L_1(\phi))^2]$$

$$\cdot \exp[-\frac{1}{2\sigma_w^2}(q_2 - L_2(\phi))^2]$$

$$\cdot \exp[\frac{1}{2\sigma_w^2}(L_1^2(\phi) + L_2^2(\phi))]\, dq_1\, dq_2 \qquad (4\text{-}27)$$

The integration with respect to q_1 and q_2 may be easily accomplished by realizing that the second and third terms in the above describe Gaussian pdf's in q_1 and q_2 respectively. Therefore, they integrate to a constant. We note that since the object of this endeavour is only to maximize the distribution $p(\phi|\underline{x}_c)$ with respect to ϕ, the actual value of the multiplicative constant is of no interest. Therefore, we may write the a posteriori pdf $p(\phi|\underline{x}_c)$ as

$$p(\phi|\underline{x}_c) = K_2 \exp[\frac{1}{2\sigma_w^2}(L_c(\phi) - \sum_n x_c^2(n))] \qquad (4\text{-}28)$$

where K_2 is a new constant, and

$$L_c(\phi) = \frac{[\sum_n x_c(n)\cos n\phi]^2}{\sum_n \cos^2 n\phi} + \frac{[\sum_n x_c(n)\sin n\phi]^2}{\sum_n \sin^2 n\phi} \qquad (4\text{-}29)$$

Therefore, maximization of (4-29) with respect to ϕ maximizes the a posteriori density function $p(\phi|\underline{x}_c)$ and gives the desired estimate $\hat{\phi}$ of ϕ. This value is called the maximum a posteriori (MAP) estimate of ϕ. Because of the fact that the prior distribution $p(q_1, q_2, \phi)$ in (4-26) was made equal to a constant, the MAP and the ML estimates of ϕ are equivalent for this case.

Following a procedure similar to that described above, we find that the maximization of the a posteriori pdf of ϕ given the quadrature component $x_s(n)$ of the received signal $x(n,t)$ is equivalent to maximizing a second function defined by

$$L_s(\phi) = \frac{[\sum_n x_s(n) \cos n\phi]^2}{\sum_n \cos^2 n\phi} + \frac{[\sum_n x_s(n) \sin n\phi]^2}{\sum_n \sin^2 n\phi}$$

which has the same structure as (4-29), except that it is fed by $x_s(n)$ instead of $x_c(n)$.

At this point we will digress from our present discussion and consider the effects of mutual coupling between the array sensors. We must emphasize that the development of this processor applies only to situations where the mutual coupling between the array sensors is negligible. The absence of mutual coupling simplifies the development in at least three ways. The first is that the equation (4-7) which defines our model (i.e., the equation

describing the elemental excitations) has a much simpler form in the absence of mutual coupling. If mutual coupling is to be considered, the excitation at a given element also consists of contributions from the field configuration present at the other elements, all of which must be taken into consideration in the analysis.

The second simplification is that if the mutual coupling is assumed to be negligible, then

$$E[w_n \, w_m^*] = \delta_{n,m} \sigma_w^2 \tag{4-31}$$

where w_n is the complex noise term at the nth sensor. In other words, the output noise contributions from different sensor elements are uncorrelated. This leads to a diagonal covariance matrix structure $[\underline{V}]$ in the resulting likelihood function (4-4), a fact which not only simplifies the analysis but also simplifies the implementation of the resulting processor.

The third manner in which mutual coupling presents difficulties has to do with the effects of mutual coupling on the driving-point impedances of the individual array elements as seen by the amplifier inputs. It is well known that the presence of mutual coupling may drastically change the elemental driving-point impedance as presented by a single isolated element [4-7], [4-8]. The elements at the ends of the array will present different impedances than those towards the centre, since the couplings are stronger

at the centre of the array. The effect that this varying driving-point impedance will have on the output noise power of the essentially identical receiver amplifiers (and hence on the diagonal elements of $[\underline{V}]$) is difficult to determine. Note, however, that if the front-end of the receiver amplifier is a cascode configuration [4-9], and that since the real part of the array element's driving-point impedance has no associated thermal noise voltage, the receiver amplifier output noise power would not change significantly from element-to-element.

As mentioned previously, the presence of mutual coupling will cause the noise terms w(n) and w(m) to become correlated, $n \neq m$, because noise from one receiver front-end will radiate over to the other element's front-end sections. In this case, the covariance matrix $\underline{V}$ in (4-4) takes the form

$$\underline{V} = \begin{bmatrix} \sigma_w^2 & \sigma_{12}^2 & \cdots & \sigma_{1N}^2 \\ \sigma_{21}^2 & \sigma_w^2 & & \vdots \\ \vdots & & \ddots & \\ \sigma_{N1}^2 & \cdots & & \sigma_w^2 \end{bmatrix} \tag{4-32}$$

The analytical evaluation of the off-diagonal terms of $\underline{V}$ is a difficult issue, and would depend among other things, on the receiver front-end design. The nondiagonal nature of $\underline{V}$ above makes the development and the implementation of the ML processor much more difficult.

As we have seen in this past discussion, many additional factors must be taken into account when the effects of mutual coupling are considered. However, we see from Appendix A that the mutual couplings between the elements of the experimental array are indeed very small. Because arrays with negligible mutual couplings may certainly exist and are practical, the remainder of this chapter will consider only the case where mutual coupling between the array sensors may be ignored. However, the evaluation of the performance of the ML processor in the presence of mutual coupling exists is obviously an area which requires further exploration.

The receiver structure for $L_c(\phi)$ and $L_s(\phi)$, for the case of equal noise powers, is shown in Fig. 4-1. Note that for a given value of ϕ, the two branches operating on cos $n\phi$ and sin $n\phi$ in Fig. 4-1, corresponding to the denominator terms in the right-hand side of (4-29), represent the equalization which must be applied to the two principal branches of the receiver operating on $x_c(n)$ or $x_s(n)$ in order to correct for the fact that cos $n\phi$ and sin $n\phi$ have unequal energy over the spatial interval spanned by the array.

In this section we have developed two functions $L_c(\phi)$ and $L_s(\phi)$. The value of ϕ for which the sum of these two functions is maximized is the maximum-likelihood estimate of

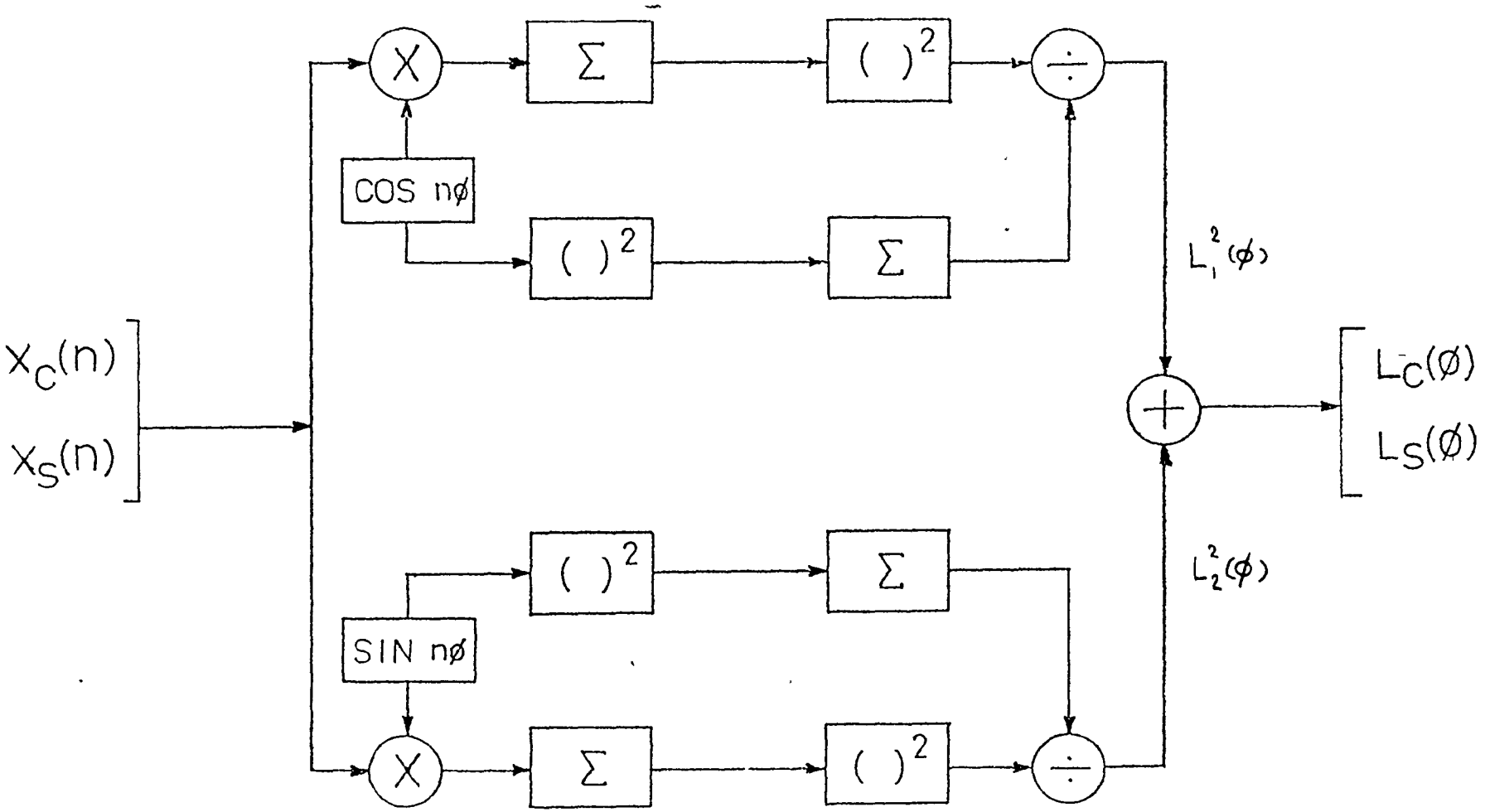

Fig. 4 - 1 Maximum likelihood receiver structure when all N noise variances are equal.

ϕ. Since the terms $w_c(n)$ and $w_s(n)$ in (4-8) and (4-12) respectively are Gaussian-distributed and uncorrelated, the corresponding likelihood functions $p(\underline{x}_c | u_1, u_2, \phi)$ and $p(x_s | v_1, v_2, \phi)$ are statistically independent. Therefore, the ML estimate of ϕ given both $\{x_c\}$ and $\{x_s\}$ is obtained by maximizing, with respect to ϕ, the sum of $L_c(\phi)$ and $L_s(\phi)$. Thus, the function of interest will be $L(\phi)$, given by

$$L(\phi) = L_c(\phi) + L_s(\phi) \tag{4-33}$$

where

$$L_c(\phi) = \frac{\left[\sum_n x_c(n) \cos n\phi\right]^2}{\sum_n \cos^2 n\phi} + \frac{\left[\sum_n x_c(n) \sin n\phi\right]^2}{\sum_n \sin^2 n\phi} \tag{4-34}$$

and

$$L_s(\phi) = \frac{\left[\sum_n x_s(n) \cos n\phi\right]^2}{\sum_n \cos^2 n\phi} + \frac{\left[\sum_n x_s(n) \sin n\phi\right]^2}{\sum_n \sin^2 n\phi} \tag{4-35}$$

The remainder of this chapter will be devoted to a discussion on the characteristics of the estimator (4-33).

4.3 Implementation of the Estimator

Equation (4-33) must be maximized with respect to ϕ to give the desired estimate of both the electrical angles corresponding to the direct and multipath waves incident on the array in a specular multipath environment. This maximization is with respect to a single variable, a fact which allows for simple implementation of this ML estimator.

We now shall discuss a simple efficient algorithm as presented by Bandler in [4-10], called the Golden Section search, which may be employed to effect this required maximization. The algorithm in its standard form always minimizes; however, the technique may be used to maximize simply by minimizing the negative of the appropriate objective function. Therefore, we seek to minimize the objective function $[-L(\phi)]$ given by (4-33).

At the outset of the computation, we assume an interval of uncertainty in ϕ for which $L(\phi)$ is known to be unimodal. The object of the algorithm is to sequentially reduce the width of the pertinent interval until the value of ϕ is known within an acceptably narrow range.

At the beginning of the jth iteration, the interval of uncertainty, I_j by referring to Fig. 4-2, is given by

$$I_j = u - l \tag{4-36}$$

Note that we take

$$l < a < b < u \tag{4-37}$$

After evaluating L(a) and L(b), one of two conclusions can be drawn:

1. If $L(a) > L(b)$, the minimum lies in $[a,u]$ and $I_{j+1} = u-a$, as in Fig. 4-2 (a), (b).

2. If $L(a) < L(b)$, the minimum lies in $[l,b]$ and $I_{j+1} = b-l$, as in Fig. 4-2 (c), (d).

Whatever the outcome of comparing $L(a)$ and $L(b)$, we want

$$I_{j+1} = u-a = b-l \ , \tag{4-38}$$

which is achieved by symmetrical placement of a and b on $[l,u]$. Also, in the new interval I_{j+2}, we wish to use one of the points used in I_{j+1} again, which leads to

$$I_{j+2} = u-b = a-l \tag{4-39}$$

Combining (4-36) to (4-39) we get

$$I_j = I_{j+1} + I_{j+2} \tag{4-40}$$

The interval of uncertainty is to be reduced by a constant factor τ each iteration, which implies that

$$\frac{I_j}{I_{j+1}} = \frac{I_{j+1}}{I_{j+2}} = \tau \ . \tag{4-41}$$

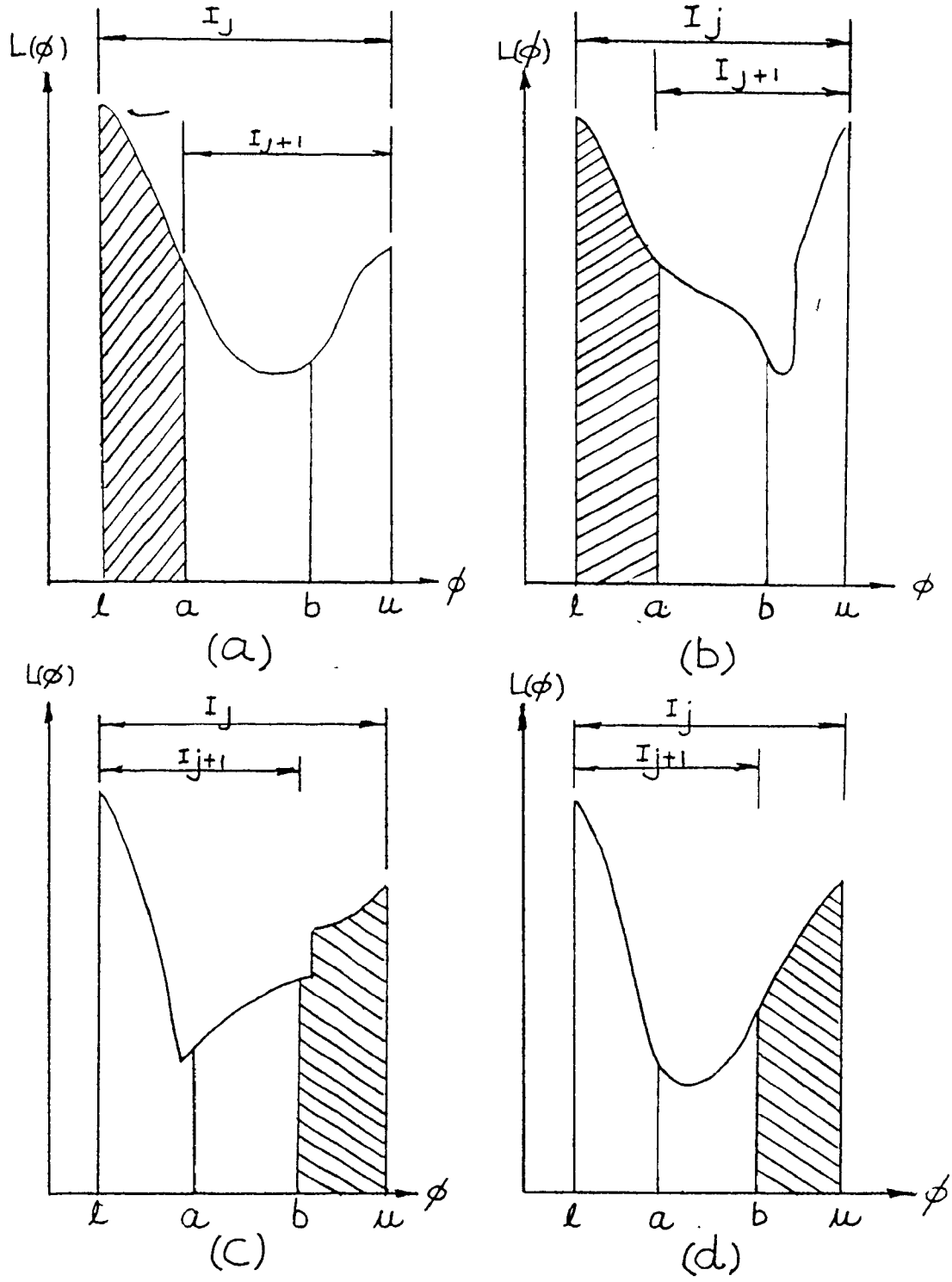

Fig 4-2 Reduction of the interval of uncertainty [4-10]

Combining (4-40) and (4-41), we get

$$\tau^2 = \tau + 1 \qquad (4\text{-}42)$$

the solution of relevance being $\tau = 1.618034$. The division of a line according to this ratio is called the Golden Section of a line.

At the jth iteration of this method,

$$\phi_a^j = \frac{1}{\tau^2} I_j + \phi_1^j$$

and (4-43)

$$\phi_b^j = \frac{1}{\tau} I_j + \phi_1^j \quad j = 1, 2, 3 \ldots$$

where ϕ_a^j, ϕ_b^j and ϕ_1^j are the values of ϕ at the jth iteration corresponding to the positions a, b or 1 respectively.

Note that each iteration except the first involves only one function evaluation due to the symmetry of the positioning of the points a and b in the interval. Depending on the outcome of the jth iteration, the appropriate conditions are set for the (j+1)th iteration and

the procedure repeats.

One of the features of this scheme is that for a desired accuracy in ϕ, and for a given initial interval of uncertainty width, the number of iterations required is fixed in advance. After n function evaluations

$$\frac{I_1}{I_n} = \tau^{n-1} \tag{4-44}$$

Therefore, for a desired accuracy of $\Delta\phi$, n should be chosen so that

$$\tau^{n-2} < \frac{\phi_u^1 - \phi_l^1}{\Delta\phi} \leq \tau^{n-1} \tag{4-45}$$

For example, if the initial interval is chosen to be 1.0 BW, and it is desired to obtain an accuracy of 0.001 BW, then 16 iterations are necessary.

This technique, because of its simplicity, may be amenable to implementation on a microprocessor. The method, when programmed in Fortran IV, requires only about 25 lines of source code when the function to be evaluated is computed in a separate subroutine. In a microprocessor implementation, the computation of the objective function (4-33) may be made faster through the use of table lookups. For example, since the denominators in the expressions (4-34) and (4-35) are independent of the observed data and

are functions only of ϕ, the value of the entire sums in both denominators may be determined through one lookup.

We will now determine the number of bits required in order to obtain a dynamic range in ϕ between 0.001 and 4 standard beamwidths. (Note that for an 8-element array, 4 standard beamwidths is the limit of the visible range of the array). This range is a ratio of 4000, for which 12 bits are required, giving an actual dynamic range of a factor of 4096. Therefore, 2^{12} memory locations ($\equiv$4K) are necessary to evaluate one of the denominators in either expression (4-34) or (4-35). A total of 8K memory locations are then required to determine both the sin and the cos denominators through the use of table lookups.

Lookup tables may also be employed in the evaluation of the numerators in the expressions for $L_c(\phi)$ and $L_s(\phi)$. Here, however, the entire sum may not be determined directly in one lookup as in the previous case, because the individual terms in the sum depend on the observed data. However, the cos $n\phi$ and sin $n\phi$ terms may be evaluated by lookups. For an 8-element array, 3 bits are required for the n, and as before, 12 bits are needed to give the required dynamic range in ϕ, which means that a total of $2x2^{15} \equiv$ 64K memory locations are needed to provide complete lookup facility to evaluate these terms. The total requirement of (8+64)K = 72K of ROM (read-only memory) is a

significant quantity, but may not be a prohibitive factor in actual practical implementations of this processor.

Let us now examine the computational effort required in the maximization of ϕ based on data obtained from one snapshot. We have observed previously that sixteen iterations are required to acquire the desired accuracy in ϕ; therefore, seventeen function evaluations are needed when using the Golden Section search method. Each function evaluation requires $4(N+2)$ operations with the aid of lookups, and each iteration of the search method requires only 1 additional multiplication. Therefore, a total of $17x[4(8+2)] + 16 = 696$ operations are needed in the maximization of ϕ when $N = 8$ elements, when a resolution of 0.001 BW is desired.

At time of writing, 16x16 bit multipliers are available commercially capable of a single multiply in 150 nS. If external multipliers such as this are used in conjunction with a 16-bit microprocessor, all 696 operations could be performed in 104.4 μS. It would therefore seem that the microprocessor would have adequate time for executing the algorithm logic for operating real-time at pulse rates in the order of 1 KHz. A suggestion for further work would be to determine if this algorithm would be amenable to implementation on a microprocessor. One problem may exist with arithmetic precision in a 16-bit machine.

However, it has been noted that Intel is developing a 32-bit microprocessor scheduled for delivery in 1982.

4.4 Results and Performance

In this section, we shall explore in some detail the characteristics of the estimator given by (4-33). The performance will be evaluated both by means of computer simulation by experiment. Also, theoretical variances, valid only for high SNR, will be determined and presented, and then compared to the estimator variances obtained by the other two methods.

It is interesting to examine the behaviour of the objective function $L(\phi)$ for various parameter values. Figure 4-3 shows plots of the objective function for total signal separations of 0.25, 0.5, 1.0 and 2.0 beamwidths, when N = 21 and ρ = 0.9. The curves were evaluated by first generating artificial data according to (4-8) and (4-12) for selected values of ρ, ~~γ and~~ N, for an infinite value of SNR. These data were then substituted into (4-33) and evaluated for various values of ϕ to give the results which appear in the figure. The position of the vertical arrow indicates the true target angle.

There are several interesting considerations which arise from this set of curves. First, when BW < 1.0 beamwidth, all curves are unimodal over the range $0 \leq \phi \leq .3$

radians, which, for N = 21 corresponds almost exactly to the range $0 \leq \phi \leq 2.0$ standard beamwidths. Therefore, the restriction that the respective objective function must be unimodal in order to apply the Golden Section search imposed no difficulty in using the method in this situation.

Also, when BW < 1.0 beamwidth, we note that the maxima are relatively well-defined for $\Psi = 0^{\circ}$, but become progressively more dispersed as Ψ approaches 180°. Thus, we expect that the confounding effects of noise will be greater for the case $\Psi = 180^{\circ}$ than when $\Psi = 0^{\circ}$. Later, in the section on theoretical variances, we shall indeed find this to be true.

We note that for a fixed value of Ψ, the maxima become more distinct as BW increases (up to a value of 1.0 standard beamwidths). Therefore, we should again anticipate better estimation behaviour in the presence of noise as BW increases up to this value. This statement shall also be verified later in the discussion on theoretical variances.

We note that for many cases, the curves in Fig. 4-3 are non-symmetrical about their maxima. They generally fall off much more quickly on the high side of the maximum than on the low side. This non-symmetric behaviour is a consequence of the nonlinear characteristics of the estimator, and as such, generally leads to biased results [4-3].

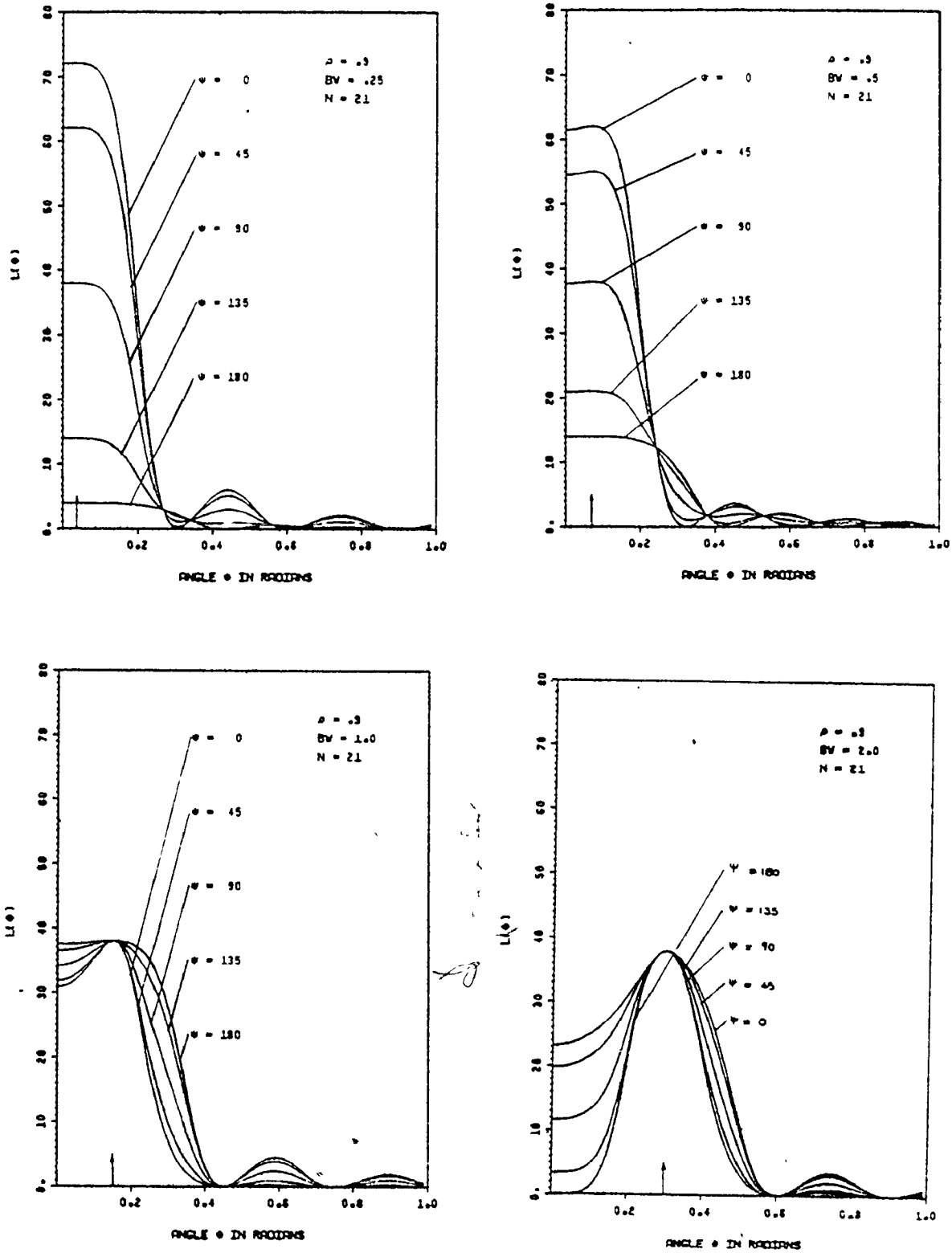

Fig. 4 - 3 The objective function $L(\phi)$ vs. ϕ for N = 21 and varying ψ and BW.

The fact that a nonlinear estimator generally leads to biased results may be understood better by considering the confidence interval around the estimated parameter value. When the estimator is linear in the desired parameter, the corresponding confidence interval is easily ascertained to be symmetric around the estimated value, e.g. [4-11], [4-12]. However, in the nonlinear case, the appropriate confidence interval will generally be asymmetric about the estimated value, and hence the expected value of the estimate will shift away from the true parameter value towards the centre of the confidence interval. Another way of looking at the problem is that the nonlinearity in the estimator tends to compress the additive noise in the observed data more on one side of the true parameter value than it does on the other. Thus, after many repetitions of the same experiment, the effect of additive noise will be to move the expected value of the estimate away from the true parameter value towards the side of the interval which is less compressed.

The curves of Fig. 4-3 are actually plots which are proportional to the log-posterior probability density function of ϕ. This is easily verified by reference to (4-28) and remembering that the second term in the exponent is a constant. With this in mind, it is easy to determine that the confidence interval for ϕ will extend further to

the left than to the right for most of the cases in the figure. Consequently, the estimates will generally tend to be biased low, a fact which except for a few exceptions, will be verified later as a result of the computer simulations.

We shall now develop the form of the theoretical variance of the ML estimator. The technique used will be to treat $L(\phi)$ as if it were linear in ϕ, which of course is true only over a small range of ϕ. However, within this small range, the estimator may be shown to be linear and unbiased; hence, the Cramer-Rao bound applies and the conditions necessary for the equality are satisfied. Therefore, the variance of the estimate $\hat{\phi}$ may be determined by evaluating the pertinent value of the bound.

Again, we shall consider only the analysis pertaining to the in-phase component $\underline{x}_c$ of the received data, because an exactly analagous derivation applies to the quadrature case.

Let us now express the in-phase received data as

$$x_c(n) = f_c(n,\phi_T) + w_c(n) \qquad (4-46)$$

where $f_c(n,\phi_T)$ is defined through (4-8), and ϕ_T is the (unknown) true value of ϕ. We now expand $f_c(n,\phi)$ in a Taylor series about some arbitrary point $\phi = \phi^*$, where ϕ^* is close to ϕ_T, and retain only the first two terms:

$$x_c(n) \approx f_c(n,\phi^*) + \frac{\partial}{\partial\phi} f_c(n,\phi) \Big|_{\phi=\phi^*} (\phi_T - \phi^*) + w_c(n) \qquad (4\text{-}47)$$

We may now write

$$r_c(n) = A_c(n)\ \Delta\phi_T + w_c(n) \qquad (4\text{-}48)$$

where

$$r_c(n) = x_c(n) - f_c(n,\phi^*) \qquad (4\text{-}49)$$

$$A_c(n) = \frac{\partial}{\partial\phi} f_c(n,\phi)\Big|_{\phi=\phi^*} \qquad (4\text{-}50)$$

$$\Delta\phi_T = \phi_T - \phi^* \qquad (4\text{-}51)$$

We note that (4-48) is a linear function in transformed variables. Therefore, the linearized likelihood function $p_L(\underline{x}_c|\phi)$ corresponding to (4-48) is

$$p_L(\underline{x}_c|\phi) = \frac{1}{(2\pi\sigma_w^2)^{1/2}} \exp\left[- \frac{1}{2\sigma_w^2} \sum_n \left(r_c(n) - A_c(n)\Delta\phi_T\right)^2 \right] \qquad (4\text{-}52)$$

In order for the variance of the estimate $\hat{\phi}$ of ϕ_T to satisfy the equality in the Cramer-Rao bound, the estimator must be unbiased, and the following condition must be satisfied [4-3]

$$\frac{\partial \ln p_d(\underline{x}_c|\phi)}{\partial\phi_T} = [\ \hat{\phi} - \phi_T\ ]\ k(\phi) \qquad (4\text{-}53)$$

where $k(\phi)$ is an arbitrary function of ϕ. We shall now show that the condition (4-53) is satisfied for the likelihood function of (4-52). Substituting (4-52) into (4-53) we get

$$\frac{\partial \ln p_d(\underline{x}_c|\phi))}{\partial \phi_T} = \frac{1}{\sigma_w^2}\left[\sum_n (r_c(n) - A_c(n)\ \Delta\phi_T)\ A_c(n)\right] \qquad (4\text{-}54)$$

$$= \left[\frac{\sum_n A_c^2(n)}{\sigma_w^2}\right]\left[\frac{\sum r_c(n)\ A_c(n)}{\sum A_c^2(n)} - \Delta\phi_T\right] \qquad (4\text{-}55)$$

Therefore, if $\hat{\Delta\phi}$ is chosen so that

$$\hat{\Delta\phi} = \hat{\phi} - \phi^*$$

$$= \frac{\sum r_c(n)\ A_c(n)}{\sum A_c^2(n)} \qquad (4\text{-}56)$$

and by substituting for $\Delta\phi_T$ from (4-51) into (4-55), we indeed see that the condition (4-53) is satisfied where $k(\phi)$ is the first square bracket expression in (4-55). In order to show that the estimator is unbiased, we must evaluate $E[\hat{\Delta\phi}]$. By use of (4-56), we get

$$E[\hat{\Delta\phi}] = E\left[\frac{\sum r_c(n)\ A_c(n)}{\sum A_c^2(n)}\right]$$

$$= E\left[\frac{\sum [A_c(n)\ \Delta\phi_T + w_c(n)]\ A_c(n)}{\sum A_c^2(n)}\right] \qquad (4\text{-}57)$$

where use has been made of (4-48). Evaluating (4-57) we get

$$E\,[\Delta\hat{\phi}] = \Delta\phi_T \tag{4-58}$$

which therefore shows that the estimator (4-56) is unbiased. Therefore, since the two required conditions are satisfied, the variance of the maximum likelihood estimate $\hat{\phi}$ of ϕ corresponding to the likelihood equation (4-52) will satisfy the equality of the Cramer-Rao bound.

As an aside, we note that the value $\Delta\hat{\phi}$ is, of course, that which maximizes the left-hand side of (4-52), and the actual value $\Delta\hat{\phi}$ is determined by (4-56). This procedure is not intended to have any practical significance. However, it is interesting to note that (4-56) is also the least-squares estimate of $\Delta\phi$ as obtained through linear regression.

We now turn our attention to the original form of the ML estimator. Because we have used a uniform prior pdf in the derivation, we note that

$$p(\phi|\underline{x}_c) \propto p(\underline{x}_c|\phi) \tag{4-59}$$

where $p(\phi|\underline{x}_c)$ is defined in (4-28). After substituting (4-59) into (4-28) we get

$$p(\underline{x}_c|\phi) \propto K_2 \exp\left[\frac{1}{2\sigma_w^2}\,(L_c(\phi) - X_c)\right] \tag{4-60}$$

where

$$X_c = \sum_n x_c^2(n) \tag{4-61}$$

We now note that the likelihood functions defined by (4-52) and by (4-60) are derived from exactly the same model. The only difference between these two forms is that the likelihood function corresponding to (4-52) applies to the linearized case, and hence is a valid form only when (4-47) holds true. Therefore, provided that (4-47) is valid, the two forms of the likelihood functions given by (4-52) and (4-60) are equivalent.

We have seen that (4-52) has the appropriate form required for the variance of $\hat{\phi}$ to satisfy the equality of the Cramer-Rao bound. Therefore, we may conclude that the likelihood function (4-60) also leads to an estimator which attains the equality of the bound, provided the corresponding model (i.e., (4-8)) is linear in ϕ over the range of interest.

The form of the Cramer-Rao bound of interest to us is given by [4-3]

$$\text{Var}[\hat{\phi}] = E\left[(\hat{\phi}-\phi_T)^2\right]$$

$$\geq \left\{ -E\left[\frac{\partial^2 \ln p(\underline{x}_c|\phi)}{\partial \phi^2}\right]\right\}^{-1} \tag{4-62}$$

Substituting (4-60) into (4-62) we get the desired result:

$$\mathrm{Var}[\hat{\phi}] = -2\sigma_w^2 \left\{ E \left[\frac{\partial^2 L_c(\phi)}{\partial \phi^2} \right] \right\}^{-1} \qquad (4\text{-}63)$$

An exactly equivalent form as above applies to the quadrature case. Because of the fact that the noise components $w_c(n)$ and $w_s(n)$ are uncorrelated, it follows that the total variance of $\hat{\phi}$ when both the in-phase and quadrature components are considered is given by

$$\mathrm{Var}[\hat{\phi}] = -2\sigma_w^2 \left\{ E \left[\frac{\partial^2 L_c(\phi)}{\partial \phi^2} + \frac{\partial^2 L_s(\phi)}{\partial \phi^2} \right] \right\}^{-1} \qquad (4\text{-}64)$$

provided (4-47) holds.

Equation (4-47) is valid when σ_w is small compared to $f_c(n,\phi_T)$ most of the time, i.e., when the signal-to-noise ratio is high. This is because the linearization in (4-47) is valid only when ϕ^* is close to ϕ_T, which will be true provided $w_c(n)$ is small most of the time. Hence, the expression (4-64) given for the variance of $\hat{\phi}$ is applicable only to the case when the SNR is high. We also note that at high SNR's, the ML estimator is essentially unbiased. However, at low SNR's, the estimate $\hat{\phi}$ will be neither unbiased nor will its variance satisfy (4-64).

Plots of $\mathrm{Var}[\hat{\phi}]$ as given by (4-64) are shown in Fig. 4-4 when N = 21 elements, and in Fig. 4-5 for N=8 elements. For the curves in both these figures, 0 dB on the ordinate

corresponds to 1(degree)^2. In the numerical evaluation of (4-64) the expectation may be determined simply by using data without noise in (4-33), the expression for $L(\phi)$. In both cases, we see that the variances depend very strongly on the parameter BW (the total beamwidth-separation of the two incident signals), and on the parameters Ψ and ρ. The dependence on Ψ is not surprising; if $\Psi = 180^\circ$ and ρ is high, then the two incident signals will be largely cancelled out at the centre of the array, thereby decreasing the effective SNR. Also, as the signal separation BW goes to zero (for $\Psi = 180^\circ$), the total power received by the array decreases, because the two signal components cancel over a larger span of the array. This explains why the variances increase very sharply for $\Psi = 180^\circ$ as BW $\rightarrow$ 0. This effect is more pronounced for larger ρ because the signal cancellation in this case is more complete.

On the other hand, when $\Psi = 0^\circ$, we see the variances are much lower than the previous case, for BW < 1.8. This is because the power incident on the array from the multipath component adds to the direct component power and increases the overall SNR. We also note that the effect of variation in Ψ becomes less pronounced as ρ decreases. This is because the strength of the multipath component diminishes in this case, thereby causing the total received signal to become less sensitive to changes in the parameters

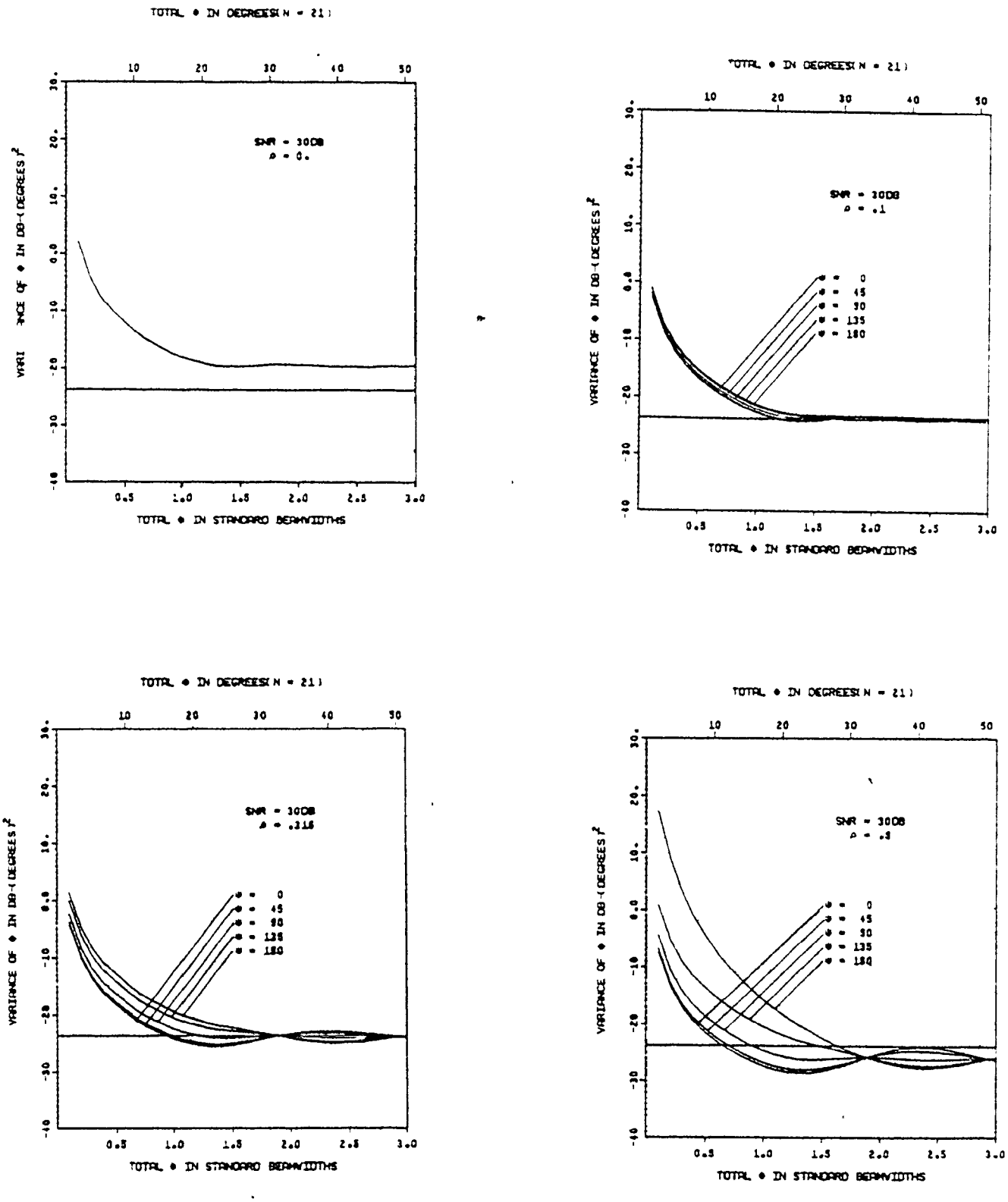

Fig. 4 - 4 Theoretical high SNR variances for N = 21 elements.

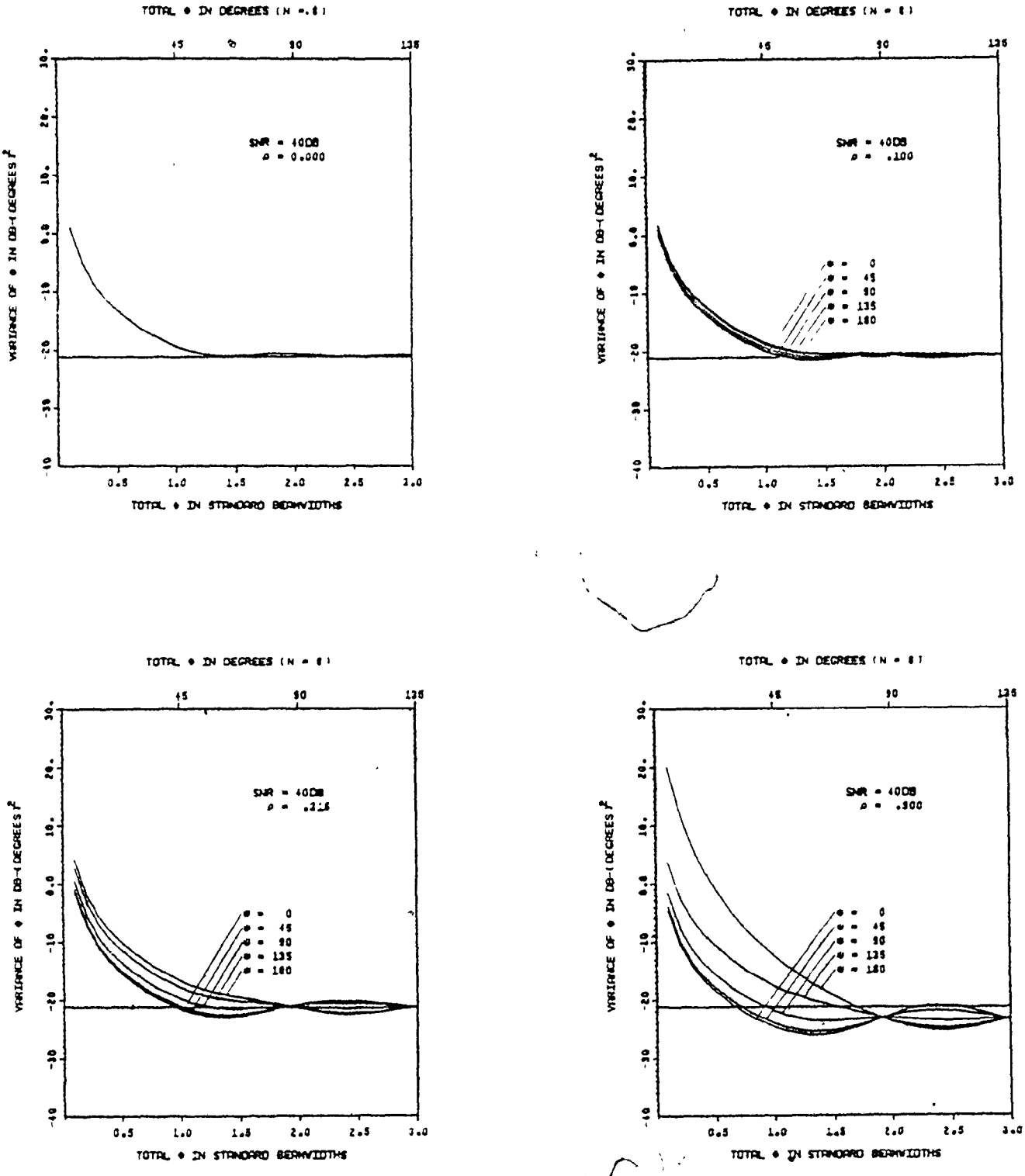

Fig. 4 - 5 Theoretical high SNR variances for N = 8 elements.

of the multipath component. When $\rho = 0$, the variance becomes independent of Ψ.

The solid horizontal line in all the curves in Figs. 4-4 and 4-5 shows the equivalent variance of $\hat{\phi}$ when it is known that only one plane wave is incident on the array. A different model was used to derive these results. These figures are thus a good indication of the manner in which the multipath interference alters the performance of the direction-finding estimator.

We note that the variances in Fig. 4-4 (for N=21) are substantially lower than those for N=8, in Fig. 4-5. The ratio by which they differ is not equal to 21/8, which implies that the variances vary nonlinearly with N. This fact may be easily verified by referring to (4-64). The manner in which $\mathrm{Var}[\hat{\phi}]$ varies with N is shown in Fig. 4-6, for ρ=0.9 and several different values of BW. The abscissa is plotted on a log scale, and it may be observed that doubling the number of elements decreases the variance by 9dB in all situations when N is higher than about 5. Thus, we see that a "3dB increase" in N improves the variance by 9dB, which implies that the variance of $\hat{\phi}$ varies as N^3. Therefore, increasing the number of elements in percentage terms buys a considerable margin in increased performance. For example, if two corresponding points in Figs. 4-4 and 4-5 are selected, it may be seen that the difference in the

corresponding variances is equal to $10\log(21/8)^3 \approx 12.5$dB. (Bear in mind that the SNR in Fig. 4-5 is 10dB higher than that in Fig. 4-4).

4.4.1 Simulation Results

Let us now compare the theoretical results as previously discussed with those obtained by simulation. Simulations were run for parameter values corresponding to those used in Figs. 4-4 and 4-5, and the results are shown for N=21 in Fig. 4-7, and for N=8 in Fig. 4-8. The variances obtained by simulation are shown as a dot, and the theoretical variances are shown superimposed as dashed lines. The simulations were executed at 30dB SNR for N=21 elements, and at 40dB for N=8 elements; these values were sufficiently high for the resulting simulation variances to agree with the high-SNR theoretical variance expression as given by (4-64). The simulation variances shown are the result of 99 trials. We see excellent agreement between the predicted theoretical variances and those obtained by simulation.

We shall now examine the behaviour of the mean and variance of $\hat{\phi}$ as a function of the elemental SNR. We again remark that the SNR value used with regard to this discussion is the SNR which would occur in the absence of multipath, i.e., for $\rho=0$. In Fig. 4-9(a)-(d) the values of

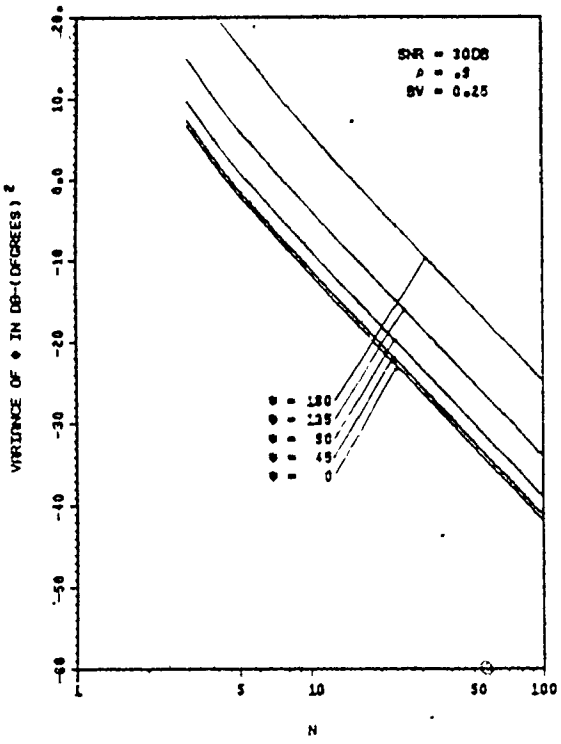

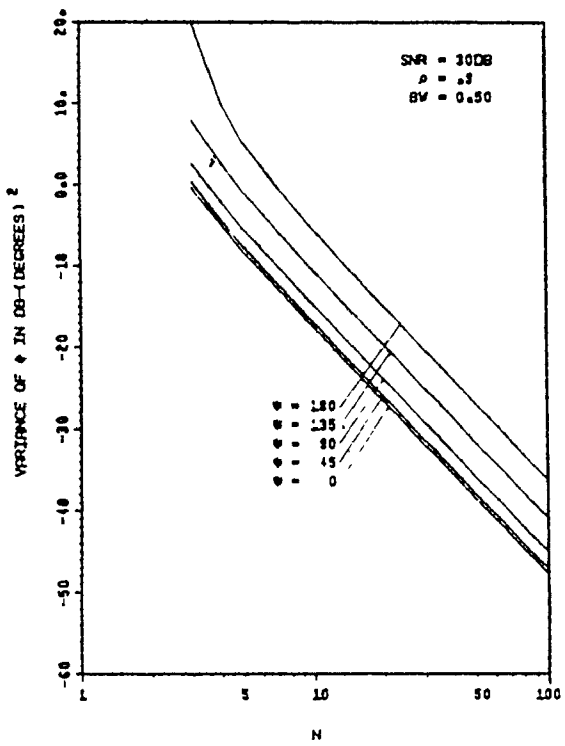

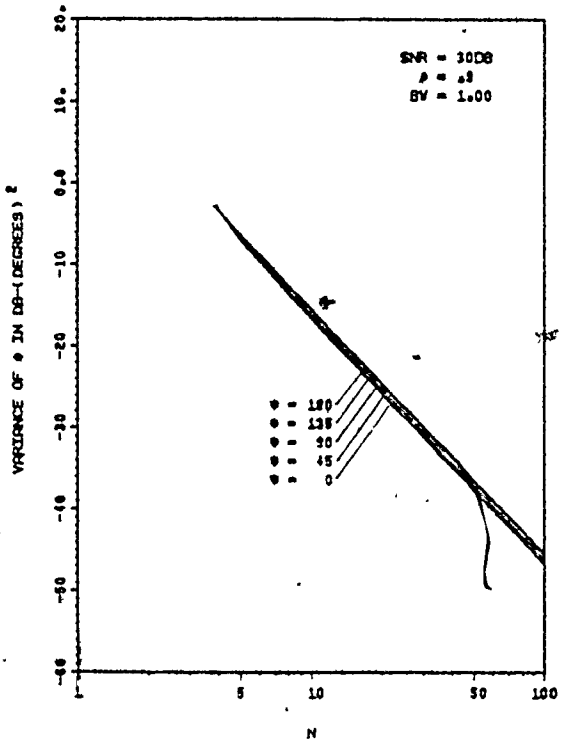

Fig. 4 - 6 Behaviour of the variance of $\hat{\phi}$ vs. N.

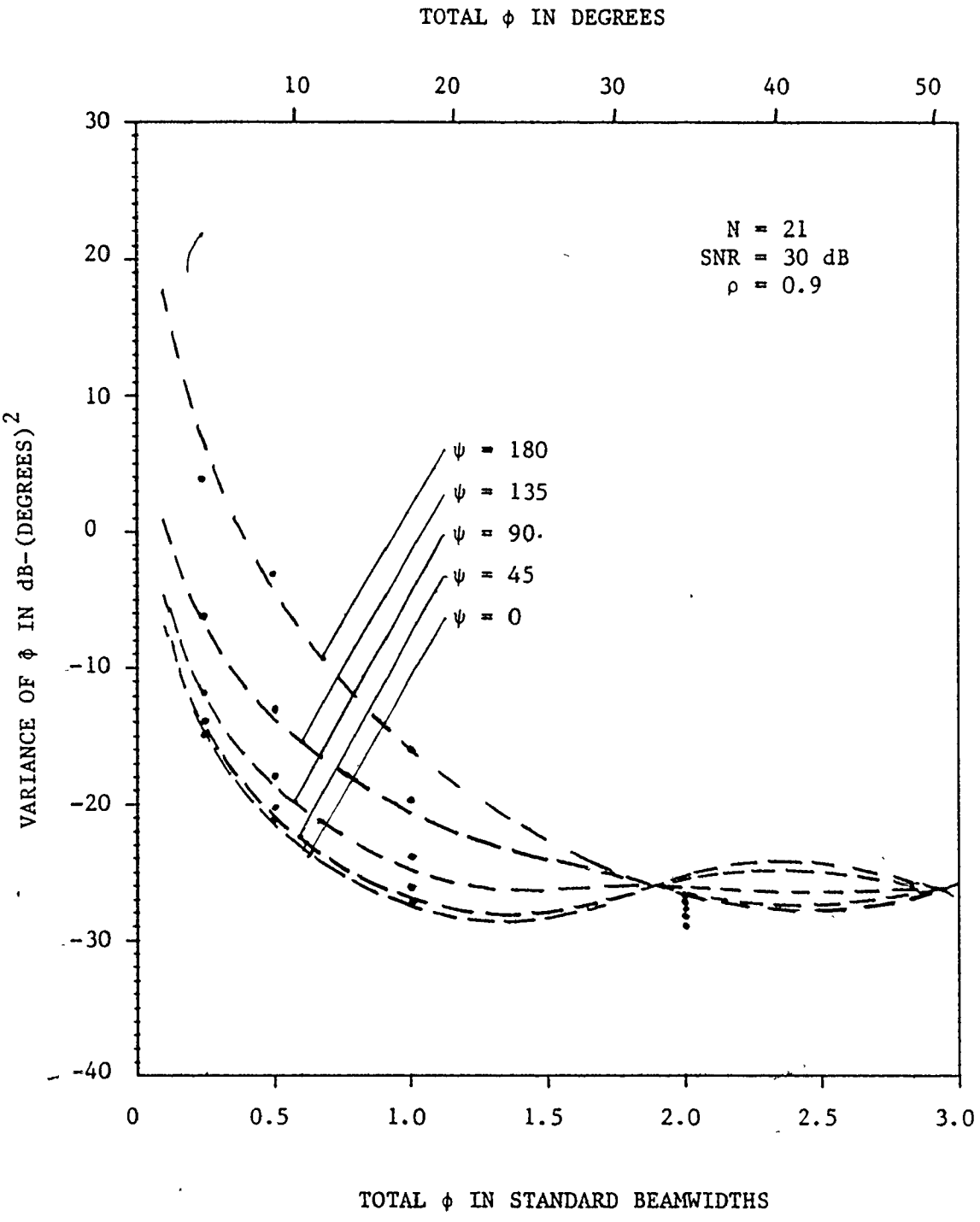

Fig. 4 - 7 Estimator variances obtained through computer simulation for N = 21 elements.

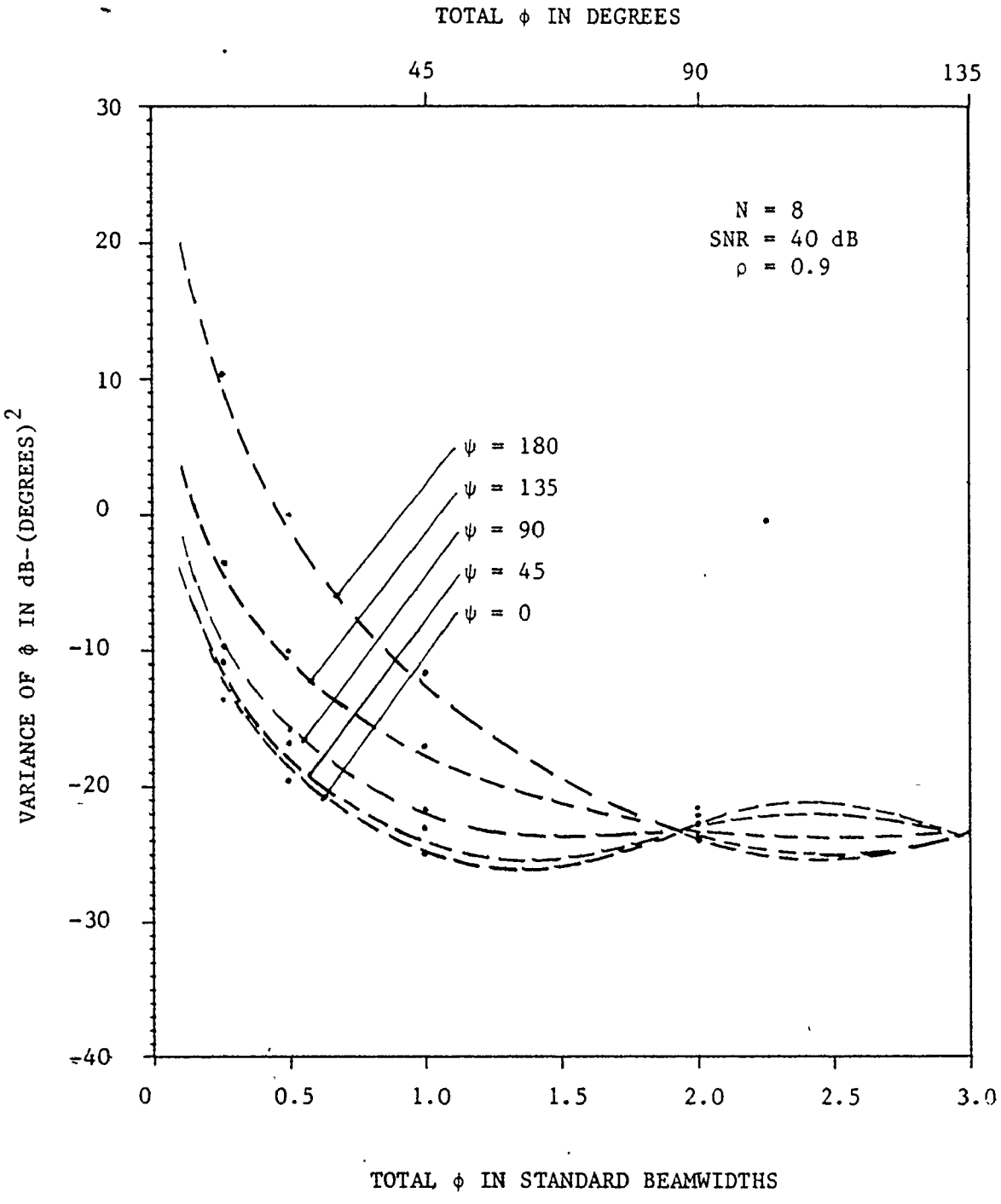

Fig. 4 - 8 Estimator variances obtained through computer simulation for N = 8 elements.

the mean of $\hat{\phi}$ are shown plotted versus SNR for various values of BW for N=21 elements. Also, in Fig. 4-10(a)-(d) the variances of $\hat{\phi}$ for the same parameter values are plotted. The results shown in both these figures are obtained by computer simulation.

There are several interesting points which arise from these figures. First, we note that for small values of BW and/or low SNR's, the mean of $\hat{\phi}$ exhibits a significant bias. For example, in Fig. 4-9(c), for BW=0.5, ρ=0.9, we note that the bias is negative for Ψ=0, 90 degrees, but positive for SNR < 15dB and negative for SNR > 15dB when Ψ=180 degrees. The reason for this phenomena is as follows. The simulations were performed using the Golden Section search algorithm (Sect. 4-3) where the initial interval of uncertainty was chosen to lie between ϕ=0 and ϕ=0.28 radians. When Ψ=0 or 90 degrees, the maximum of the objective function $L(\phi)$ is sufficiently distinct so that none of the 99 estimates of $\hat{\phi}$ generated by the simulation had values which lay outside this interval. Therefore, the mean of $\hat{\phi}$ will be biased low because of the behaviour of $L(\phi)$ as discussed previously.

However, when $\Psi=180^{\circ}$, the value of $\hat{\phi}$ will become limited by a lower bound of 0 radians as the SNR decreases from a high value, because this is the value of the lower limit of the initial interval of uncertainty. Likewise, the

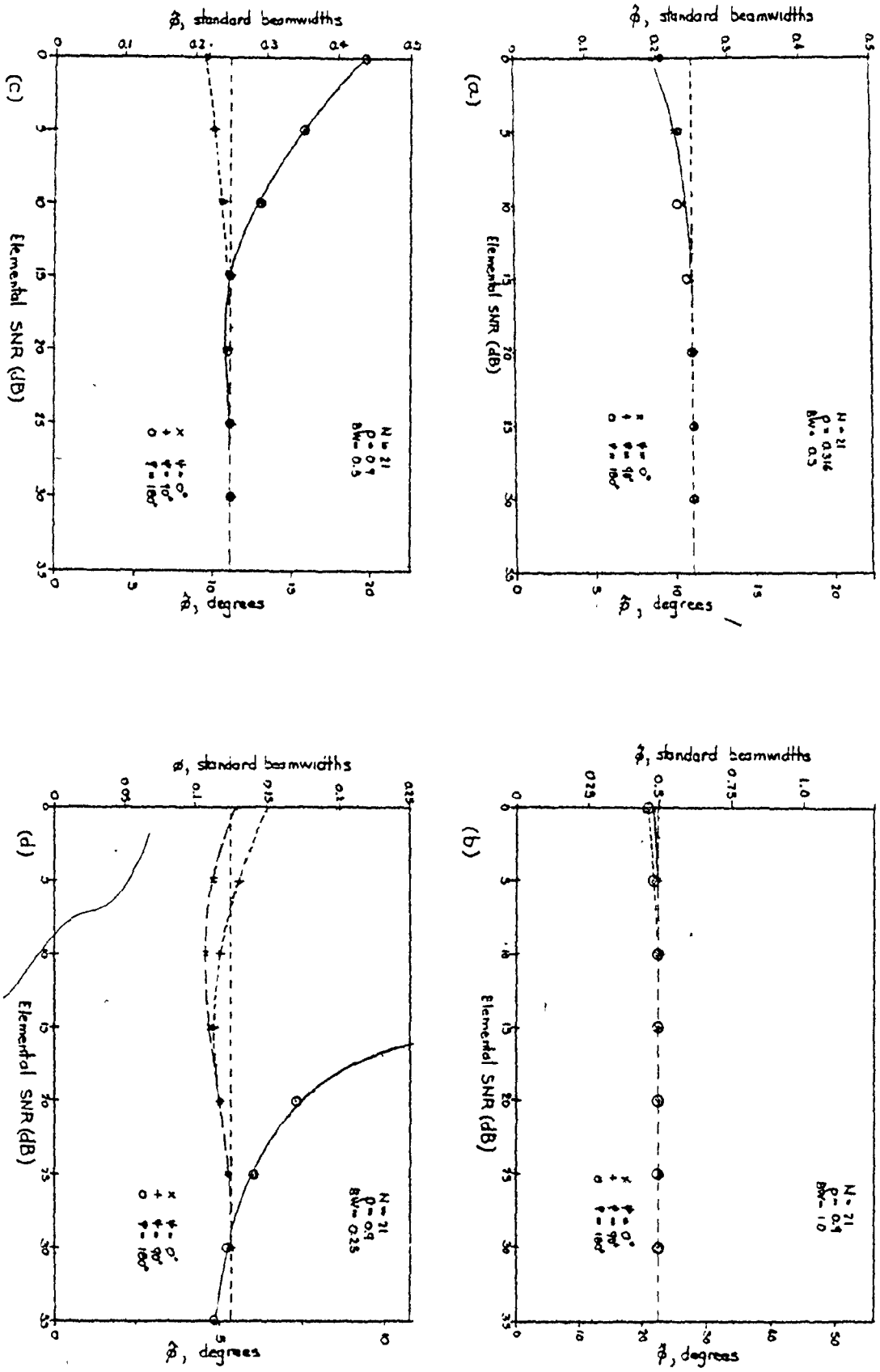

Fig. 4 - 9 Means of $\hat{\phi}$ vs. elemental SNR, as obtained by computer simulation, for N = 21 elements.

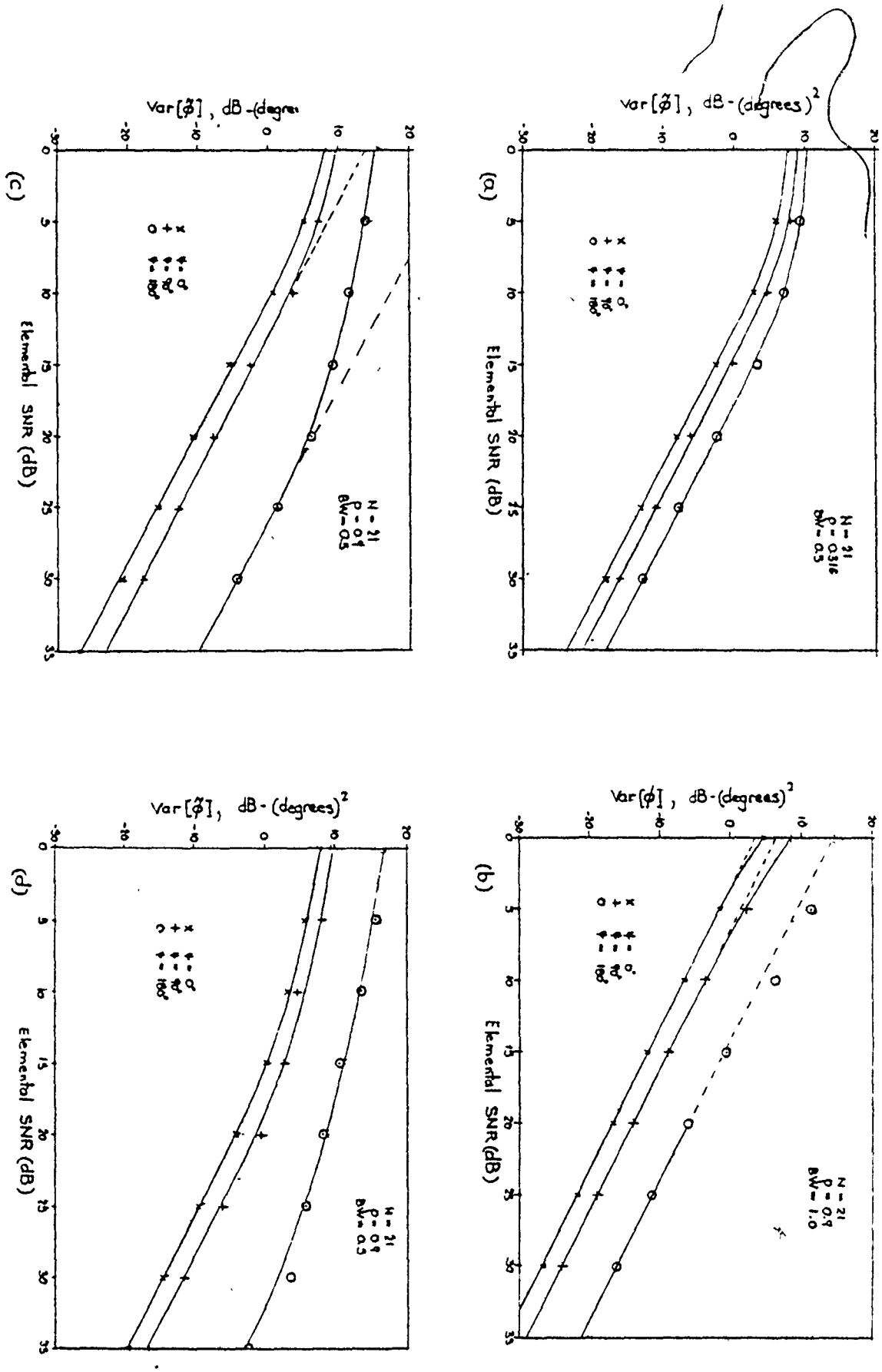

Fig. 4 - 10 Variances of $\hat{\phi}$ vs. elemental SNR, as obtained by computer simulation, for N = 21 elements.

estimate $\hat{\phi}$ has an upper bound of 0.28 radians (0.93 standard beamwidths), but because this value is much further away from the true value of ϕ (0.0748 radians, or 0.25 standard beamwidths) than is the lower bound, its limiting effect is not significant at the value of SNR where the lower bound begins to limit. Therefore, as the SNR decreases from a high value, some values of $\hat{\phi}$ given by the simulation routine will become limited to zero radian; this will have the effect of pushing the mean of $\hat{\phi}$ upwards, away from its true value. This is the behaviour indicated in Fig. 4-9(c).

We now examine the behaviour of the variance of the estimate $\hat{\phi}$, as shown in Fig. 4-10(a)-(d). At sufficiently high SNR, for any value of the parameter BW, the variance is a linear function of the elemental SNR; however, for lower SNR's, the variances are no longer linear and asympotically approach an upper limit. It is interesting to note that the input SNR threshold, SNR_T, where the variance departs from linearity (for any curve in Fig. 4-10) is the same value for which the corresponding curve showing the mean of the estimate $\hat{\phi}$ (as in Fig. 4-9) departs from its true value.

These phenomena are both results of the model becoming sufficiently nonlinear at the signal-to-noise ratio SNR_T for neither (4-47) nor (4-64) to hold.

We note by comparing Fig. 4-9(a) with 4-9(c) that the effect of the multipath interference on the bias of the

estimate is more severe for higher values of ρ. Also, as may be confirmed with reference to Fig. 4-4, the variation of $\mathrm{Var}[\hat{\phi}]$ with respect to γ is far greater for larger values of ρ.

As a result of these simulation curves, it is apparent that elemental SNR's greater than 15dB are required in order to obtain an estimate with negligible bias for a target at an elevation 0.25 standard beamwidths above the horizon (i.e. when the direct signal and the multipath reflection are separated by 0.5 standard beamwidths), when using a 21-element array, (as indicated in Fig. 4-9(c)). The rms angular error in this case would be approximately 4 degrees. However, when estimates are required for targets 0.125 standard beamwidth above the horizon (0.25 standard beamwidth separation total), SNR's in excess of 35dB are needed in order to yield unbiased results, as indicated by Fig. 4-9(d).

Curves showing the mean and variance of $\hat{\phi}$ for an array of N=8 elements are presented in Figs. 4-11(a)-(d) and 4-12(a)-(d) for the same parameter values as used for Figs. 4-9 and 4-10. We notice the same overall behaviour for the N=8 case as was exhibited for the N=21 situation; however, the input SNR thresholds occur about 13dB higher than was the case previously. This value of 13dB is the difference in variances between N=8 and N=21 as predicted by the curves

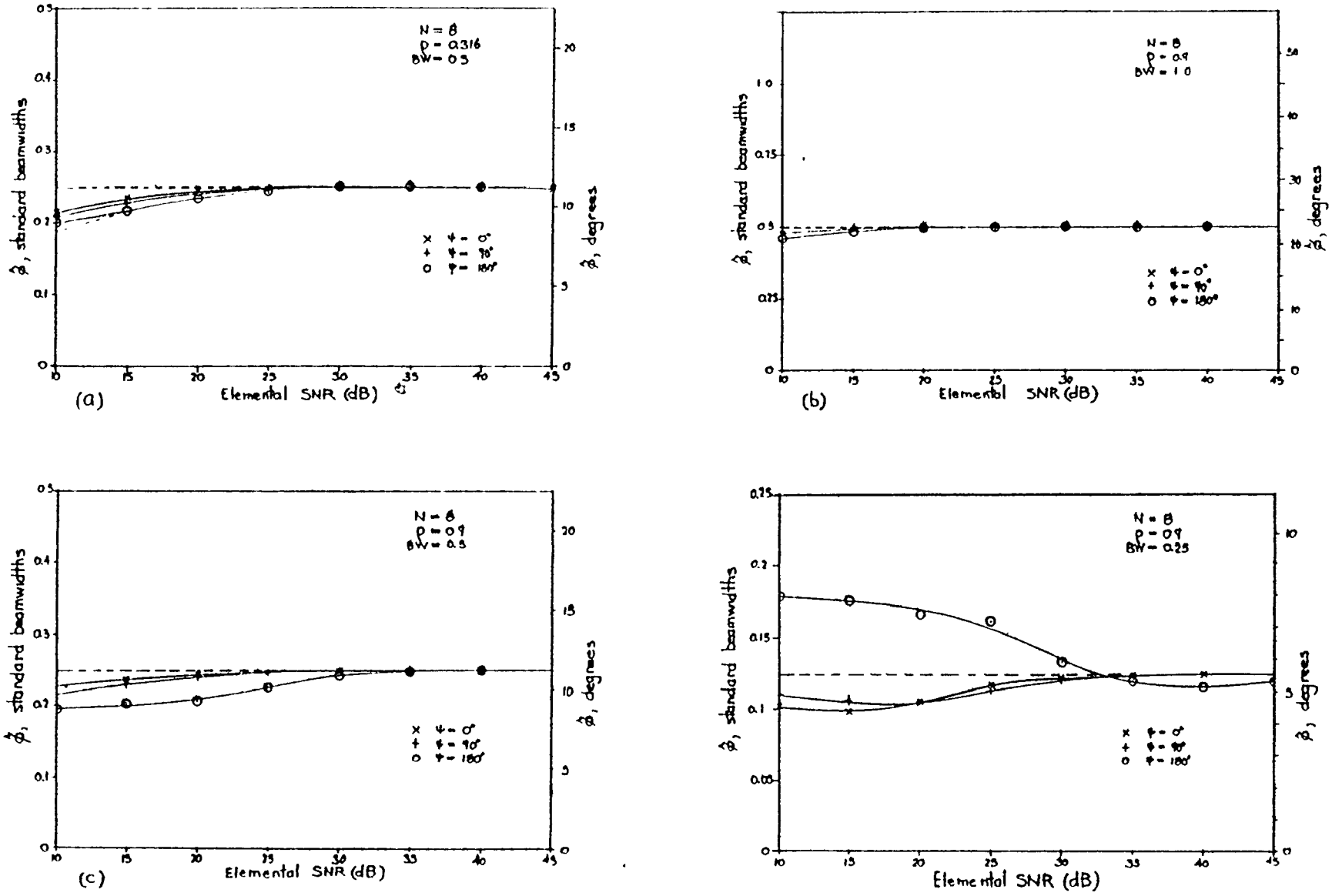

Fig. 4 - 11 Means of $\hat{\phi}$ vs. elemental SNR, as obtained by computer simulation, for N = 8 elements.

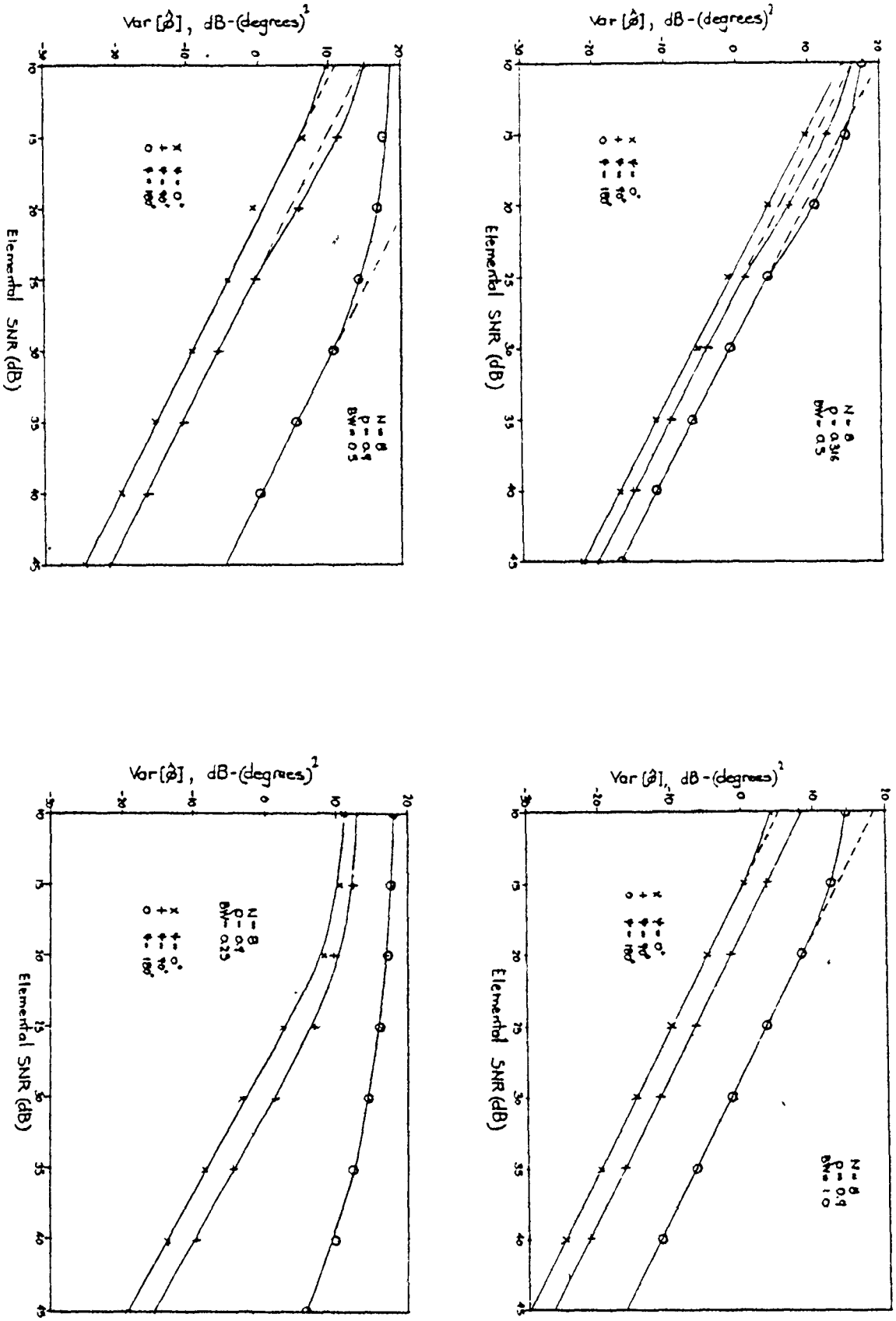

Fig. 4 - 12 Variances of $\hat{\phi}$ vs. elemental SNR, as obtained by computer simulation, for N = 8 elements.

shown in Fig. 4-6.

4.4.2 Experimental Results

Experimental results have been obtained for parameter values approximately the same as those used in the N=8 simulations. There are however, some fundamental differences between the philosophies used to obtain the experimental results compared to those obtained by simulation.

The first difference is with respect to the measure of the elemental SNR. As noted in Appendix A, the effects of elemental misalignment and 60 Hz hum are predominant over the effects of front-end receiver noise in the experimental system used in this study. Since it is not possible to measure directly the "noise power" corresponding to the elemental misalignments, we cannot produce an overall SNR figure directly for an actual experimental situation. However, an estimate of the overall SNR of the spatial sequence produced by the array may be estimated as follows. We rewrite (4-60) for the case where both the in-phase and quadrature data are considered:

$$p(\underline{x}|\phi) = K_3 \exp \frac{1}{2\sigma_w^2} [L(\phi) - \Sigma_n^2 x_c(n) - \Sigma_n^2 x_s(n)] \qquad (4\text{-}65)$$

Provided that the effects of elemental misalignment etc. are at least approximately Gaussian-distributed and are uncorrelated with each other and the signal, then, as shown in Appendix B, the expected value of the term within the square brackets of (4-65) is the sum of squares of the noise components $w_c(n)$ and $w_s(n)$ (i.e., the residual sum of squares). Hence, this term represents the total energy of the noise present in the available data. Also, it is evident that the term S_x, defined by

$$S_x = \sum_n x_c^2(n) + \sum_n x_s^2(n) \tag{4-66}$$

defines the total power of the combined signal plus noise, provided the signal and the noise are uncorrelated over the spatial interval considered. In view of these considerations, the numerical value of the quantity $L(\hat{\phi})$ then gives an estimate of the total energy of the signal present over the pertinent interval.

An estimate of the total SNR, denoted by $\hat{SNR}$, of a given spatial sequence derived from the specular multipath model may then be given by

$$\hat{SNR} = \frac{L(\hat{\phi})}{L(\phi) - \sum_n x_c^2(n) - \sum_n x_s^2(n)} \tag{4-67}$$

This is the expression used to estimate the overall SNR of the spatial sequence provided by the experimental apparatus.

We note at this point that the SNR estimate provided by (4-67) is an estimate of the actual SNR of the sequence, i.e., the ratio of the total signal power to the total noise power of the sequence. The SNR values used previously were those which would result in the absence of multipath. Hence, the SNR given by (4-67) would be a function of Ψ; the SNR figure given with reference to the computer simulation results is not a function of Ψ.

In order to get an idea of the manner in which the experimental results vary with the overall SNR, artificial Gaussian noise of mean zero and scaled for the proper variance was added to the observed data sequence in order to decrease the total SNR. Another method of accomplishing the same result would be simply to decrease the transmitted signal power and increase the receiver amplifier gain by a corresponding amount. This method, however, would have been very cumbersome experimentally, because the receiver mixers each had a different nonlinear characteristic with respect to the input level. This would have resulted in each amplifier requiring a different gain for each individual input level and hence each output noise variance would differ at each input level.

Because of these considerations, the former method was chosen.

Another difference in philosophy between the experimental and simulation results is the calculation of the variances. In the computer simulations, the noise from trial-to-trial may be made completely independent. However, in the experimental situation, a large component of the "noise" is the error caused by the elemental misalignment. The experimental data was gathered by first setting up the array corresponding to a desired set of parameters, and then gathering a large number of records of data, where a record constitutes the elemental excitations at all sensors at the same time instant. Each record represents the excitations at a different time instant. Therefore, it may be seen that while the receiver noise contribution changes from record to record, the effect of elemental misalignment does not. Therefore the errors from one record to the next are not independent, and it is not possible to produce a valid estimate of $\mathrm{Var}[\hat{\phi}]$ by forming the variance of the individual estimates of $\hat{\phi}$ obtained from each record of experimental data. For a similar reason, it is also not possible to give an accurate assessment of the bias of $\hat{\phi}$ from these experimental results.

Despite these problems, the experimental results give a good test of the applicability of this symmetric maximum-

likelihood method to real situations. The effects of mutual coupling, elemental misalignments, R.F. mismatches etc., which are easily overlooked in computer simulation exercises, may be subjectively evaluated with the experimental system.

The estimates $\hat{\phi}$ obtained from experimental data are shown in Fig. 4-13(a)-(d) as a function of the overall estimated SNR, which was varied by adding in controlled amounts of Gaussian noise to the experimental data. The dashed lines in each case correspond to the true value of ϕ and agree closely with the corresponding values of ϕ used in the simulations. In any figure, the point with the highest estimated SNR, for a given γ, corresponds to the estimate obtained directly from the experimental data without extra artificial noise.

The experimental curves of Fig. 4-13 show a close resemblance to those in Fig. 4-11. There are minor discrepancies between the two sets of curves, arising from various sources of experimental error as discussed previously. However, the trends exhibited in a particular set of simulation results in Fig. 4-11 are also apparent in the corresponding experimental results in Fig. 4-13. We also note from the figure that in no case are any of the errors in the experimental values of $\hat{\phi}$ greater than 0.05 beamwidths. The variances of $\hat{\phi}$ as calculated on the basis

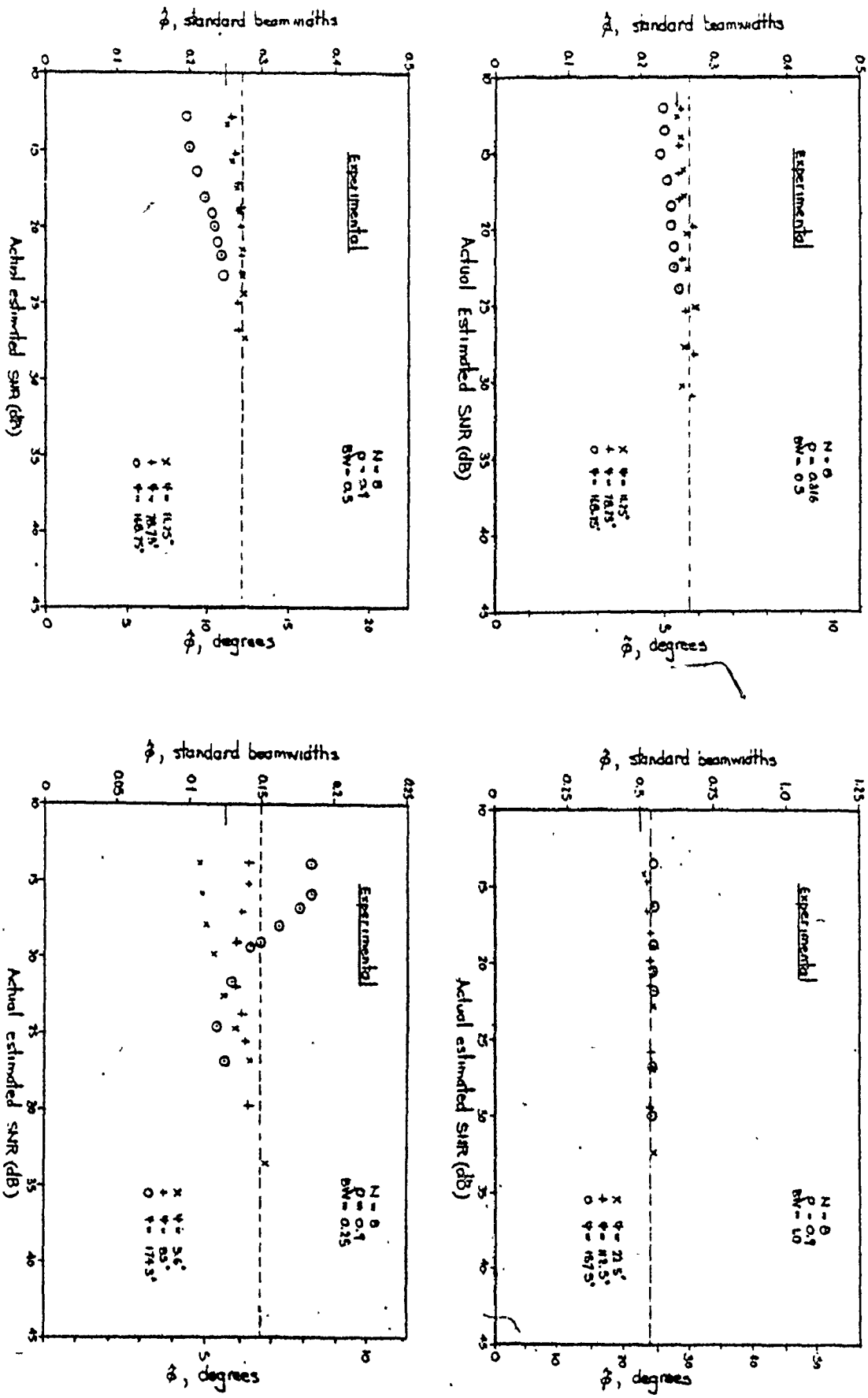

Fig. 4 - 13 Experimental plots of $\hat{\phi}$ vs. SNR for various parameter values.

of the experimental data are in the range 20-25dB below the variances obtained from simulation; however, for reasons discussed previously, the experimental determination of $\mathrm{Var}[\hat{\phi}]$ does not lead to valid results.

4.4.3 Sensitivity of Errors to Lack of Symmetry

One further point will be considered in this section. At the outset of this discussion, the assumption was made concerning the symmetric geometry of the incident signal configuration. In some cases, however, this assumption is not perfectly valid (e.g. a shipboard radar system), and it is necessary to determine the sensitivity of the estimator to errors in the symmetry.

Shown in Fig. 4-14 are curves showing the absolute value of the estimation error due to lack of symmetry, versus the symmetry error itself. Data were generated according to (4-8) and (4-12), with no noise added, but then the data were artifically shifted so that the angle of incidence of both signals were moved by the amount $\Delta\phi$. The quantity $\Delta\phi$ is then the symmetry-error. The data were then analyzed, assuming symmetry, and the resulting estimation errors appear in the curves. The cusps which are evident in the figures are the result of a change of polarity in the estimation error as the symmetry error increases. Also, it is evident in many cases that the error limits at a fixed

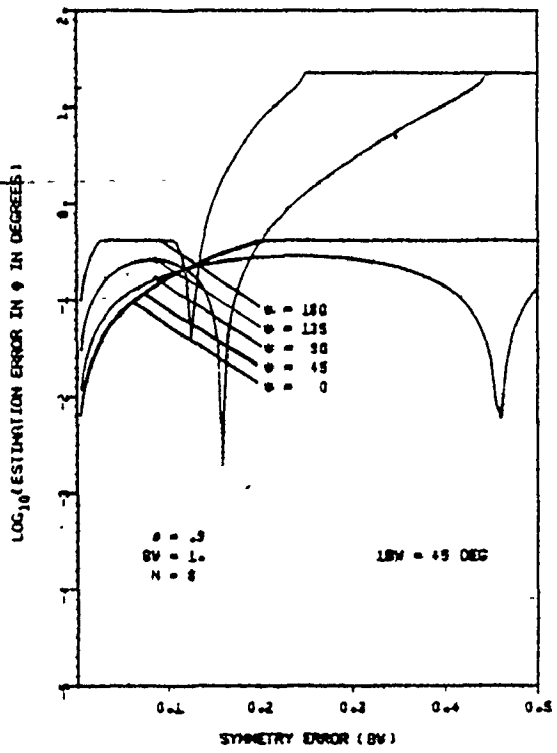

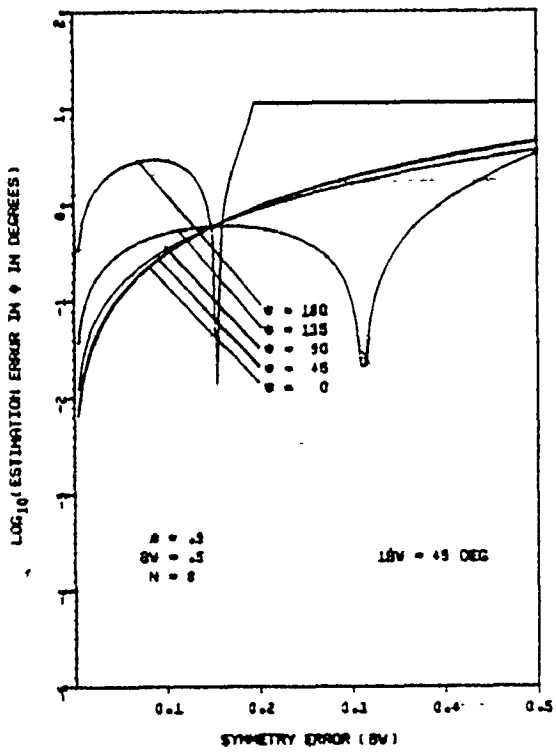

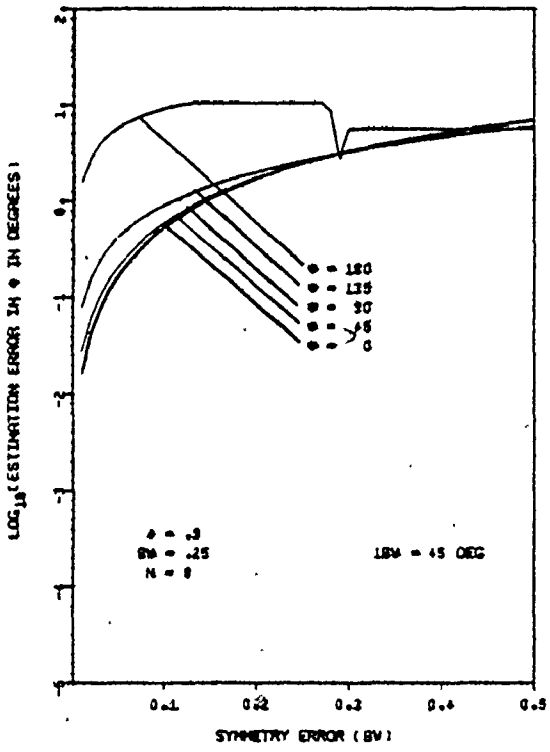

Fig. 4 - 14 Error in ϕ vs. symmetry error in standard beamwidths for various parameter values.

value. This is due to the restriction that the estimated value $\hat{\phi}$ must lie inside the initial interval of uncertainty established in the Golden section search. If the global minimum of the objective function lies outside this interval, the estimate will be fixed at the appropriate edge of the initial interval of uncertainty.

It appears on the basis of Fig. 4-14 that in all cases (except for BW=0.25, 0.5 and $\Psi=180^{\circ}$) that an acceptable estimation error is produced provided the symmetry error is less than 0.1 standard beamwidths.

In this section we have presented results indicating the performance and the behaviour of the symmetric ML bearing estimator. We have seen that, at high SNR's, the performance of the estimator approaches the equality of the Cramer-Rao bound. Therefore, it is an efficient estimator. The results also indicate that as the signal separation decreases, the elemental SNR needed to produce an acceptable elevation estimate increases. When the signal separation is less than 1.8 standard beamwidths, the performance of the estimator is considerably degraded when $\Psi=180$ degrees. We have also noted good agreement between the theoretical, simulation, and experimental results.

4.5 Discussion

Attention in this section will be directed towards a

few remaining aspects of the ML estimator which we are considering. Some of the points to be discussed are: time-dependence removal, confidence interval on $\hat{\phi}$, and comparison with this technique to other similar processors which have appeared in the literature.

4.5.1 Time-Dependence Removal

In the practical situation where many snapshots of the same environment are available, the same problem as discussed in Chapter 3 also exists in this context; that is, how to utilize all the available data to produce the best overall direction estimator. The technique stressed in Chapter 3 was to collapse the time-dependence of the data to yield a one-dimensional sequence varying in space only. The method to be used here is much more straightforward and is based on maximum-likelihood principles.

In a typical radar system, the pulse width is in the order of 1 μS, and the pulse period is about 1 mS. The receiver bandwidths are usually very close to the reciprocal of the pulse width, which then implies bandwidths in the order of 1 MHz. Based on these parameter values, it is fair to assume that the noise present at the receiver output is uncorrelated from pulse-to-pulse. With the assumption of Gaussian noise, the noise samples are then statistically independent between pulses.

We now investigate the nature of the likelihood function of ϕ given data from each sensor over K snapshots in time. We assume only one snapshot is gathered per pulse. Using (4-65) and (4-28), and the assumption of statistical independence between snapshots, we may write

$$p(\underline{X}|\phi) = K_4 \exp\left\{ \frac{1}{2\sigma_w^2} \sum_{i=1}^{K} \left[L_i(\phi) - \sum_n x_c^2(n,i) - \sum_n x_s^2(n,i) \right] \right. \tag{4-68}$$

where $\underline{X}$ refers to the matrix of all available data over the complete ranges of n and i, and $L_i(\phi)$ is defined by (4-33) using the ith snapshot as data. That is,

$$L_i(\phi) = L_{ci}(\phi) + L_{si}(\phi) \tag{4-69}$$

where

$$L_{ci}(\phi) = \frac{\left[\sum_n x_c(n,i) \cos n\phi\right]^2}{\sum_n \cos^2 n\phi} + \frac{\left[\sum_n x_c(n,i) \sin n\phi\right]^2}{\sum_n \sin^2 n\phi} \tag{4-70}$$

A similar form holds for $L_{si}(\phi)$.

It is now obvious from (4-67) that in order to maximize the likelihood function $p(X|\phi)$, we must maximize the quantity Q, given by

$$Q = \sum_{i=1}^{K} L_i(\phi) \qquad (4-71)$$

The value $\hat{\phi}$ of ϕ which maximizes (4-71) is the ML estimate of ϕ over all available snapshots. We therefore note that the form (4-71) implicitly involves the removal of the time-dependence of the data.

We note that the objective function implied in (4-71), is very similar to the single snapshot form used previously. The estimate is $\hat{\phi}$ obtained by finding that value of ϕ which maximizes the sum of all the L-functions formed from each snapshot of data. We note that the time-dependence removal process implied by (4-71) is more direct and straightforward than the processes used in conjunction with the time-series techniques discussed in Chapter 3.

In Fig. 4-15 we show the performance of this time-dependence removal technique. Variances of $\hat{\phi}$ as

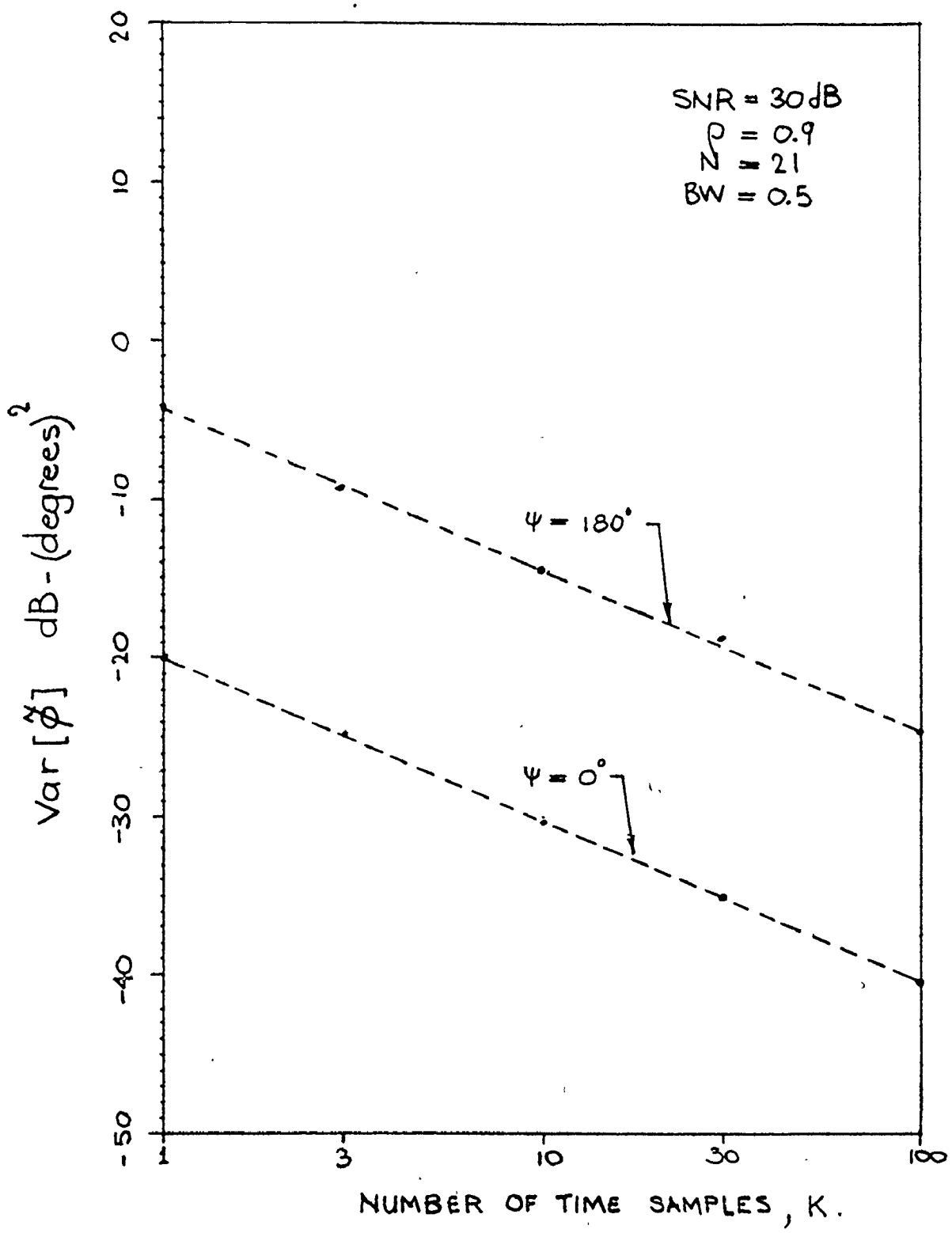

Fig 4-15 Performance of time-dependence removal technique, showing Var[$\hat{\phi}$] vs. number of time samples K.

obtained by computer simulation, are shown vs. the number of time samples used, K. The parameters are: BW=0.5, ρ=0.9, N=21, and SNR=30dB. We note from the figure that the estimator variance varies inversely with K; if 100 time samples are used the variance improves by 20 dB over that obtained with a single snapshot. Therefore, we note that the performance of this receiver structure varies approximately as N^3 and linearly with K. It should be emphasized, however, that this improvement with respect to the number K of snapshots assumes that the environmental conditions remain essentially unchanged during the period of time for which the set of K snapshots is collected.

It would also be possible to develop an ML structure which would optimally track a changing target. This may be accomplished by using an estimator which weights the most present L_i's heavily, and past values lightly, instead of the uniform window implicit in (4-71). A weighting function in common use is that corresponding to a first order filter response, which is an exponential decaying into the past. The time constant of this exponential would depend on how fast the environment changes with respect to the time interval

between the observations.

4.5.2 Confidence Interval on the Estimate $\hat{\phi}$

In statistical estimation problems, it is all very well to produce an estimate of a desired quantity, but we know in actual fact there is an interval of uncertainty associated with that estimate. This interval is referred to as a confidence interval.

The confidence interval associated with $\hat{\phi}$ may be determined easily if the SNR is high enough for the model to be assumed linear, i.e., for (4-47) to hold true. In this case, the estimate $\hat{\phi}$ is Gaussian-distributed, and the approximate confidence interval I_α on $\hat{\phi}$ at the $100(1-\alpha)\%$ level of significance is easily established to be, e.g. [4-13]

$$I_\alpha = \hat{\phi} \pm t_\gamma\,(\alpha/2)\,\sqrt{\text{Est. Var}[\hat{\phi}]} \qquad (4\text{-}72)$$

where

$t_\gamma(\alpha/2)$ = the student's t statistic, with γ degrees of freedom, and argument $\alpha/2$.

γ = the number of degrees of freedom, equal to the number of independent observations minus the number of parameters, or 2N-1, for in-phase and quadrature data.

The expression under the square root sign is the estimated variance of $\hat{\phi}$, and is given by (4-64). The evaluation of (4-64) requires knowledge of the value σ_w^2; this may be obtained, preferably, by prior measurement in the absence of signal, or an estimate s^2 of σ_w^2 may be obtained through the term in the square brackets in (4-65):

$$s^2 = \frac{1}{2N-1} \left[L(\hat{\phi}) - \sum_n x_c^2(n) - \sum_n x_s^2(n) \right] \qquad (4-73)$$

in the case of a single snapshot.

In the case where linearity may not be assumed, a number of results which are true for the linear case no

longer apply, e.g., the estimate $\hat{\phi}$ is no longer Gaussian-distributed and (4-72) no longer applies. Based on the fact that the curves of $L(\phi)$ are proportional to the a posteriori probability of ϕ, a confidence interval may still be defined by use of the expression [4-11]

$$L(\phi) = L(\hat{\phi}) \left[1 + \frac{1}{2N-1} F(1, 2N-1, 1-\alpha) \right] \qquad (4-74)$$

where $F(\cdot)$ is the Fisher F- statistic. Much more will be said concerning this statistic in Chapter 5. Equation (4-74) provides a $100(1-\alpha)\%$ confidence region in the linear model, Gaussian error situation, but the confidence coefficient will not be $(1-\alpha)$ in the nonlinear case. We do not know in general what the confidence will be but we can call such intervals approximate $100(1-\alpha)\%$ confidence intervals in ϕ. The two values of ϕ which satisfy (4-74) (if they exist) define the extremities of the confidence interval.

4.5.3 Comparison with other Techniques

White [4-2] has developed an estimator which is somewhat similar in nature to the symmetric ML estimator developed in this chapter. His approach is simply to take the model form of the elemental excitations as given by (4-8) and (4-12) and form the resulting pdf of the data given all the parameter values, which is also the joint likelihood function of all the parameters. He then devises an analog computer structure, which involves nulling out an error voltage in a loop, to solve for the maximum of the likelihood function with respect to all five parameter values. His structure is quite complex, involving 2N programmable phase shifters, two beam forming networks, a multitude of programmable attenuators, adders, multipliers, as well as a computer which must calculate the value of a variety of functions.

The symmetric ML estimator structure which has been developed in this chapter is inherently much simpler than White's because the estimator is a function solely of the one parameter of interest; all of the other undesired parameters have been integrated out. As we have seen previously, the symmetric ML estimator is

simple enough that implementation on a microprocessor may be feasible.

The high-SNR theoretical performances of both the symmetric ML and the White estimator are identical. The curves shown in his paper are calibrated on the basis of the degradation of the performance of the system in the presence of multipath as compared to the performance of the system without multipath. That is, his curves hare plotted with the solid line in Figs. 4-4 and 4-5 as the reference. However, once this change in calibration is made, the theoretical variances of both techniques are the same.

Trunk et al [4-14] have presented results which compare the variances given by the Cramer-Rao bound and the variances obtained by simulation using the method of White. They found that the White simulation variances are lower than the Cramer-Rao bound when the estimate of ϕ is biased. This, of course coincides with the results presented in this chapter [e.g. see Fig. 4-10], and is no surprise since the C-R bound in the form they have used does not apply to biased estimators. The parameter values they have chosen are such that they lead to very

biased results, and they make no mention of the fact that the composite biasedness/departure from the C-R variance bound behaviour is due to the nonlinearity of the model. If Trunk et al had chosen higher SNR's, the White simulation variances would have approached the values given by the C-R bound, as is indicated in this thesis.

The results shown in [4-14] are difficult to compare directly with those presented here, because the former uses 3-dB beamwidths instead of standard beamwidths. However, if the assumption is made that one 3-dB beamwidth equals one-half a standard beamwidth, the results agree within about 4dB.

4.5.4 Application of Method to Diffuse Reflections

As is pointed out early in this chapter, the symmetric ML estimator is valid only in the presence of pure specular multipath, and hence limits its application to low-angle elevations or to smooth reflecting surfaces. However, because the diffuse multipath spans a fairly wide spatial region and arrives at the receiving array incoherently, it would be perhaps useful to approximate

the effects of the diffuse multipath as coloured spatial noise. Since the diffuse multipath is incoherent from pulse-to-pulse, the use of the multi-snapshot form of the ML estimator as given by (4-69) would decrease the diffuse multipath power incident on the array by the factor K. Thus, if a sufficient number of snapshots are used in forming the estimate through (4-69), the effects of the diffuse multipath may be rendered negligible. We therefore note that while the single snapshot version of the estimator (4-33) is not particularly amenable to situations where significant diffuse multipath incident power exists, the more general version given by (4-69) may indeed be well-suited for application in these cases. This is clearly an area which needs more investigation.

4.6 Summary

In this chapter a novel form of an estimator leading to an estimate of the elevation angle of a target has been developed. An efficient algorithm useful for its implementation has been presented, and theoretical, simulation and experimental results were shown

demonstrating the performance of the estimator. Finally, discussion leading to a multi-snapshot version of the estimator, and the determination of a confidence interval for the estimator, was presented.

CHAPTER 5

MAXIMUM LIKELIHOOD ESTIMATION TECHNIQUES (II)

In the last chapter an ML structure, which depended on the symmetry of the direct and multipath components, was developed and discussed. This chapter will be devoted to the development of a more general ML technique which is applicable in situations where the incident signal components arrive at the array from arbitrary directions. The resulting structure, however, will be somewhat more complex than that discussed in the previous chapter.

First in this chapter we shall discuss the motivation and some applications for this type of processor. Secondly, the asymmetric ML structure will be developed, and thirdly, results will be presented. The chapter will conclude with a "discussion" section.

5.1 Motivation for an Asymmetric ML Processor

In certain low-angle tracking problems, where the range of the target is sufficient for the curvature of the earth to become significant, the symmetric specular multipath model (Fig. 2-1) is no longer valid.

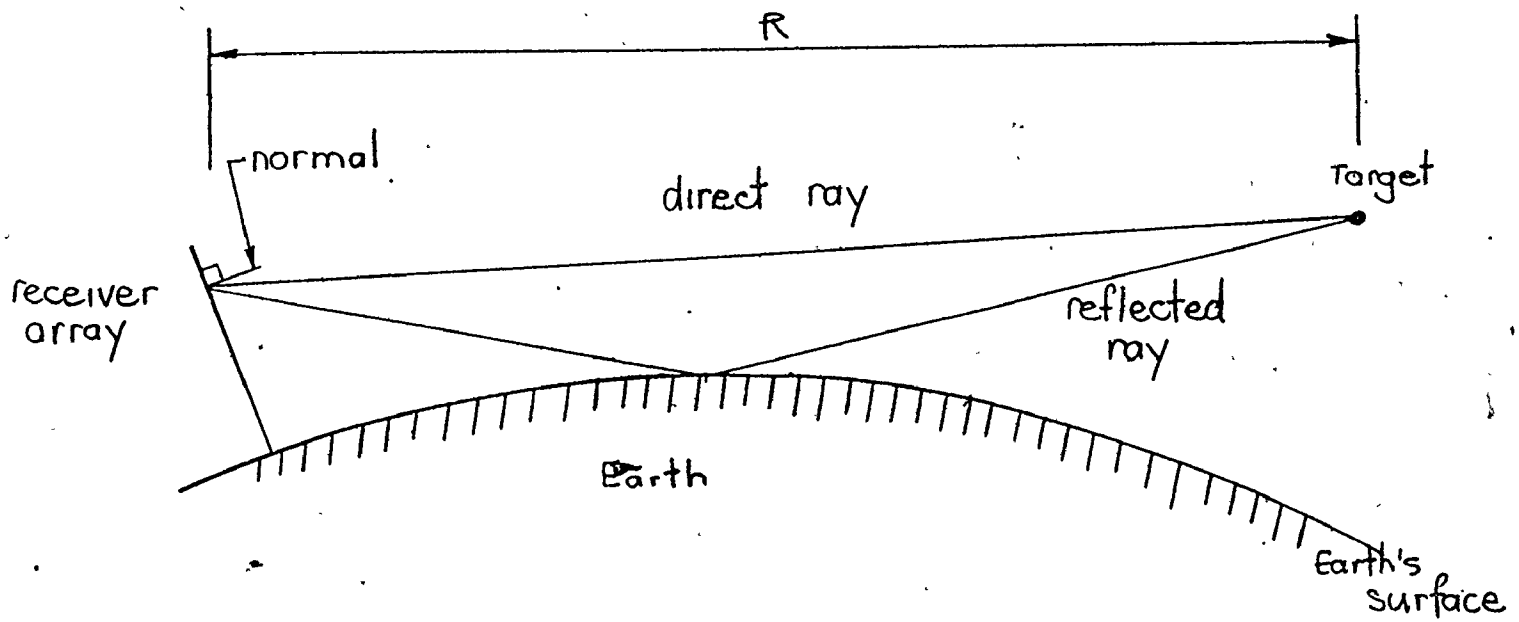

Fig 5-1 Geometry of long-range specular multipath

This fact is made evident by reference to Fig. 5-1, where it may be observed that both the direct and multipath components are incident from below the normal of the array. Also, the situation is exacerbated by the phenomenon of atmospheric bending, e.g. [1-11], where the EM radiation from the radar propagates along a path which bends towards the ground. This effect is caused by refraction due to a variation in atmospheric density with altitude. Hence, the use of the symmetric ML structure may lead to considerable error, as is pointed out from Fig. 4-14. In tracking applications where these geometries are prevalent, it is therefore necessary to develop a more general form of estimator.

As we shall see, the estimator which will be developed is also applicable to the general problem of determining the frequencies of multiple sinusoids which are embedded in white noise. Therefore, this estimator may be applied to many problems in radio-astronomy, acoustics, speech, etc. Also, this processor will be applicable to the situation where it is desired to track, in both elevation and azimuth, multiple targets present within the radar's scanning volume.

5.2 Development of the Processor

Consider the baseband form of the in-phase elemental excitations $x_c(n)$ which result from M plane waves incident

upon a linear array from arbitrary angles θ_1, θ_2, ..., θ_M (in azimuth or elevation, depending on the orientation of the array). These plane waves produce a corresponding set of electrical angles ϕ_1, ϕ_2, ... ϕ_M. The excitations may be given (by analogy with (4-8)) in terms of ϕ_1, ϕ_2, ... ϕ_M by

$$x_c(n) = \sum_{m=1}^{M} u_m \cos n\phi_m + \sum_{m=1}^{M} v_m \sin n\phi_m + w_c(n) \qquad (5\text{-}1)$$

$$n = -(N-1)/2, \ldots, (N-1)/2.$$

where

$$u_m = a_m \cos \Psi_m \qquad (5\text{-}2)$$

$$v_m = -a_m \sin \Psi_m \qquad (5\text{-}3)$$

a_m = the amplitude of the mth plane wave (as previously defined)

Ψ_m = the initial phase of the mth plane wave (as previously defined.)

The noise component $w_c(n)$ is also as defined previously.

Let us now consider the following signal matrix

$$\underline{R} = \{r_k(n)\}, \qquad k = 1, \ldots, 2M$$

given by

$$\underline{R} = \begin{bmatrix} \cos[-\phi_1(N-1)/2] & \ldots & \cos \phi_1 \cdot 1 & \ldots & \cos[\phi_1(N-1)/2] \\ \sin[-\phi_1(N-1)/2] & \ldots & \sin \phi_1 \cdot 1 & \ldots & \sin[\phi_1(N-1)/2] \\ \cos[-\phi_2(N-1)/2] & \ldots & \cos \phi_2 \cdot 1 & \ldots & \cos[\phi_2(N-1)/2] \\ \sin[-\phi_2(N-1)/2] & \ldots & \sin \phi_2 \cdot 1 & \ldots & \sin[\phi_2(N-1)/2] \\ \vdots & & \vdots & & \vdots \\ \cos[-\phi_M(N-1)/2] & \ldots & \cos \phi_M \cdot 1 & \ldots & \cos[\phi_M(N-1)/2] \\ \sin[-\phi_M(N-1)/2] & \ldots & \sin \phi_M \cdot 1 & \ldots & \sin[\phi_M(N-1)/2] \end{bmatrix} \qquad (5\text{-}4)$$

In other words, the complete set $\underline{R}$ is composed of a cos (.) and a sin (.) function defined over the complete range of n (as in (5-1)) for each angle ϕ_m, m=1, ..., M.

We now define the signal matrix $\{s_k(n)\}$, k=1, ..., 2M, which is obtained from $\underline{R}$ by performing a Gram-Schmidt orthogonalization process [5-1] over the rows of $\underline{R}$. We note that the Gram-Schmidt process introduces a linear transformation in the original signal space $\underline{R}$, which results in a set of 2M orthonormal basis vectors $\underline{s}_k$. Provided the row vectors of $\underline{R}$ are linearly independent over the corresponding ranges of n,m, the number of basis signals $\underline{s}_k$ will equal the number of signals (rows) in the original set, i.e., 2M. We note that the $\underline{s}_k$ are still functions of the ϕ_m.

We may therefore write (5-1) as

$$x_c(n) = \sum_{k=1}^{2M} q_k \, s_k(n) + w_c(n) \qquad (5\text{-}5)$$

where the q_k are the projections of the $u_m \cos n\phi_m$ or the $v_m \sin n\phi_m$ from (5-1) onto the corresponding $\underline{s}_k$. The resulting likelihood function then becomes (again for the assumption of negligible mutual coupling and equal receiver noise powers)

$$p(\underline{x}_c \mid \underline{q}, \underline{\phi}) = K \exp\left[- \frac{1}{2\sigma_w^2} \sum_n \left[x_c(n) - \sum_{k=1}^{2M} q_k \, s_k(n) \right]^2 \right] \qquad (5\text{-}6)$$

where $\underline{x}_c$, $\underline{\phi}$, and $\underline{q}$ are the vectors of all $x_c(n)$, ϕ_k, and q_k. If we now define the quantity $L_{ck}(\underline{\phi})$ as

$$L_{ck}(\underline{\phi}) = \sum_n x_c(n)\, s_k(n) \,, \qquad k = 1, \ldots, 2M \tag{5-7}$$

substitute the above into (5-6), and change the order of summation, we get

$$p(\underline{x_c}|\underline{q}, \underline{\phi}) = K \exp\left[- \frac{1}{2\sigma_w^2} \sum_n x_c^2(n) \right] \cdot \exp\left[- \frac{1}{2\sigma_w^2} \left[- 2 \sum_k q_k L_{ck}(\underline{\phi}) + \sum_k q_k^2 \right] \right] \tag{5-8}$$

where the last line follows by virtue of the orthonormality of the $s_k(n)$. We now may complete the square in (5-8) and write

$$p(\underline{x_c}|\underline{q},\underline{\phi}) = K \exp\left[- \frac{1}{2\sigma_w^2} \left[\sum_n x_c^2(n) - \sum_k L_{ck}^2(\underline{\phi}) \right] \right] \cdot \exp\left[- \frac{1}{2\sigma_w^2} \sum_k [q_k - L_{ck}(\underline{\phi})]^2 \right] \tag{5-9}$$

The above is now in a convenient form for removal of the q_k. By analogy with the application of Bayes' rule used in Chapter 4, and through (4-25), we may write

$$p(\underline{\phi}\,|\underline{x}_c) = \frac{1}{p(\underline{x}_c)} \int_{q_1} \cdots \int_{q_{2M}} p(\underline{x}_c|\underline{q},\underline{\phi})\, p(\underline{\phi},q_1 \cdots q_{2M})\, dq_1 \cdots dq_{2M} \tag{5-10}$$

Again, we assume a uniform prior $p(\underline{\phi},\underline{q})$. After substituting (5-9) into (5-10), and lumping the constants, K, $1/p(\underline{x}_c)$, and the constant of the prior pdf together into a new constant K_2, we get

$$p(\underline{\phi}|\underline{x}_c) = K_2 \exp\left[-\frac{1}{2\sigma_w^2}\left[\sum_n x_c^2(n) - \sum_k L_{ck}^2(\underline{\phi})\right]\right] \cdot \int_{q_1} \cdots \int_{q_{2M}} \exp\left[-\frac{1}{2\sigma_w^2}\sum_k (q_k - L_{ck}(\underline{\phi}))^2\right] dq_1 \cdots dq_{2M} \tag{5-11}$$

Because of the fact that the last line has the form of a Gaussian pdf, the total 2M-fold integral reduces to a constant. By lumping the value of this constant together with K_2 to form K_3, we get

$$p(\underline{\phi}|\underline{x}_c) = K_3 \exp\left[\frac{1}{2\sigma_w^2}\left[\sum_k L_{ck}^2(\underline{\phi}) - \sum_n x_c^2(n)\right]\right] \tag{5-12}$$

Following a procedure similar to that described above, the a posteriori pdf of $\underline{\phi}$ given the quadrature data $\underline{x}_s$ may be determined to be

$$p(\underline{\phi}|\underline{x}_s) = K_4 \exp\left[-\frac{1}{2\sigma_w^2}\left[\sum_n x_s^2(n) - \sum_k L_{sk}^2(\underline{\phi})\right]\right] \qquad (5\text{-}13)$$

where

$$L_{sk}(\underline{\phi}) = \sum_n x_s(n)\, s_k(n) \qquad (5\text{-}14)$$

Again, since the in-phase and quadrature data are statistically independent in the presence of Gaussian noise, it follows that the total a posteriori pdf of $\underline{\phi}$ given $\underline{x}_c$ and $\underline{x}_s$ is

$$p(\underline{\phi} \mid \underline{x}_c, \underline{x}_s) = K_5 \exp\left[-\frac{1}{2\sigma_w^2}\left[\sum_n (x_c^2(n) + x_s^2(n)) - \sum_k (L_{ck}^2(\underline{\phi}) + L_{sk}^2(\underline{\phi}))\right]\right] \qquad (5\text{-}15)$$

This pdf is maximized, by maximizing the expression $L_A(\underline{\phi})$ given by

$$L_A(\underline{\phi}) = \sum_k \left[L_{ck}^2(\underline{\phi}) + L_{sk}^2(\underline{\phi}) \right] \qquad (5\text{-}16)$$

with respect to the ϕ_k, k=1,...,M. The desired joint MAP estimate $\hat{\underline{\phi}}$ of the vector $\underline{\phi}$ is that which maximizes expression (5-16).

We note that the estimation procedure presented here requires the estimation of only one parameter per plane wave incident on the array. That is, if M waves are impinging on the array, only an M-dimensional nonlinear maximization is

required. We note that we could have formed the likelihood function directly from (5-1) and found an ML estimate of the ϕ_m, u_m and the v_m, for m=1, ..., M by maximizing the corresponding likelihood function. This procedure would have required a 3M-dimensional maximization. Since the order of the computational complexity varies as the dimensionality cubed, the proposed method is in the order of being nine times more efficient. Therefore the effort involved in integrating out all the undesired parameters in the model (5-1) is, as it was in Chapter 4, expended to produce a more computationally efficient estimator.

5.3 Implementation

In the usual specular multipath environment, no more than two plane waves will be incident on the array. Hence, in the application of this ML estimator, a maximization must be performed in two variables. Unfortunately, the algorithms in existence for multi-dimensional optimization are considerably more complex than the Golden Section Search, and hence are not amenable for implementation on a micro-processor.

The most widespread multidimensional optimization algorithms are the conjugate gradient methods developed by Fletcher and Powell [5-2], and others. These algorithms are well documented from the statistical viewpoint in Bard [4-1]

and from the numerical viewpoint by Bandler [4-10]. An efficient, well debugged software version of this algorithm [FLOPT V] is available [5-3].

Figure 5-2 shows a flow-chart implementation of the asymmetric ML estimator. We note that the number of incident plane waves, M is assumed known, whereas in practical applications, this may not be the case. A statistical test to determine whether or not the value of M used in the computation is sufficiently high is presented in Sect. 5-5. A receiver structure is shown in Fig. 5-3.

We note that the first step in the computation is to form the 2MXN matrix $\underline{R}$ of values of cos $n\phi_k$ and sin $n\phi_k$ using initial estimates $\underline{\phi}$. We note that for each ϕ_k, two rows of $\underline{R}$ are formed; one for cos $n\phi_k$ and one for sin $n\phi_k$. The $\underline{R}$-matrix is then input to the Gram-Schmidt orthonormalization process, where the input vectors are the individual $r_k(n)$, $n = -(N-1)/2, \ldots, (N-1)/2$. The output is then another 2MXN matrix $S(\cdot)$, the rows of which all have unit energy and are all mutually orthogonal.

Each row of the $S(\cdot)$ matrix is then correlated with the in-phase data $x_c(n)$ and the quadrature data $x_s(n)$ over the range of n. The sum of the squares of all 2X 2M correlations is then determined, and this sum determines the objective function used in the maximization routine. The process iterates, each time with a better guess of $\underline{\phi}$, until

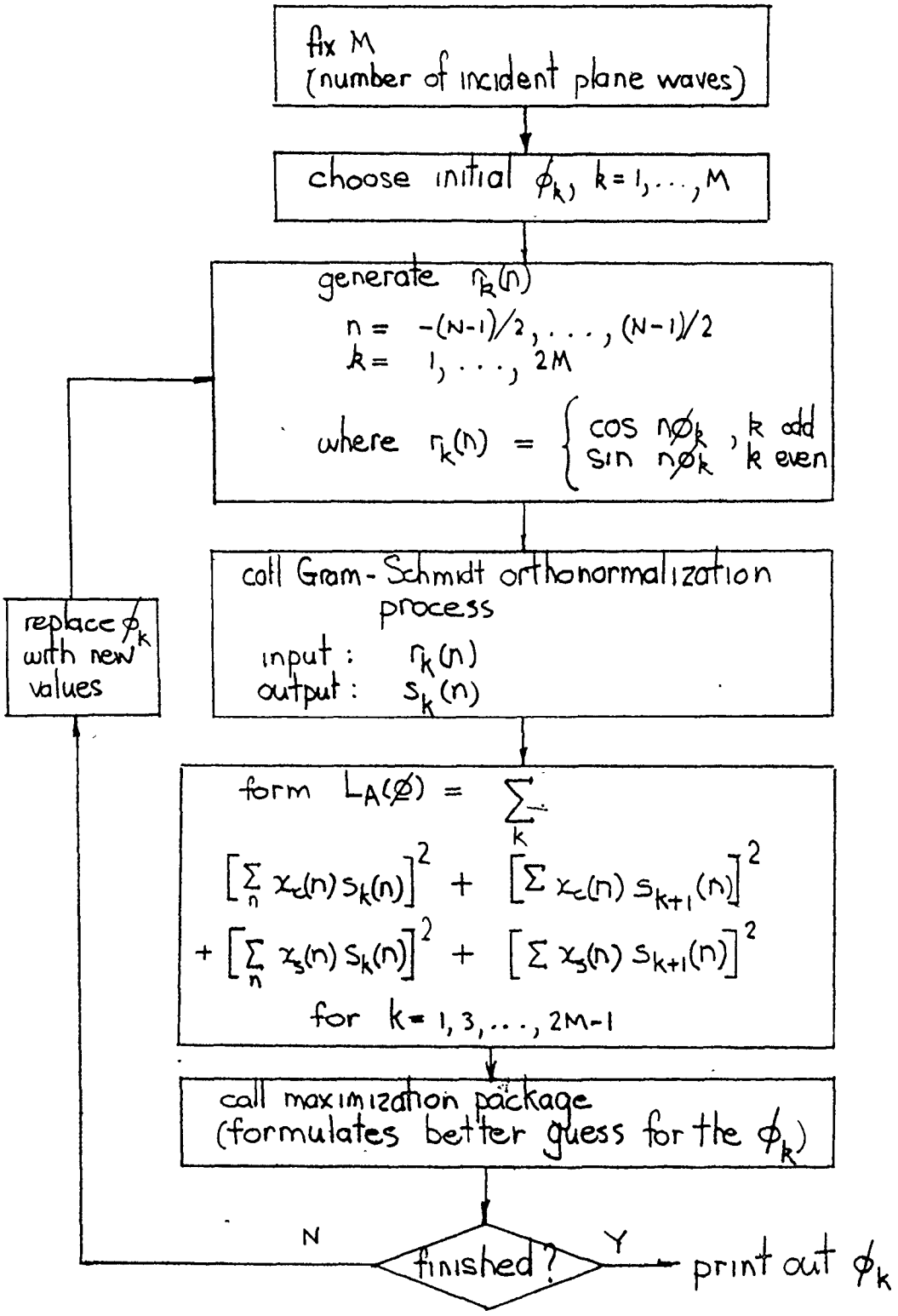

Fig 5-2 Flowchart of asymmetric ML processor

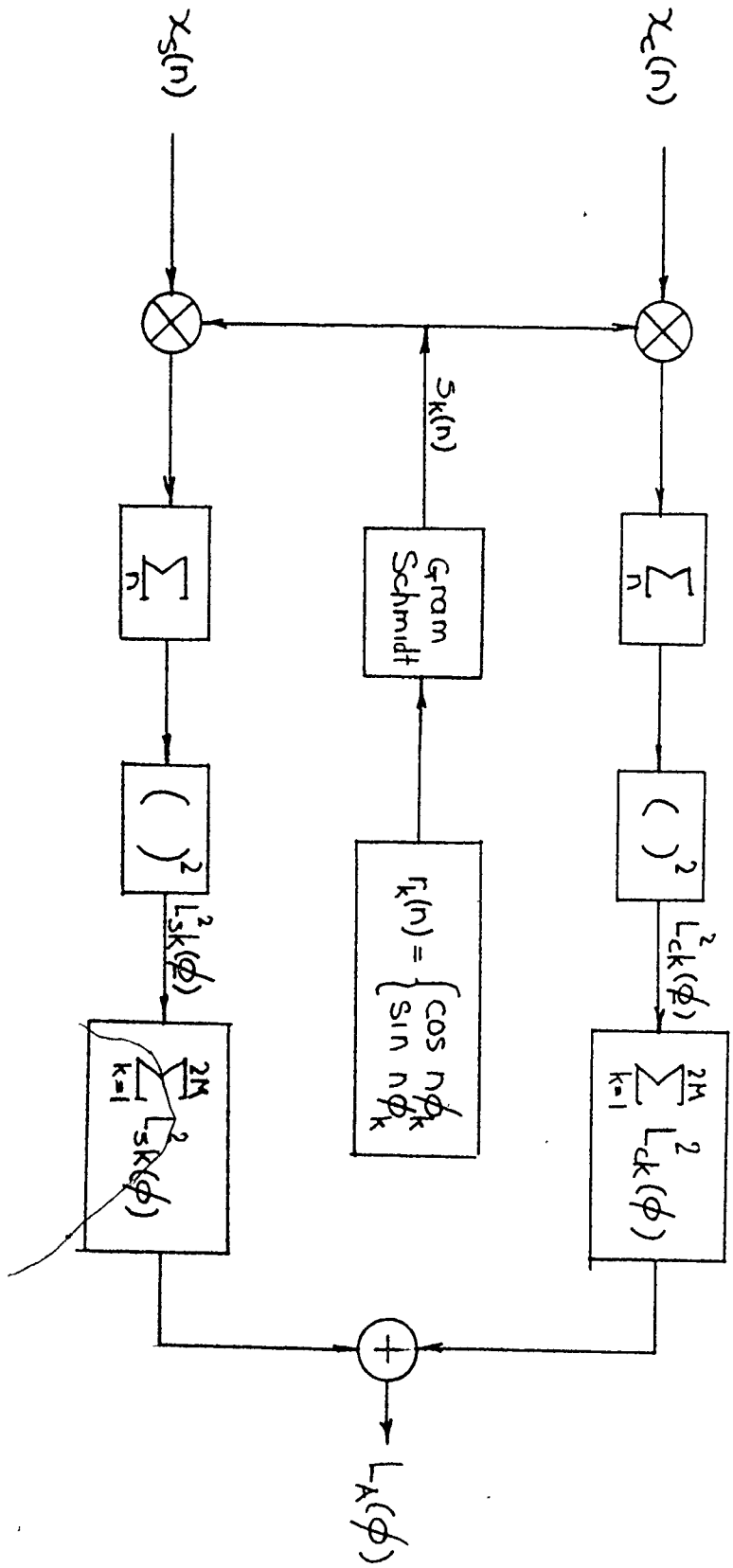

Fig 5-3 Receiver structure for asymmetric ML estimator

the estimates have sufficiently converged.

In the application of any of the efficient multidimensional optimization algorithms, the gradient of the objective function with respect to each parameter must be determined. In the results which follow, all the derivatives used in the evaluation of the gradient were calculated numerically. Because of the presence of the Gram-Schmidt procedure, the derivatives are difficult to determine analytically. There is no doubt that the optimization routines behave much better and are much more efficient with analytic derivatives; therefore, a suggestion for further work would be to develop the closed-form expressions for the required derivatives.

5.4 Results

5.4.1 Theoretical Results

The high-SNR theoretical variances for this estimator may be determined by exactly the same method as was used in Chapter 4. The validity of these variances are also subject to the same linearity conditions as expressed by (4-47). The high-SNR theoretical expression for the variance of the jth element of the vector $\hat{\underline{\phi}}$ is therefore given through (5-16) and (4-64) by

$$Var[\phi_j] = 2\sigma_w^2 \, p^{jj} \qquad (5\text{-}17)$$

where p^{jj} is the j,j'th element of the square matrix $\underline{P}^{-1}$ where the elements of $\underline{P}$ are

$$p_{ij} = -E\left[\frac{\partial^2 L_A(\underline{\phi})}{\partial\phi_i \partial\phi_j}\right]$$

where as before, the expectation is evaluated by using artificial data with no added noise in the calculation of the $L_A(\hat{\phi})$.

Figure 5-4 shows plots of high SNR theoretical variance evaluated numerically from (5-17) for the case N=21 elements and M=2. Again, the ordinate is calibrated in dB above 1(degree)^2. The SNR value (30dB) in this instance, and throughout this chapter, again refers to the equivalent free-space SNR which would occur in the absence of multipath. The results shown in the figure correspond to the geometric configuration where one incident plane wave is fixed at an actual angle corresponding to the electrical phase angle of 26.4° (= 1.5 standard beamwidths for a 21 element array) below the normal. The other plane wave is situated so that it is incident from below the former by the number of standard beamwidths indicated by the abscissa. For example, if the signal separation is 0.5 standard beamwidths, then $\phi_1 = 26.4^\circ$ and $\phi_2 = 26.4^\circ + 8.57^\circ = 34.97^\circ$. The quantity 8.57° is the electrical phase angle corresponding to 0.5 standard beamwidths for N=21.

There are some interesting facts which are evident

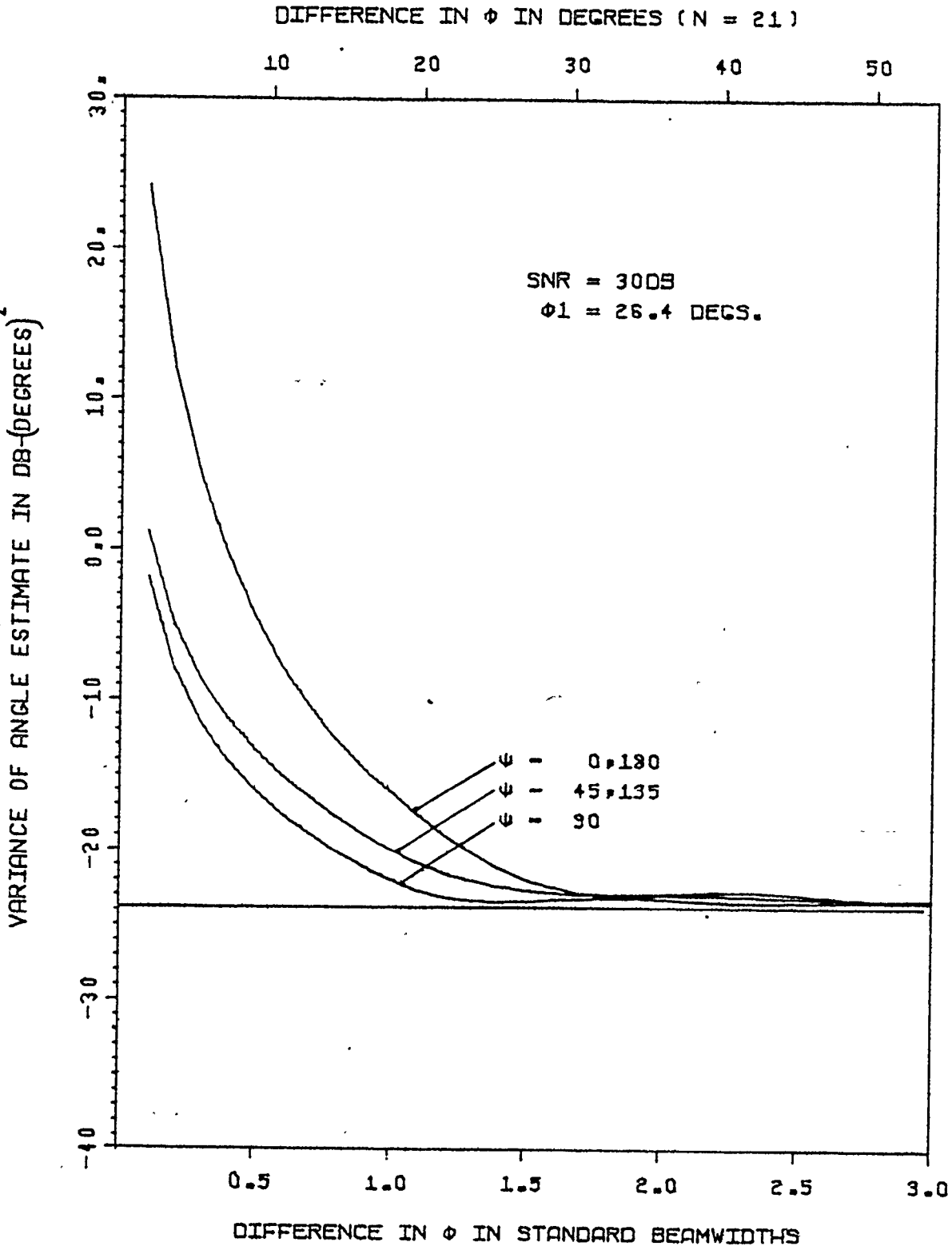

Fig. 5-4 Theoretical high SNR variances for the asymmetric ML processor vs. BW for N = 21 elements.

from Fig. 5-4. The first is that whereas the equivalent set of curves for the symmetric ML estimator (Fig. 4-4) show that the variances are best for $\Psi = 0^{\circ}$ and degrade steadily as $\Psi \rightarrow 180^{\circ}$, the variances shown in Fig. 5-4 are best for $\Psi = 90^{\circ}$. Also, the behaviour is symmetric in Ψ, with the variances degrading as Ψ approaches either 0° or 180°. We note that when $\Psi = 90^{\circ}$, the two incident signal components are spatially uncorrelated over the span of the array for any incident direction angles.

We also note from Fig. 5-4 that the best variances attainable with the asymmetric estimator are about 5 dB worse than the best attainable with the symmetric case. This is because the extra knowledge gleaned in the model by assuming symmetric incidence angles is not available in this realization. The curves of Fig. 5-4 display a poorer variance at low-angle separations (e.g. 0.1 beamwidth), but are not necessarily uniformly worse. For example, for $\Psi = 180^{\circ}$ and BW = 1.0 in Fig. 4-4 for $\rho = 0.9$, the variance is about -16 dB. This is about the same value of variance for the corresponding parameter values as appears in Fig. 5-4.

The solid line in these figures again indicates the variance attainable with an estimator which knows that only one plane wave is incident on the array. Thus, we see that for this asymmetric estimator, the presence of more than one incident plane wave always degrades the performance of the

estimator. This is in contrast to the symmetric structure, which in some cases (e.g. Fig. 4-4), exhibits performance which improves in the presence of an additional incident wave.

Since this asymmetric ML technique is a multivariate estimator, there is a different variance associated with each ϕ_j, j=1, .., M. The curves in Fig. 5-4 correspond to the case where M=2 and ρ = 0.9, and show only the results having the better variance. That is, they show the variances associated with the stronger (direct) signal. The variances associated with the reflected signal are uniformly about 1 dB worse than those shown.

The curves in Fig. 5-5 (a)-(c) again show variances calculated from (5-17), and correspond to M = 2, $\Psi = 90^\circ$ and ρ = 0.9. In this case, the variances associated with both ϕ_1 and ϕ_2 are given. The difference between the three curves is that ϕ_1 is fixed at 90° in (a), 26.4° in (b), and 5.7° in (c). Thus, the three situations correspond to identical parameter values, except that the average angle of incidence moves closer to the normal of the array as one goes from (a) to (c). We therefore note from this figure that the performance of the estimator depends on the position of the average of the elevation angles of the incident plane waves and degrades as the average moves towards the normal of the array.

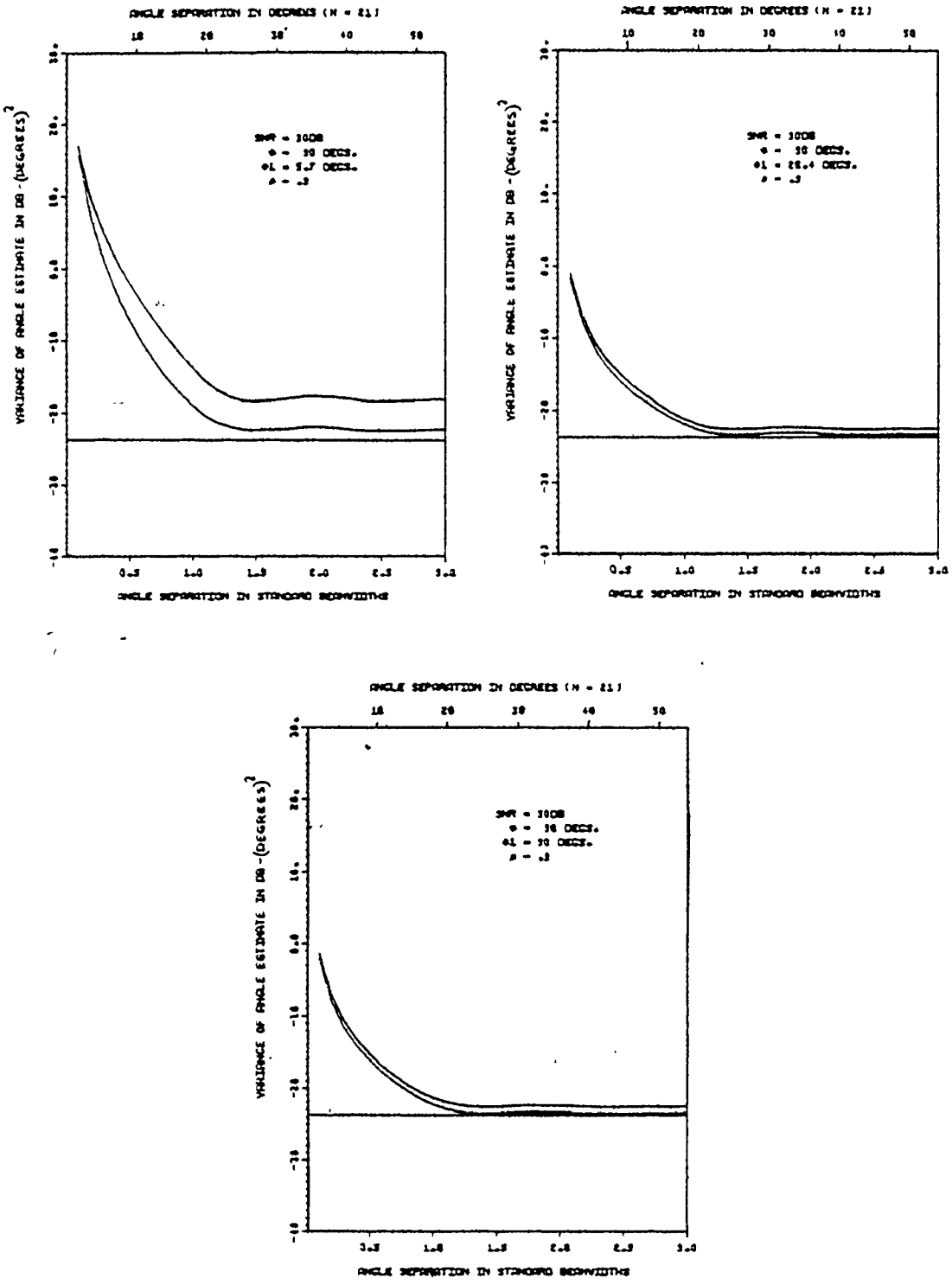

Fig. 5-5 Theoretical high SNR variances vs. BW for fixed ψ = 90 degrees and varying ϕ_1.

Figure 5-5 shows results for the best-case value of Ψ, i.e., 90°. In Fig. 5-6, we show results identical to those in Fig. 5-5, except that the curves correspond to the worst-case values of Ψ, i.e., 0° or 180°.

There will be more said concerning the behaviour of these results in Section 5-5.

Three dimensional plots of the objective function as defined by (5-16) versus ϕ_1 and ϕ_2 are shown in Fig. 5-7 and 5-8 for various parameter values. These plots are somewhat analogous in purpose to the curves shown in Fig. 4-3, except that in this case, since the estimator is multivariate, multidimensional surfaces are required to plot the desired function.

Again in this case, it is easy to ascertain (by reference to (5-15)) that a certain equivalue contour on these plots corresponds to a contour of equal a posteriori probability of the joint estimate $\hat{\underline{\phi}}$. This may be seen as follows. Suppose that we wish to establish a set of points $\{\phi_1, \ldots, \phi_M\}$ all with the same a posteriori probability. Then it follows from (5-15) that these points define equivalue contours of the objective function $L_A(\phi)$. It therefore follows that all points on the interior of a particular contour define a confidence region on the estimate $\hat{\underline{\phi}}$, the level of significance being related to the value associated with the contour.

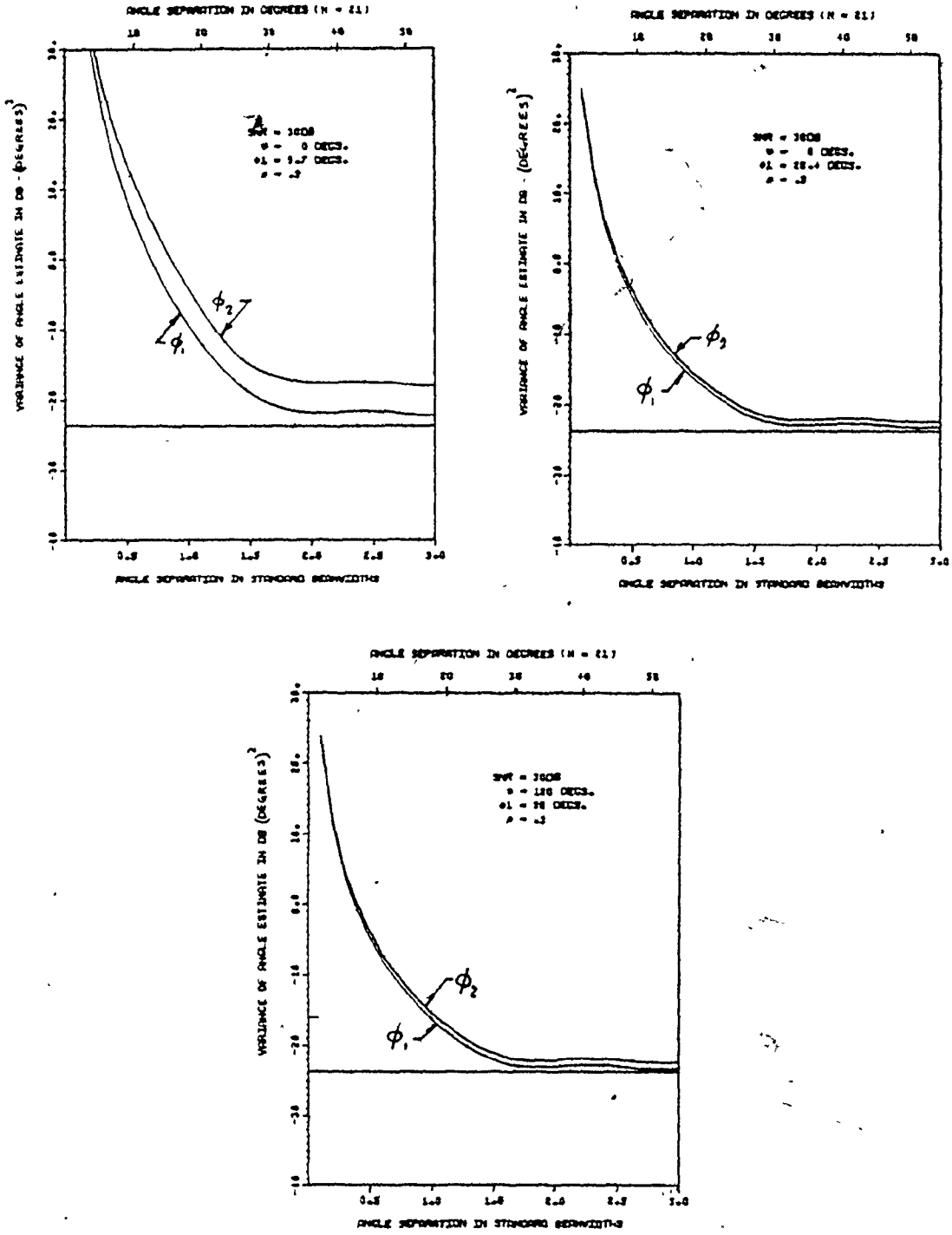

Fig. 5-6 Theoretical high SNR variances vs. BW for fixed $\psi = 0$ degrees and varying ϕ_1.

Both Figs. 5-7 and 5-8 corresond to ϕ_1 fixed at 90^o, but Fig. 5-7 is for 0.5 beamwidth signal separation, and Fig. 5-8 shows results for a signal separation of 1.0 beamwidth. We note that for the smaller separation situation (0.5 BW), that the maximum is not as distinct as it is for the 1.0 BW case. This implies the noise will have a greater confounding effect for the first situation, a fact which is confirmed by reference to Fig. 5-4.

Both figures show multiple maxima. This is not an undesirable situation, since the second maximum corresponds in both cases to the point where the ordered pair (ϕ_1, ϕ_2) is reversed in order. Hence, the plot is saying in the case of Fig. 5-8 that (1.87, 1.57) is almost as good as estimate of $\underline{\phi}$ as is (1.57, 1.87), which of course, is true.

Numerical problems may sometimes be encountered in the optimization routines because in both cases, the surfaces are poorly conditioned. The maxima in Fig. 5-7 are quite broad and hence computer truncation errors may create problems in the inversion of the Hessian matrix (which is required in the conjugate gradient routines). Also, in Fig. 5-8, it may be observed that many saddle points and ridges exist, the presence of which slows down the rate of convergence of the algorithm. If these problems are found to exist in practice, it would be necessary to move to a different starting point, and/or use higher precision

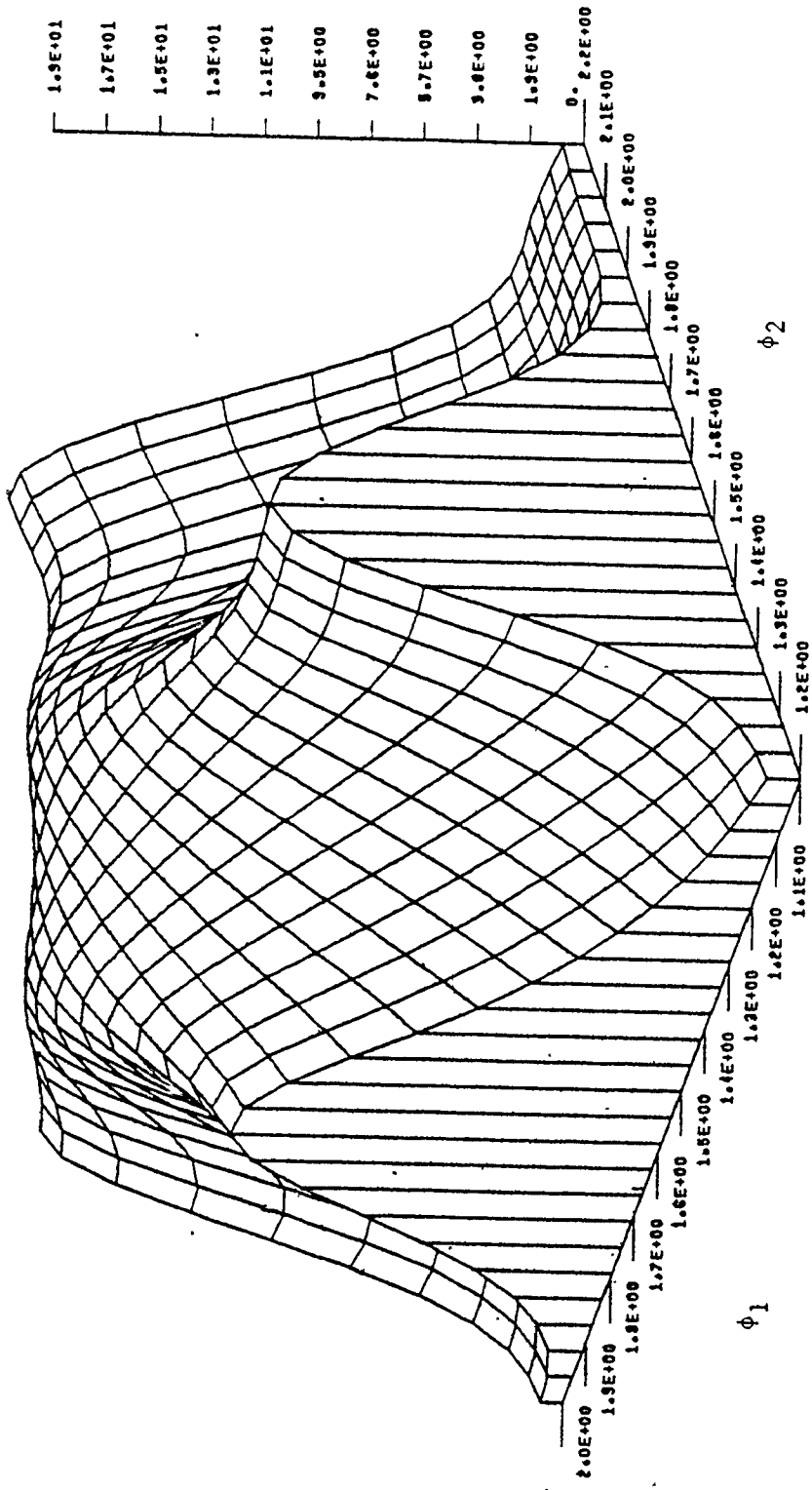

Fig. 5-7 Asymmetric processor's objective function for ψ = 90 degrees, N = 21, ϕ_1 = 90 degrees, ρ = 0.9, and BW = 0.5.

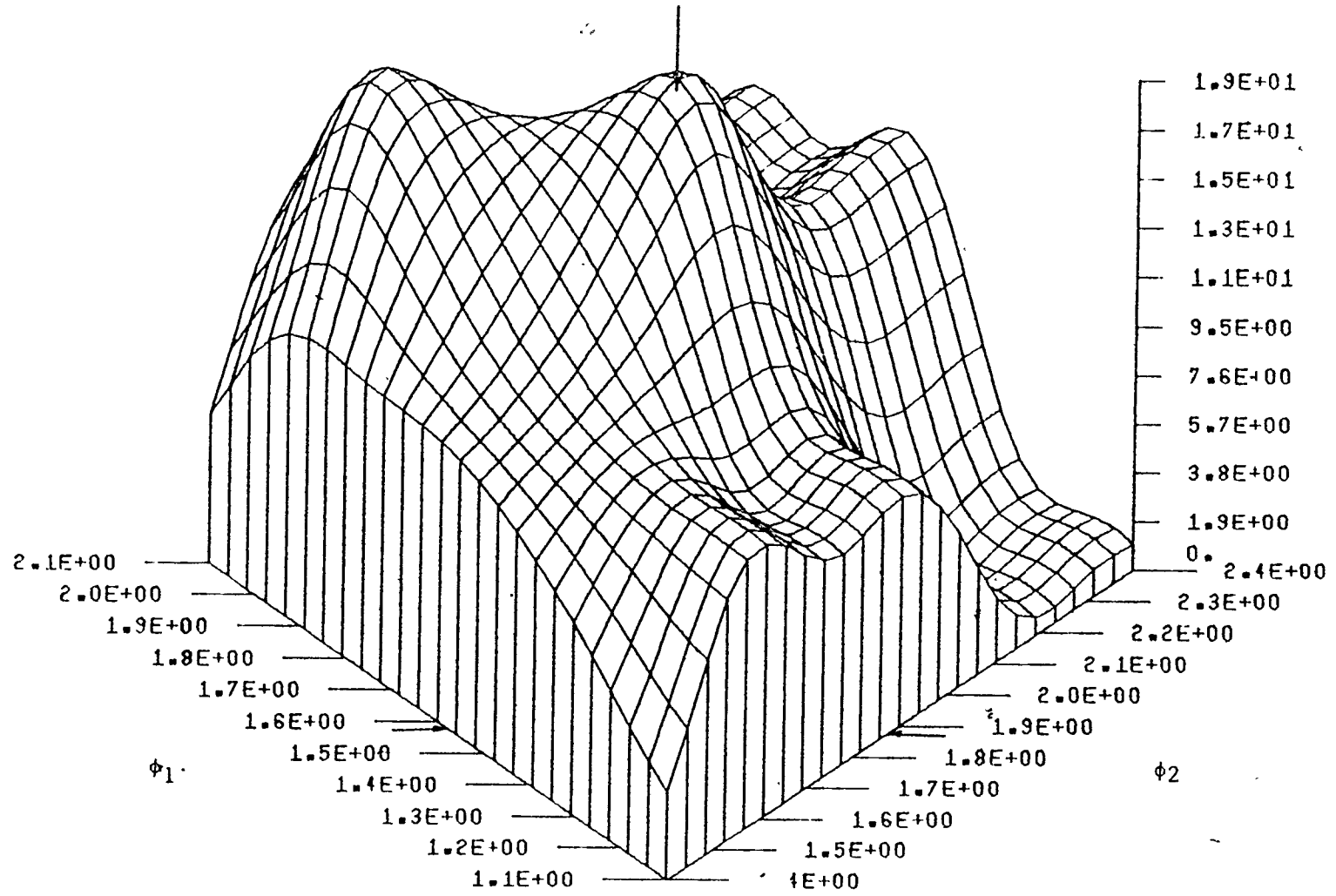

Fig. 5-8 Asymmetric processor's objective function for ψ = 90 degrees, N = 21, ρ = 0.9, ϕ_1 = 90 degrees, and BW = 1.0.

arithmetic in the software package.

The behaviour of the variance of $\hat{\phi}_1$ vs N is shown in Fig. 5-9, for ρ=0.9 and BW=0.25, 0.5 and 1.0. In this case we see the same behaviour as was demonstrated for the symmetric case. That is, for N greater than about 7, a doubling of the number of elements improves the variance by 9 dB, which implies that var[$\underline{\phi}$] varies as N^3. Therefore, we see that for this case also, an increase in the number of elements in percentage terms results in a considerable improvement in performance.

So far, only results for the case ρ = 0.9 have been considered. In Fig. 5-10, we show theoretical variances for the case ρ = 0.5, when ϕ_1 is fixed at 26.4 degrees. Results are shown for Ψ equal to integer multiples of 45^o. In this case, we note that the difference in variance between the estimates $\hat{\phi}_1$ and $\hat{\phi}_2$ is 6 dB, within a few tenths of a dB; i.e., the value given by the expression 20 $\log_{10}(\rho)$. Also, note that the corresponding difference in variance for the case ρ = 0.9 is about 0.7 dB as shown in Fig. 5-5(b). This value is within a few tenths of a dB of the value given by the expression 20 $\log_{10}$ (0.9) = 0.46 dB. We therefore see that the variance of the angle estimate associated with the reflected signal component (ϕ_2) varies linearly with ρ. This is not surprising, since it is the result predicted theoretically, through (5-17), because of the fact that the

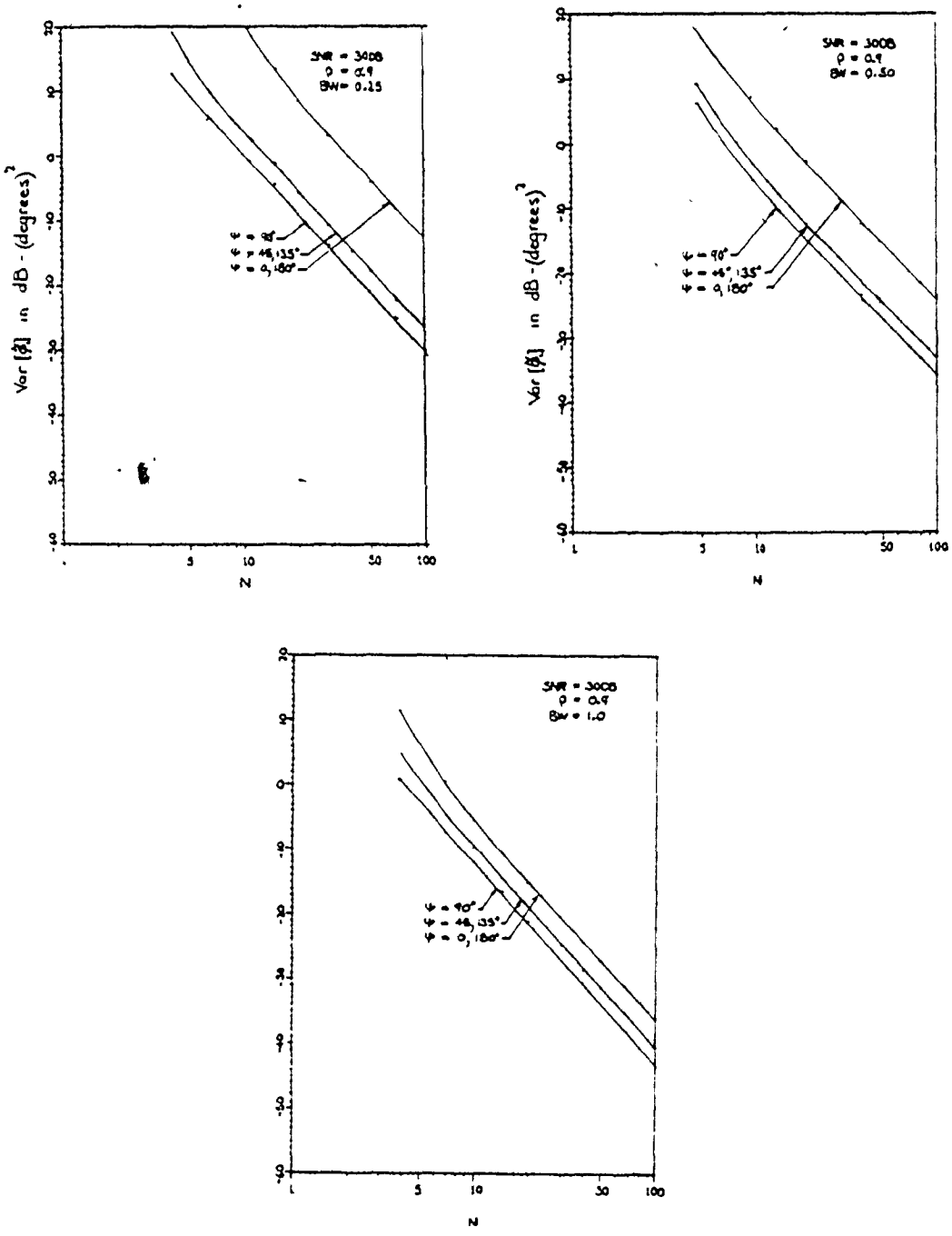

Fig. 5-9 Behavior of the variance of $\hat{\phi}_1$ vs. number of elements, N for various parameter values.

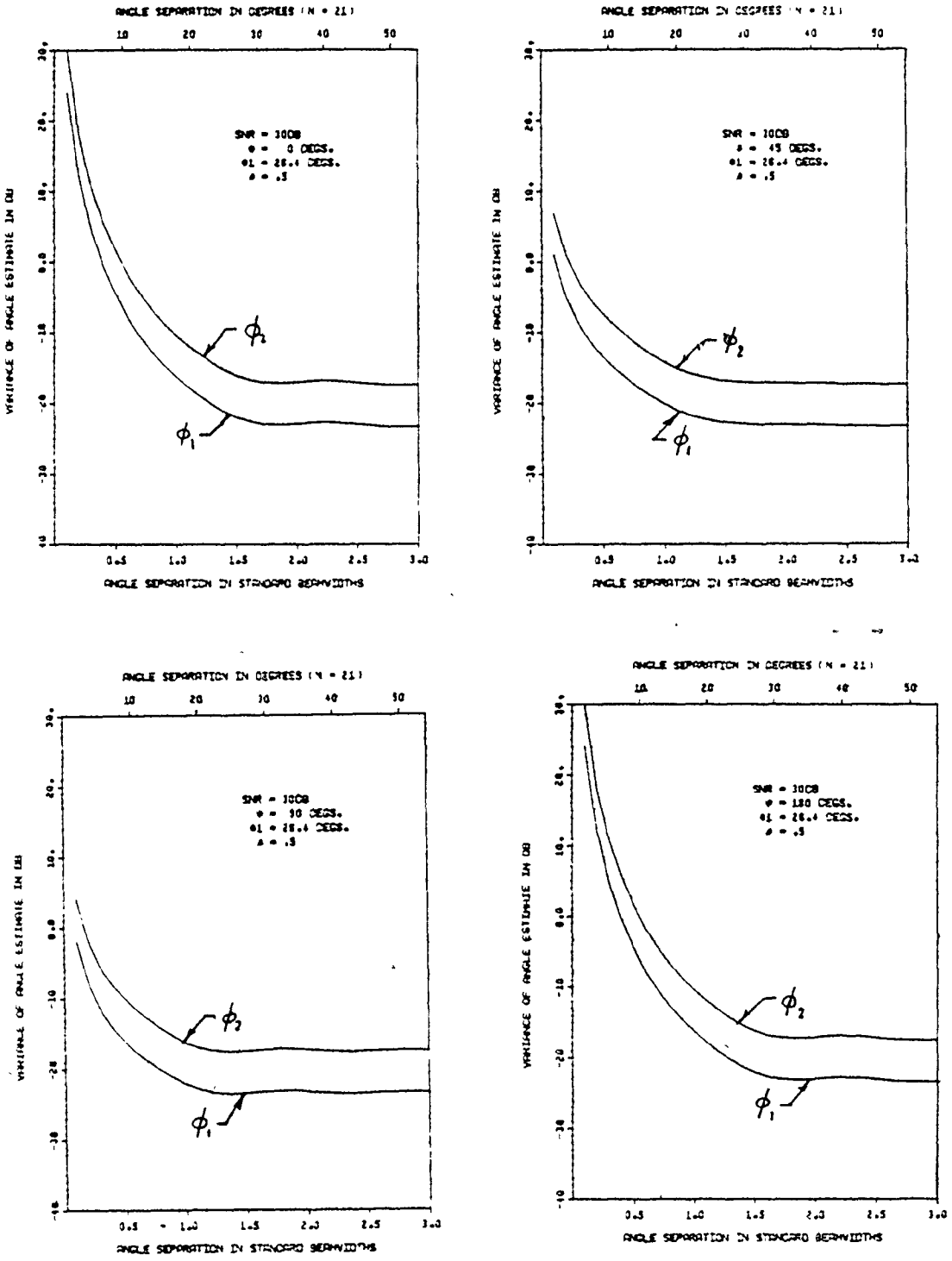

Fig. 5-10 Theoretical high SNR variances of $\hat{\phi}_1$ and $\hat{\phi}_2$ for the asymmetric processor for $\rho = 0.5$. The higher variance is that associated with the weaker signal.

model equation (5-1) is linear in the quantity ρ.

This discussion does not imply that $\mathrm{Var}[\hat{\phi}_1]$ will always be $20 \log_{10}(\rho)$ dB better than $\mathrm{Var}[\hat{\phi}_2]$. The parameters can take on values which cause the shape of the surface of the objective function (as shown in Fig. 5-7, 5-8) to have a different second derivative with respect to ϕ_1 than ϕ_2, even if $\rho = 1$. An example of this situation is shown in Figs. 5-5(c) and 5-6(c) ($\phi_1 = 5.7$ degrees), where it may be noted that the difference between $\mathrm{Var}[\hat{\phi}_1]$ and $\mathrm{Var}[\hat{\phi}_2]$ is many dB more than that given by $20 \log_{10}(.9)$. However, the variance $\mathrm{Var}[\hat{\phi}_2]$ will always change in a linear fashion with ρ if ρ varies and all other parameters remain constant.

5.4.2 Simulation Results

In Figs. 5-11 and 5-12 we see variances of ϕ_1, ϕ_2 obtained by computer simulation versus signal separation in standard beamwidths, for the equivalent free-space SNR=30dB, and ϕ_1 fixed at 90°. In each case we notice that the simulation variances, obtained as a result of 99 trials, agree very well with the values predicted from the theoretical expression (5-17), shown in the dashed lines. The points at 0.25 beamwidth separation deviate somewhat from the theoretical values; however this is because the SNR is not sufficiently high for the expression (5-17) to hold

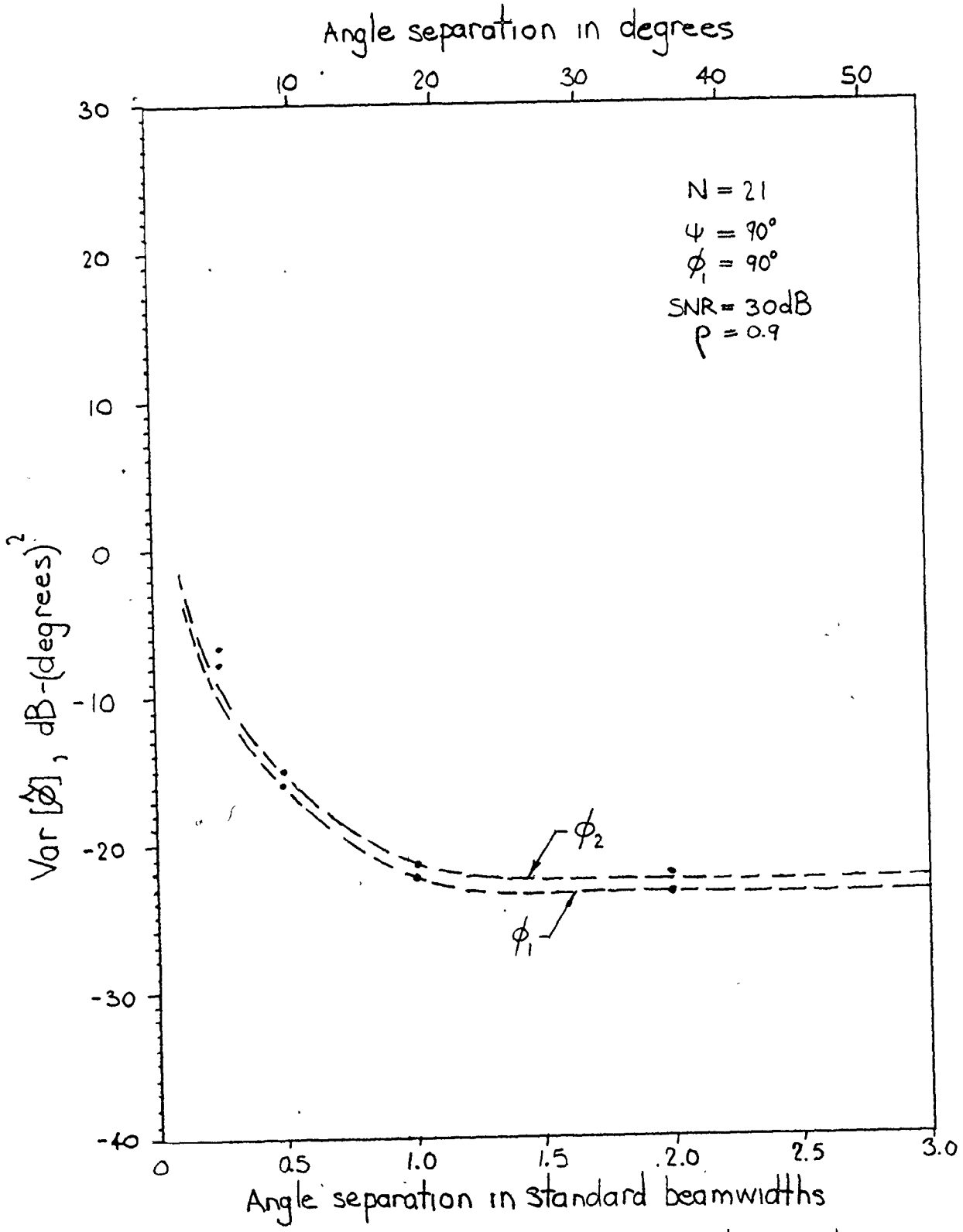

Fig 5-11 Variances of estimates $\hat{\phi}_1, \hat{\phi}_2$ vs. signal separation, for $\psi = 90°$, obtained by computer simulation. Dashed line is the theoretical high SNR result, defined by (5-17).

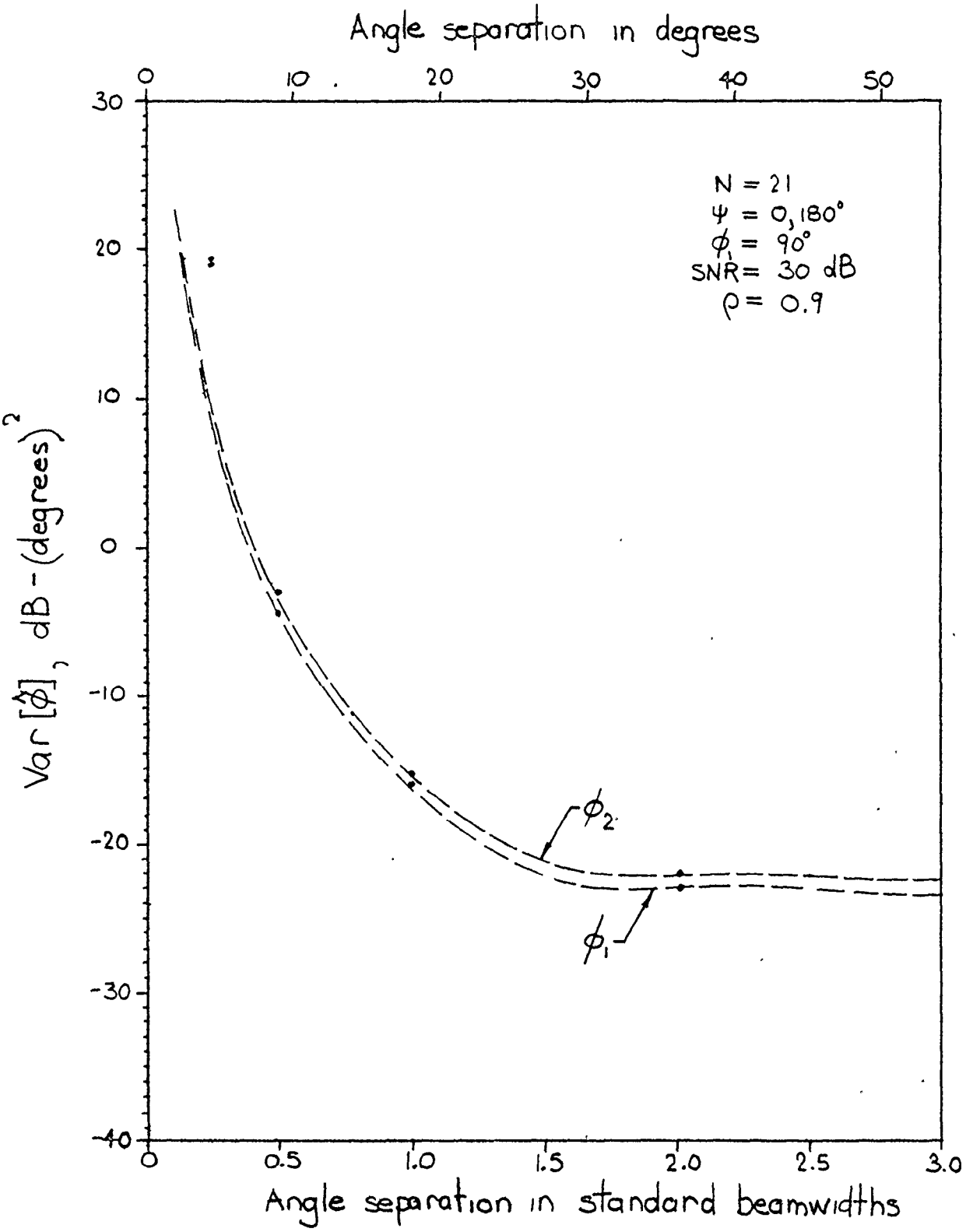

Fig 5-12 Variances of estimates $\hat{\phi}_1, \hat{\phi}_2$ vs. signal separation for $\Psi = 0, 180°$, obtained by computer simulation.

TABLE 5-1

$\phi_{ave} = 90^{\circ}$, N = 21, M = 2, ρ = 0.9, SNR = 30 dB

	BW	0.25	0.5	1.0	2.0
true values ϕ_1, ϕ_2 degs		90.00	90.00	90.00	90.00
		85.72	81.42	72.85	55.71
ψ 0°, 180°		90.04	89.96	90.00	90.00
		85.33	81.28	72.84	55.61
90°		90.04	90.00	89.98	90.00
		85.63	81.41	72.82	55.71

ϕ_1 upper

ϕ_2 lower

Table 5-1 Means of $\hat{\phi}_1$ and $\hat{\phi}_2$ obtained by computer simulation. All entries are in degrees.

for this value of signal separation.

Table 5-1 shows values of the means of the estimates $\hat{\phi}_1$ and $\hat{\phi}_2$ obtained from the same simulations which produced the variances in Figs. 5-11 and 5-12. In all cases, we note that the estimates are essentially unbiased, including the values for BW = 0.25. In the latter instance, since the

corresponding variances departed from the theoretical values, we may have expected the estimates to be biased; however, such is not the case. The behaviour of the asymmetric ML estimator versus the SNR is depicted in Figs. 5-13 and 5-14, for BW = 0.5, ρ=0.9, and the average value of ϕ_1 and ϕ_2, ϕ_{ave}, equal to 90 degrees (5.25 standard beamwidths). The means of $\hat{\phi}_1$ and $\hat{\phi}_2$ are shown in Fig. 5-14, for Ψ = 0, 90 and 180 degrees, whereas the variances $Var[\hat{\phi}_1]$ and $Var[\hat{\phi}_2]$ are shown in Fig. 5-13.

The values of $Var[\hat{\phi}_1]$ and $Var[\hat{\phi}_2]$ predicted by (5-17) are shown in Fig. 5-13 by the dashed lines. We note that the variances obtained by simulation agree roughly with the theoretical results down to an SNR of 9 dB, except for the case when $\phi = 180^{o}$. In this instance, the simulation variances dip sharply below the predicted values, because the high SNR assumption is no longer valid for this particular set of parameter values.

The true values of ϕ_1 and ϕ_2 for these simulation runs are shown by the dashed lines in Fig. 5-14. We see that the means of $\hat{\phi}_1$ and $\hat{\phi}_2$ obtained by simulation are close to their true values; the bias is less than 0.1 standard beamwidth in all cases. The results for Ψ = 90 degrees show insignificant bias over the range of SNR considered, whereas the results for Ψ = 0 and 180 degrees both show some small bias for values of SNR below 15 dB. A surprising

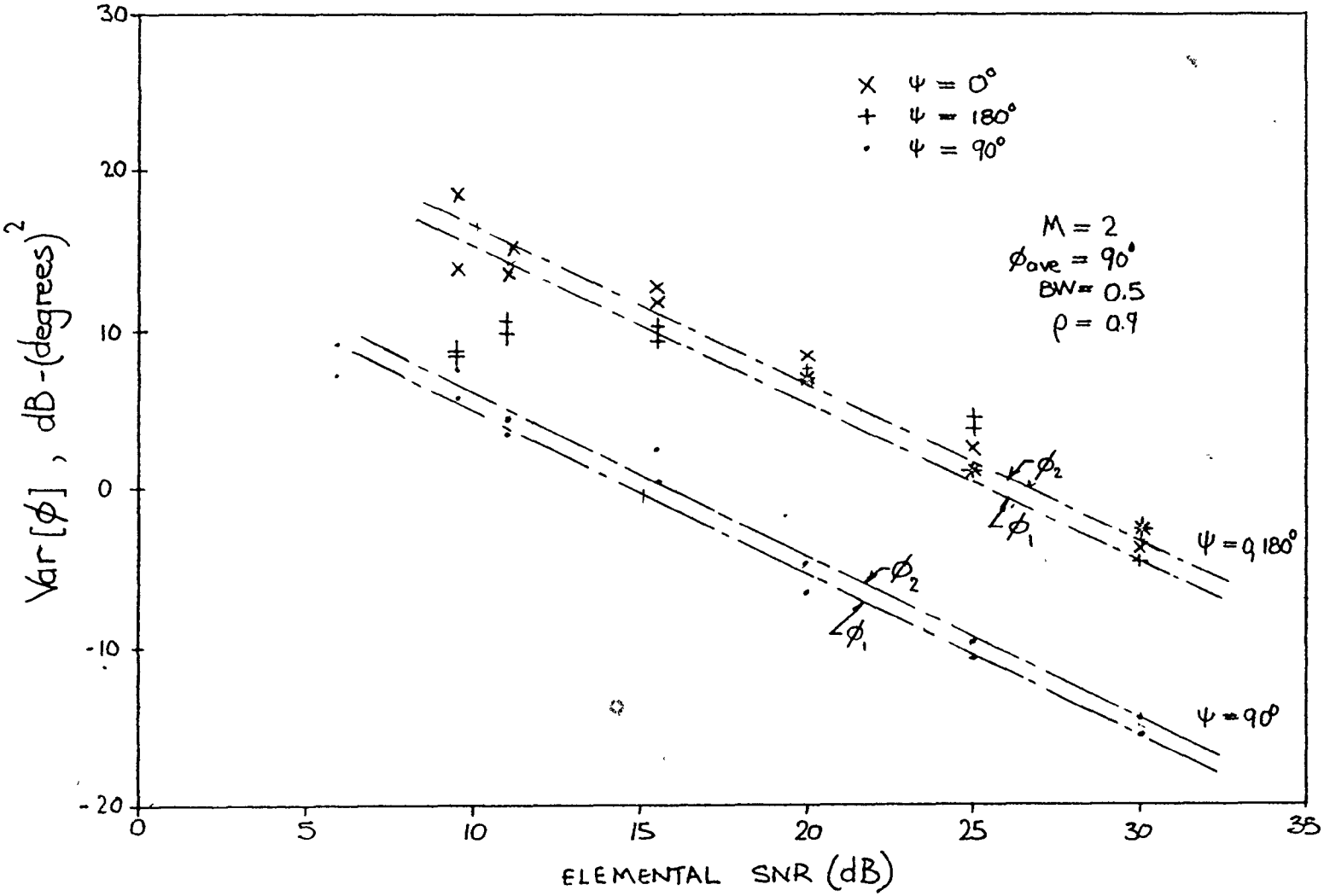

Fig 5-13 Variances obtained by simulation vs. elemental SNR, for the asymmetric ML estimator. Signal separation is 0.5 BW.

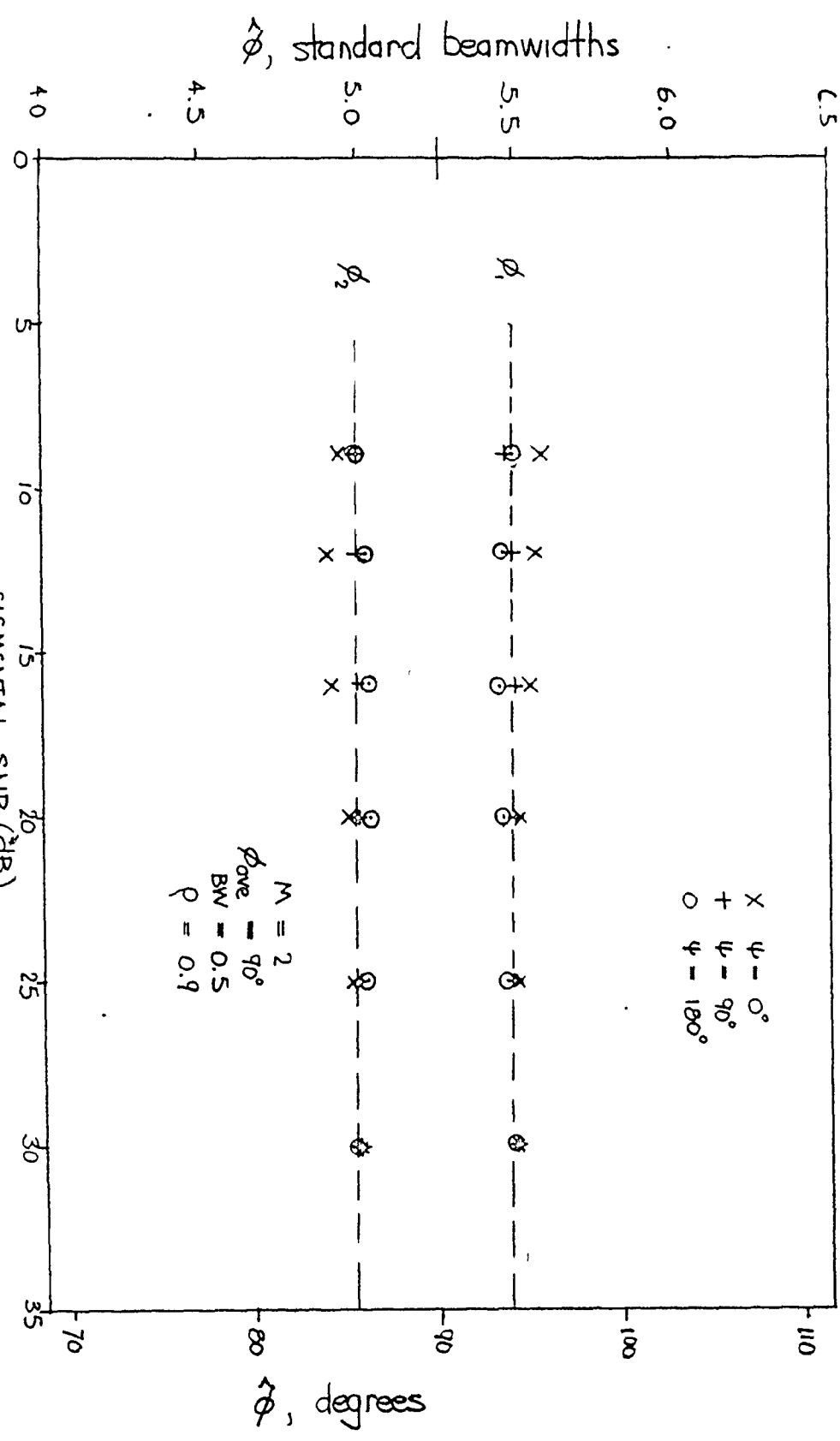

FIG 5-14 Means of $\hat{\phi}_1$, $\hat{\phi}_2$ vs. free-space elemental SNR, for BW = 0.5, N = 21, and for ϕ_{ave} = 90° (5.25 BW)

result here is that the means for Ψ = 180 degrees are not more biased for low SNR's, since their corresponding variances deviate substantially from the high SNR values.

5.5 Discussion

In this section, we shall be discussing some further ideas pertinent to the asymmetric ML estimator. They are: (1) comparison between the symmmetric and asymmetric ML estimators, (2) determination of M through the F-test, (3) a multi-snapshot version of the asymmetric ML structure, (4) the estimation of a joint confidence region of the estimates, and (5) comparison of this structure with those proposed by other researchers.

5.5.1 Comparison with the Symmetric ML Estimator

It is obvious that the symmetric processor is easier to implement than the asymmetric structure. It is also apparent that the symmetric version leads to better results, since in many cases, the variances of the latter case are much better. On the other hand, use of the symmetric structure is restricted to a limited class of environmental configurations, whereas the asymmetric processor may be applied in more diverse situations. Since the two structures are the result of similar mathematical derivations, we shall be finding that the two forms share

other characteristics in common; e.g., we shall show that the symmetric is a special form of the asymmetric estimator, and that they share the same form of multi-snapshot realization.

By comparing Figs. 4-4 and 5-4, we see that the variances of the estimates are almost always better for the symmetric case. Also, we note that by comparing Figs. 4-9(c) and 5-14, we see that the worst-case bias is slightly better for the symmetric estimator. For an SNR of 5dB, the maximum bias in Fig. 4-9(c) is about 0.1 standard beamwidth; this bias occurs in Fig. 5-14 for a range of SNR between 9 dB and 15 dB. Therefore, the asymmetric structure produces somewhat poorer performance than does the symmetric version.

As mentioned previously, the symmetric estimator is actually a special case of the asymmetric case; the former can be derived from the latter. To see this, consider the asymmetric structure for M=2 targets, and let us see what happens when the two incident plane waves become symmetrically spaced about the normal of the array. The sets $\cos\{n\phi_1\}$ and $\sin\{n\phi_2\}$, $n = -(N-1)/2, \ldots, (N-1)/2$, as defined in (5-1) are then linearly dependent for $\phi_1 = -\phi_2$; such is also the case for the sets $\{\sin n\phi_1\}$ and $\{\sin n\phi_2\}$. Therefore, application of the Gram-Schmidt orthonormalization process is not valid in this situation, since the input signals (vectors) must form a linearly independent set

[5-1]. A linearly independent set may be formed with the given signal set if the dimensionality of the signal space is reduced from 4 to 2. We are then left with the signals $\{\cos n\phi\}$ and $\{\sin n\phi\}$, where $\phi = \phi_1 = -\phi_2$. Now, note that these two signals are orthogonal, but not orthonormal, over the prescribed range of n. Therefore, the signals $s_1(n)$ and $s_2(n)$ with unit energy produced by the Gram-Schmidt process from the $\{\cos n\phi\}$ and $\{\sin n\phi\}$ set are given by

$$s_1(n) = \left[\frac{1}{\sum_n \cos^2 n\phi} \right]^{1/2} \cos n\phi \tag{5-18}$$

and

$$s_2(n) = \left[\frac{1}{\sum_n \sin^2 n\phi} \right]^{1/2} \sin n\phi \tag{5-19}$$

$$n = -(N-1)/2, \ldots, (N-1)/2$$

By substituting the above into (5-7), (5-14), and (5-16), we get

$$L_A(\phi) = \frac{\left[\sum_n x_c(n) \cos n\phi \right]^2}{\sum_n \cos^2 n\phi} + \frac{\left[\sum_n x_c(n) \sin n\phi \right]^2}{\sum_n \sin^2 n\phi}$$

$$+ \frac{\left[\sum_n x_s(n) \cos n\phi \right]^2}{\sum_n \cos^2 n\phi} + \frac{\left[\sum_n x_s(n) \sin n\phi \right]^2}{\sum_n \sin^2 n\phi} \tag{5-20}$$

which is identical to the symmetric ML estimator defined by (4-33). We have therefore shown that the special symmetric structure is a special case, and may be derived from the

more general asymmetric structure.

We have noted from Figs. 5-5 and 5-6 that the variances of $\hat{\phi}_1$ and $\hat{\phi}_2$ degrade as their average approaches the normal of the array (0 degrees). This is because the magnitude of the signal sets $\{\cos n\phi_i\}$, i=1,2 become more correlated with each other as ϕ_1 approaches $-\phi_2$. This has the effect of causing the projection of at least one of the elements of the set $\{\cos n\phi_i\}$ onto the corresponding $\{s_k(n)\}$, k=1, ...4 to decrease in magnitude. The magnitude of this projection is the quantity q_k in (5-2), and a decrease in its value leads to a diminished effective SNR for the joint estimation problem. This results in the observed increase in $\mathrm{Var}[\hat{\phi}_1]$ and $\mathrm{Var}[\hat{\phi}_2]$ as observed in Figs. 5-5 and 5-6 for ϕ_1 fixed at 5.7 degrees. If this phenomenon leads to problems in practice, a simple solution would be effected as follows: multiply the complex excitation at the nth element by the factor $e^{jn\phi_s}$, $n=-(N-1)/2, \ldots, (N-1)/2$ where $0 < \phi_s < \pi - \phi_2$. This would have the effect of shifting the entire incident wavenumber spectrum away from the normal by the amount ϕ_s, and would cause the average electrical phase angle of two incident waves to move away from the normal, as desired. The estimates so obtained must then be corrected by the amount $-\phi_s$.

5.5.2 Statistical Determination of the Model Order

In the development of this processor, we have assumed that the number M, of plane waves incident on the array is known. In usual tracking applications, M will be 2; one for the direct signal and one corresponding to the reflected signal. If however, two or more targets of significant strength appear within the radar's scanning volume, the more general (arbitrary M) case must be used; however, this implies a priori knowledge of the value of M, which is not available in practice. In this section, we shall explain the use of the Fisher F-test as a method to determine if the model order M is sufficient.

The F-statistic developed by the great statistician R.A. Fisher, may be defined as follows [4-1]. Let P and Q be two independent random variables with χ^2 distributions, with p and q degrees of freedom (df), respectively. Then the random variable R, defined by

$$R = \frac{P/p}{Q/q} \tag{5-21}$$

has an F-distribution, with p,q degrees of freedom, written F(p,q).

Let us now examine how this statistic may be used to our advantage. Consider the sum $S(\hat{\underline{\phi}})$, defined by

$$S(\hat{\underline{\phi}}) = \sum_n \left(x_c(n) - \sum_m u_m \cos n\hat{\phi}_m - \sum_m v_m \sin n\hat{\phi}_m\right)^2 + \sum_n \left(x_s(n) + \sum_m v_m \cos n\hat{\phi}_m - \sum_m u_m \sin n\hat{\phi}_m\right)^2 \quad (5\text{-}22)$$

The above equation is the residual sum of squares, i.e., it is the sum of squares of the in-phase plus the quadrature noise components $w_c(n)$ and $w_s(n)$, from (5-1). This is true, however, only if the physical circumstances obey the model (5-1), i.e., there is no "lack of fit", and the estimate $\hat{\underline{\phi}}$ is valid. The quantity $S(\hat{\underline{\phi}})$ then has a χ^2 distribution, with 2N-M degrees of freedom. It is shown in Appendix B that the quantity $RSS(\hat{\underline{\phi}})$, given by

$$RSS(\hat{\phi}) = -[L_A(\hat{\underline{\phi}}) - \sum_n x_c^2(n) - \sum_n x_s^2(n)] \quad (5\text{-}23)$$

which is proportional to the exponent in (5-15), is approximately equal to $S(\hat{\underline{\phi}})$ in (5-22). Therefore, $RSS(\hat{\underline{\phi}})$ is also approximately χ^2 distributed for large N.

The object of our test is to determine if there is any lack of fit between the observed data and the assumed model, based on our knowledge of the quantities $RSS(\hat{\underline{\phi}})$ and σ_w^2. If the number of incident waves used in the maximization is too low, there will be a lack of fit. If the number is correct or is too high, there will not be a lack of fit.

It is shown in Appendix E that $S(\hat{\underline{\phi}})$ defined by (5-22)

may be partitioned into two components as follows:

$$S(\hat{\underline{\phi}}) = SSMM(\hat{\underline{\phi}}) + SSN(\hat{\underline{\phi}}) \qquad (5\text{-}24)$$

where SSMM is the sum-of-squares of the differences between the values given by the model, and the values given by the data in the absence of noise. If the model is adequate, SSMM will be equivalent to zero.

The quantity SSN in (5-24) is simply the sum-of-squares due to the noise components only. The expectation of $SSN(\hat{\underline{\phi}})/(2N-M)$ is σ_w^2.

We wish to determine whether or not SSMM/(2N-M) is significant compared to the variance of the noise. By replacing $S(\hat{\underline{\phi}})$ in (5-24) with $RSS(\hat{\underline{\phi}})$ given by (5-23) and rearranging we get a value for SSMM which can be used in the comparison with σ_w^2:

$$SSMM(\hat{\underline{\phi}}) = RSS(\hat{\underline{\phi}}) - SSN(\hat{\underline{\phi}}) \qquad (5\text{-}25)$$

The quantity $SSMM(\hat{\underline{\phi}})$ is assumed to be approximately χ^2 distributed.

The quantity σ_w^2 may be determined to any desired degree of accuracy by measuring the amplifier output powers over as long a period as necessary. This is done during periods when no signals are incident on the array. Let us form the sum S_σ from the measured noise values as follows:

$$S_\sigma = \sum_{i=1}^{L} w_c^2(n,i) + \sum_{i=1}^{L} w_s^2(n,i) \qquad (5\text{-}26)$$

where i is the index in time, and L is the number of time samples, assumed large. The above invokes the temporal ergodicity of the noise process, and the spatial index n is arbitrary, since we assume all amplifier output noise variances equal. The random variable S_σ has a χ^2 distribution with $2L \approx \infty$ degrees of freedom.

Since $SSMM(\hat{\underline{\phi}})$ and S_σ are both χ^2 random variables, we can now substitute (5-26) and (5-25) into (5-21), to obtain

$$R = \frac{(RSS(\hat{\underline{\phi}}) - SSN(\hat{\underline{\phi}}))/(2N-M)}{S_\sigma/2L}$$

$$\approx \frac{RSS(\hat{\underline{\phi}})/(2N-M) - \sigma_w^2}{\sigma_w^2} \qquad (5\text{-}27)$$

where the approximation is valid for large L, which is true in practice. Equation (5-27) is the ratio of the sum-of-squares due to a misfitting model, and the noise variance. Therefore, if the model is correct we would expect the value of R to approach zero as (2N-M) becomes large, since the residuals are caused by the noise contributions $w_c(\cdot)$ and $w_s(\cdot)$. Also, if the ratio R is significantly large, it may be assumed that the residuals are mainly the result, not of the elemental noise contributions, but of a model which does not fit the observed data. The F-distribution determines, for given degrees of freedom and perfectly fitting model, the pdf of the ratio R. Therefore, chance dictates that the

value of the ratio R will exceed the value of the corresponding F-statistic at probability level α, only 100α % of the time.

Since σ_w^2 is known accurately, the denominator of (5-27) may be considered to have infinite degrees of freedom. Therefore, R is distributed as $F(\infty, 2N-M)$. If N=21 and M=2, this statistic has a value 1.51 [4-13] at the 5% level of significance, as shown in Fig. 5-15. The statistic $F(\infty,2N-M)$ is also a χ^2 distribution with 2N-M degrees of freedom.

The use of the test is summarized as follows. We assume a value for M, e.g. 2, and proceed to produce the M-dimensional estimate $\hat{\underline{\phi}}$. Equation (5-27) is then evaluated using this estimate and the known value σ_w^2 established by accurate prior measurement. If the right-hand side of (5-27) is less than 1.51, the model (and hence the choice of M) may be assumed correct. By using the F-statistic 1.51, we will be wrong in saying the model is incorrect 5% of the time. If a 1% level is desired, 1.81 is the number to use. If the test fails, the value of M must be incremented (probably by 2) and the process repeated until the test succeeds. We note that for reasons which will be evident later this test is only valid if the high SNR assumption is invoked.

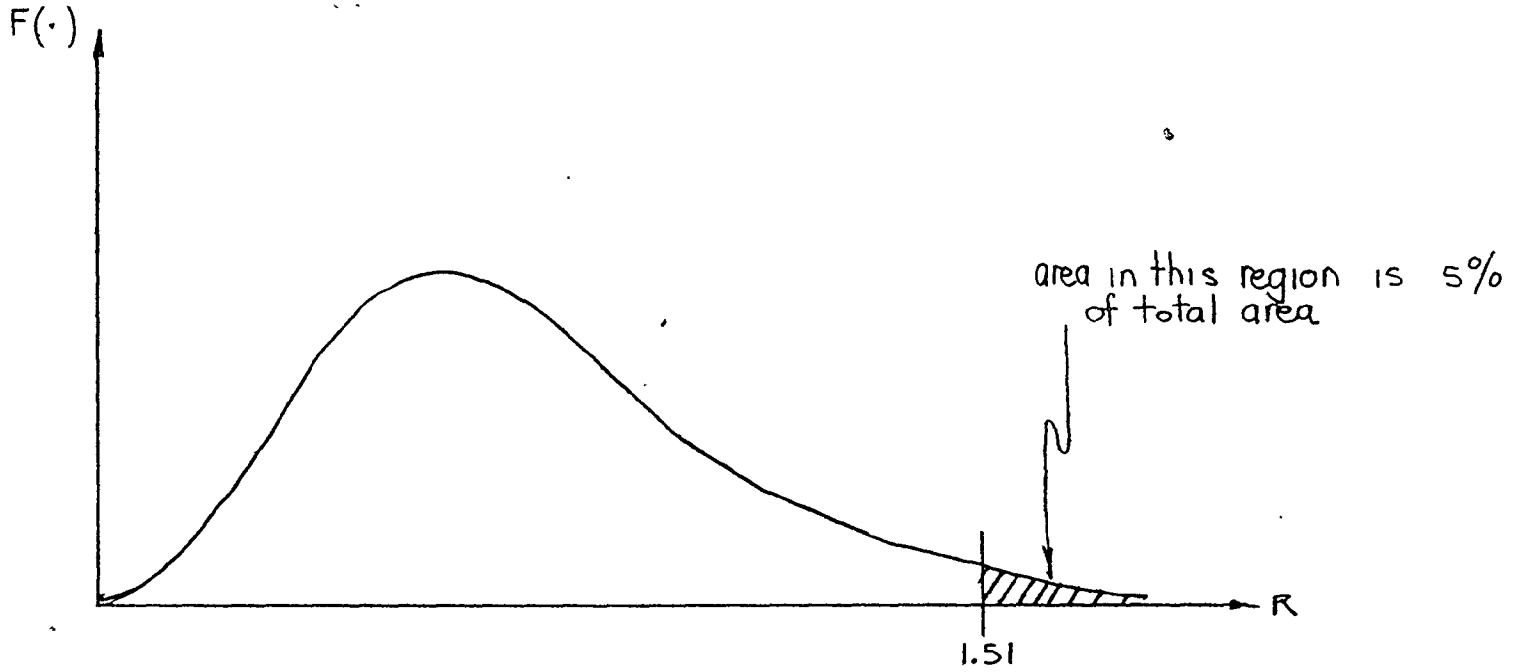

Fig. 5-15 Use of the F-distribution to determine if the model form is appropriate.

Example

The validity of this test was determined using computer simulations. Artificial data were generated assuming three incident waves, 2 of which were 1 BW apart, and the third of which was 1/2 a beamwidth outside the first 2. The true value of M is thus 3. The relative amplitudes were 1.0, 0.9 and 1.0, respectively, whereas the values of ψ were chosen to be 0°, -90°, 0° respectively. Gaussian noise was then added to the data. The data were then analyzed assuming various values of M, and the process repeated many times.

Table 5-2 gives results which show the values of the ratio R from (5-27) as a consequence of analyzing the data for M = 2,3,4 respectively for various values of SNR. Here, we see that for SNR $\geq$ 25 dB, the value of R exceeds 1.51 in the vast majority of trials when the value of M used in the analysis is less than the true value. When the SNR falls below 25 dB, the results are not as conclusive. This is because the error power due to the misfitting model must be larger in this case in order to say with confidence that a lack of fit actually exists. Note that when the value of M used in the analysis equals or exceeds its true value, the values of R drop considerably.

True value of M - 3

No. of trials in each case - 100

DATA VALUES

Component	Frequency	Phase	Amplitude
1.	1.87	0.0	1.0
2.	1.57079	-1.57079	0.9
3.	2.0196	0.0	1.0

SNR (dB)	No. of Trials R > 1.51	No. of Trials R > 1.0	Value of M used
30	100	100	2
30	0	0	3
30	0	0	4
25	94	100	2
25	0	0	3
25	0	0	4
22	24	64	2
22	0	0	3
22	0	0	4

Table 5-2 Values of the R ratio (5-27) as determined by computer simulation.

In practical situations, it may be advantageous to use a lower value of F-statistic, closer to unity, as the threshold value. This is because the residuals will not always be exactly Gaussian variates, and because the 95% confidence level indicated could be much too high for practical considerations.

The test as it is described applies only to the case where the incident signal configuration obeys the model equation (5-1) closely. Therefore, the test is also not valid, in a strict sense, in the presence of diffuse multipath.

5.5.3 Time-dependence removal

Time-dependence removal in this case may be accomplished in exactly the same manner as for the symmetric processor in Chapter 4. The derivations are identical, but for the sake of completeness, the multi-snapshot version of the asymmetric processor will be developed here. The basic concept of this development is taken from Box and Draper [5-4]. Because of the fact that the individual observations may be assumed independent (in both space and time), the method given here is simpler than that given in the reference.

We assume, as in the previous case, that K snapshots describing the same environment are available from each sensor, and that the observations are independent.

The likelihood function $p(\underline{X}|\underline{\phi})$ (where $\underline{X}$ is again the

space-time matrix of observed data) of $\underline{\phi}$ given K independent snapshots of observed data may be formed. Since, because of the uniform prior, the likelihood function is proportional to the a posteriori pdf, we may write from (5-15)

$$p(\underline{X}|\underline{\phi}) = K_5 K_6 \prod_{i=1}^{K} \exp\left[\frac{1}{2\sigma_w^2}\left[L_{Ai}(\underline{\phi}) - \sum_n x_c^2(n,i) - \sum_n x_s^2(n,i)\right]\right] \tag{5-28}$$

$$= K_7 \exp\left[\frac{1}{2\sigma_w^2}\sum_{i=1}^{K}\left[L_{Ai}(\underline{\phi}) - \sum_n x_c^2(n,i) - \sum_n x_s^2(n,i)\right]\right] \tag{5-29}$$

where K_6 is the constant of proportionality between the a posteriori pdf and the likelihood function, and the $L_{Ai}(\underline{\phi})$ are the $L_A(\underline{\phi})$'s from (5-16) corresponding to the ith snapshot. From the above, it is obvious that the ML estimate $\hat{\underline{\phi}}$ of $\underline{\phi}$, given data from multiple snapshots, is obtained by

$$\hat{\underline{\phi}} = \max_{\underline{\phi}}\left[\sum_{i=1}^{K} L_{Ai}(\underline{\phi})\right] \tag{5-30}$$

The above has the same form as (5-16) except that the joint estimate $\hat{\underline{\phi}}$ in this case is obtained by maximizing the sum of the individual objective functions obtained from each snapshot.

Therefore, in the practical situation where many snapshots describing essentially the same radar environment are available, the estimator (5-30) should be used in place of (5-17), in order to utilize, in an optimal fashion, all

the observed data. It has been noted, as a result of computer simulation, that this time-dependence removal technique behaves similarly to that developed for the symmetric case, as shown in Fig. 4-15. That is, the variance of the estimator (5-30) improves linearly with the number of snapshots included in the sum.

5.5.4 Joint Confidence Region on the Estimates

Since we are concerned in this chapter with a multi-dimensional estimation problem, the joint confidence region corresponding to the estimate $\underline{\hat{\phi}}$ will form an M dimensional volume in space, rather than the linear confidence interval encountered in Chapter 4. In the high SNR case, the confidence regions will be ellipsoidal in shape.

It is shown in Appendix C that

$$RSS(\underline{\phi}^*) - RSS(\underline{\hat{\phi}}) \approx (\underline{\hat{\phi}}-\underline{\phi}^*)^T \underline{V}^{-1} (\underline{\hat{\phi}}-\underline{\phi}^*) \qquad (5\text{-}31)$$

where $\underline{\phi}^*$ is some arbitrary point close enough to $\hat{\phi}$ so that (4-47) is valid (i.e. linear model), and $\underline{V}$ is the variance-covariance matrix of the estimates $\phi_1, \ldots, \phi_M$. The quantity $RSS(\underline{\phi})$ is the sum of squares of the residuals about the point $\underline{\phi}$, defined for the case $\underline{\phi} = \underline{\hat{\phi}}$ by (5-23). This quantity is also enunciated in Appendix C. Note that $RSS(\underline{\phi})$ is always positive, and that $RSS(\underline{\hat{\phi}})$ has the smallest

absolute value for all possible values of $\underline{\phi}$. All values of $\underline{\phi}^*$ which satisfy RSS($\underline{\phi}^*$) = constant = K are given by

$$(\hat{\underline{\phi}} - \underline{\phi}^*)^T \underline{V}^{-1} (\hat{\underline{\phi}} - \underline{\phi}^*) = K - RSS(\hat{\underline{\phi}}) \qquad (5\text{-}32)$$

The above represents the equation of a closed ellipsoidal contour surrounding the point $\hat{\underline{\phi}}$. When $K_1 > K_2$ the contour RSS($\underline{\phi}^*$) = K_1 completely encloses the contour RSS($\underline{\phi}^*$) = K_2, and $\hat{\underline{\phi}}$ lies in the centre of these nested M-dimensional "eggs". A 100(1-α) % confidence region for the true (but unknown) value of $\underline{\phi}$ is enclosed by the contour which is such that

$$\frac{[RSS(\underline{\phi}^*) - RSS(\hat{\underline{\phi}})]/M}{RSS(\hat{\underline{\phi}})/(2N-M)} = F(M, 2N-M, \alpha) \qquad (5\text{-}33)$$

In which the expression on the right-hand side is the constant value that defines the contour.

The denominator of (5-33) is the mean-square residual, and it is an estimate of the noise variance of the receiver amplifiers. The F-distribution at probability level α tells us by what factor the mean-square represented by the numerator must be greater than the denominator so that the ratio is exceeded by chance alone only 100α% of the time. Therefore, the set of points $\underline{\phi}^*$ satisfying (5-33) determine the region which the estimate $\hat{\underline{\phi}}$ will fall 100(1-α)

% of the time; i.e., it defines the joint confidence region of the estimate $\hat{\underline{\phi}}$.

By substituting (5-31) into (5-33) and rearranging, we get

$$(\hat{\underline{\phi}}-\underline{\phi}^*)^T \underline{V}^{-1} (\hat{\underline{\phi}}-\underline{\phi}^*) = \frac{RSS(\hat{\underline{\phi}})\ M}{2N-M} F(M, 2N-M, \alpha) \qquad (5-34)$$

Another form defining the joint confidence region is obtained directly by rearranging (5-33):

$$RSS\ (\phi^*) = RSS(\hat{\phi})\ [\ 1 + \frac{M}{2N-M} F(M, 2N-M, \alpha)\ ] \qquad (5-35)$$

The set of all $\underline{\phi}^*$ which satisfies (5-35) also defines the boundary of the $100(1-\alpha)$ % joint confidence region.

As we have emphasized in this discussion, the expressions that have been developed only hold when the model form may be assumed linear, which is valid at high SNR. At lower SNR's, the form (5-34) is an elliptical approximation, at an approximate confidence level, of the true $100(1-\alpha)$ % joint confidence region. The form (5-35) at lower SNR's describes a confidence region of the correct shape, but only at an approximate probability level α. This is because the residuals are no longer Gaussian-distributed when the model is nonlinear; hence, the F-distribution cannot be used to ascertain the level of confidence exactly.

Example A simulation run was conducted for the following parameter values: N=21, ϕ_1 = 1.6456 radians, ϕ_2 = 1.496 radians ($\phi_{ave} = \pi/2$), ρ = 0.9, BW = 0.5, and $\Psi = 0^\circ$. The artificial data were generated according to the model excitations, and then independent Gaussian noise samples scaled for an SNR of 30 dB were added to the calculated data. The optimization routines then evaluated $\hat{\phi}_1$ and $\hat{\phi}_2$. By the method discussed at the end of Appendix C, the covariance matrix of the parameter estimates $\hat{\phi}_1$ and $\hat{\phi}_2$ was determined by the conjugate gradient optimization algorithm to be

$$\underline{V}^{\hat{}} = \begin{bmatrix} 1.5352 & 1.2992 \\ 1.2992 & 1.17474 \end{bmatrix} \times 10^{-4} \qquad (5\text{-}36)$$

Therefore, the inverse of the covariance matrix is

$$\underline{V}^{-1} = \begin{bmatrix} 1.01576 & -1.12334 \\ -1.12334 & 1.327444 \end{bmatrix} \times 10^{5} \qquad (5\text{-}37)$$

where the entries in both matrices have units $(\text{radians})^2$ and $(\text{radians})^{-2}$ respectively. The estimates $\underline{\hat{\phi}}$ obtained for this particular run were

$$\underline{\hat{\phi}} = \begin{bmatrix} 1.646 \\ 1.494 \end{bmatrix} \text{ radians} \qquad (5\text{-}38)$$

and the value RSS($\underline{\hat{\phi}}$) was 44.036. At this value of SNR, the

model behaves linearly, so (4-47) is valid. Substituting these values into (5-34), where F(2, 40, .05) = 3.23, the 95% joint confidence region of ϕ_1 and ϕ_2 satisfies

$$[\phi_1-1.646 \quad \phi_2-1.494] \begin{bmatrix} 1.01576 & -1.12334 \\ -1.12334 & 1.327444 \end{bmatrix} x10^5 \begin{bmatrix} \phi_1-1.646 \\ \phi_2-1.494 \end{bmatrix}$$

$$= \frac{44.036 \text{ x } 2 \text{ x } 3.23}{40}$$

$$= 7.112 \qquad (5\text{-}39)$$

The ellipse is drawn out in Fig. 5-16. Notice the elongated shape of the confidence region, indicating high correlation between the two variables. The coefficient of correlation ρ, is easily determined from the standard formula to be 0.967. This high correlation coefficient stems from the fact that the two incident signals are themselves highly spatially correlated, because the angle $\Psi=0^\circ$.

To compare with the situation when $\Psi=90^\circ$, i.e., when the two incident signals are spatially uncorrelated, the confidence region resulting from another separate computer simulation, corresponding to $\Psi=90^\circ$, is also drawn in Fig. 5-16. All parameter values, except Ψ, are identical. In this case, $\underline{V}$ was determined as

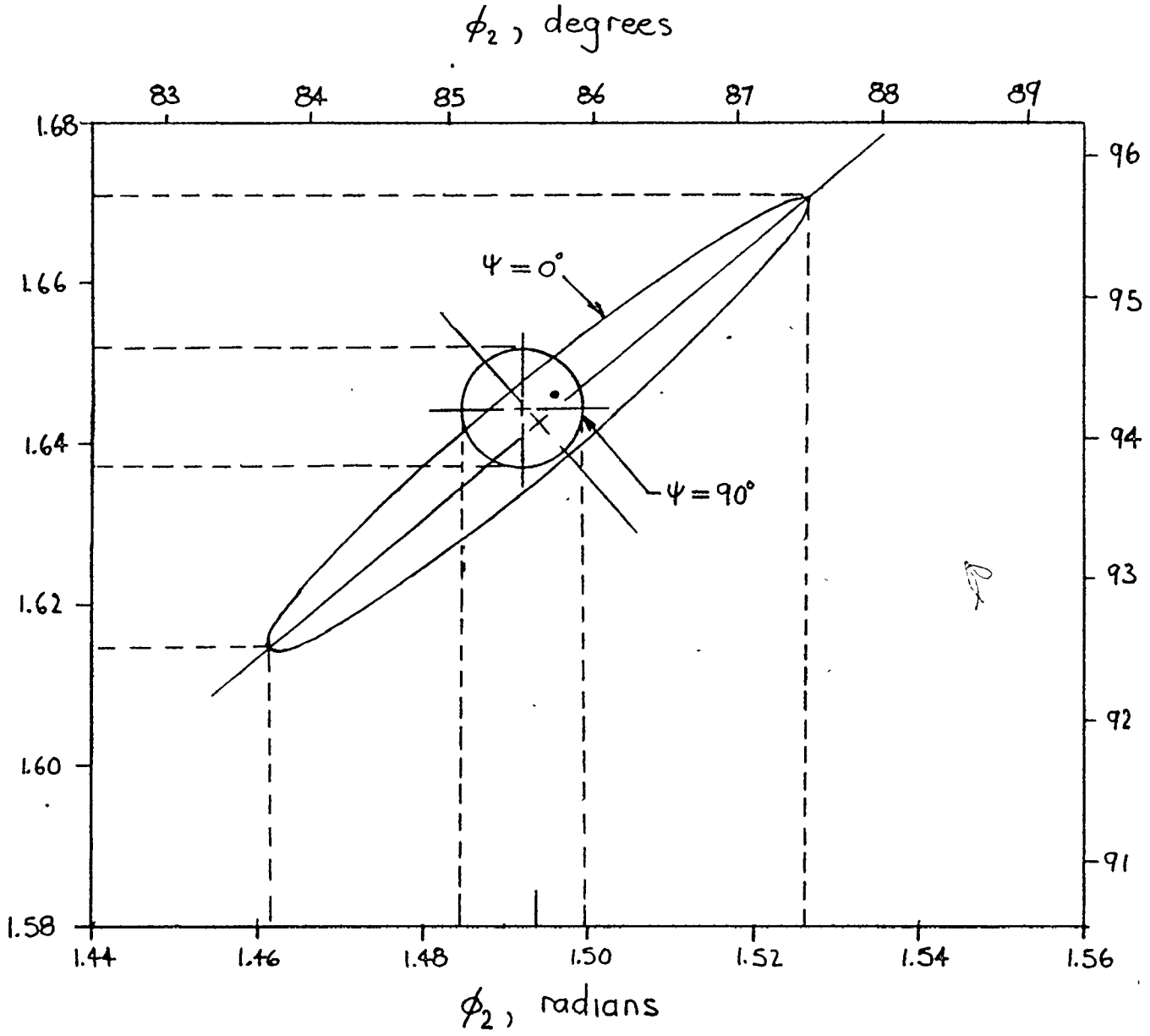

Fig. 5-16 95% confidence region for angle estimates

$$\underline{V} = \begin{bmatrix} 7.62179 & 8.56722\text{x}10^{-2} \\ 8.56722\text{x}10^{-2} & 8.93602 \end{bmatrix} \text{x}10^{-6} \qquad (5\text{-}40)$$

and the inverse $\underline{V}^{-1}$ is then

$$V^{-1} = \begin{bmatrix} 1.3212\text{x}10^{5} & -1.258\text{x}10^{3} \\ -1.258\text{x}10^{3} & 1.119\text{x}10^{5} \end{bmatrix} \qquad (5\text{-}41)$$

The estimates obtained by computer simulation were

$$\hat{\phi} = \begin{bmatrix} 1.644 \\ 1.492 \end{bmatrix} \text{ radians .} \qquad (5\text{-}42)$$

The value of RSS($\underline{\phi}$) was 42.831. The equation determining the 95% joint confidence region in this case is then

$$[\phi_1\text{-}1.644 \quad \phi_2\text{-}1.492] \begin{bmatrix} 1.312\text{x}10^{5} & -1.258\text{x}10^{3} \\ -1.2.58\text{x}10^{3} & 1.119\text{x}10^{5} \end{bmatrix} \begin{bmatrix} \phi_1\text{-}1.644 \\ \phi_2\text{-}1.492 \end{bmatrix}$$

$$= \frac{42.831 \text{ x } 2 \text{ x } 3.23}{40}$$

$$= 6.917 \qquad (5\text{-}43)$$

which is shown drawn in Fig. 5-16. Here, we note that since the estimates ϕ_1 and ϕ_2 are virtually uncorrelated, the joint confidence region is almost circular. Also, the individual confidence intervals on each parameter (as shown by the dotted lines) are much smaller for this example than for the case when $\Psi=0^{o}$. Thus, we see that the individual confidence intervals, and hence the variances, of the parameters decrease considerably when the respective para-

meters are uncorrelated. This behaviour is well illustrated in Fig. 5-4 where the variances for the curve corresponding to $\Psi=90^{\circ}$ are considerably lower than those for the other values of Ψ.

5.5.5 Comparison to Other Researchers

In a recent paper by Tufts and Kumaresan [3-40] three separate methods for estimating the frequency of sinusoids in noise were proposed. The first is a method quite similar to that described in this chapter. The second method is an improvement on the Pisarenko technique, while the third is the complex form of the LS algorithm proposed by Marple [3-13], as opposed to the form given in this thesis [Chapter 3].

In their first method, the estimates of the M frequencies are obtained by maximizing the quantity Q_2 with respect to f_i, i=1, M, where

$$Q_2 = || \underline{x}^H \underline{S} \underline{C}^H || \qquad (5-44)$$

where H denotes the Hermitian transpose, and $||\cdot||$ denotes the norm. The vector $\underline{x}$ is the complex-valued set of observations, and

$$S = [\underline{s}_1, \underline{s}_2, \ldots, \underline{s}_n] \qquad (5-45)$$

where

$$s_i^T = [\ 1\ e^{j2\pi f_i}\ e^{j2\pi f_i}\ \ldots\ e^{(N-1)j2\pi f_i}\ ] \qquad (5\text{-}46)$$

and the matrix $\underline{C}$ is the lower triangular matrix resulting from the Gram-Schmidt decomposition of the matrix $[S^H S]^{-1}$.

Note that the quantities $\underline{x}^H \underline{S}$ are the discrete-Fourier transform (DFT) values of the observed data at the particular frequency estimates. Thus, the function Q_2 to be maximized is the squared magnitude of a linear combination of the DFT values of the observed data.

The structure proposed in this chapter is somewhat more efficient in implementation, since it operates with real arithmetic instead of complex. Both methods require a Gram-Schmidt orthogonalization process, and our method requires a 2M dimensional process instead of the M dimensional situation needed by Tuft's method. However, a 2M real evaluation is still about two times faster than an M complex computation. Also, our method effectively involves the maximization of the quantity Q_3, where

$$Q_3 = || \underline{x}_c^T \underline{S}_1 || + || x_s^T S_2 || \qquad (5\text{-}47)$$

where S_1 and S_2 are the matrices of the Gram-Schmidt signal values $s_k(n)$ in (5-5). Again, two multiplications of two real matrices is faster than one multiplication of two complex matrices, but more important, the form in (5-44) involves the multiplication of three matrices, whereas our method involves the multiplication of only two. Thus, our

method is computationally more efficient.

It is, no doubt, possible to extend the treatment of Tuft's to include the special symmetric form, a test for the number of targets, and a multi-snapshot structural form as has been undertaken in this chapter.

The results of these two methods are quite similar. Tuft's results, obtained by computer simulation, attain the C-R bound as they have in our case, for high SNR. However, a threshold also appears in his results, which for N=25 points, N=2, $\Psi=90^{\circ}$, and BW equivalent to 0.5, occurs at 3 dB input SNR. As seen from Fig. 5-12, no threshold effect is evident down to SNR's of 6 dB for our method (for $\Psi=90^{\circ}$, N=21). Therefore, it is likely that the thresholds of the two methods will occur within 1 or 2 dB of each other, which is a small difference.

White, in [4-2] has also proposed a "non-symmetric" bearing estimator structure, as well as the symmetric case discussed earlier. His structure, as proposed, is fixed for M=2, and does not allow any variation in the model with M. As is also pointed out in Chapter 4, White's processor is a complex analog structure which appears difficult to implement. Also, his structure implicitly involves the estimation of the unnecessary amplitude and phase parameters. Since the implementation of the asymmetric processor is not as simple as the symmetric version, the

argument of simplicity cannot be argued as strongly against White's structure in this case. However, the asymmetric processor developed in this chapter is still a more versatile form applicable to a broader class of problems than either the symmetric processor or the processor of White's.

It is of interest to note that the theoretical variances resulting from White's method again are identical to those developed here, after the change in calibration of the ordinate is made. However, the assymetric processor developed here does give advantages either in terms of efficiency or versatility.

5.6 Summary

In this chapter, we have developed a ML estimator for determining the frequency of sinusoids embedded in Gaussian white noise. The estimator is simple in nature because the implicit optimization procedure need only be performed in one parameter for each sinusoid, rather than the three which are usually needed to characterize a sine wave. The performance of this estimator was evaluated theoretically and by computer simulation, and was found to reach the equality of the Cramer-Rao bound, for SNR values above threshold. This structure was found to be a generalization of the symmetric processor discussed in Chapter 4. Methods

of handling multi-snapshot data were discussed, and a simple test was given whereby the most likely number of sinusoids present could be determined.

CHAPTER 6

CONCLUSIONS, RECOMMENDATIONS, AND FURTHER DISCUSSION

In this thesis we have examined the problem of array processing in multipath environments, with emphasis on radar. Several methods of dealing with this situation were presented, and three such techniques which behaved well when applied to this problem were developed and tested.

In Chapter 2, the phenomenon of both types of multipath was discussed. Also, in Appendix A, the details of an experimental system designed to model a specular multipath environment were presented. The implementation of this experimental system included a novel I-Q sampling technique.

In Chapter 3, we discussed various methods applicable to array processing that were derived from time series analysis. Three techniques were considered. They are: (1) the Burg algorithm, (2) the LS algorithm, and (3) the ARMA (Pisarenko) technique. Only the LS algorithm was found to be useful in this application.

The results obtained by the LS algorithm are much better in comparison to the Burg method. The formulation does not depend on a Toeplitz matrix structure, and hence is amenable to the analysis of nonstationary time series. The performance of this spectral estimator used with several

sinusoids in noise as input is subject to a threshold effect. Also, the LS algorithm is capable of providing a complete (wavenumber) spectral estimate, a quality which may be very useful in the analysis of diffuse multipath.

In Chapter 4, a computationally efficient form of maximum-likelihood (ML) direction-finding estimator has been developed. This estimator is valid only in the presence of symmetric specular multipath. Specifically, the ML value of ϕ, given the received data, is that which maximizes the expression $L(\phi)$ given by

$$L(\phi) = \frac{[\Sigma\, x_c(n)\, \cos n\phi]^2}{\Sigma\, \cos^2 n\phi} + \frac{[\Sigma\, x_c(n)\, \sin n\phi]^2}{\Sigma\, \sin^2 n\phi}$$

$$+ \frac{[\Sigma\, x_s(n)\, \cos n\phi]^2}{\Sigma\, \cos^2 n\phi} + \frac{[\Sigma\, x_s(n)\, \sin n\phi]^2}{\Sigma\, \sin^2 n\phi} \qquad (6\text{-}1)$$

Since $L(\phi)$ is a function of only one variable, a Golden Section search may be employed to effect efficiently the required maximization.

The estimator defined by (6-1) is computationally efficient, because all the parameters describing the incident sinusoidal plane waves have been integrated out, except for the one of interest.

It is noted that the estimator performance at high SNR attains the equality of the C-R bound, and the bias of the estimate is negligible. At low SNR's, a bias becomes

evident and the variances depart from the value given by the bound. Because of the nonlinearity of the structure of (6-1), the estimator variances in some cases are better than the value given by the bound.

The method was validated by experimental results. An extension of the method was developed which enables the estimation of the angle from multiple snapshots. A method for determining the confidence interval about a paticular estimate was also presented.

In Chapter 5, another more general type of ML direction-finding estimator was developed, which determines the direction of multiple incident plane waves. These plane waves may arrive from arbitrary directions, provided the average direction angle (in the case of two incident waves) of the two components is sufficiently far removed from the normal of the array. This latter ML method involves an M-dimensional maximization of the quantity $L_A(\underline{\phi})$, $\underline{\phi}$ being an M-dimensional vector, defined by

$$L_A(\underline{\phi}) = \sum_{k=1}^{2M} L_{ck}^2(\underline{\phi}) + L_{sk}^2(\underline{\phi}) \tag{6-2}$$

where

$$L_{ck}(\underline{\phi}) = \sum_n x_c(n)\ s_k(n) \tag{6-3}$$

and

$$L_{sk}(\underline{\phi}) = \sum_n x_s(n)\ s_k(n) \tag{6-4}$$

The quantities $s_k(n)$ are obtained from a Gram-Schmidt orthonormalization process of the signals $\{\cos n\phi_k, \sin n\phi_k\}$, $n = -(N-1)/2, \ldots, (N-1)/2$ and $k = 1, \ldots, 2M$.

Previous works [4-5], [4-2], [4-14], have developed ML estimators of incident direction angle in array processing, but these require estimation and hence maximization with respect to 3M variables. The ML structure discussed here is unique because the estimation is required in only M variables. This ML processor is also applicable to the general problem of finding the frequencies of closely spaced sinusoidals embedded in white Gaussian noise.

It has been shown that the variance of this asymmetric ML estimator reaches the equality of the C-R bound, with negligible bias, at high SNR's. As with the symmetric structure, the variance at low SNR depart from those given by the bound, and a bias becomes evident.

A multi-snapshot version of this ML technique was presented. Also, a method for determining the point confidence region for the estimates was discussed, as was a method for determining statistically the most likely number of incident signals on the array.

It may be pointed out that both these ML structures give valid results when the various incident components are temporally correlated - the worst case situation for most types of processors.

Comparison of Methods

Each one of the three best methods (LS, symmetric, and asymmetric ML) has its individual advantages and disadvantages. First, we consider the LS algorithm. It is relatively complex in that it involves finding a set of coefficients by solving a set of linear equations, and the evaluation of the spectrum corresponding to these coefficients. It has a threshold which occurs at a relatively high SNR. However, it is applicable in a broad class of environments, and yields the complete spatial spectrum. Therefore, it is possible that it is also applicable in situations where the diffuse multipath environment predominates.

Second, consider the symmetric ML technique. This technique is very easy to apply, simple computationally, and gives the best performance of all three methods. However, it is useful only in the specific case of a specular multipath environment with symmetry about the normal of the array.

Thirdly, the asymmetric ML structure is applicable in a wider class of environments than the symmetric case, but is not as general as the LS technique. Computationally, it lies between the LS algorithm and the symmetric ML technique. Performance-wise, it gives better results than the LS method, but somewhat poorer performance is noted in

comparison to the symmetric structure.

The relative performances of the three methods are shown in Fig. 6-1. The left hand end of the curves indicates the onset of the threshold. We note that in all cases shown in the figure, the threshold of the LS algorithm occurs at a much higher SNR than it does for the ML methods. Also, the variances of the LS estimator are uniformly worse than those of the maximum likelihood techniques.

We therefore see that the choice of algorithm to be used in any specific situation is not an obvious decision, and will depend greatly on the details of the particular application.

The presentation in this thesis has emphasized the situation where two waves, which are temporally correlated, are incident on an array from angles which are less than one standard beamwidth. This specific problem is much more difficult than the one which is usually considered in the literature; that is, the two incident waves are temporally uncorrelated and are separated by more than one standard beamwidth. The three techniques which are useful in this application have been developed and tested by computer simulation, and where possible tested by experiment. The theoretical variances attainable from these algorithms have been determined where possible, and have been found to compare well with the results obtained from simulation.

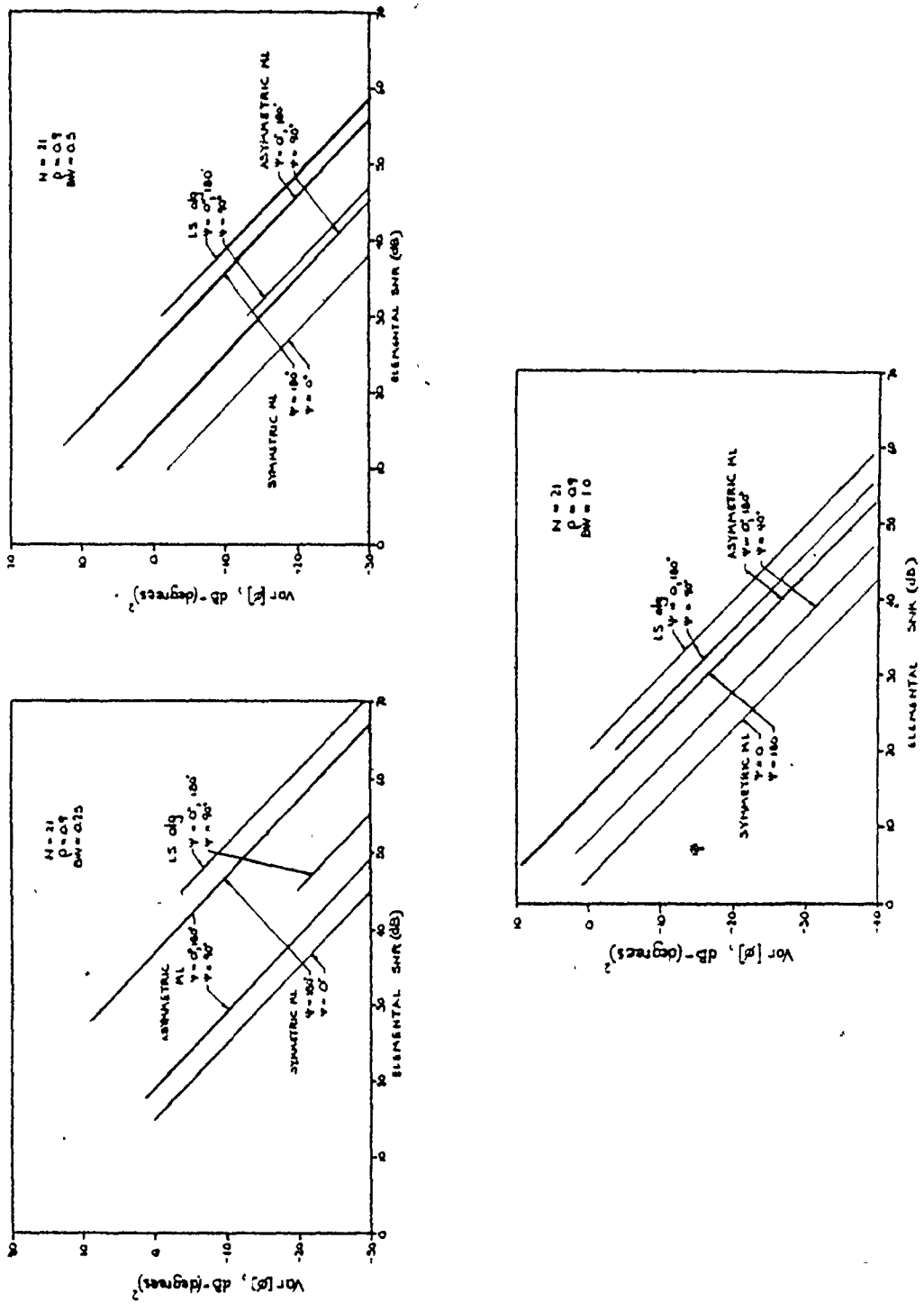

Fig. 6-1 Comparison of performances of the LS algorithm, and the symmetric and asymmetric ML processors.

Suggestions for Further Research

The following is a list of suggestions for work which has not been covered in this thesis, yet will enhance and complement understanding of this subject material:

1. The effect of mutual coupling between the elements of the array on any one of these three estimation techniques has not been evaluated. The effect of mutual coupling is a complicated issue, and it would be interesting to learn what it does to the applicability and performance of these algorithms.

2. This thesis has only seriously considered the specular multipath environment. However, pure specular multipath only occurs in very special applications in practice; hence the diffuse multipath environment must also be given attention. How do the three methods behave in the presence of diffuse multipath? It seems that on a single snapshot basis, the LS algorithm is probably well suited to this problem, because of its general applicability. However, it may well be that if many snapshots are available, the multiple snapshot versions of the two ML techniques would be applicable. This is because the signal caused by the diffuse reflection is incoherent in time, whereas the direct signal from the target is coherent. Hence, the effect of time

averaging the received snapshots over an extended period of time may render the contributions from the diffuse multipath negligible. It would be interesting to determine if this hypothesis has any merit.

3. The theoretical treatment of any processor considered in this thesis has, at least implicitly, assumed uniform spacing between the elements. In the case of the two ML techniques this is not a necessary constraint. In fact, it has been suggested, [6-1] that the performance of the processor could improve if the positioning of the elements was carefully chosen. In fact, a preliminary study on this idea showed considerable promise. The element positions were optimized by evaluating the variances resulting from a given spacing over all values of ψ and over all signal separations of interest. The resulting variances from the optimized spacings were considerably better than those attainable from uniform spacings. This is a suggestion which shows some promise. However, in order to be evaluated properly, this idea requires considerable effort.

4. It would be interesting to see if the multiple snapshot versions of the ML methods could be made adaptive in a more efficient manner. The forms of

these estimators may be implicitly adaptive, but they require more computational effort than what is perhaps necessary.

5. The symmetric ML direction-finder should be implemented using a microprocessor in order to evaluate its actual performance and cost.

6. Computationally, the asymmetric ML processor would behave much better if the derivatives were evaluated analytically instead of numerically. Therefore, it would be desirable to have a closed-form expression for evaluating efficiently the analytic derivatives for this structure.

7. The symmetric and the asymmetric ML structures have been considered completely separate entities. It would be worthwhile considering a scheme applicable to the real-world situation which combines the two methods. The processor would normally operate using the asymmetric structure, but if the system becomes linearly dependent (which is tested easily in the Gram-Schmidt procedure) the processor would switch over to the symmetric version. Presumably, this composite processor would utilize the multiple snapshot versions of the ML algorithms.

Contributions

The following is a list of what the author considers contributions to the state of the art, resulting from the material presented in this thesis.

1. A patent application has been submitted on the novel I-Q sampling procedure discussed in Appendix A.
2. An investigation of the Burg algorithm for computing the maximum-entropy wavenumber spectrum has been conducted, as it applies to array processing. Results have been verified experimentally.
3. A new Pisarenko spectral estimator has been developed in terms of array processing applications.
4. We have developed and investigated the complex least-squares algorithm as it applies in the array processing context.
5. A new efficient maximum-likelihood (ML) structure for estimating target elevations in the presence of specular multipath has been developed and tested. Results have been verified experimentally.
6. A new efficient ML technique applicable to the problem of determining the frequencies of closely spaced sinusoids embedded in white Gaussian noise has been developed and tested.

REFERENCES

[1-1] Bernard D. Steinberg, "Principles of aperture and array system design", Ch. 5, John Wiley and Sons, 1976.

[1-2] E.C. Jordan and K.G. Balmain, "Electromagnetic waves and radiating systems", 2nd Ed., Prentice Hall, 1968.

[1-3] A.V. Oppenheim and R.W. Schafer, "Digital signal processing", Prentice-Hall, 1975.

[1-4] R.N. McDonough, "Application of the maximum-likelihood method and the maximum-entropy method to array processing" in "Nonlinear methods of spectral analysis", Simon Haykin Ed., Springer-Verlag, 1979.

[1-5] H.V. Cottony and A.C. Wilson, "A high resolution rapid-scan antenna", Nat. Bur. Stand. J. Res., 65, 101-110, 1961.

[1-6] H.E. Shanks, "A new technique for electronic scanning", IRE Trans. Antennas and Propag., AP-9, p. 162-166, 1961.

[1-7] S. Haykin, "Performance analysis of a radar signal processing system with continuous electronic array scanning", Inf. Sci. 13, p. 201-227, 1977.

[1-8] D.E.N. Davies, "A fast electronically scanned radar recieving system", Br. Inst. Radio Eng. J., 21, p. 305-318, 1961.

[1-9] J.M. Butler, "Digital, matrix and intermediate frequency scanning, in "Microwave scanning antennas", Vol. 3, Ed. R.C. Fansen, pp. 217-288 Academic press, 1966.

[1-10] M.I. Skolnik, "Introduction to radar systems", McGraw-Hill, 1962.

[1-11] M.I. Skolnik, "Radar handbook", McGraw-Hill, 1970.

[1-12] D.K. Barton Ed., "Radars", Vol. 1, Artech House, 1975.

[1-13] D.K. Barton, "Radar systems analysis", Prentice-Hall, 1964.

[1-14] J. Capon, "Maximum-likelihood spectral estimation", in "Nonlinear methods of spectral analysis", S. Haykin Ed., Springer-Verlag, 1979.

[1-15] J. Capon, "High-resolution frequency wavenumber spectrum analysis", Proc. IEEE, Vol. 57, pp. 1408-1418, Aug. 1969.

[1-16] W.F. Gabriel, "Antenna spatial pattern viewpoint of MEM, MLM, and adaptive array resolution", Proc. RADC Spectrum Estimation Workshop, Oct., 1979.

[1-17] J.E. Evans, "Aperture sampling techniques for precision direction finding", Electro 78, International Electronics Convention Boston, Mass., May 1978.

[2-1] D.K. Barton, "Low-angle radar tracking", Proc. IEEE, Vol. 62, No. 6, June 1974.

[2-2] D.K. Barton, "Multipath fluctuation effects in track-while-scan radar", IEEE Trans. on Aerospace and Electronics Systems, Vol. AES-15, No. 6, Nov. 1979.

[2-3] W.T. Fishback, "Methods for calculating field strength with standard refraction", in Propagation of Short Radio Waves, Vol. 13, M.I.T. Rad. Lab. Ser., D.E. Kerr, Ed., McGraw-Hill, pp. 112-130, 1951.

[2-4] L.V. Blake, "Prediction of radar range", in Radar Handbook, M.I. Skolnik, Ed., Ch. 2, McGraw-Hill, 1970.

[2-5] P. Beckman and A. Spizzichino, "The scattering of EM waves from rough surfaces", Pergamon, 1963.

[2-6] D.K. Barton, Ed., "Radars", Vol. 4, Sect. on Radar Resolution and Multipath Effects, Artech House, 1975.

[2-7] S. Haykin, "Communication Systems", J. Wiley and Sons, 1978.

[2-8] J.P. Reilly and S. Haykin, "Method and apparatus for providing the in-phase and quadrature components of a bandpass signal, U.S. file no. 265-6995-1, Feb. 1980.

[3-1] R.B. Blackman and J.W. Tukey, "The measurement of power spectra", Dover, 1958.

[3-2] D.G. Childers, Ed., "Modern Spectrum Analysis", IEEE press, 1978.

[3-3] P.D. Welch, "The use of the Fast Fourier Transform for the estimation of power spectra: a method based on time averaging over short modified periodograms, IEEE Trans. on Audio and Acoustics, June 1967.

[3-4] G.U. Yule, "On a method of investigating periodicities in distrubed series, with special reference to Wolfer's sunspot numbers", Phil. Trans., A226, 1927.

[3-5] G.E.P. Box and G.M. Jenkins, "Time series analysis: forecasting and control", Holden-Day, 1976.

[3-6] T.J. Ulrych and M. Ooe, "Autoregressive and mixed autoregressive-moving average models and spectra", in "Nonlinear Methods of Spectral Analysis", S. Haykin Ed., Springer-Verlag, 1979.

[3-7] N. Levinson, J. Math. Phys., 25, 261-278, (1947).

[3-8] J. Durbin, Rev. Inst. Int. Statist., 28, (3), 233-243.

[3-9] S. Haykin and S. Kesler, "Prediction-error filtering and maximum-entropy spectral estimation", in "Nonlinear Methods of Spectral Analysis", S. Haykin, Ed., Springer-Verlag, 1979.

[3-10] J. Makhoul, "Linear prediction: a tutorial review, Proc. IEEE, Vol. 63, pp. 561-580, April 1975. Correction in Proc. IEEE, Vol. 64, p. 285, Feb. 1976.

[3-11] S. Haykin and J.P. Reilly, "Mixed autoregressive - moving average modeling of the response of a linear array antenna to incident plane waves", Proc. IEEE Vol. 68, No. 5, pp. 622-623, May 1980.

[3-12] S.L. Marple, "Conventional Fourier autoregressive and special ARMA methods of spectrum analysis", Eng. degree Thesis, Stanford University, Dec. 1976.

[3-13] S.L. Marple, "High resolution autoregressive spectrum analysis using noise power cancellation", Int. Conf. on Acoustics, Speech and Signal Processing, 1978.

[3-14] V.F. Pisarenko, "The retrieval of harmonics from a covariance function", Geophys. J. R. Astr. Soc. 33, pp. 347-366, 1973.

[3-15] T.J. Ulrych and R.W. Clayton, "Time series modelling and maximum entropy", J. Phys. of the earth and planetary interiors, 12, pp. 188-200, 1976.

[3-16] O.L. Frost, "Power spectrum estimation", NATO Advanced Study Institute on Signal Processing, Sept. 1976.

[3-17] J.P. Burg, "Maximum entropy spectral analysis", Proc. 37th Meeting of the Soc. Exploration Geophysicists, 1967.

[3-18] J.P. Burg, "Maximum entropy spectral analysis", Ph.D. Dissertation, Stanford University, Stanford, CA, 1975.

[3-19] J.E. Evans, "Comments on 'Angular spectra in radar applications'", IEEE Trans. on Aerospace and Electronics Systems, AES-15, No. 6, Nov. 1979.

[3-20] J.P. Reilly and S. Haykin, "An experimental study of the MEM applied to array processing in the presence of multipath", Proc. ICASSP80, April, 1980.

[3-21] J.P. Reilly and S. Haykin, "Direction finding in array processing using MEM spectral estimators", Communications Research Lab Report No. CRL-85, McMaster University, Hamilton, Canada, Feb. 1981.

[3-22] R.N. McDonough, "Maximum-entropy spatial processing of array data", Geophys. Vol. 39, pp. 843-851, Dec. 1974.

[3-23] D.P. Skinner, S.M. Hedlicka, A.D. Mathews, "Maximum Entropy Array Processing", J. Acoust. Soc. Am., 66(2) Aug, 1979.

[3-24] J.G. Ables, "Maximum entropy spectral analysis", Astron. Astrophys. Suppl. Series, Vol. 15, pp. 383-393, Proc. Symp. on the Collection and Analysis of Astrophysical Data, Nov. 1972.

[3-25] A van den Bos, "Alternate interpretation of maximum entropy spectral analysis", IEEE Trans. Inform. Theory, Vol. IT-17, pp. 493-494, July 1971.

[3-26] S. Kesler and S. Haykin, "The complex form of the maximum entropy method for spectral estimation", Proc. IEEE, Vol. 64, No. 5, pp. 822-823, May 1976.

[3-27] H. Akaike, "Fitting autoregressive models for prediction", Ann. Inst. Statist. Math., Vol. 21, pp. 243-247, 1969.

[3-28] H. Akaike, "Statistical predictor identification", Ann. Inst. Statist. Math., Vol. 22, pp. 203-217, 1970.

[3-29] A.H. Nuttal, "Multivariate linear predictive spectral analysis employing weighted forward and backward averaging: a generalization of Burg's algorithm", N.U.S.C., New London CT, report no. TR-5501, Oct. 1976.

[3-30] M. Morf, A Vieira, D.T.L. Lee, T. Kailaith, "Recursive multichannel maximum entropy spectral estimation", IEEE Trans. on Geoscience Elect., Vol. GE-16, No. 2, Apr. 1978.

[3-31] O.N. Strand, "Multichannel complex maximum entropy (autoregressive) spectral analysis", IEEE Trans. on Automatic Control, Vol. AC-22, No. 4, Aug. 1977.

[3-32] R.H. Jones, "Multivariate autoregression estimation using residuals", Applied Time Series Anal. Symp., Tulsa, OK, May 1976.

[3-33] L. Marple, "A new autoregressive spectrum analysis algorithm", presented at the 12th Annual Asilomar Conference on Circuits and Systems, Asilomar CA, Nov. 1978.

[3-34] W.D. White, "Angular spectra in radar applications", IEEE Trans. Aerospace and Elect. Sys., AES 15, No. 6, Nov. 1979.

[3-35] W.F. Gabrial, "Spectral analysis and adaptive array superresolution techniques", Proc. IEEE, pp. 654-666, June 1980.

[3-36] L.J. Griffiths, "Rapid Measurement of digital instantaneous frequency", IEEE Trans. Acoust. Speach and Signal Processing, Vol. ASSP-23, No. 2, April, 1975.

[3-37] P.F. Fougere, "A solution to the problem of spontaneous line splitting in maximum entropy power spectrum analysis, J. Geophys. Res., Vol. 82, No. 7, pp. 1051-1054, Mar. 1977.

[3-38] R.W. Herring, "A comparison of the Burg and the known-autocorrelation autoregressive spectral analysis of complex sinusoidal signals in additive white noise", Proc. RADC Spectrum Estimation Workshop, Rome, N.Y., Oct. 1979.

[3-39] S.W. Lang, "Performance of maximum entropy spectral estimators, Master's Thesis, M.I.T., May 1979.

[3-40] D.W. Tufts and R. Kumaresan, "Improved spectral resolution II", Proc. ICASSP80, Denver, CO, 1980.

[4-1] Y. Bard, "Nonlinear parameter estimation", Academic Press, 1974.

[4-2] W.D. White, "Low angle radar tracking in the presence of multipath", IEEE Trans. on Aerospace and Elect. Sys., Vol. AES-10, No. 6, pp. 835-852, Nov. 1974.

[4-3] H.L. van Trees, "Detection, estimation and modulation theory", Part 1, J. Wiley and Sons, 1968.

[4-4] S. Haykin, J.P. Reilly and D.P. Taylor, "New realization of maximum-likelihood receiver for low-angle tracking radar", Electronics Letters, Vol. 16, No. 8, pp. 288-289, 10th April, 1980.

[4-5] G.E. Pollon, G.W. Lank, "Angular tracking of two closely spaced radar targets", IEEE Trans. on Aerospace and Elect. Sys., Vol. AES-4, No. 4, pp. 541-550, July 1968.

[4-6] P.Z. Peebles, "Multipath angle error reduction using multiple target methods", IEEE Trans. on Aerospace and Electr. Sys., Vol. AES-7, No. 6, pp. 1123-1130, Nov. 1971.

[4-7] R. deBuda, Private Communication, May 1980.

[4-8] S.A. Schelkunoff and H.T. Friis, "Antennas, theory and practice", John Wiley and Sons, 1952.

[4-9] D.L. Schilling and C. Belove, "Electronic circuits: discrete and integrated", McGraw-Hill, 1968.

[4-10] J.W. Bandler, "Computer-aided circuit optimization", in "Modern filter theory and design", G.C. Temes and S.K. Mitra Ed., Wiley, 1973.

[4-11] N. Draper and H. Smith, "Applied regression analysis", J. Wiley and Sons, 1966.

[4-12] J.F. MacGregor, Private Communication, Feb. 1979.

[4-13] N.M. Downie and R.W. Heath, "Basic statistical methods", Harper and Row, 1970.

[4-14] G.V. Trunk, B.H. Cantrell, and W.B. Gordon, "Bounds on elevation error estimates of a tartet in multipath", IEEE Trans. on Aerospace and Elect. Sys., Vol. AES-15, No. 6, pp. 883-887, Nov. 1979.

[5-1] J.M. Wozencraft and I.M. Jacobs, "Principles of communication engineering", J. Wiley and Sons, 1965.

[5-2] R. Fletcher and M.J.D. Powell, "A rapidly convergent descent method for minimization", Comput. J. 6, p. 163-168, 1963.

[5-3] J.W. Bandler and N. Sinha, "FLOPT V - A program for minimax optimization using the accelerated least-pth algorithm", S.O.C. Report, Faculty of Engineering, McMaster University, Hamilton, Canada, Feb. 1980.

[5-4] G.E.P. Box and N.R. Draper, "The Bayesian estimation of common parameters from several responses", Biometrica, 52, 3 and 4, pp. 355-365, 1965.

[6-1] P.M. Reilly, Private Communication, Oct. 1979.

[B-1] A. Papoulis, "Probability, random variables, and stochastic processes", McGraw-Hill, 1965.

APPENDIX A

DESIGN DETAILS OF EXPERIMENTAL MULTIPATH SIMULATION SYSTEM

A.1 Experimental System

An experimental system was built to test the various array processing algorithms which have been discussed in Chapters 3 - 5. This system was designed to model the specular multipath environment as discussed in Chapter 2, inside a microwave anechoic chamber. A complete description of the system details pertaining to this experimental setup will now be given.

This section will be divided into four sub-sections. The first three will give a fairly detailed overall view of the experimental system as depicted in Fig. A-1. A description of a novel in-phase-quadrature (I-Q) demodulation method which was used in these experiments will also be presented. The fourth section will give comments pertaining to some relevant system features and to effects contributing to the degradation of the system performance.

A.2 R.F. System Configuration

As may be seen in Fig. A-1, two active transmitters are placed inside an anechoic chamber for the purpose of modelling the direct and reflected signal components

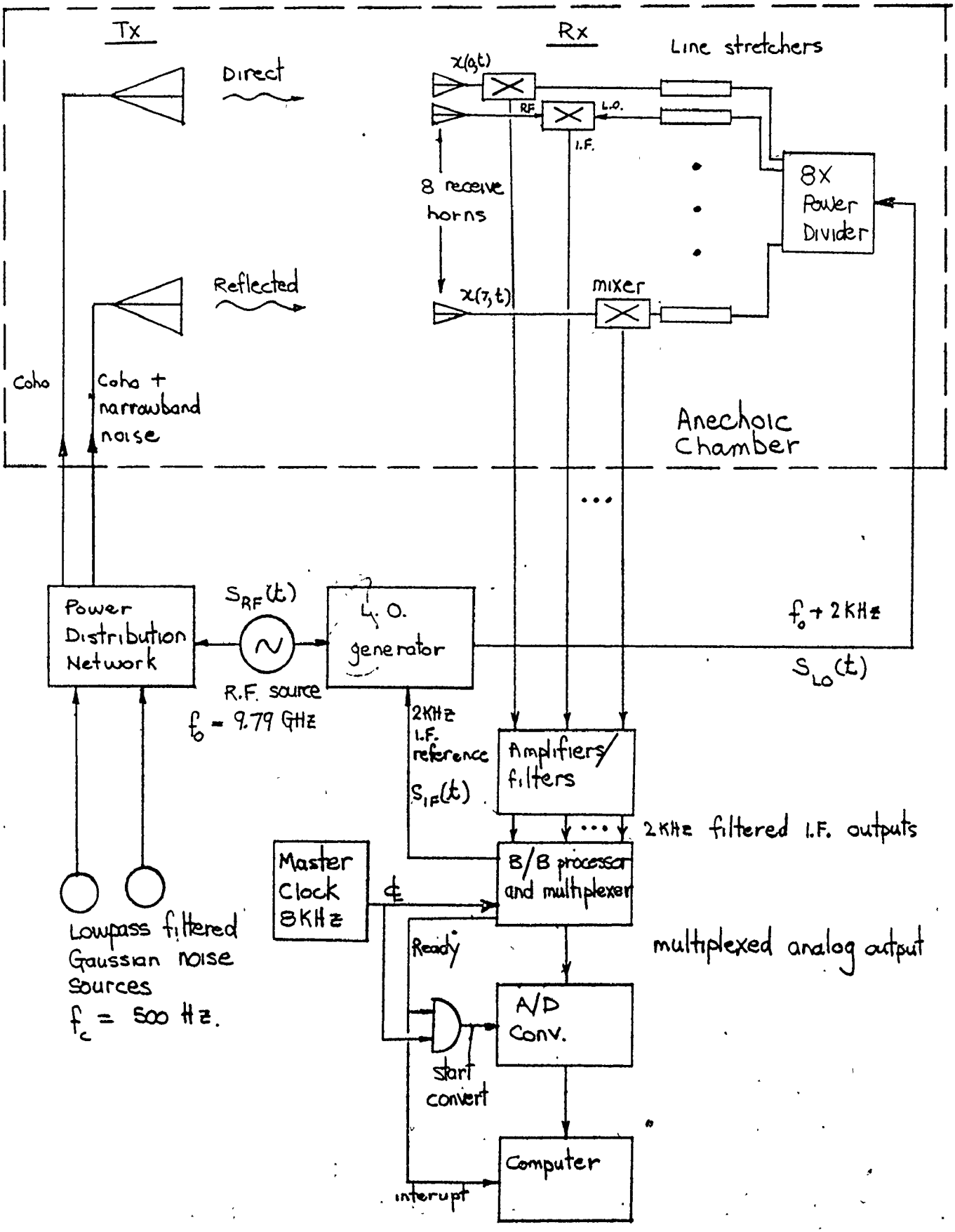

Fig. A-1 Overal configuration of experimental setup

corresponding to the specular multipath environment. The modelling of the diffuse multipath situation is much more complex than that corresponding to the purely specular case, and consequently, was not attempted during the course of this project. However, at time of writing, a program was underway which would also allow the system to include the simulation of diffuse multipath environments. A holographic reconstruction technique is used in this program to create the effect of the diffuse multipath environment on the field configuration at the face of the receiver array.

The "direct" antenna transmits a signal derived directly from the radio frequency (R.F.) source, at frequency 9.79 GHZ. The signal transmitted by this antenna is a pure continuous wave (CW) signal, and is called "Coho", because the received I.F. signal due only to this transmitted component is coherent in nature. The "reflected" antenna transmits a signal which is composed of a pure CW signal, a pure narrow-band noise signal, or any combination of these two components. The inclusion of the narrow-band noise is intended to allow for the simulation of the effects of minor variations and ripples in the smooth reflecting surface, factors which would at least partially remove the coherence of the reflected signal component. The feeds of these antennas are provided by the "Power distribution network", as shown in the figure. This network

as we shall see, is designed so that the relative phases and amplitudes of the direct and reflected signal components may be varied. More details pertaining to this network will be given later.

For reasons which will be discussed later, it was desired that the signal received at the nth element of the array, x(n,t), be mixed to an intermediate frequency (I.F.) of 2KHZ, rather than being mixed coherently to baseband. Because of the fact that the signal produced by the R.F. source, $s_{RF}(t)$ jitters with a bandwidth of about 30KHZ, it is necessary to construct another signal $s_{LO}(t)$ which is 2KHZ removed from $s_{RF}(t)$ but follows the jitter in $s_{RF}(t)$ exactly. When $s_{LO}(t)$ is used to mix the signal x(n,t) to I.F., a signal $x_{IF}(n,t)$ is produced, which to a first-order approximation, has the same complex envelope as x(n,t). The approximation is valid provided that the time difference t_D is small compared to the inverse bandwidth of the R.F. jitter. The quantity t_D is the time difference between the signal path which originates at the R.F. source and terminates at the receiver port of one of the mixers, and the signal path which also originates at the R.F. source but terminates at the L.O. port of the same mixer. In the setup described here, this time difference condition is easily met.

The L.O. generator, which produces $s_{LO}(t)$, is a

single-sideband (SSB) generator, where the "phase discrimination" method of SSB generation is used [2-7]. The alternative "frequency discrimination" technique cannot be utilized in this situation because the two modulation products out of the single mixer would only be 4 KHZ apart. Since the input spectrum of $s_{RF}(t)$ is about 30 KHZ wide, there would be too much overlap between the two spectral components at the output of the mixer, and the isolation of one of these components would be impossible by means of filtering. More details of the construction of the Power distribution network and the L.O. generator will now be given.

A diagram of the Power distribution network is shown in Fig. A-2. As may be seen from part (a), the network consists of a series of "Magic T" hybrid junctions, which are used as power dividers. Variable attenuators and a variable phase shifter are included in the network in order to adjust the relative levels and phases of the two antenna feeds. Narrow-band R.F. noise, which can be transmitted by the reflected antenna, is generated by the Narrow-band noise generator (part (b)), and added to the CW signal component by junction A. The relative levels of the noise and CW signal components may be controlled by the variable attenuator B, and the TWT amplifier.

Narrow-band Gaussian noise n(t) at centre frequency

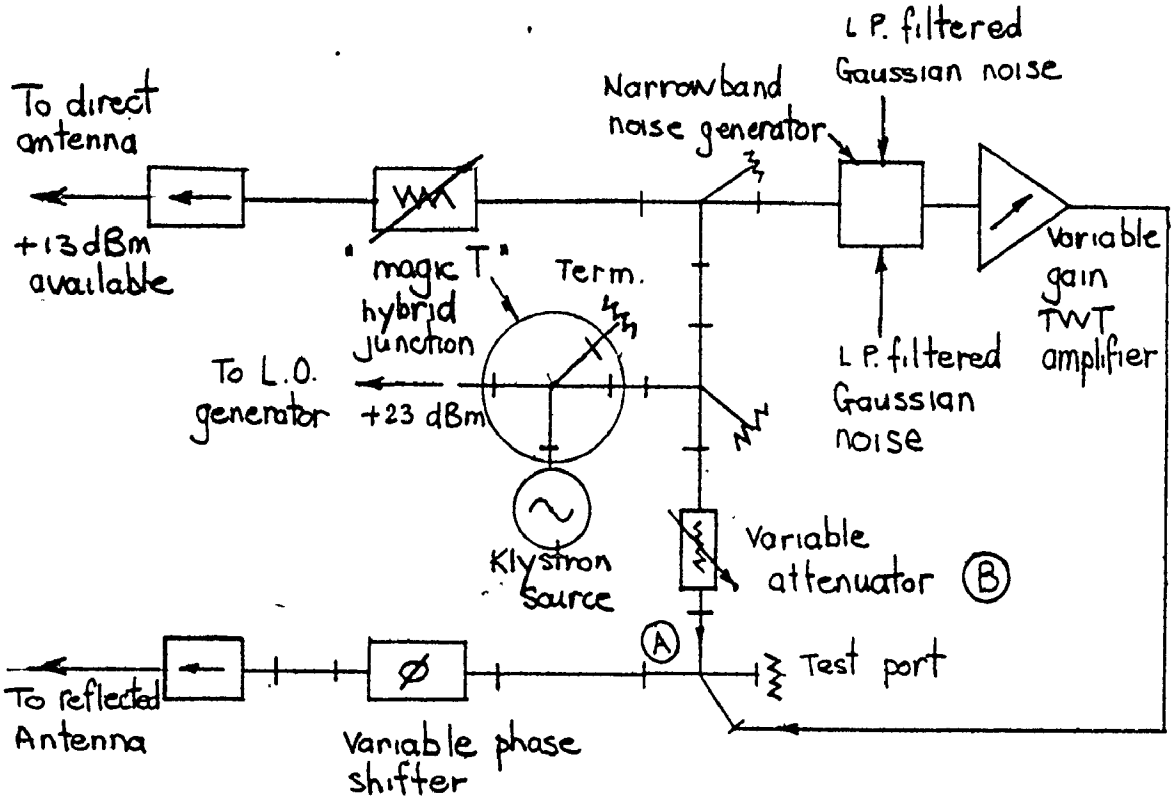

* All connections are 1"X 0.5" X-band waveguide

(a)

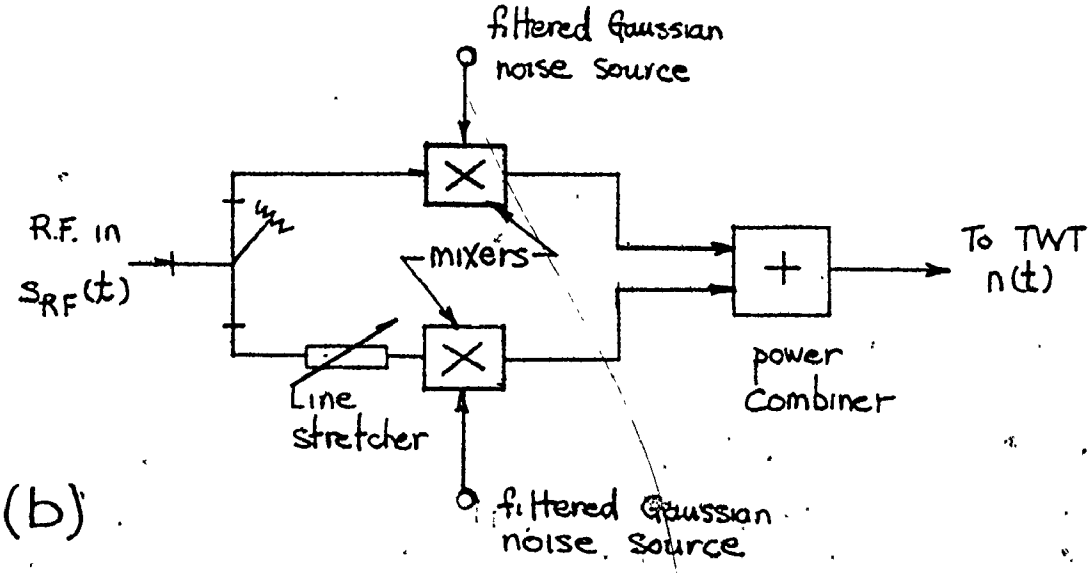

(b)

Fig. A-2 Power distribution network (a) general configuration, and (b) details of narrow-

f_o may be represented mathematically by [2-7]:

$$n(t) = n_c(t) \cos 2\pi f_o t - n_s(t) \sin 2\pi f_o t \qquad \text{(A-1)}$$

where $n_c(t)$ and $n_s(t)$ are independent, low-pass Gaussian noise processes. The quantities $n_c(t)$ and $n_s(t)$ are actually a Hilbert transform pair. The narrow-band noise generator in Fig. A-2(b) operates on the model of (A-1). The signal out of the mixer in the top branch of the figure is represented by the first term of (A-1), while by virtue of the line stretcher, (adjusted to a 1/4 wavelength corresponding to the R.F. frequency) the signal out of the lower mixer represents the second term. The two noise sources feeding the mixers are not actually a Hilbert transform pair; however, the received signal components corresponding to these two noise sources will become Hilbert transforms of each other after n(t) is transmitted and passed through the receiver I.F. filters (Fig. A-1). Therefore, this realization of the narrow-band noise generator accurately implements the mathematical model (A-1) for narrow-band noise.

A diagram of the L.O. generator is shown in Fig. A-3. As may be seen, this implementation follows the canononical form of the phase discrimination SSB generation technique [2-7], with the only difference being that a narrow-band 90^o

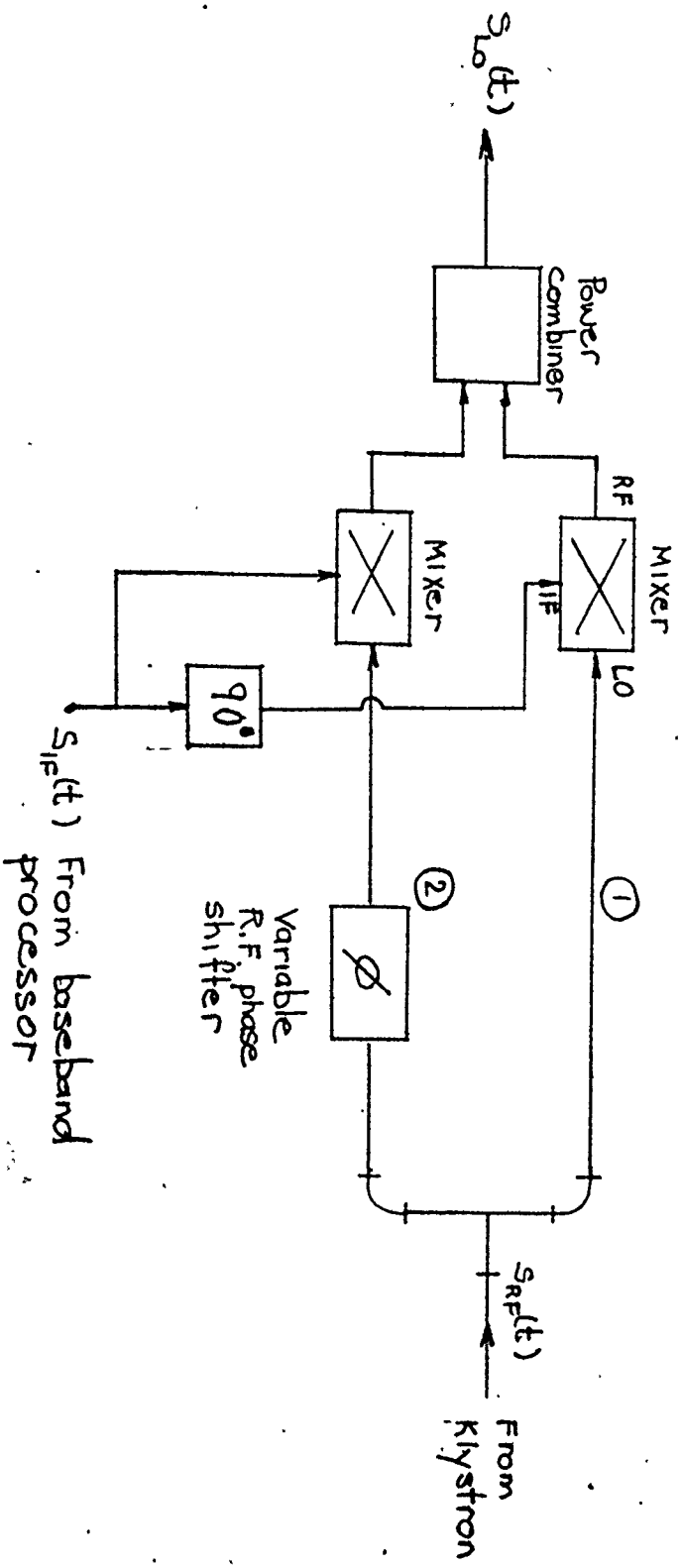

Fig. A-3 LO generator

phase-shifter is used instead of a wide-band Hilbert transformer. The variable R.F. phase-shifter is included so that the difference in path lengths 1 and 2 may be adjusted easily to 90 electrical degrees. In the practical implementation of the generator, the lower sideband was chosen to be suppressed. This suppression was in the order of 45 dB below the level of the upper sideband.

A.3 Receiver Configuration

The receiver section shown in Fig. A-1 is fairly straightforward. The receiver consists of a vertical array of N = 8 elements, spaced so that $d/\lambda = 1.681$. The distance between the transmit and receive antennas is 28.5 feet, which is just sufficient to assume far-field conditions. The received signals $x(n,t)$, $n=0, \ldots, N-1$, from each of the N = 8 array elements are heterodyned to an I.F. of 2 KHZ by a power-divided version of the signal $s_{LO}(t)$, thus producing the signal set $\{x_{IF}(n,t)\}$. The phase of the signal $x_{IF}(n,t)$ may be controlled by adjusting the line stretcher at the nth element as shown in the figure. Since the relative bandwidth of the signal $s_{LO}(t)$ is small, varying the length of the line has the effect of adding a controllable phase-shift to the $s_{LO}(t)$. This phase-shift is transmitted through the mixer to the signal $x_{IF}(n,t)$. When the array is aligned so that the Coho transmitter antenna is on

boresight, the magnitudes and phases of the signals $x_{IF}(n,t)$, n=0, ..., N-1 should be all equal.

By virtue of the method by which $s_{LO}(t)$ is generated, the trace of the signal $x_{IF}(n,t)$ for the nth element, corresponding to a pure CW transmit signal, is indiscernably different on an oscilloscope from the trace of a pure 2 KHZ tone produced by a signal generator. This fact is verified by Fig. A-4. The upper trace shows the "I.F. 2KHZ reference signal", as shown in Fig. A-1, straight from an HP 200CD signal generator, while the lower trace shows the received I.F. signal at the first element.

The received signal set $\{x_{IF}(n,t)\}$ is amplified and filtered before being fed into a baseband processor and multiplexer unit. The amplifier-units are built with 3140 and 741 operational amplifiers (op-amps), and have a voltage gain which is adjustable between 30 and 1000. The 3140 op-amps are used in the first amplification stage because of the very low noise voltage produced by these devices. The maximum output voltage swing which these amplifier units can deliver is about $\pm$ 5V. The filter-units are a 6-pole active-filter Chebyshev design, with a centre frequency of 2 KHZ, a total bandwidth B of 150 HZ, and a voltage gain of approximately unity. The filters were designed for a $\pm$1/2 dB passband ripple. Also included in the filter units are variable phase-shift sections. These are provided to give a

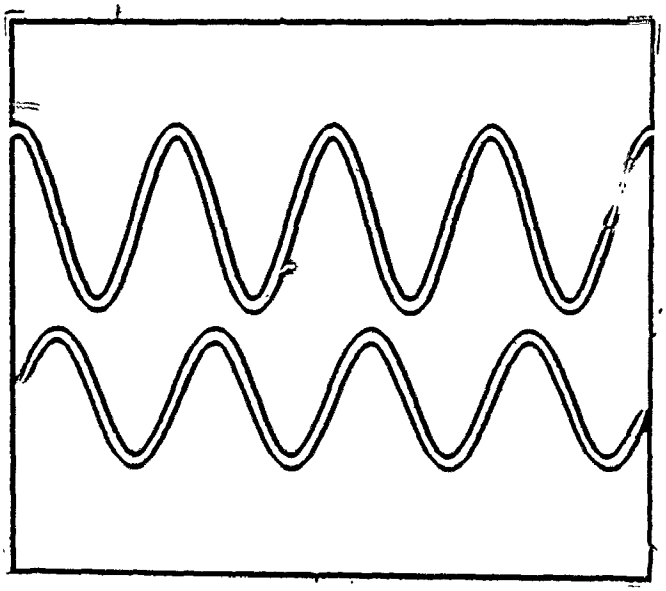

Fig. A-4 Oscilloscope traces of 2 KHz tones. The top is the trace from an HP 200CD signal generator, $s_{IF}(t)$, while the bottom is the amplified received I.F. signal from channel 7, $x_{IF}(7,t)$, when the Coho transmitter only is active.

Vertical scale: 0.5 V/div
Horiz scale: 0.2 mS/div

fine-tuning control for the phase-alignment procedure of each of the I.F. channels. Fine-tuning over a range of $\pm 15^{o}$ is possible using these extra phase-shift sections. Coarser adjustments outside this range must be made with the variable line stretchers on the R.F. mixers.

Figure A-5 shows the response of an HP audio spectrum analyzer to the signal $x_{IF}(0,t)$ out of the filter of the zeroth channel. The direct transmitter antenna is turned off completely, and the reflected antenna transmits pure narrowband noise of bandwidth 500 HZ. The response shown in the figure is then approximately the same as that which would occur if the receiver channel were excited by white Gaussian noise, and therefore corresponds to the frequency response of the amplifier/filter section of the zeroth receiver channel. The response shown is typical of that of the other channels.

The complete demodulation of the set $\{x_{IF}(n,t)\}$ to baseband is accomplished by a novel I-Q sampling technique. The method, along with variations, is discussed by Reilly and Haykin in [2-8], and will now be treated here.

The signal $x_{IF}(n,t)$ which is bandlimited to the interval $f_{IF} \pm B/2$ may be written (e.g. [2-7])

$$x_{IF}(n,t) = x_I(n,t)\cos(2\pi f_{IF}t) - x_Q(n,t)\sin(2\pi f_{IF}t) \qquad (A\text{-}2)$$

$$n = 0, \ldots, N-1$$

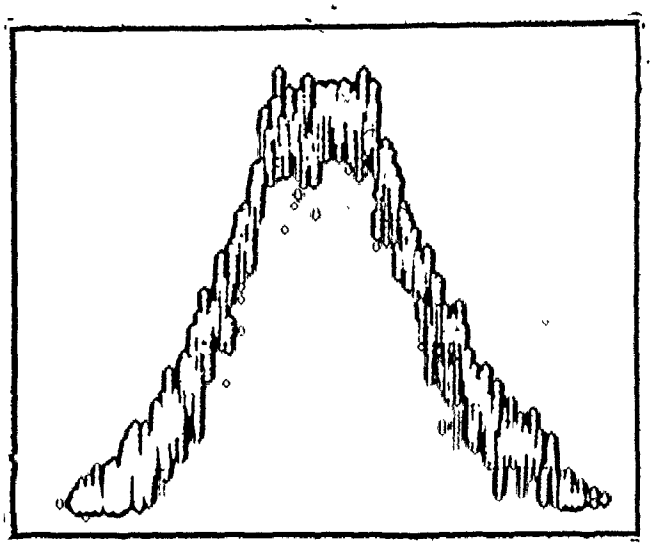

Fig. A-5 Audio spectrum analyzer response to I.F. channel 7, when the reflecting antenna transmits pure Gaussian noise. The response of the I.F. filter is evident.

Vertical scale: 10dB/div
Horiz scale: 100 Hz/div
Analyzer I.F. bandwidth: 10 Hz.

where $x_I(n,t)$ and $x_Q(n,t)$ are the in-phase I, and quadrature Q, baseband (lowpass) signal components respectively, and f_{IF} is the I.F. frequency (≡ 2 KHZ in this example). The bandpass sampling method must acquire from $x_{IF}(n,t)$ sampled versions of both $x_I(n,t)$ and $x_Q(n,t)$.

In conventional methods (as described in [2-7]), the I- and Q-components are obtained by feeding the signal $x_{IF}(n,t)$ from the nth element into two mixers, the local oscillator feeds of which are $\{\cos 2\pi f_{IF}t\}$ and $\{\sin 2\pi f_{IF}t\}$ respectively. After sampling the outputs of these mixers at a rate at least equal to 1/B seconds (where B is the total bandwidth of $x_{IF}(n,t)$), the sampling process is realized.

Note that this conventional sampling method requires two extra mixers in the demodulation of the signal from I.F. to baseband. Also, any practical implementation of this technique would be likely to require the use of D.C. amplifiers, which are much more cumbersome to implement than their A.C. counterparts. Both these requirements, would add greatly to the expense and overall complexity of the experimental system; therefore, it is desirable to seek alternative methods to effect the sampling of the received signal.

It would also be possible to demodulate to baseband in one step, thus avoiding the necessity of I.F. processing. The received signal x(n,t) would be fed into an X-band power

divider, and each output of the power divider fed into a separate X-band mixer, whose L.O. feeds are 90^{o} apart in phase. The two sampled mixer outputs would then represent sampled versions of the signals $x_I(n,t)$ and $x_Q(n,t)$, as required. However with this implementation, two X-band mixers and one X-band power divider are required per channel. These components are extremely expensive. The alignment of the L.O. feeds to each of the mixers is very difficult, and amplification must again be accomplished with D.C. amplifiers.

The new technique used with this experimental system avoids the pitfalls of both these conventional methods. In this case, the signal $x_{IF}(n,t)$ is sampled once at time instants iT_S, where $i = 0, 1, 2, \ldots, K-1$ and $T_S = m/f_{IF}$. The integer K is the number of samples gathered in the available data record. The role of the integer m will be discussed later. The signal $x_{IF}(n,t)$ is also sampled again at instants $iT_S + 1/4f_{IF}$. We will now show that the first set of samples corresponds to the sample set $\{x_I(n,iT_S)\}$, while the second corresponds to the set $\{x_Q(n,iT_S)\}$.

The signal at the output of the first sampler $x_A(n,i)$ may be obtained by evaluating (A-2) at times iT_S:

$$x_{Ai}(n) = x_I(n,iT_S)\cos(2\pi f_{IF} iT_S) + x_Q(n,iT_S)\sin(2\pi f_{IF} iT_S) \qquad (A-3)$$

$$i=0, 1, 2, \ldots, K-1$$

Since $f_{IF} iT_S = im$, which is integer, (A-3) becomes

$$x_{Ai}(n) = x_I(n, iT_S) \quad , \quad i=0,1,2,\ldots K-1 \tag{A-4}$$

Therefore, the first sampler output gives us our desired result; namely, a sampled version of the baseband signal $x_I(n,t)$ at the nth array element.

The signal at the output of the second sampler $x_{Bi}(n)$ may be obtained by evaluating (A-2) at times $iT_S + 1/4f_{IF}$:

$$\begin{aligned} x_{Bi}(n) = {} & x_I(n,\ iT_S + 1/4f_{IF}) \cos\left[2\pi f_{IF}\ (iT_S + 1/4f_{IF})\right] \\ & - x_Q(n,\ iT_S + 1/4f_{IF}) \sin\left[2\pi f_{IF}\ (iT_S + 1/4f_{IF})\right] \end{aligned} \tag{A-5}$$

Again recognizing that $f_{IF}\ iT_S$ is always integer, we have

$$x_{Bi}(n) = - x_Q(n,\ iT_S + 1/4f_{IF}) \tag{A-6}$$

Therefore, the second sampler output gives us a sampled version of the signal $x_Q(\cdot)$; however, the sampling instants at which $x_Q(\cdot)$ is evaluated in this situation are delayed by 1/4 of a period of the I.F. frequency with respect to the sampling instants used to obtain $x_I(\cdot)$. In some situations this time-delay effect may be objectionable; in others, it may not. In narrowband systems where the envelope of the

signal does not change significantly over the centre-frequency period, this time delay effect may be ignored. The experimental system we are describing here may be considered narrowband; therefore, no additional steps were taken to compensate for this time-delay effect of the Q-samples.

In the more general broadband situation, the effect of the time-delay induced on the Q samples by the sampling may be objectionable. In order to compensate for this effect, the Fourier transform $X_B(n,f)$ of $x_B(n,iT_S)$ must be considered. Since the Fourier transform of $x_B(n, iT_S-T_o)$ is $X_B(n,f)\cdot\exp[-j2\pi fT_o]$, the following quantities are a Fourier transform pair:

$$x_B(n, iT_S + 1/4f_{IF}) \overset{+}{\div} X_B(n,f)\ \exp[j2\pi f/4f_{IF}] \qquad (A-7)$$

where $\overset{+}{\div}$ denotes Fourier transformation. The effects of the time shift $1/4f_{IF}$ in $x_B(n, iT_S + 1/4f_{IF})$ may be corrected by multiplying its frequency domain representation $X_B(n,f)$. $\exp[j2\pi f/4f_{IF}]$ by the exponential factor $\exp[-j2\pi f/4f_{IF}]$ to produce the desired frequency representation $X_B(n,f)$ of the unshifted time signal $x_B(n,iT_S)$. This procedure is repeated over each of the N elements, for n=0, ..., N-1. Since the true spectrum of $x_{Bi}(n)$ is composed of periodic repetitions of $X_B(f,n)$ spaced by $1/T_S$ Hz, the phase correction procedure

need only be applied over the interval $-1/2T_S \leq f < 1/2T_S$ corresponding to one spectral period of $X_B(f,n)$ and not over the entire range $-\infty < f < \infty$.

We noted previously that the sampling time T_S is given by

$$T_S = m/f_{IF} \tag{A-8}$$

Therefore, we see by the nature of the above equation, this sampling technique provides a sample of $x_I(\cdot)$ and $x_Q(\cdot)$ every m periods corresponding to the frequency f_{IF}. In the physical implementation of this sampling technique, means were provided to adjust the parameter m between the values 1 and 2048. The actual value chosen during the course of the experiments was 5; this means that $T_S = 1/400$ seconds, and the spectral segments $X_B(n,f)$ repeat every 400 HZ.

A spectral estimate of the signal $x_{IF}(0,t)$ obtained by use of the Burg algorithm from samples derived from this new sampling method is shown in Fig. A-6. The estimate corresponds to the situation where the system was driven by Gaussian noise with bandwidth much wider than that of the I.F. filters, and where a record length K of 384 samples was used. We see that this spectral estimate agrees fairly well with the original I.F. filter design specifications. Note that this curve corresponds to the superposition of all the

periodic repetitions of the original spectrum (as shown in Fig. A-5) spaced 400 HZ apart. A description of the Burg MEM algorithm is given in Chapter 3. Through Fig. A-6, we see that the use of this new sampling technique leads to an accurate spectral estimate of the corresponding input process.

A.4 Baseband Processor System Configuration

The baseband processor and multiplexer, shown in Fig. A-1, looks after time multiplexing the received signals from each of the eight elements onto a single line which is fed to the computer analog/digital (A/D) converter. The processor is fed by an 8 KHZ master clock from which is derived the 2 KHZ I.F. reference signal $s_{IF}(t)$, and a "ready" signal, which is used to interrupt the computer and initiate the A/D conversion routines. There are two modes of operation of the processor. The first is the simultaneous or "Simult" mode, where the values of all eight input lines from the array elements are held simultaneously at a given sampling instant in an "I" register, and then held again 1/4 period later in a "Q" register. All 16 of these sampled values are then fed sequentially out to the A/D converter. This is the usual mode of operation. The second is the "sequential" or "Sequen" mode where, for a programmable number of periods, the zeroth channel is

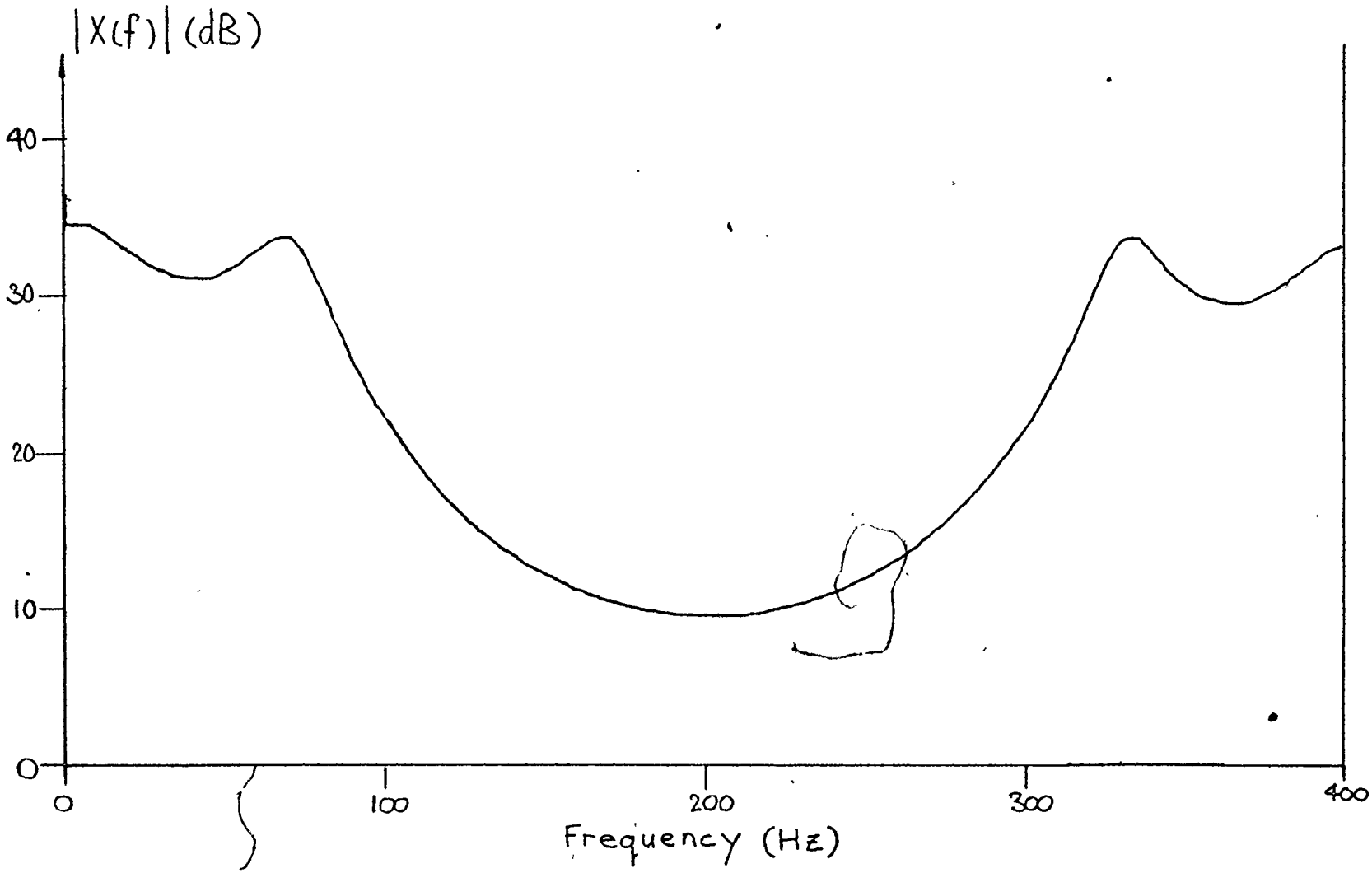

Fig. A-6 Burg spectral estimate of I.F. channel response using samples obtained by the novel sampling technique [2-8]

switched directly to the output line. An A/D conversion is performed 4 times per period of the frequency f_{IF}. After the appropriate count is reached, the first channel is then switched to the output line, and so on, until the count for the seventh line is reached. Then, the process repeats.

A more comprehensive understanding of the baseband processor may be appreciated by referring to Fig. A-7, which is shown for the Simult mode of operation. Each dashed box in the figure corresponds to a separate card of the complete system. On the left-hand side of the diagram are eight I and eight Q track/hold registers, each of which are fed by the eight analog input lines. When the appropriate "Hold" line is Lo, a direct connection is made between input and output lines. At the instant the HOLD line goes Hi, the input signals at that time instant are held fixed, and these fixed values are then transmitted to the corresponding output lines.

Let us now assume that the programmable counter has reached its count (set by a bank of 8 switches on the front panel). The counter then generates an output pulse, which under normal operating conditions, is transmitted through the logic box and is fed into the sequencer as an "initialize" pulse. This pulse initiates the sequencer to perform the following actions, which occur on successive pulses of the 8 KHZ clock.

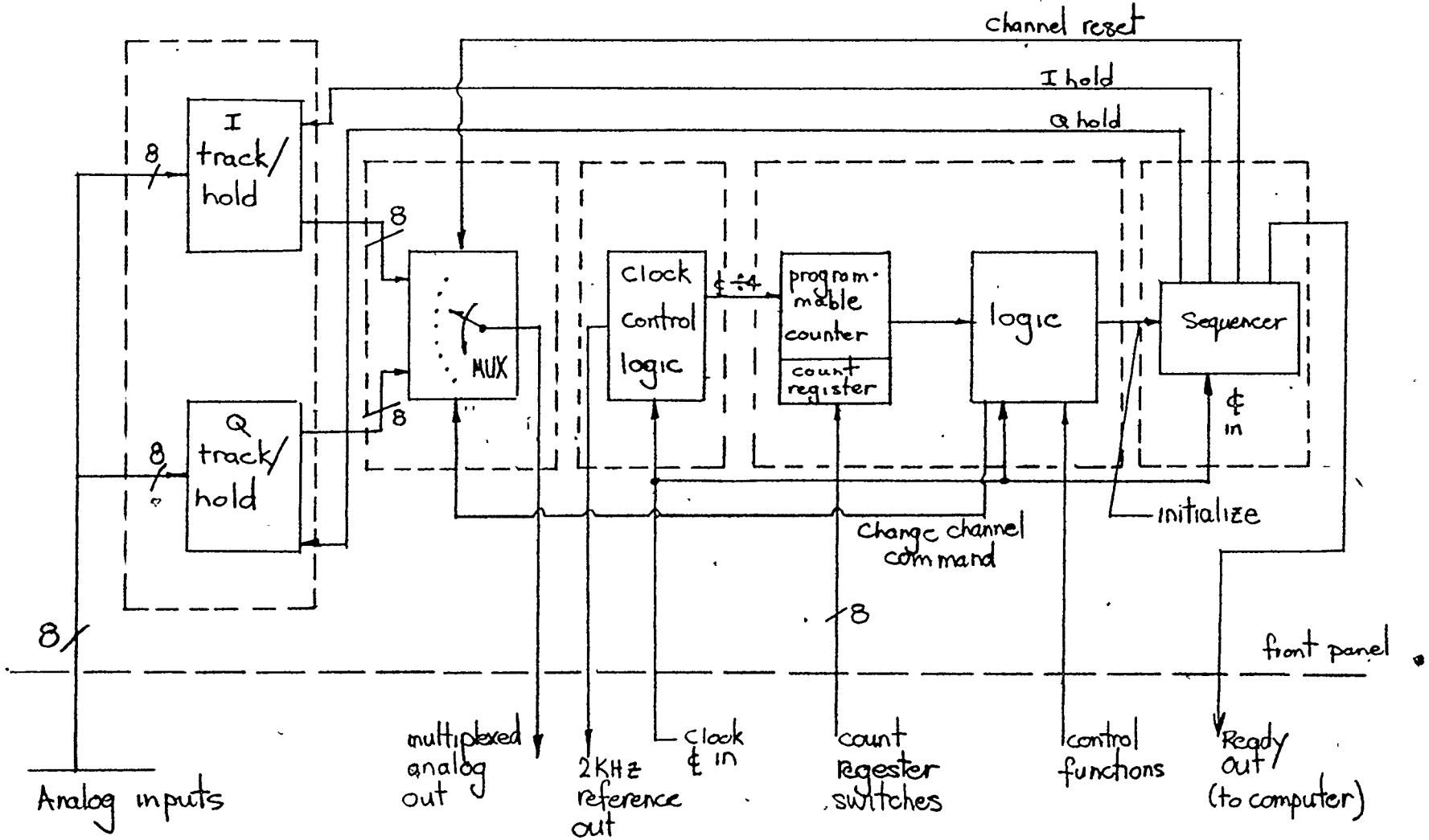

Fig. A-7 Block diagram of baseband processor

1. Set I-hold line high
2. Set Q-hold line high
3. Set Ready-out line high (computer interrupt)
4. Reset the multiplexer back to Channel 0.

The multiplexer section then advances one channel on each of the next 16 clock pulses. As shown in Fig. A-1, the A/D convertor is synchronized by the same 8 KHZ master clock that is used for the baseband processor. Therefore, we are guaranteed that one A/D conversion will be performed on each of the 16 multiplexer input lines per sample period. The 16 digital samples so obtained are then stored on disk to await further processing.

After this control sequence is executed, the processor idles until the next Initialize pulse is generated. In normal operation of this system, the count register is set on 5, (5 cycles of $s_{IF}(t)$) which means an Initialize pulse is generated every 20 clock pulses. Therefore, one I and one Q sample of $x_{IF}(n,t)$, for n=0, ... 7, is obtained every 2.5 mS, or every 5 cycles of $s_{IF}(t)$. A photograph of the complete baseband processor system is shown in Fig. A-8.

A.5 General Comments on the Experimental System

One of the important functions provided by the baseband processor is the generation of the 2 KHZ I.F. reference signal $s_{IF}(t)$. The 8 KHZ input clock is divided

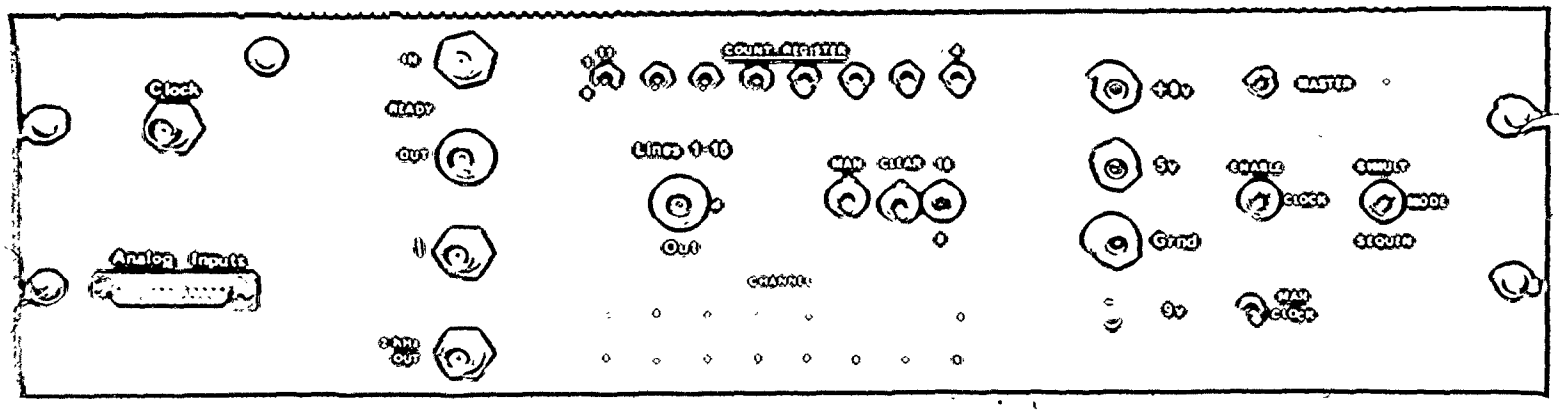

Fig. A-8 Photograph of baseband processor.

by 4, and this divided output is fed into a narrow bandpass filter with centre frequency 2 KHZ. The output of this filter is a clean 2 KHZ sine wave, and is used by the L.O. generator as shown in Fig. A-1.

It is seen that the baseband processor implements the new sampling technique as previously discussed. When the Initialize pulse occurs, all 8 analog inputs are held simultaneously on the rising edge of the I-hold line, thus providing the I-samples. Also, since the 8 KHZ clock is exactly 4 times the centre frequency of the $x_{IF}(n,t)$ signals, the rising edge of the Q-hold line (which occurs on the next clock pulse), again holds all 8 analog inputs simultaneously, but exactly 1/4 period later as required, thus providing the Q-samples.

An important feature of the design of this experimental setup is the immunity of the system to either drift and/or jitter in the R.F. source, or to drift in the master clock frequency. We have seen previously that the centre frequency of the received signals $x_{IF}(n,t)$ is insensitive to moderate jitter of the R.F. source. Also, because of the fact that all pertinent signals and control functions (i.e., the baseband processor clock, the A/D synchronization, and the I.F. reference signal $s_{IF}(t)$) are derived from the same master clock source, any drift in this signal will not adversely affect system performance. These

facts are verified by considering the case where a pure CW signal is transmitted by the direct antenna. The samplers will then always catch the received signals $x_{IF}(n,t)$ at the same point on their waveforms, and the respective numbers stored on disk do not change significantly from sample-to-sample, even over periods as long as an hour in duration.

It must be remarked at this point that the I.F. centre frequency of 2 KHZ which was used in this experimental system is unusually low. The reason for choosing this value was that the reliable A/D conversion rate on the CDC 1700 computer was only about 8 KHZ. Since it was desired to convert at a rate equal to 4 times the I.F. frequency the value 2 KHZ resulted. This value was also convenient because the I.F. amplifiers and filters could be implemented from inexpensive, easily available op amps.

There are several factors which contribute to the degradation of the overall system performance. The three most predominant of these listed in inverse order of effect, are receiver noise, 60 HZ hum, and elemental misalignment. The effect of receiver noise is almost negligible. Attainable signal-to-noise ratios (SNR) are in the order of 40 dB if receiver noise only is considered. The 60 HZ hum is about 25-30 dB down from the signal level, so we see that this factor dominates the effect of the receiver noise.

When the system is arranged so that only one transmitting antenna is aligned on the boresight of the array, all the received elemental signals should be adjusted so that their magnitudes and phases are identical. This is impossible to achieve exactly. Also, the phase difference of two elemental signals (for the case of CW transmission) should change linearly and smoothly as the inclination angle of the array is changed. However, because of mismatches in the receiver mixers and poor output-to-output isolation of the 8X-power divider shown in Fig. A-1, this phase variation is slightly ripply. Because of these two effects, the elemental signals will always be slightly misaligned, and as a result the system performance will be degraded. The rms error due to this effect is also about 25-30 dB below signal level.

In Table A-1 we show experimental data obtained from this system. The data entries are the I- and Q-components, and the corresponding magnitudes and phases, of each of the eight elemental excitations. The data corresponds to the situation where a pure CW signal is transmitted through both antennas. Both these antennas were arranged symmetrically about the boresight of the receiver array, and equal power was transmitted through each. We therefore see that the experimental environment used to produce these data simulates the multipath environment as depicted in Fig. 2-1,

for the case $\rho=1$. Also, the choice of parameters used in the generation of this data corresponds to those used to produce the curves shown in Fig. 2-3. The correspondence between the data produced by this experimental system for a particular set of parameter values, and that produced by the model (2-1) (for the same parameter values), is evident.

The data correspond to angular separations between the direct and reflected antennas for BW equal to 1.0, 0.5, 0.25 beamwidths (BW). The data corresponding to BW = 1.0 separation show considerable variation from element-to-element, and the whole 8-element spatial record extends over an entire spatial beat as produced by the interference pattern of the two radiators. However, note that the data corresponding to BW = 0.25 shows small variation even over the entire 8-element span of spatial samples. It is for this reason that the estimation of angular position is difficult when rays incident on the array are closely spaced together.

Data corresponding to different values of the parameter ψ (as defined in (2-1)) are shown in the table. We note that the effect of this parameter is to adjust the portion of the total field configuration pattern produced by the radiating environment that is visible to the receiving array.

In this appendix, an experimental system which was

I-component	Q-component	Magnitude	Phase (degrees)
-146	-469	491	-107
-522	-1669	1749	-107
-799	-2561	2683	-107
-819	-2970	3081	-105
-845	-2789	2914	-106
-605	-2238	2319	-105
-300	-1262	1297	-103
0	22	22	90

(a)

1439	-2367	2770	-89
1785	-2537	3102	-55
1730	-2444	2995	-54
1367	-1911	2350	-54
631	-990	1174	-57
-28	38	47	126
-705	1146	1346	121
-1373	1916	2357	125

(b)

Table A-1: Experimental data, with parameters corresponding to the curves in Fig. 2-3, for BW = 1. (a) ψ = -22.5 degrees, (b) ψ = -112.5 degrees.

I-component	Q-component	Magnitude	Phase (degrees)
-40	5	40	172
73	1447	1449	87
424	2549	2584	80
551	3542	3585	81
908	4742	4828	79
566	5749	5777	84
452	4970	4991	84
125	5996	5997	88

(c)

-2964	-2394	3811	-141
-1541	-1781	2355	-130
-717	-1011	1240	-125
11	64	65	79
1020	690	1232	34
1971	1778	2655	42
2411	2531	3496	46
3123	3606	4770	49

(d)

Table A-1 (cont'd): Experimental data, with parameters corresponding to the curves in Fig. 2-3, for $BW_o = 0.5$, (c) $\psi = 101.25^o$, (d) $\psi = 168.75^o$.

I-component	Q-component	Magnitude	Phase (degrees)
9	23	25	67
222	51	228	13
453	84	461	10
726	200	753	15
857	206	881	13
1027	199	1046	10
1262	232	1283	10
1370	268	1396	11

(e)

-7	-643	643	-90
-83	-426	434	-101
-33	-245	247	-97
13	-12	18	-41
-13	160	161	94
37	353	355	83
79	622	627	82
101	748	755	82

(f)

Table A-1 (cont'd): Experimental data, with parameters corresponding to the curves in Fig. 2-3, for BW = 0.25. (e) $\psi = 140.625^{\circ}$, (f) $\psi = 174.375^{\circ}$.

designed to simulate a predominant specular multipath environment was discussed in considerable detail. A novel I-Q bandpass sampling technique which was incorporated into the system was developed, and several results, indicative of the system performance, were presented.

APPENDIX B

Derivation of Expression for Residual Sum of Squares

A very important quantity used in statistical analysis is the sum of squares of the residuals (RSS). The residuals are the differences between the observed data and the corresponding values predicted by the model equation. Usually in statistical analysis, it is straightforward to evaluate the residual sum of squares once the parameters have been estimated. However, since many of the parameters of the estimator in Chapters 4 and 5 have been integrated out, it is not possible to estimate directly the quantity RSS in that particular case. It is therefore the purpose of this appendix to develop an expression which approximates the value of the residual sum of squares for use with the asymmetric ML estimator.

We may define the observed in-phase data by the following equation:

$$x_c(n) = f_c(n) + w_c(n) \qquad \text{(B-1)}$$

where the form of $f_c(n)$ is apparent from (5-1). Therefore,

$$\sum_n x_c^2(n) = \sum_n [f_c^2(n) + 2f_c(n)\ w_c(n) + w_c^2(n)] \qquad \text{(B-2)}$$

We now note that the quantity $w_c(n)$ accounts for any discrepancy between the model and the observed data. This

includes the effects of a model which does not adequately describe the underlying process, as well as noise.

We now assume that the residual $w_c(n)$ and the model are uncorrelated over the interval of interest.* That is,

$$\sum_n f_c(n)\ w_c(n) = 0 \tag{B-3}$$

After decomposing the $f_c(n)$ by the Gram-Schmidt process as discussed in Chapter 5, we may ascertain that

$$\sum_n f_c^2(n) = \sum_{k=1}^{2M} q_k^2 \tag{B-4}$$

where the symbols are defined as in Ch. 5. By substituting (B-4) and (B-3) into (B-2), we obtain

$$\sum_n x_c^2(n) \approx \sum_k q_k^2 + \sum_n w_c^2(n) \tag{B-5}$$

Let us now examine the expression for $L_{ck}(\phi)$ defined by (5-7), reproduced here for convenience

$$\begin{aligned} L_{ck}(\phi) &= \sum_n x_c(n)\ s_k(n) \\ &= \sum_n [f_c(n) + w_c(n)]\ s_k(n) \end{aligned} \tag{B-7}$$

Again, we assume that the residual $w_c(n)$ and the signal $s_k(n)$ are uncorrelated over the interval considered. Then,

$$\begin{aligned} L_{ck}(\phi) &\approx \sum_n f_c(n)\ s_k(n) \\ &= q_k \end{aligned} \tag{B-8}$$

---

* This always holds true for a least-squares fit. See, for example, [B-1].

where the last line follows by definition. Therefore,

$$\sum_k L_{ck}^2(\phi) \approx \sum_k q_k^2 \qquad \text{(B-9)}$$

By comparing (B-9) with (B-5), we get an approximate expression for the residual sum of squares of the in-phase components only

$$\sum_n w_c^2(n) = \sum_n x_c^2(n) - \sum_n L_{ck}^2(\phi) \qquad \text{(B-10)}$$

Using a derivation identical to that given above, an expression for the RSS pertaining to the quadrature data is given by

$$\sum_n w_s^2(n) = \sum_n x_s^2(n) - \sum_n L_{sk}^2(\phi) \qquad \text{(B-11)}$$

Equation (B-11) uses approximations corresponding to those used in the derivation of (B-10). We now make the additional assumption that the in-phase residuals are uncorrelated with the quadrature residuals. In this case then, the total RSS is given by

$$\text{RSS} = \sum_n w^2(n) = \sum_n w_c^2(n) + \sum_n w_s^2(n) \qquad \text{(B-12)}$$

Combining (B-10) and (B-11), and using (B-12) and (5-16), we obtain the desired result:

$$\text{RSS}(\underline{\phi}) = \sum_n x_c^2(n) + \sum_n x_s^2(n) - L_A^2(\underline{\phi}) \qquad \text{(B-13)}$$

As indicated by the notation, RSS is a function of $\underline{\phi}$. Note that RSS($\underline{\phi}$) given by (B-13) is positive semi-definite, and that RSS($\underline{\hat{\phi}}$), where $\underline{\hat{\phi}}$ is the ML estimate of $\underline{\phi}$, has the minimum value of RSS($\underline{\phi}$) for all valid $\underline{\phi}$.

APPENDIX C

Derivation of Quadratic Form

In this appendix, we shall develop the quadratic form which is required in forming a confidence region of the parameters $\underline{\phi}$.

First, we shall start by determining the equivalent linearized structure, which may be assumed for high SNR's. Some further manipulations leads to the desired formulation. We may start by writing the observed data x(n) in the form

$$x(n) = f(n,\underline{\phi}) + w(n)$$

$$n = 1, \ldots, 2N \qquad \text{(C-1)}$$

This form includes both the in-phase and quadrature data, and the indexes have been adjusted accordingly. The term $f(n,\underline{\phi})$ describes the elemental excitations in the absence of noise, and is similar in form to (5-1) except that it also includes the quadrature contributions.

Since $f(n,\underline{\phi})$ is nonlinear in $\underline{\phi}$, it may be expanded in a Taylor series about some aribitrary point $\underline{\phi}_o$

$$f(n,\underline{\phi}) \approx f(n,\underline{\phi}_o) + \sum_{k=1}^{M} \left[\frac{\partial f(n,\underline{\phi})}{\partial \phi_k}\right]\Bigg|_{\underline{\phi}=\underline{\phi}_o} (\phi_k - \phi_{ok}) \qquad \text{(C-2)}$$

$$+ \text{higher order terms}$$

where M is the number of parameters. Let the quantity $a_o(n,k)$ be defined as

$$a_o(n,k) = \left.\frac{\partial f(n,\underline{\phi})}{\partial \phi_k}\right|_{\underline{\phi}_{ok}} \qquad \text{(C-3)}$$

then

$$f(n,\underline{\phi}) \approx f(n,\underline{\phi}_o) + \sum_{k=1}^{M} a_o(n,k)(\phi_k - \phi_{ok}) + \text{higher order terms} \qquad \text{(C-4)}$$

In a manner similar to that used in Chapter 4, we may neglect the higher-order terms, and the function $f(n,\underline{\phi})$ is linearized with respect to $\underline{\phi}$. The approximation again is valid for high SNR. By substituting (C-4) into (C-1), we get

$$x(n) \approx f(n,\underline{\phi}_o) + \sum_{k=1}^{M} a_o(n,k)(\phi_k - \phi_{ok}) + w(n) \qquad \text{(C-5)}$$

Let us now define the N X M matrix $\underline{A}_o$ as

$$\underline{A}_o = \begin{bmatrix} a_o(1,1) & \cdots & a_o(1,M) \\ \vdots & \ddots & \vdots \\ a_o(N,1) & & a_o(N,M) \end{bmatrix} \qquad \text{(C-6)}$$

and the 2N- column vectors $\underline{X}$, $\underline{F}(\underline{\phi}_o)$, and $\underline{W}$ as the vectors comprising all the values corresponding to the equivalent lower case quantities. We may then write

$$\underline{X} - \underline{F}(\underline{\phi}_o) = \underline{A}_o(\underline{\phi} - \underline{\phi}_o) + \underline{W} \qquad \text{(C-7)}$$

Finally, let us define the 2N-vector $\underline{Y}_o$ as

$$\underline{Y}_o = \underline{X}_o - \underline{F}\ (\underline{\phi}_c) \tag{C-8}$$

and the M-vector $\underline{\beta}$ as

$$\underline{\beta} = \underline{\phi} - \underline{\phi}_o \tag{C-9}$$

We may then write

$$\underset{(2Nx1)}{\underline{Y}_o} = \underset{(2NxM)}{\underline{A}_o}\ \underset{(Mx1)}{\underline{\beta}} + \underset{(2Nx1)}{\underline{W}} \tag{C-10}$$

which is the desired linearized form describing the observed data. If the vector $\underline{W}$ is Gaussian, ML estimates $\underline{\hat{\beta}}$ of $\underline{\beta}$ may be obtained by linear least-squares regression [4-11], [4-12]. Once the model form has been linearized, the well-established theory of linear regression may now be applied to give expressions for the confidence regions of the parameters.

An interesting geometrical interpretation of linear least squares is shown in Fig. C-1. The object of least squares regression is to find that value of $\underline{\beta}$ which minimizes the quantity $S(\underline{\beta})$, given by

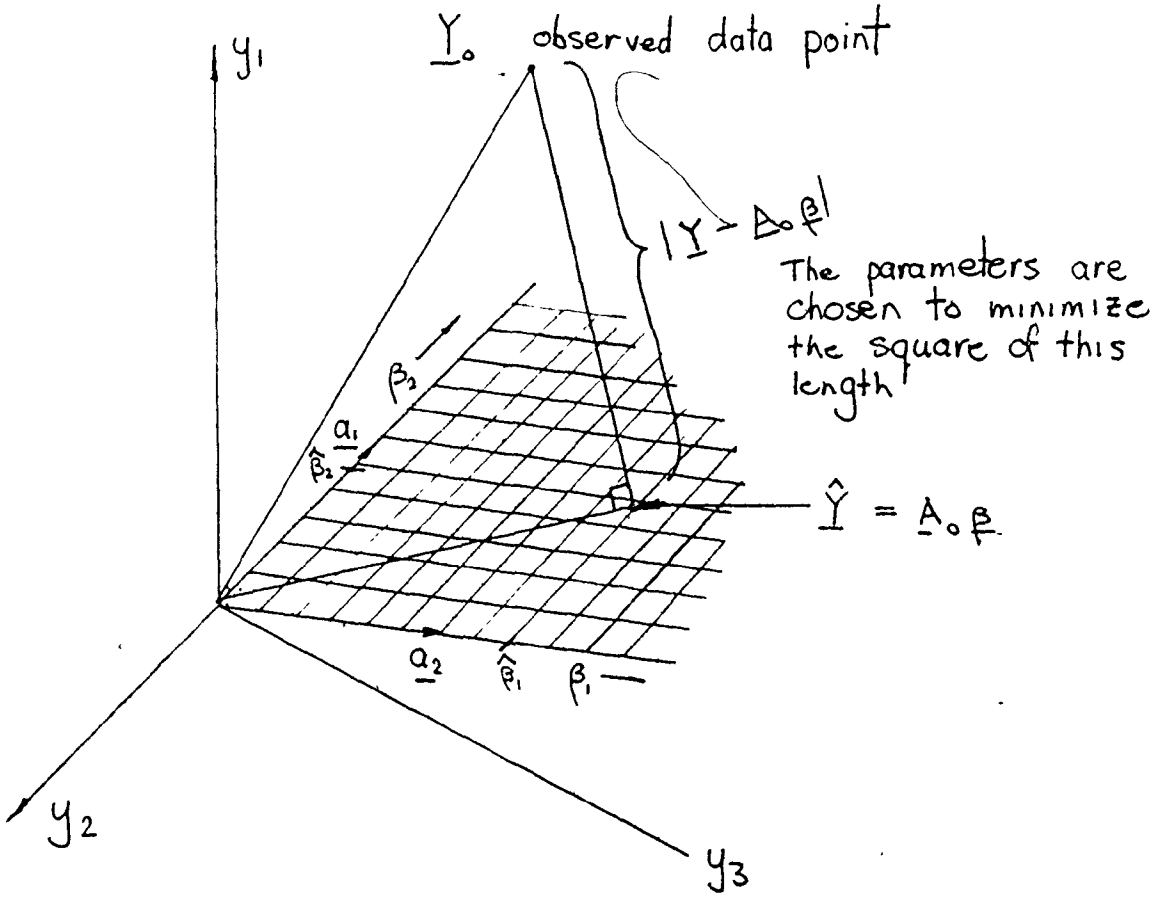

Fig. C-1 Geometric interpretation of linear least squares estimation

$$S(\underline{\beta}) = (\underline{Y}_o - \underline{A}_o \underline{\beta})^T (Y_o - \underline{A}_o \underline{\beta}) \qquad (C\text{-}11)$$

The quantity $S(\underline{\beta})$ is actually the sum of squares of the residuals about the estimate $(\underline{\beta})$.

Figure C-1 shows the configuration when N=3 and M=2. The point $\underline{Y}_o$ corresponds to the vector of observed data, and the cross-hatched plane (response plane) represents all possible values which may be taken on by the model. The point on this plane corresponding to the true value of $\underline{\beta}$ corresponds to the expectation of the observed data.

It is easy to ascertain, either geometrically or algebraically, that $S(\underline{\beta})$ is minimized by choosing $\underline{\beta}$ by dropping a perpendicular from the point $\underline{Y}_o$ to the response plane.

The value $\hat{\underline{Y}}$ as shown in Fig. C-1 is defined by

$$\hat{\underline{Y}} = \underline{A}_o \underline{\beta} \qquad (C\text{-}12)$$

and is the expected value of $\underline{Y}_o$.

Now, let us consider forming the quantity $S(\underline{\beta})$ about some other arbitrary value $\underline{\beta}^*$ of $\underline{\beta}$ in the response plane. The value $\underline{\beta}^*$ must be chosen so that (5-27) is still valid. We can write

$$
\begin{aligned}
S(\underline{\beta}^*) &= (\underline{Y}_o - \underline{A}_o\,\underline{\beta}^*)^T\,(\underline{Y}_o - \underline{A}_o\,\underline{\beta}^*) \\
&= (\underline{Y}_o - \hat{\underline{Y}} + \hat{\underline{Y}} - \underline{A}_o\,\underline{\beta}^*)^T\,(\underline{Y}_o - \hat{\underline{Y}} + \hat{\underline{Y}} - \underline{A}_o\,\underline{\beta}^*) \\
&= (\underline{Y}_o - \hat{\underline{Y}})^T\,(\underline{Y}_o - \hat{\underline{Y}}) + (\hat{\underline{Y}} - \underline{A}_o\,\underline{\beta}^*)^T\,(\hat{\underline{Y}} - \underline{A}_o\,\underline{\beta}^*) \\
&\quad + 2(\underline{Y}_o - \hat{\underline{Y}})^T\,(\hat{\underline{Y}} - \underline{A}_o\,\underline{\beta}^*) \qquad \text{(C-13)}
\end{aligned}
$$

The last term in (C-13) is zero, because the two vectors are orthogonal. The geometric configuration corresponding to (C-13) is shown in Fig. C-2, from which it may be ascertained that (C-13) is actually a statement of 'Pythagorus' theorem.

Since the second term in (C-13) also zero if $\underline{\beta}^* = \hat{\underline{\beta}}$, (by (C-12)), we may write

$$
\begin{aligned}
S(\underline{\beta}^*) - S(\hat{\underline{\beta}}) &= (\hat{\underline{Y}} - \underline{A}_o\,\underline{\beta}^*)^T\,(\hat{\underline{Y}} - \underline{A}_o\,\underline{\beta}^*) \\
&= (\hat{\underline{\beta}} - \underline{\beta}^*)^T\,(\underline{A}_o^T\,\underline{A}_o)\,(\hat{\underline{\beta}} - \underline{\beta}^*) \qquad \text{(C-14)}
\end{aligned}
$$

which is the linearized form of the desired result.

It is of interest to note that the variance covariance matrix $\underline{V}$ of $\hat{\underline{\beta}}$ may be shown to be [4-11]

$$\underline{V} = [\underline{A}_o^T\,\underline{A}_o]^{-1} \qquad \text{(C-15)}$$

Also, it may be shown that the above also corresponds to the "first derivative squared" form of the Cramer-Rao bound [4-3], and we note from (C-15) that the equality of the

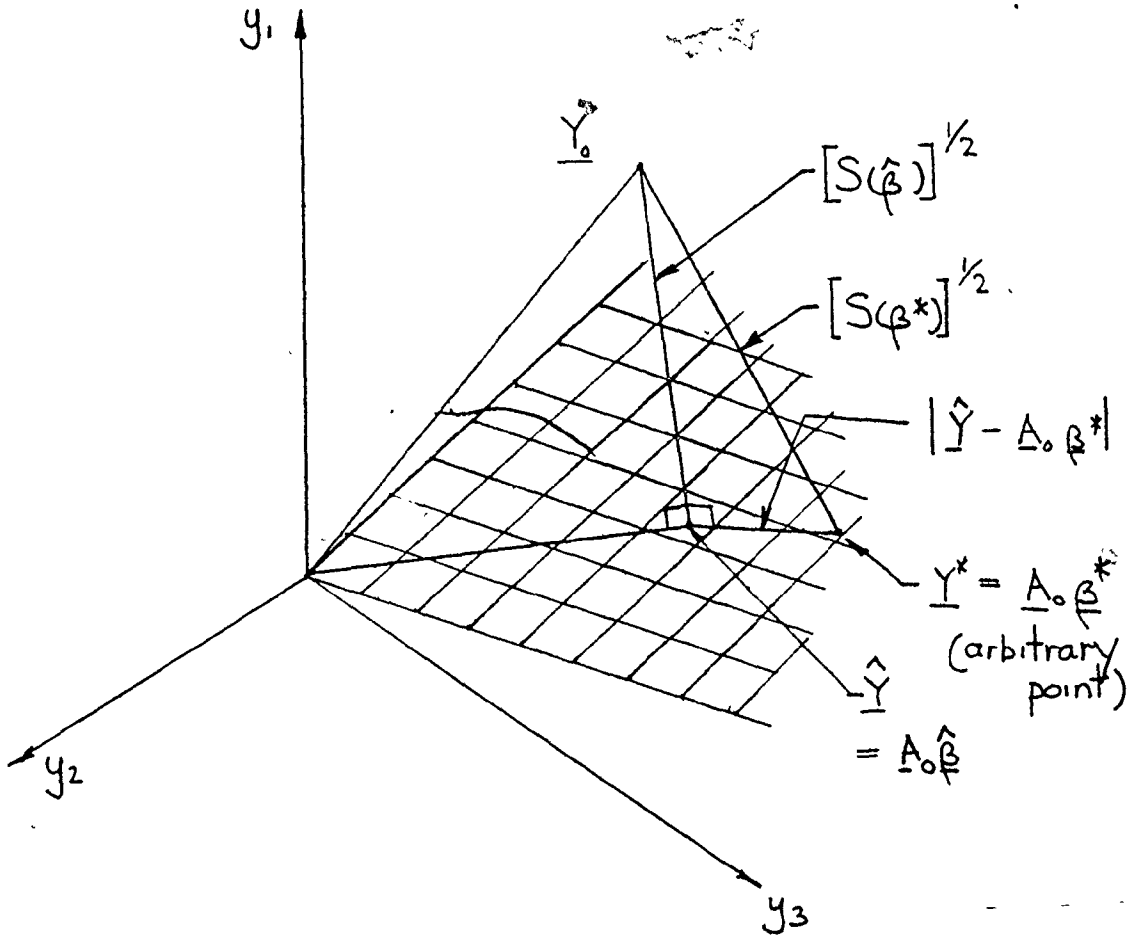

Fig C-2 Geometry of least squares about an arbitrary point Y^* in the response plane

bound is attained.

We now wish to translate the linearized result (C-14) into a form involving the actual variables of interest. By substituting (C-9) and (C-15) into (C-14), we get

$$S(\underline{\phi}^* - \underline{\phi}_o) - S(\underline{\phi} - \underline{\phi}_o) = (\underline{\hat{\phi}} - \underline{\phi}^*)^T \underline{V}^{-1} (\underline{\hat{\phi}} - \underline{\phi}^*) \qquad \text{(C-16)}$$

We have seen that $S(\underline{\phi})$ is the sum of squares of the residuals (RSS) about the point $\underline{\phi}$. Using the result of Appendix B, which states that for a given set of data, an approximation value of $S(\underline{\phi})$ (about the point $\underline{\phi}$), is given by $RSS(\phi)$:

$$RSS(\underline{\phi}) = -[L_A(\underline{\phi}) - \sum_n x_c^2(n) - \sum_n x_s^2(n)] \qquad \text{(C-17)}$$

The above is valid provided that the point $\underline{\phi}$ is close enough to $\underline{\hat{\phi}}$ for (5-27) to hold.

By substituting $RSS(\underline{\phi})$ for $S(\underline{\phi})$ in (C-16), we finally arrive at our desired result

$$RSS(\underline{\phi}^*) - RSS(\underline{\hat{\phi}}) \approx (\underline{\hat{\phi}} - \underline{\phi}^*)^T \underline{V}^{-1} (\underline{\hat{\phi}} - \underline{\phi}^*) \qquad \text{(C-18)}$$

We note that the matrix $\underline{V}$ may be determined through (C-15), or equivalently, may also be determined through the second derivative form of the C-R bound. By analogy with (5-17), the elements p_{ij} of the matrix $\underline{V}^{-1}$ are given by

$$p_{ij} = - E\left[\frac{\partial^2 L_A(\underline{\phi})}{\partial \phi_i \, \partial \phi_j}\right] \qquad \text{(C-19)}$$

It is of interest to note that the conjugate gradient optimization packages provide an estimate of the Hessian matrix, the elements of which are defined by (C-19). Therefore, an estimate of the variance-covariance matrix of the parameter values is provided "at no extra charge", by inverting the final Hessian matrix of the objective function.

APPENDIX D

Details of Computer Simulation

There are three basic computer simulation packages which were developed and used in the course of this work. They are simulations for (1) the MEM processor (both the Burg and the LS algorithms), (2) the symmetric ML, and (3) the asymmetric ML processors. The objective in each case was to establish the means and variances of the angle estimates obtained from each of the processors. The technique used in each case was basically the same. That is, data simulating the elemental excitations corresponding to a particular set of desired parameters was generated. Gaussian noise samples of zero mean and variance determined by the desired SNR were then added to the data. The bearing estimates were determined using any one of the three techniques mentioned above. The process was then repeated many times (usually 100-200), where for each trial, the same original data was used but different noise samples added on each occasion.

The variance of the estimated bearing estimates were calculated according to the following formula:

$$\text{Var}[x] = \frac{1}{M} \sum_i x_i^2 - \left(\frac{1}{M} \sum_i x_i\right)^2 \qquad \text{(D-1)}$$

where x_i are bearing estimates

M is the number of trials.

Whereas the mean is determined from

$$\text{Mean}[x] = \frac{1}{M} \sum_i x_i \qquad \text{(D-2)}$$

The use of equation (D-1) simplifies the computation of the variance considerably, compared to the conventional formula. All that is required using this method is the evaluation of the sum of squares, and the sum of the data. Note that neither of these evaluations requires extra storage.

A flowchart of the routine used to generate the data (DETDAT) is shown in Fig. D-1. In order to increase the efficiency of the program, the uncorrupted data are generated only on the first trial. On subsequent trials, a branch is made directly to the block which adds the Gaussian noise records.

We now consider the simulation of each of the processors in more detail.

D-1 MEM Processor

This is the most difficult simulation computationally because of the problem of identifying and processing the single peak spectra which occur with the Burg algorithm when ψ is close to zero, or with the LS algorithm when the SNR is below threshold. This package calls DETDAT to set up the

data, then calls either the LS or Burg algorithm programs to evaluate the PEF coefficients. After the spectra corresponding to these coefficients have been determined, the positions of the spectral peaks are identified and sorted into their proper categories. The single peak results are processed by recording the number of times of occurrance, and also calculating the mean and variance of the single-peak estimate. The spectral peak values are then accumulated into the individual sums in (D-1), and the procedure is repeated many times. The process is illustrated in the flowchart shown in Fig. D-2.

D-2 Symmetric ML Processor

This simulation package evaluates the performance of the symmetric ML processor discussed in Chapter 4. The inherent one-dimensional search is accomplished using the Golden Section search algorithm.

The details of this simulation routine are quite straightforward. First, as with the MEM simulation, the noisy elemental excitations are generated with routine DETDAT, for a symmetric incident wave configuration. Then, these data are passed to routine LATMAP which returned the corresponding ML estimate of ϕ given the data. LATMAP calls OBJFUN to evaluate the objective function by (4-33). The returned value of ϕ is then accumulated into the sums of

(D-1), and the estimation procedure repated many times, each with a different noise record. This simulation package is illustrated in the flowchart shown in Fig. D-3.

D-3 Asymmetric ML Processor

This simulation package is very similar to the symmetric case discussed previously. The exception is that one parameter per incident wave must be estimated per trial, a fact which precludes the use of the Golden section search algorithm. The maximization was accomplished with a routine IROC4, written by Prof. P.M. Reilly, University of Waterloo. IROC4 uses a conjugate gradient optimization technique, where the user supplies his own subroutine defining the objective function to be maximized. In this study, all simulations were performed for the case where two waves are incident on the array.

The asymmetric ML objective function uses the Gram-Schmidt orthonormalization procedure as discussed in Chapter 5. Also, the conjugate gradient methods require evaluation of the derivatives of the objective function with respect to each of the variables. These derivatives were evaluated numerically. The inverse Hessian matrix evaluated at the maximum of the objective function may be printed out by the program, in order to establish a confidence region on the parameter estimates.

The flowchart for the asymmetric ML simulation package is shown in Fig. D-4.

The computational procedure used with the analysis of the experimental data was virtually identical to the computer simulation procedures outlined here. The only difference is that the elemental excitations are obtained through a routine which reads the experimental data in from magnetic tape, instead of being generated artificially through subroutine DETDAT.

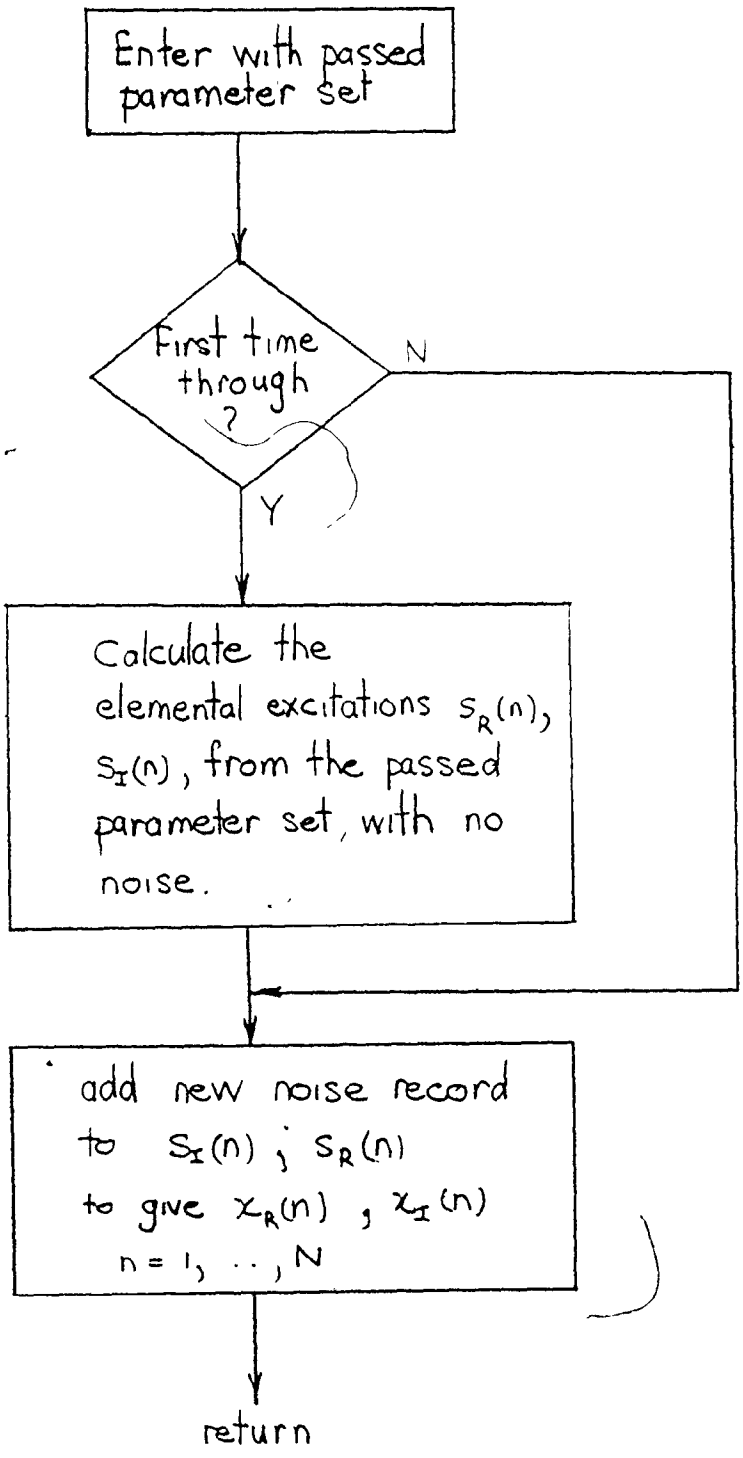

Fig. D-1 Flowchart for routine DETDAT

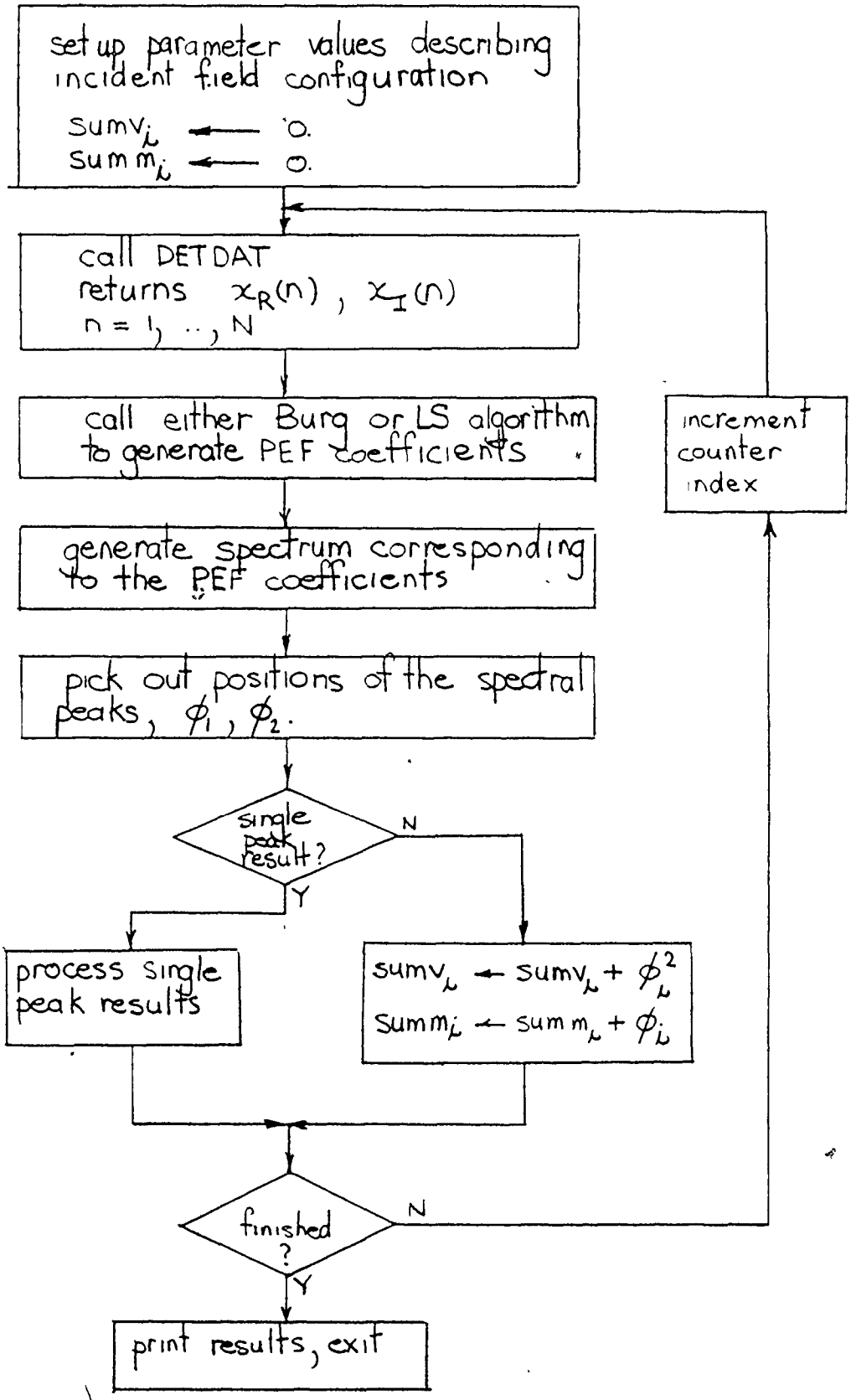

Fig. D-2 Flowchart of the MEM simulation program

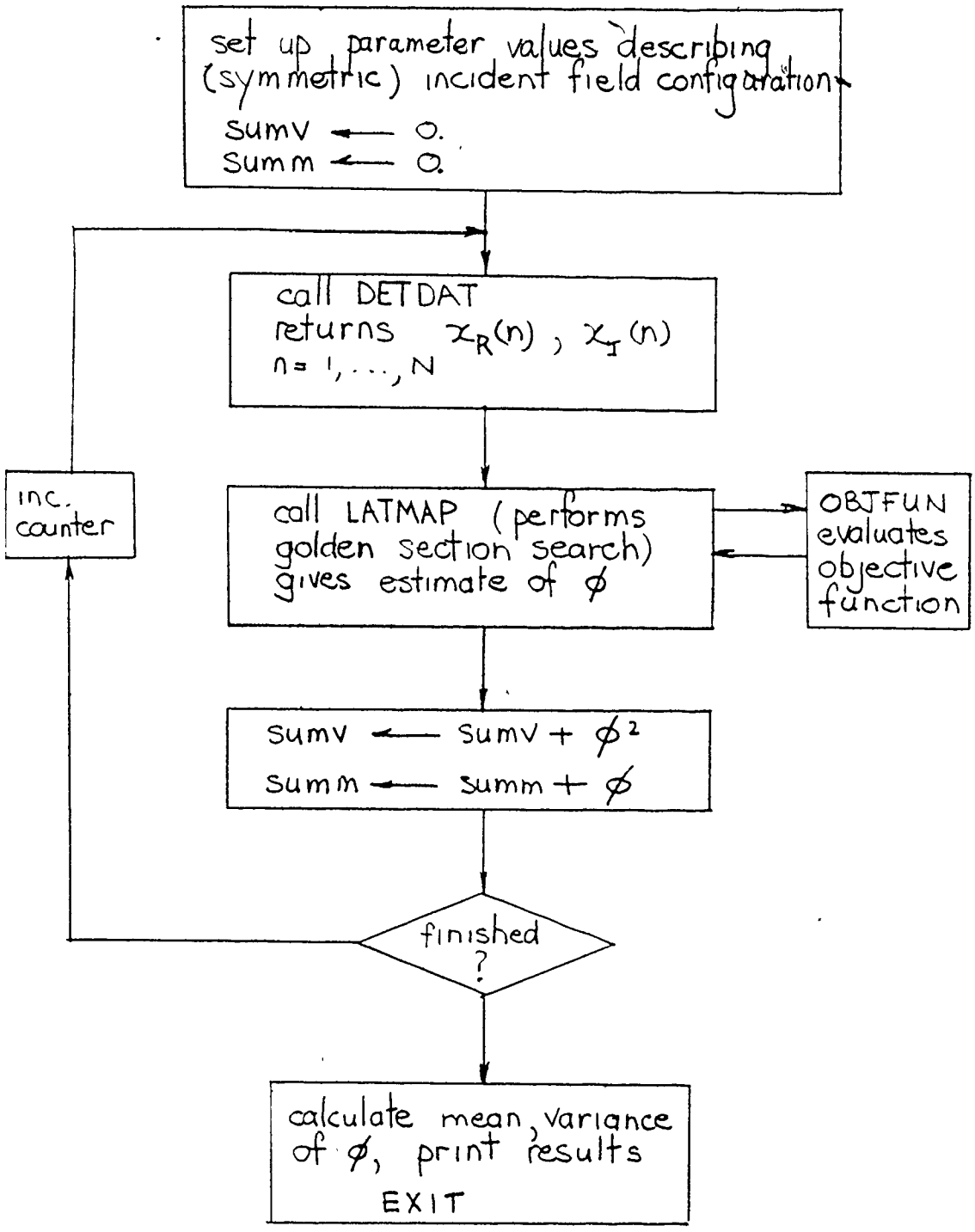

Fig. D-3 Flowchart of the symmetric ML simulation program

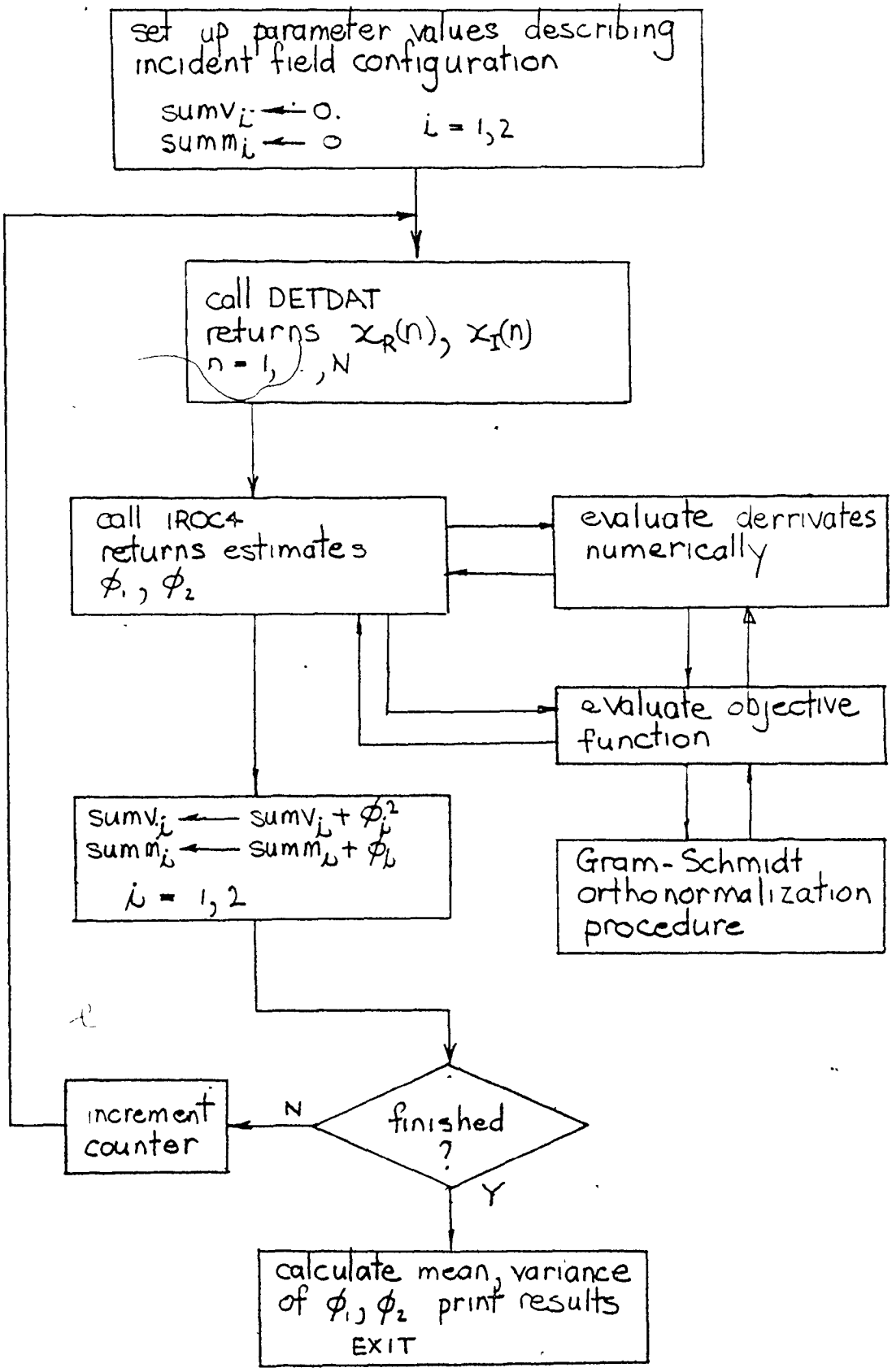

Fig. D-4 Flowchart of the asymmetric ML simulation program

APPENDIX E

Partitioning of the Sum-of-Squares

In this appendix we wish to show that the residual sum-of-squares can be approximately partitioned into two components. One component is the sum-of-squares due to a misfit between the observed data, in the absence of noise, and the values predicted by the model equation. This term will be called SSMM. An example of this component would be the differences between the data corresponding to three incident plane-waves (with no noise), and the model equation (5-1) for M=2 (i.e., only two incident plane-waves).

The second component in the partitioned sum-of-squares is that resulting from the noise term w(n) acting alone. We will call this component SSN.

The residual sum-of-squares $S_c(\underline{\phi},M)$ for a given value of M, due to the in-phase data component $x_c(n)$, may be written:

$$S_c(\underline{\phi},M) = \sum_n (x_c(n) - f(n,\underline{\phi},M))^2 \qquad \text{(E-1)}$$

where $f_c(n,\underline{\phi},M)$ is the value predicted by the model equation (5-1) for a given value of M. We may rewrite (E-1) as

$$S_c(\hat{\underline{\phi}},M) = \sum_n [(x_c(n) - f_{ct}(n,\hat{\underline{\phi}}) + f_{ct}(n,\hat{\underline{\phi}}) - f_c(n,\hat{\underline{\phi}},M)]^2 \qquad \text{(E-2)}$$

where $f_{ct}(n,\hat{\underline{\phi}})$ is the value given by the true model for the

correct (unknown) value of M. The above becomes

$$S_c(\underline{\phi},M) = \sum_n [f_{ct}(n,\underline{\phi}) - f_c(n,\underline{\phi},M)]^2 + \sum_n [x_c(n) - f_{ct}(n,\underline{\phi})]^2 + 2\sum_n [x_c(n) - f_{ct}(n,\underline{\phi})][f_{ct}(n,\underline{\phi}) - f_c(n,\underline{\phi},M)] \quad (E-3)$$

The first term in (E-3) is the sum-of-squares of the difference between the values predicted by the true model (which corresponds to what is actually going on) and the model actually used in the analysis. This component is thus $(SSMM)_c$.

The second term in (E-3) is the sum-of-squares of the pure noise components, and hence is $(SSN)_c$.

The third component in (E-3) is the correlation between the (white) noise signal and the difference signal (between the two model equations). As such, this term is justifiably assumed to be zero, for values of N greater than about 25. We may therefore approximate (E-3) as

$$S_c(\hat{\underline{\phi}},M) \cong (SSMM)_c + (SSN)_c \quad (E-4)$$

The residual sum-of-squares $S_s(\hat{\underline{\phi}},M)$ due to the quadrature data component $x_s(n)$ may be treated in a similar way. We therefore write:

$$S_s(\hat{\underline{\phi}},M) \cong (SSMM)_s + (SSN)_s \quad (E-5)$$

Finally, adding these two contributions together in the manner of (5-22), we obtain

$$S(\hat{\phi},M) \cong SSMM + SSN \qquad (E-6)$$

which was to be shown.